University of Liège
Applied Sciences
Aerospace and Mechanics

Optimization of thermal background suppression through Principal Component Analysis

Application to nulling interferometric observations of warm exozodiacal dust

Thesis submitted in partial fulfillment of the requirements for the degree of Doctor of Philosophy (PhD) in Engineering Science
submitted by

Hélène Rousseau

supervised by:
prof. Jérôme Loicq
co-supervised by:
prof. Denis Defrère
doct. Steve Ertel
prof. Virginie Faramaz-Gorka

Liège, June 2025

Université de Liège / University of Liege

THÈSE / THESIS

pour obtenir le grade de / to obtain the rank of

DOCTEUR DE L'UNIVERSITÉ DE LIÈGE /
PHD OF THE UNIVERSITY OF LIEGE

présentée par /presented by

Hélène Rousseau

Thèse dirigée par / Thesis directed by **Jérome Loicq**
Et co-dirigee par / And co-directed by **Denis Defrère, Steve Ertel**

Préparée au sein du **Département de sciences appliquées d'aérospatiales et mécanique** et de **l'Observatoire Steward**
Prepared in the **Departement of applied sciences in aerospace and mechanis** and **Steward Observatory**

Optimization of thermal background suppression through Principal Component Analysis

membres du jury / jury members:

ABSIL Olivier, Professeur (membre du comité de thèse), Université de Liège, Belgique, olivier.absil@uliege.be
CANTALLOUBE Faustine, Docteur, Université de Grenoble, France, faustine.cantalloube@univ-grenoble-alpes.fr
DEFRERE Denis, Professeur (co-superviseur), Université Catholique de Louvain, Belgique, denis.defrere@kuleuven.be
ERTEL Steve, Docteur (co-superviseur), Université d'Arizona, États-Unis d'Amérique, sertel@lbto.org
FARAMAZ-GORKA Virginie, Professeur (co-superviseur), Université d'Arizona, États-Unis d'Amérique, vfaramaz@arizona.edu
LOICQ Jerome, Docteur (superviseur), Université de Technologie de Delft, Pays-Bas, j.j.d.loicq@tudelft.nl
VAN DROOGENBROECK Marc, Professeur (président de jury), Université de Liège, Belgique, m.vandroogenbroeck@uliege.be

University of Liège
Applied Sciences
Aerospace and Mechanics

Optimization of thermal background suppression through Principal Component Analysis

Application to nulling interferometric observations of warm exozodiacal dust

Thesis submitted in partial fulfillment of the requirements for the degree of Doctor of Philosophy (PhD) in Engineering Science
submitted by

Hélène Rousseau

supervised by:
prof. Jérôme Loicq
co-supervised by:
prof. Denis Defrère
doct. Steve Ertel
prof. Virginie Faramaz-Gorka

Liège, June 2025

Résumé

En astrophysique, l'infrarouge moyen ou thermique permet de sonder pratiquement tout, depuis la naissance de notre univers tout entier à la naissance des exoplanètes. De manière générale, l'infrarouge moyen ou thermique peut aussi sonder à peu près tout, depuis l'atmosphère terrestre jusqu'à la chaleur d'un ordinateur. En d'autres mots, en infrarouge moyen, le background thermique est une limite majeure à la sensibilité des observations astronomiques. Durant cette thèse, nous avons développé une méthode de soustraction de background basée sur l'Analyse en Composante Principale (PCA). Cette méthode a, à l'origine, été développée dans le contexte du survey interférométrie de nulling en bande N, Hunt for Observable Signature of Terrestrial Systems (HOSTS), et incorpore dans le pipeline dédié à la soustraction du background de ses données. Initialement, la soustraction du background du pipeline utilise des régions largement en dehors de la position de l'étoile pour estimer le background, résultant en une procédure sensible aux variations spatiales du background. Notre nouvelle méthode prend en compte ces variations et améliore l'exactitude de la soustraction du background. Plus généralement, cette méthode peut aussi s'appliquer à l'imagerie de haut contraste et à la photométrie d'ouverture, que nous présentons également.

En plus de sa soustraction imparfaite et ses structures résiduelles spatiales, la variation temporelle du background peut aussi limiter la sensibilité des données. De plus, la correction du background est généralement construite à partir d'images acquises avant et après les images scientifiques, et le background peut changer entre ces expositions. Cela introduit une erreur temporelle dans la soustraction du background, limitant son exactitude et sa précision. Pour cela, nous avons développé une seconde méthode basée sur PCA pour corriger les variations temporelles du background, en addition des variations spatiales corrigées par la première méthode. Dans cette thèse, nous présentons les résultats obtenus avec la méthode du PCA temporel ainsi que ses actuelles limites.

Finalement, nous nous concentrons sur un set de données spécifique, 110 Her, pour lequel le survey HOSTS a détecté une quantité significative de poussière exozodiacale. Cette poussière, orbitant dans et autour de la zone habitable (HZ), peut cacher des exoplanètes en son sein. Détecter et comprendre cette poussière est donc de première importance pour préparer les futures missions d'imagerie directe dédiées à la détection et à la caractérisation de planètes semblables à la Terre. La quantité de poussière détectée dans le système 110 Her empêcherait la détection de planètes telluriques. Cependant, la modélisation de ce système, présentée dans cette thèse, suggère que la poussière orbite plus loin, permettant la détection d'exoplanètes dans le HZ. Nous présentons également l'impact sur la modélisation de la soustraction du background par PCA.

Abstract

Astronomically speaking, mid-IR/thermal emission can be used to probe pretty much anything in between the birth of our entire universe and the birth of exoplanets. Generally speaking, mid-IR/thermal emission can also be used to probe pretty much anything in between the Earth atmosphere and the heat of a computer. In other words, at mid-IR wavelengths, thermal background emission is a major limit to the sensitivity of astronomical observations. During this thesis, we developed a Principal-Component-Analysis(PCA)-based method of thermal background subtraction. The method was primarily developed in the context of N-band (11 μm) nulling interferometric data obtained by the Hunt for Observable Signature of Terrestrial Systems (HOSTS) survey, and incorporated into the dedicated pipeline. Initially, the pipeline's background subtraction used regions well outside of stellar positions for background estimates, leading to a procedure sensitive to spatial variations of this background. Our new method accounts for these variations and increases the accuracy of background subtraction. More generally, this method also finds its applications in high-contrast imaging and aperture photometry, which we present as well.

In addition to imperfect background subtraction, resulting in residual spatial structures, the sensitivity of the data can also be limited by the temporal variation of the background. Indeed, the background correction is usually built on images acquired before and after the scientific frames, and the background might change between these exposures. This situation leads to the introduction of a temporal error in the correction, which might limit both the accuracy and the precision of the background subtraction. In order to tackle this problem, we developed a second PCA-based method to correct the temporal background variations in addition to the spatial variation corrected by the first method. In this thesis we present the results obtained with this temporal-PCA-based method, as well as its current limitations.

Finally, we focused on a specific dataset among the HOSTS survey, 110 Her, for which the HOSTS survey has detected a significant amount of exozodiacal dust. This dust, lying in and around the habitable zone (HZ), can outshine rocky planets and hide them. Detecting and understanding this dust is thus of primary importance to prepare future direct imaging missions dedicated to the detection and characterization of Earth-like planets. The amount of dust found in 110 Her would prevent the detection of terrestrial planets. However, the modeling of this system, presented in this thesis, suggests that the dust is located further away from the star than the HZ and might thus not prevent exoplanet detection in the HZ. We also present the impact on the modeling that PCA background subtraction would have.

Acronyms

1Nod background library with 1 adjacent Nod

2Nod background library with 2 adjacents Nod

ADI Angular Differential Imaging

ADU Analog Digital Unit

AllNod background library with All empty Nods

ALMA Atacama Large Millimeter Array

AO Adaptive Optics

AP Aperture Photometry

ATs Auxiliary Telescopes

AU Astronomical Unit

BLINC BraceweLl Infrared Nulling Cryostat

CAL CALibrator target

CHARA Center for High Angular Resolution Astronomy

DRAGONFLY

ELTs Extremely Large Telescopes

E-ELT European Extremely Large Telescopes

EEID Earth Equivalent Insolation Distance

FLUOR Fiber Linked Unit for Optical Recombination

FOV Field Of View

FWHM Full Width at Half Maximum

GLINT Guided-Light Interferometric Nulling Technology

GMT Giant Magellan Telescope

HCI High Contrast Imaging

HOSTS Hunt for Observable Signature of Terrestrial Systems

HWO Habitable Worlds Observatory

HZ Habitable Zone

JCMT James Clerk Maxwell Telescope

JouFLU Jouvence of FLUor

JWST James Webb Space Telescope

KIN Keck Interferometer Nuller

L1/2/ Level 1/2 files

LBT Large Bicnocular Telescope

LBTI Large Binocular Telescope Interferometer

LIFE Large Interferometer For Exoplanets

MC Monte Carlo

MCMC Markov Chain Monte Carlo

METIS Mid-infrared ElT Imager and Spectrograph

MMT Multiple Mirror Telescope

NIC Nulling Infrared Camera

NOMIC Nulling-Optimized Mid-Infrared Camera

NOTT Nulling Observations of exoplaneTs and dusT

NSC Nulling Self Calibration

OB Observation Block

PA Position Angle

PCA Principal Component Analysis

PDI Phase Differential Imaging

PHASECam PHASE Camera

PSF Point Spread Function

RDI Reference-star Differential Imaging

RMS Root Mean Square

ROI Region Of Interest

SCEXAO Subaru Coronagraphic EXtreme Adaptive Optics

SCI SCIentific target

SCUBA Submillimetre Common-User Bolometer Array

SDI Spectral Differential Imaging

SED Spectral Energy Distribution

SNR Signal to Noise Ratio

SVD Singular Value Decomposition

TMT Thirty Meter Telescope

TPCA Temporal Principal Component Analysis

UT Universal Time

UTs Unit Telescopes

V principal component Vector

VIP Vortext Image Processing

VLT Very Large Telescope

VLTI Very Large Telescope Interferometer

VM principal component Vector Masked

WISE Wide-field Infrared Survey Explorer

WSPSF Without Subtraction of the Point Spread Function

Contents

Chapter 1

Context and thesis outline

Contents

1.1 Introduction

Since the first exoplanet detection in 1995 by Mayor & Queloz (1995), the number of new discoveries has never ceased to increase, reaching several thousands in the span of the last thirty years (NASA Exoplanet Archive). As the number of detections has grown, we have discovered an extremely wide variety of systems and planets, and the field of exoplanetology is now operating its transition from its detection era to its characterization era. With incrinsingly precise ground-based instruments, such as GRAVITY (Gillessen *et al.,* 2010), and the launch of new space-based facilities, such as the James Webb Space Telescope (Gardner *et al.,* 2006), atmospheric spectra of brown dwarf and giant planets have been obtained with unprecedented precision. Future ground-based Extremely Large Telescopes (ELTs) – such as the European Extremely Large Telescope (E-ELT, Gilmozzi & Spyromilio, 2007), the Thirty Meter Telescope (TMT, Sanders, 2013), and the Giant Magellan Telescope (GMT, Fanson *et al.,* 2022) – and space-based missions – such as the Habitable World Observatory (Decadal Survey) – are dedicated to the direct imaging and characterization of terrestrial-like planets in their habitable zones. Thus, these missions will be a vast improvement in terms of the angular separation at which direct imaging is usually performed. In addition, exoplanets detected so far via direct imaging are also preferentially massive giant planets, and being able to detect small rocky planets will be another improvement brought by these facilities, this time in terms of sensitivity.

Facilities dedicated to directly image Earth-like planets in their habitable zones face two main challenges: i) the contrast between the star and the planet, which

Figure 1.1: Zodiacal light seen from Mount Teide, in the Canary Islands, Spain. Image credit: StarryEarth Flickr/CC BY-NC 2.0

requires an effective way to suppress starlight, such as a coronagraph or via nulling interferometry, and ii) the inner working angle, which constitutes a real challenge when using a coronagraph. However, in the context of ground-based observations, the Earth atmosphere is equally challenging due to its own thermal emission. This is particularly true at mid-infrared wavelengths, where the star-planet contrast is at its best for Earth-like planets. Those challenges are well-known within the exoplanetary science community. However, another less known challenge is that of the presence of exozodiacal dust (Roberge *et al.,* 2012).

Similarly to the Zodiacal cloud in the solar system (see Figure 1.1), made of micrometer-sized dust grains in which the Earth, Venus, and Mars are embedded, exozodiacal dust is defined as the dust lying in and around the habitable zone of their hosts stars. Exozodiacal dust emits at infrared wavelengths and scatters visible light from their host star. In our solar system, the amount of dust is rather small (1 zodi). However, if we were to look at the solar system from the outside, the zodiacal cloud would be the brightest component after the Sun at mid-infrared wavelengths (Defrère *et al.,* 2012). Such an effect could severely hinder our efforts to detect Earth-like planets in their habitable zones, and it is thus important to better characterize exozodiacal disks.

Currently, we are limited by the sensitivity of our exozodis observations, which prevents both fainter detections and their precise characterization. One of the main factors that limits this sensitivity is the imperfect thermal background removal (Defrère *et al.,* 2016). It introduces significant errors and uncertainties in the data that prevent

strong detections of exozodiacal dust levels lower than several tens that of the Zodiacal cloud, and leads to large error bars in the measurements, preventing in turn strong constraints on the structure of those disks to be set. Improving the thermal background removal is thus of primary importance to better understand this dust and to prepare future habitable zone exoplanet direct imaging missions. This is the topic of this thesis.

1.2 Observing Exozodiacal dust

How can we detect the exozodiacal dust? The straightforward solution would be to measure the photometry of the star and to extract the infrared excess which comes from the exozodiacal dust. Unfortunately, the current precision of this technique barely allows us to detect extremely bright exozodis , that is, more than a thousand times brighter than the zodiacal cloud. In order to detect fainter exozodis, one needs to spatially resolve the habitable zone. At visible wavelengths, this requirement might not pose a strong challenge; however, the contrast between the starlight and the light scattered by an exoplanet (10^{-10}, Kasper *et al.,* 2017; Wagner *et al.,* 2021; Werber *et al.,* 2023) or the disk is then virtually impossible to achieve .

The contrast is more favorable at mid-infrared wavelengths (10^{-7}, Kasper *et al.,* 2017; Werber *et al.,* 2023), however, the resolving power of interferometry is required to spatially resolve the habitable zone: indeed, combining the signals from two telescopes separated by a given distance yields the resolution of a telescope whose primary mirror would have a radius equal to that separation (see Section 2.1.1). The Very Large Telescope Interferometer (VLTI), the Center for High Angular Resolution Astronomy (CHARA) array, the Atacama Large Millimeter Array (ALMA), the Keck Interferometer, and the LBTI are a few examples of facilities and instruments that make use of this powerful technique.

However, the resolving power of interferometry is not sufficient in itself. Indeed, one also needs to subtract the bright light of the star to be able to detect the much fainter light coming from the exozodiacal dust. In the context of exoplanets' detection, observers face a similar challenge and usually make use of coronographs for starlight suppression. One of the drawbacks of this method is that it significantly limits the inner working angle of the instrument. In fact, the habitable zone is often masked by the coronograph itself. Evidencing exozodiacal dust with coronography is therefore severely restricted, as the region of interest would almost systematically fall behind the coronograph. To combine starlight suppression and small inner working angle, one needs to add nulling to interferometry.

Nulling interferometry allows us to suppress the starlight by making the light from the two (or more) telescopes destructively interfere. The resulting interferometric pattern presents a destructive fringe on the axis of sight, at the star position, effectively suppressing its light. While all the light coming from on-axis sources will be suppressed,

Figure 1.2: The lighthouse, the firefly and the fog analogy. Image credits: Arron Anderson (two left images), JamieZink (right image). Detecting an exoplanet with direct imaging in a system with an exozodical disk is comparable to distinguishing a firefly next to a light house, at a distance of 10 km, and through fog.

any off-axis emission, such as that of an exozodiacal dust cloud, will be transmitted, and photometric measurements of this emission can be performed. This naturally describes a perfect case, where the starlight is totally suppressed, the atmosphere is not disturbing the observation in the slightest, and the instrument is perfect. In a more realistic case, the observations need to be properly reduced to remove as much background and noise coming from the atmosphere and the instrument, and thoroughly calibrated.

1.3 Context: Direct Imaging, Exozodiacal Light, and LBTI/HOSTS Survey

When using exoplanet direct imaging, there is a widely used analogy to describe the challenges that this method has to overcome: the lighthouse and the firefly. Directly imaging exoplanets is comparable to distinguishing the light of a firefly next to that of a lighthouse, at a distance of ten kilometers. This straightforwardly illustrates the challenge due to the contrast between the planet and its host star, but also the difficulty to separate the two sources of light. This analogy is also popular among the exozodiacal community, but with a small addition: the lighthouse, the firefly, and the fog. We illustrate this analogy with Figure 1.2

What if fog adds up to those two already very challenging problems? That is in fact the very reason why it is so important to study exozodis to prepare Earth-like planet detection in the habitable zone of their host star. The fog will be problematic not only in terms of contrast and separation, but also because the planets embedded in it could create structures such as clumps, as can be seen in Figure 1.3. These clumps could in turn lead to false detections (Defrère *et al.,* 2012), and therefore it will be crucial to interpret the result of direct imaging observations in light of the context of exozodiacal dust content. In addition, Defrère *et al.* (2012) have demonstrated that, above 10 times the amount of dust present in our solar system, the detection of an

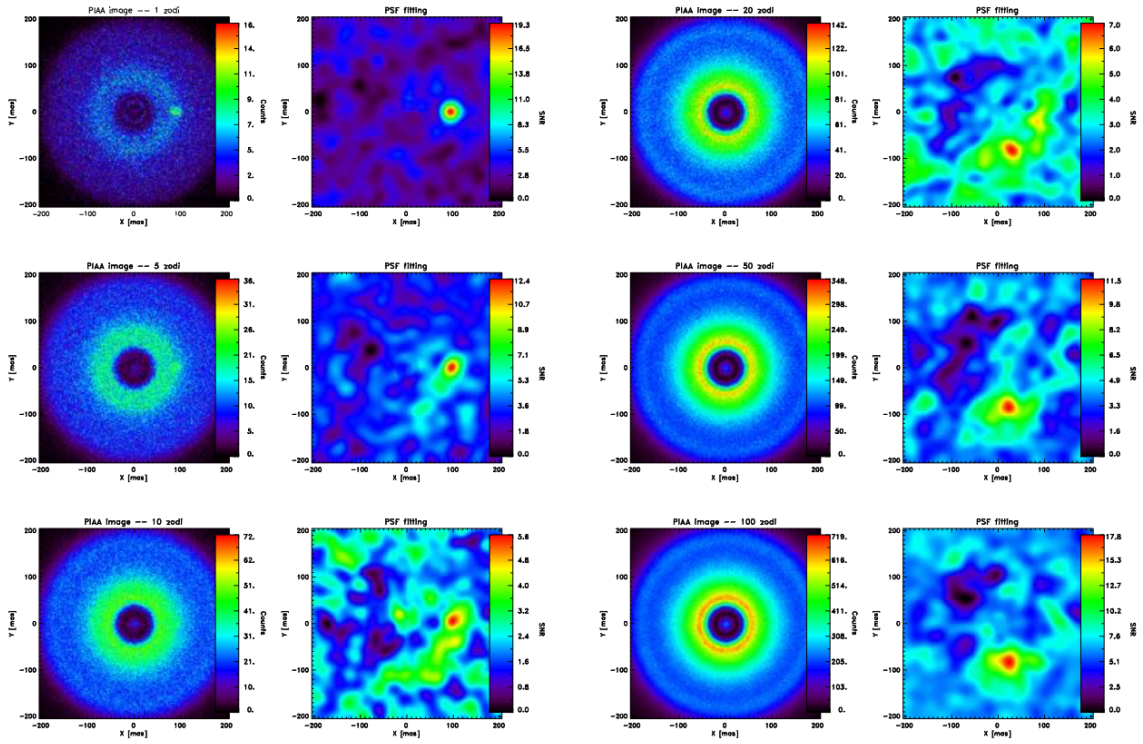

Figure 1.3: Images obtained for a generic mission architecture observing a Sun-Earth system located at 10 pc and surrounded by an exozodiacal cloud of various densities (left column: 1, 5, and 10 zodis; right column: 20, 50, and 100 zodis). For more details, see Defrère *et al.* (2012)

Earth-like planet orbiting a star at 10 parsecs would be extremely challenging and time consuming. To enable such detection, one would need a primary mirror large enough so that the resolution element only contains a small fraction of the light from the disk. Such requirements will, in turn, significantly impact the costs of the mission and increase the technical requirements to allow this mission to fly, and thus it was clearly paramount to detect those exozodi, and evaluate their frequency and dust content, in order to mitigate risks for direct imaging and inform mission designs and strategies.

The response to this need is the LBTI/Hunt for Observable Signatures of Terrestrial Systems (HOSTS) survey, which is a mid-infrared survey of 38 nearby stars whose goal was to detect mid-infrared excess produced by warm exozodiacal dust (Ertel *et al.,* 2018, 2020a). Previous surveys with instruments such as the Wide-field Infrared Survey Explorer (WISE, Kennedy & Wyatt, 2013; Morales *et al.,* 2012) and Keck Interferometer Nuller (KIN, Mennesson *et al.,* 2014; Millan-Gabet *et al.,* 2011) had much lower sensitivities and were only able to detect very bright exozodis (100-1000 zodis). Those two instruments also had low detection rates, with only 0.09 % for WISE (22 detections out of 24174 stars, Kennedy & Wyatt, 2013) and 11 % for KIN (5 detections out of 44 stars, Mennesson *et al.,* 2014). The HOSTS survey with the LBTI was able to

push down that sensitivity by a factor of 10 to a 100, and thus to detect much fainter exozodiacal disks. The goal of this survey was thus to put stronger constraints on the occurrence rate of those faint exozodiacal disks whose dust levels would already hinder searches for Earth analogs with future direct imaging missions such as the Habitable Word Observatory (HWO).

Among the 38 stars in its sample, HOSTS detected 10 exozodiacal disks, that is, a detection rate of 26 %, much higher than in previous surveys. The HOSTS survey also provided an estimate of the median zodi level of 3^{+6}_{-3} zodis, which means that exozodiacal light would not prevent direct imaging of small planets. However, in order to inform the designs and the observing plans of such missions, one would need a greater sensitivity, improved by a factor of 2 to 3. In fact, the median zodi level of 3 zodis is obtained with an uncertainty of 1 sigma and rises to 27 for a confidence of 95%. Furthermore, among the HOSTS sample, 8 additional stars could present tentative detections of several tens of zodis with only 1 to 2 sigmas. If this subsample is currently considered as nondetections, it is, however, impossible to say with certainty that those targets do not contain exozodis denser than 10 zodis. In fact, the uncertainty is too large to even rule out the detection of problematic levels of dust.

1.4 Sensitivity and Background Removal

During the analysis of data from the HOSTS survey, Defrère *et al.* (2016) identified two main factors that limit sensitivity. The first one, which is mostly problematic for bright stars, is the telescope vibrations. It has been shown that, for bright stars, a mitigation of those vibrations would drastically improve the sensitivity, but would have a very limited impact on the fainter targets. This is shown in the left panel of Figure 1.4. The second main limiting factor, that is, imperfect thermal background subtraction, affects the entire target sample. Thus, improving the thermal background removal by a factor of 2 to 3 would almost directly translate into a sensitivity improvement of a factor of 2 to 3, also, as can be seen in the right panel of Figure 1.4.

In fact, when direct imaging with ground-based facilities is performed at mid-infrared wavelengths, the thermal background is a major limitation. In raw images, without any background subtraction, the star would not be visible, let alone structures around it. To detect faint structures such as exozodiacal disks, it is thus crucial to have a background subtraction that is as performant as possible.

Contributions to this thermal background are numerous and impact it in very different ways. The impact of the atmosphere, of the warm reflection in the telescope, and of any vignetting along the light path from warm and cold optics are a few important sources of this thermal background. In addition, electronics add noise to the photometric measurements, and the photon noise directly resulting from the thermal background itself. All of these effects will have various timescales and spatial structures. In particular,

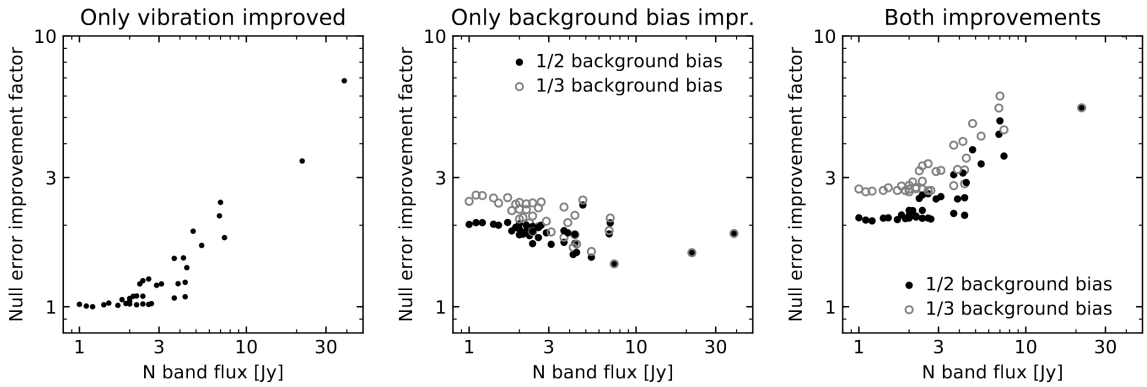

Figure 1.4: Improvement factors on the null error, with respect to the brightness of the star in the N band for improved vibration mitigation only (left panel), for improved background bias removal only (middle panel) and for both improvements (right panel).(Defrère *et al.,* 2016; Ertel *et al.,* 2020b)

the background structures coming from the atmosphere can vary on a very wide range of timescales. The meteorological conditions will, of course, have an important impact on this background, with cloud coverage increasing the mean background and thus the resulting photon noise. The seeing will impact the size and timescale variations of the structures. Those are only two examples of the multitude of sources of thermal background and noise during an observation. This variety of sources and timescales is what makes a high-quality and robust background subtraction difficult to achieve.

In the case of the LBTI, the background can be divided into three main components: the background from the atmosphere, the background from the warm optics, and the background from the optics in the cryostat. The dominant component is the warm optics. About two thirds of this background comes from pupil plane optics, for which the effects are uniform. However, the rest of the sources can produce structured background. The optics in the cryostat are relatively small and their temperature is controlled; thus, the structures they produce vary slowly and are only due to flexure in the instrument following the change in elevation. This is not the case for the background coming from the atmosphere and from the remaining warm optics. These last structures would be the most challenging to correct. In Figures 1.5 and 1.6 we present, respectively, the temporal Power Spectral Distribution (PSD) and the spatial PSD.

We can see with Figures 1.5 and 1.6 that all those PSDs are strongly dominated by low frequencies. For the temporal PSD, that translates into slowly varying or quasi-static structures. Those structures are the least problematic to correct as they remain mostly similar for all images. For the spatial PSD, that translates into large structures that cover a large proportion of the image such as gradients which run across the entire image. These large structures are also the easiest to correct as a large portion of them are found outside the region of interest and can be effectively sampled. However, to uncover faint emission, the whole temporal and spatial frequencies need to be effectively corrected.

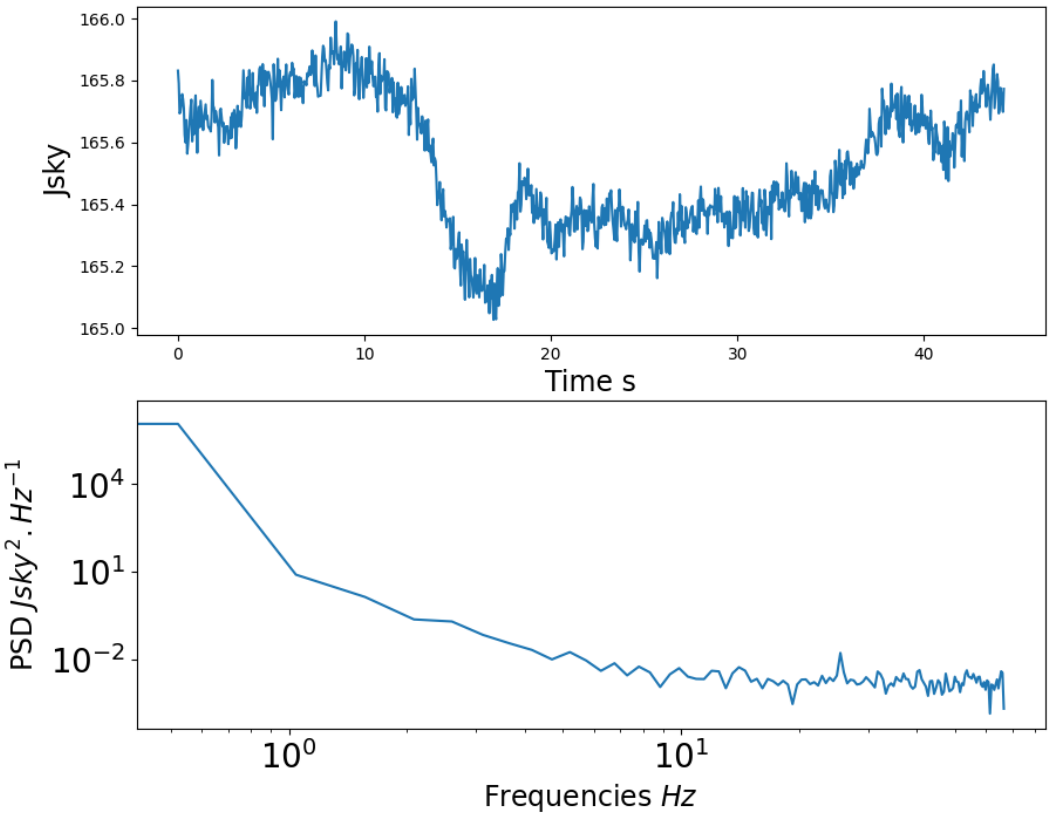

Figure 1.5: Power Spectral Distribution for the temporal axis (bottom panel) for the LBTI, obtained from a dedicated background sequence of 110 Her observations, from which the dark measurement have been subtracted and for which bad pixels have been corrected. The PSD is based on the measurement of the photometry in an aperture of 8-pixels in radius, for 1000 frames each with a 45 ms exposure time (top panel). The data have been acquired in the N band at 11 μm. The conversion in Jansky has been made by measuring the flux of a photometric sequence of 110 Her in an aperture of 8 pixels, and compared to the known flux in Jansky of 110 Her used in the HOSTS survey. We also take into account that the light was coming from two distinct telescope, and that the observations were made in the nulling mode, for which only 50 % of the light is transmitted.

The most rapidly changing structures are most problematic because the background samples used to correct the images are not representative of those structures as they would have changed in between. Similarly, the smallest structures cannot be effectively sampled outside of the region of interest as they would not extend beyond it.

In order to be corrected, the background must be sampled, which is most effectively achieved by using nodding. Rather than acquiring purely background frames, this method consists instead of shifting the position of the source on the detector, on a regular basis. In Figure 1.7 we show the two nodding positions used for the HOSTS survey data.

When data are acquired with the nodding technique, the position of the star is shifted on the detector at the end of each observing block. Depending on the observations, it can be every few hundred or thousands of frames. It is to be distinguished from the

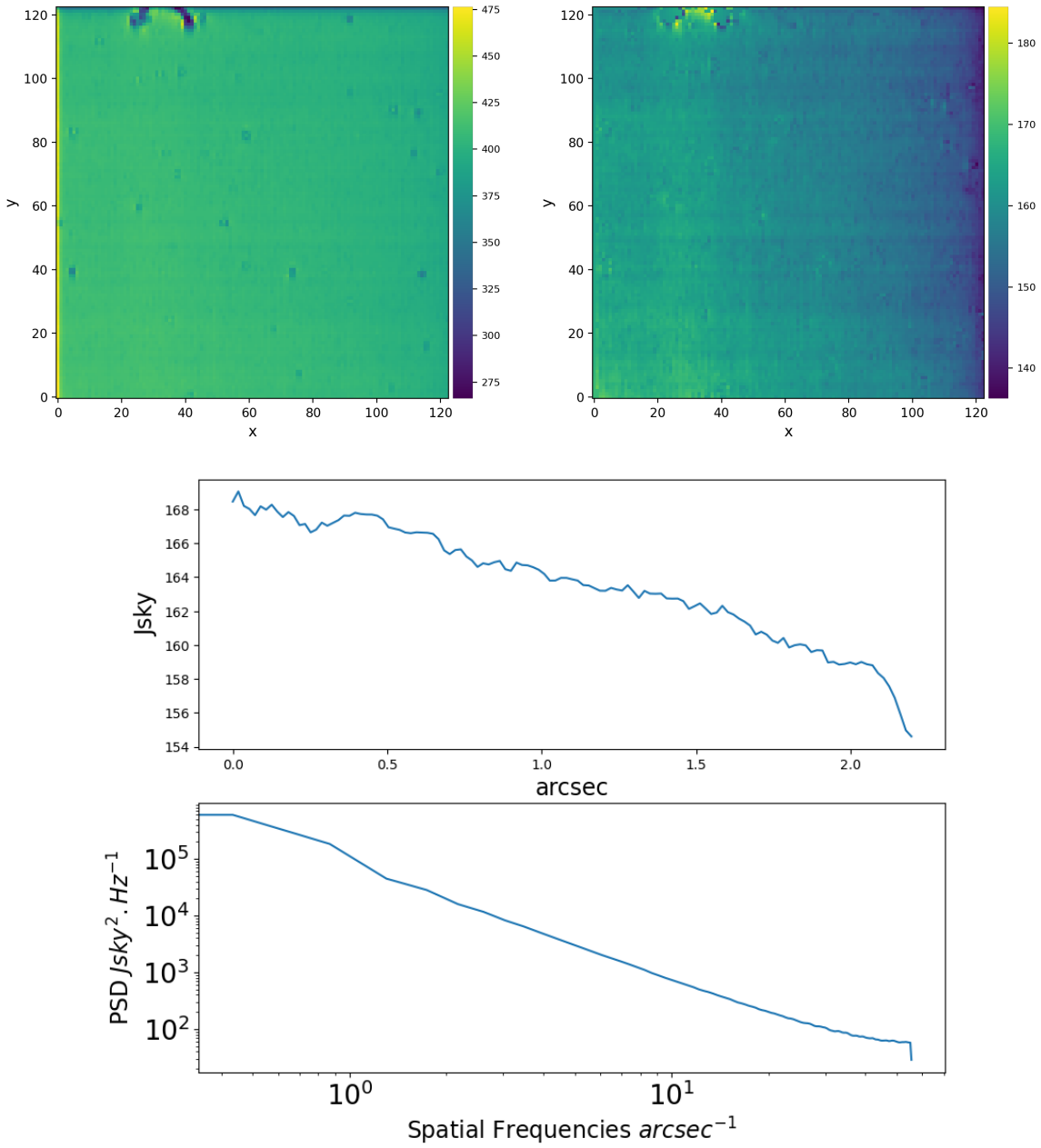

Figure 1.6: Power Spectral Distribution for the spatial dimension (bottom panel) for the LBTI, obtained from a dedicated background sequence of 110 Her observations. The PSD is obtained from a random frame (top left panel) of 123 × 123 pixels, from which the dark measurements have been subtracted and the bad pixels have been corrected (top right panel). The pixel scale corresponds to 0.018 arcsec. The data have been acquired in the N band at 11 μm.The conversion in Jansky has been made by measuring the flux of a photometric sequence of 110 Her in an aperture of 8 pixels, and compared to the known flux in Jansky of 110 Her used in the HOSTS survey. We also take into account that the light was coming from two distinct telescope, and that the observations were made in the nulling mode, for which only 50 % of the light is transmitted.

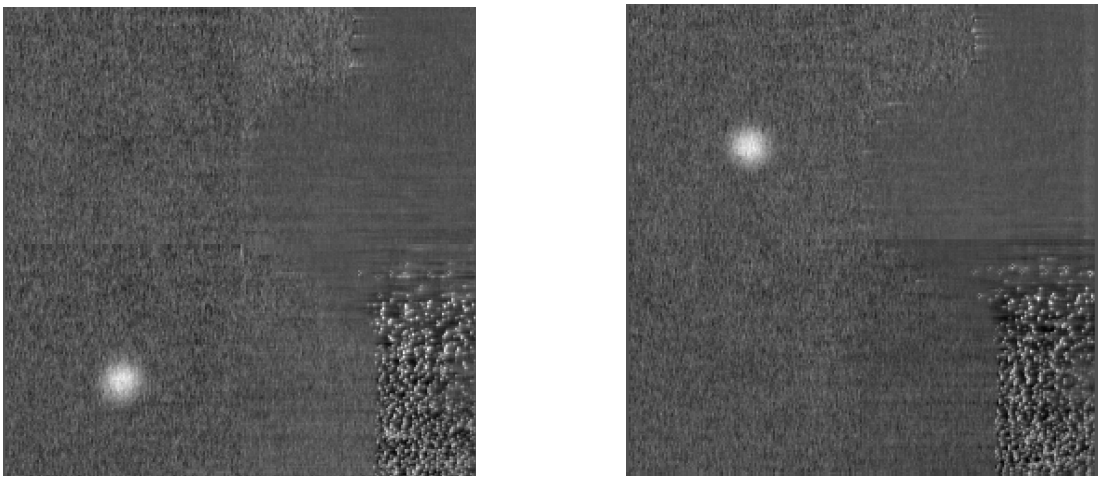

Figure 1.7: Single frames acquired during the HOST survey for the 110 Her target, when the star is in the "down" position on the left, and in the"up" position on the right. Those frames are background subtracted in order to see the star.

chopping technique, for which the star position is shifted between each frame.

With the nodding technique, we sample the background at the previous star position and use it to build the background correction. In Figure 1.7, the top left quadrant of the left image will be used to correct the top left quadrant of the right image. Similarly, the bottom left quadrant of the right image will be used to correct the quadrant on the bottom left of the left image. However, several hundred or thousands of frames separate the images used for each other's background correction. This means that the background may have changed significantly in between, hence introducing a temporal bias, which will prevent a perfect background removal. Additionally, the background quadrant is used to calibrate the quadrant containing the star with respect to the background residuals. In this case, the background used for the calibration is not at the same position, e.g., top versus bottom, which introduces a spatial bias on top of the existing temporal bias. The imperfect thermal background removal has two main effects:

- it decreases the precision of the measurements, that is, the dispersion of the measurements (RMS), and thus their error bars will be larger;
- it degrades their accuracy, that is, the value obtained by the measurement is "less true"[1]. That is what we call bias.

Of the two, bias is certainly the most problematic. Indeed, if we improve the precision without removing the bias, we will determine very precisely something inaccurate. If we reduce the bias alone, on the other hand, the measurement would already be improved and the series of measurements would be more coherent with each other. Eliminating this bias, in particular, is what this work is aiming to do.

[1]The subtle difference between precision and accuracy can be understood from the following example: if a scale consistently reads 17.4 kg for a substance that actually weighs 20 kg, the scale is precise (repeatable), but inaccurate (far from the true value)

In this thesis, I will develop a novel background subtraction method based on principal component analysis (PCA) to tackle the bias that affects exozodi observations. PCA is particularly indicated for this type of problem, as it will allow us to quantify the main contributions to the background noise in our data, without having to identify and disentangle the source of that noise (which, as mentioned above, can result from a multitude of effects).

1.5 Summary and Thesis Outline

The first detection of a planet around another star showed that Earth and its host star might not be as unique as previously thought. The thousands of detections that followed then demonstrated that a star with planets was more the norm than the exception. But as the research community discovered more and more of these exoplanets, they also came to see the huge diversity of planetary systems. Some of those exoplanets are even questioning current planet formation models. However, it is notable that within all those discoveries, we still have not found another version of our Earth around a Sun-like star.

In the search for Earth analogs, astronomers aimed to look for smaller and smaller planets, but also closer and closer to the habitable zone. In direct imaging, this translated mainly into reducing the inner working angle and improving the starlight suppression. However, as both of these challenges were tackled, new ones arised : the exozodiacal dust and the sensitivity limitations generated by the thermal background.

The thermal background is particularly problematic in the infrared regime, where exo-Earths emission will have a better SNR compared to its host star. To get a better sensitivity and allow for detections of fainter sources, one needs to address this challenge and improve the thermal background removal. The classical technique is indeed unable to correct variable structures or lack the ability to satisfactorily reconstructs the background behind the star. By developing a new background subtraction approach based on Principal Component Analysis for both spatial and temporal corrections, this thesis aims to provide a significant improvement on these sensitivity limitations. By further combining the new background subtraction approach with the detailed study of a HOSTS survey detection, this thesis also aims to contribute to the development of a better understanding of the exozodiacal light and the risks it poses for exo-Earths direct imaging.

I will introduce the concepts central to this thesis in more detail in Chapter 2. I will present observation techniques (nulling interferometry, ADI, and RDI), expand on how thermal background noise affects them, and elaborate on why PCA is well suited to limit these deleterous effects. In Chapter 3, I will present my work on the development of a PCA-based background subtraction technique, specifically aimed at reducing spatial bias, which resulted in a publication Rousseau *et al.,* 2024. I further developed a similar

method, this time aimed at reducing temporal bias, which I present in section 3.6.

Finally, in Chapter 4, I will present the impact of this method on information derived for an object around which the HOSTS survey reported an exozodi, 110 Her. I will show how the newly processed data affect the modeling efforts carried out as recommended by the NASA Exoplanet Program Study Analysis Group 23. Indeed, since a large amount of dust can hide planets or create clumps that can be mistaken for planets, studying structures in exozodis will be extremely helpful in constraining the presence of potential exoplanets that would otherwise miss our census. Thus, we will perform complementary modeling for this system, comparing the results obtained with and without spatial PCA-based background subtraction.

1.6 Personal contributions

1.6.1 Peer-review paper

In the context of this thesis, I developed a PCA-based method for background subtraction, which I applied to N-band nulling interferometric data from the HOSTS survey. In particular, I studied its impact on HCI contrast curves and aperture photometry. This work has been published in Rousseau *et al.,* 2024 in Astronomy & Astrophysics. It has also been integrated within the content of a review paper on hot exozodiacal dust, Ertel *et al.,* 2025, in the Publications of the Astronomical Society of the Pacific.

During my thesis, I also participated in Defrère *et al.,* 2021, in which I produced contrast curves with the PCA background subtraction for a star of the HOSTS survey: β Leo. In the context of the HOSTS efforts to model individual systems with detections, I also participated in Garreau *et al.,* 2025.

1.6.2 Proceedings

My work on PCA background subtraction was also mentioned in four SPIE proceedings : Defrère *et al.,* 2022, Ertel *et al.,* 2022, Isbell *et al.,* 2024 and Defrère *et al.,* 2024, to present its potential impact on nulling direct imaging data, but also directly on the sensitivity of the LBTI and the NOTT instrument.

1.6.3 Conferences and Workshops

I presented the PCA-based background subtraction method in several conferences during my thesis, notably:

- The KISS Workshop in Pasadena USA, in 2022, in which I contributed a poster to present preliminary results on PCA background subtraction, and its advantages compared to mean background subtraction. In particular those results showed that PCA background subtraction reconstruct the background behind the star

much more accuratly than mean background subtraction, and that no additional estimate of the background in another region was necessary.

- The AO4ELT7 conference in Avignon France, in 2023, where I presented a contributed talk on PCA background subtraction, demonstrating an improvement factor of 1.2 to 1.7 for HCI contrast curves, and of 2 to 3 for aperture photometry. I also discussed the concept of a temporal PCA background subtraction. This conference led to the publication of two conference proceedings : Rousseau *et al.,* 2023 which describe the method and its principle results, and Ertel *et al.,* 2023 which also present this method as a potential sensitivity improvement for the LBTI.
- The NOTT workshop in Leuven Belgium, in 2023, where I presented a contributed talk on the results of PCA background subtraction for HCI and aperture photometry, and the benefits such method would have on an instrument such as NOTT.
- The EXO24 LBTO conference in Tucson USA, in 2024, in which I contributed a talk on the results of PCA background subtraction on HCI and aperture photometry. I also presented preliminary results on a temporal PCA correction, notably demonstrating its capacity to detect residual background variation by analyzing the temporal dimension only.
- The conference WhenStarsMeetPlanets in Sesten Italy, in 2024, where I contributed a talk and presented the advantages of PCA background subtraction for both HCI and aperture photometry, and its potential to facilitate both detection and characterization of exoplanets in direct imaging.
- The conference Are We Unique Species on A Unique Planet in Copenhagen Denmark, in 2024, in which I presented the state of the art of warm exozodiacal dust studies led by the HOSTS team, as well as the benefits of a PCA background subtraction for such data.
- The Tianyu workshop II, in Shanghai People's Republic of China, in 2025, where I presented a contributed talk presenting both spatial and temporal PCA background subtraction results, and the possible adaptations of the methods for transiting exoplanets.

1.6.4 Observation support

In the context of my stay at the University of Arizona, I integrated the LBTI observing team. I supported the LBTI observations for three years either as a science camera operator, a phase camera operator, or an adaptive optics operator. As a science camera operator my duties encompass: aligning the mirror, changing the filters, changing the pointing of the telescope, offsetting the telescope, adapting the observational scripts in accordance with the proposed observations, checking requested integration time for saturation and logging any relevant information on the observations. As a phase camera operator, during nulling observations, I monitored the phase for potential phase jumps, and rectified the phase when those happened. As an adaptive optics operator, I

verify the health of the AO system when starting it (cameras structures and cooling, saturation checks, filters moving), perform the photometric checks and alignment on the AO cameras, monitor and adapt the AO corrections, log any information relevant to the observation and any system failures for further trouble shooting.

Chapter 2

Nulling interferometry: principles & data reduction

Contents

Although the detection and characterization of exozodiacal dust is important to prepare future missions dedicated to the direct imaging of exoplanets in the habitable zone of their host stars, very little is known about it. In order to improve our understanding of those objects, we need more precise observations, more sensitive measurements, and more detailed modeling and characterization. In this thesis, our aim is to contribute to both aspects, on the one hand by improving thermal background removal and data sensitivity (see Chapter 3), and on the other by studying and modeling in detail the 110 Her system for which an exozodi detection was made by the HOSTS survey (see Chapter 4).

We present here the specific observing techniques dedicated to the detection and characterization of exozodiacal dust, that is, N-band nulling interferometry, as well as the intrinsic challenges of these observations. We will then describe the various elements that contribute to the thermal background and how they can impact our data. Finally, we will dive into the heart of this thesis by introducing the principles of principal component analysis (PCA) and singular value decomposition method as well as how they are used in astronomy.

2.1 Observing techniques

A decade ago, Defrère *et al.* (2012) showed that exozodiacal disks with dust content greater than 10 times the amount of our solar system can hinder the detection of terrestrial-like planets in their habitable zones. Hence, those disks need to be detected and characterized in order to best prepare future direct imaging missions. However, observing exozodiacal disks is extremely challenging, as they are faint objects orbiting

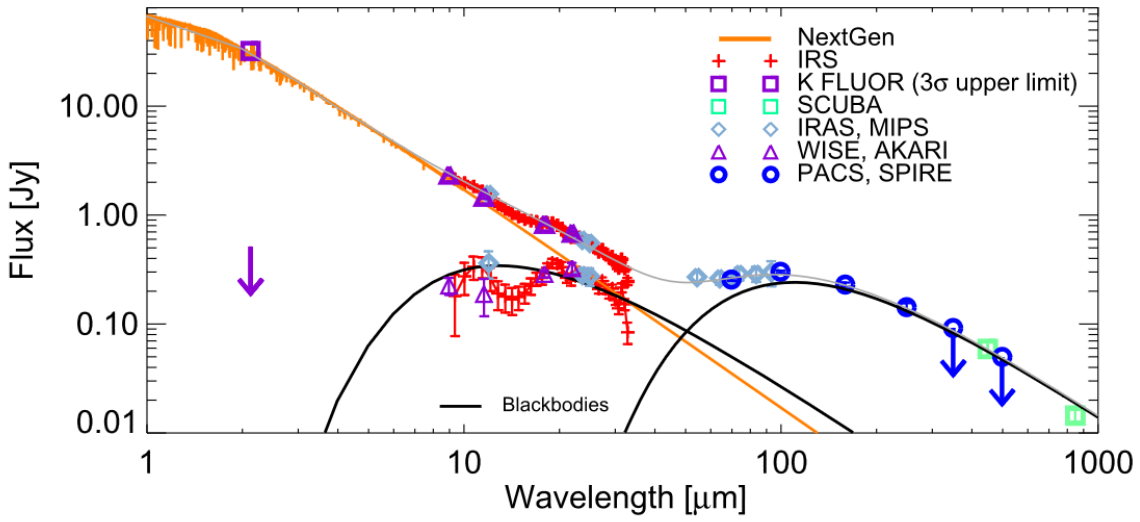

Figure 2.1: Spectral Energy Distribution (SED) of η Crv (Lebreton *et al.*, 2016). The SED includes space-borne photometry from *Spitzer*, *Herschel*, *WISE*, and *AKARI*, and submillimeter fluxes from JCMT/SCUBA. The Nextgen photosphere model with $T_{\rm eff} = 6900\,{\rm K}$ and $\log g = 4.5$ is overplotted and subtracted from the data to reveal the excess spectrum. Blackbody fits to the warm and cold parts of the SED are shown on an indicative basis.

close to their host stars, emitting in the near and mid-infrared. Figure 2.1 illustrates this by showing the photometry of an extreme system that contains an exozodiacal disk 2500 times brighter than the solar system zodiacal cloud. The impact of this exozodiacal disk – peak at 10 μm – on the global photometry is extremely low, and this figure demonstrates that an exozodiacal disk comparable to that of the solar system, that is, three orders of magnitude fainter, would not create any discernible excess to the stellar photometry. It is thus clear that, if we want to detect exozodis of interest, using a photometric approach is not an option. Consequently, one needs to spatially resolve the habitable zone. For this, we turn to the resolving power of interferometry.

2.1.1 Interferometry

A short story of the birth of Interferometry

Once upon a time, in the distant year of 1801, the young Thomas Young built an experiment to finally put an end to the argument about the nature of light. This experiment was to let light pass through two slits, close to each other. If the light was composed of particles, the light would form two bright lines corresponding to the two slits. If the light was in fact a wave, it would create a pattern of bright and dark fringes. Thomas Young conducted this experiment and found the incredible result that light is indeed a wave (Young, 1802). And so, together with the success of this experiment, and

while everyone was focused on the newborn – and half-erroneous – answer to the nature of light, interferometry was born too.

Sixty-seven years later, in 1868, Fizeau had an amazing idea: using the strength of interferometry to measure the diameter of stars [1]. The beautiful pattern of interferometry was indeed dependent on two main parameters: the distance in between the apertures and the angular size of the observed object. Fizeau and Edouard Stephan subsequently designed a mask for a telescope. In 1873, Stephan placed this mask on an 80 cm mirror-diameter telescope. With this, he obtained an interferometer with two apertures separated by 50 cm. Unfortunately, at that time, the interferometry technique was too recent and not precise enough for this hard task, and Stephan was only able to put an upper limit on the angular radius of stars.

Interferometry went on evolving, and the mask designed by Fizeau and Stephan enabled its first important successes, by measuring the angular radius of the Galilean satellites (Michelson, 1890), and resolving binary stars or large asteroids. It was not until 1920, with Michelson and Pease, that the interferometry grew much larger by dropping the use of the mask in favor of a 6m metal beam to separate the two apertures (Michelson & Pease, 1921). Using a precision of the order of micrometers, they created the first interferometer in which the apertures were separated by a larger distance than the aperture size itself. This was a great success, giving birth to the first operational stellar interferometer, and providing for the first time the diameter of Beltegeuse. Strong of this victory, Pease wanted to go even further and used a 15 meters metal beam instead, but, considering the required alignment precision, this was too soon, as adaptive optics was not yet invented.

More than 50 years later, Labeyrie (1975) revived interferometry with a novel idea: instead of using a single metal beam, why not using two completely independent telescopes? For this, Labeyrie had to build delay lines in order to make the light from the two telescopes interfere coherently. With this new concept, the interferometry technique was able to grow further, extending the original 13-meter separation between the two telescopes/apertures up to 64 meters. Finally, with this powerful technique it was finally possible to measure stellar angular radii.

Concept of Interferometry

Consider two coherent synchronous waves, ψ_1 and ψ_2, which interfere with each other:

$$\psi_1 = Re\{A_1 e^{i(\omega t - \vec{k}.\vec{r} - \phi_1)}\} \quad \text{and} \quad \psi_2 = Re\{A_2 e^{i(\omega t - \vec{k}.\vec{r} - \phi_2)}\} \quad , \tag{2.1}$$

$$\psi_1 = A_1 cos(\omega t - \vec{k}.\vec{r} - \phi_1) \quad \text{and} \quad \psi_2 = A_2 cos(\omega t - \vec{k}.\vec{r} - \phi_2) \quad , \tag{2.2}$$

[1] Fizeau's report won the Bordin Prize to the French National Academy, 1868

where A_1, A_2 are the amplitude of the waves, ω the angular frequency of the waves, $\vec{k}$ the wave vector and ϕ_1, ϕ_2 their phase. The resulting wave is given by:

$$\psi = A_1 cos(\omega t - \phi_1) \ + \ A_2 cos(\omega t - \phi_2) \qquad . \tag{2.3}$$

The total intensity is thus:

$$\begin{aligned} I =< \psi^2 >= A_1^2 < cos^2(\omega t - \vec{k}.\vec{r} - \phi_1) > \ + A_2^2 < cos^2(\omega t - \vec{k}.\vec{r} - \phi_2) > \\ +2A_1A_2 < cos(\omega t - \vec{k}.\vec{r} - \phi_1) cos(\omega t - \vec{k}.\vec{r} - \phi_2) > \quad , \end{aligned} \tag{2.4}$$

in addition the mean value of $cos^2(\omega t - \vec{k}.\vec{r} - \varphi)$, $< cos^2(\omega t - \vec{k}.\vec{r} - \varphi) >= \frac{1}{2}$ so this equation can be rewritten as:

$$I = \frac{1}{2}A_1^2 \ + \ \frac{1}{2}A_2^2 \ + 2A_1A_2 < cos(\omega t - \vec{k}.\vec{r} - \phi_1) cos(\omega t - \vec{k}.\vec{r} - \phi_2) > \quad , \tag{2.5}$$

using the trigonometric relation: $cos(\omega t - \vec{k}.\vec{r} - \phi_1) cos(\omega t - \vec{k}.\vec{r} - \phi_2) = \frac{1}{2}[cos(2\omega t - 2\vec{k}.\vec{r} - \phi_1 - \phi_2) \ + \ cos(\phi_2 - \phi_1)]$, with $< cos(2\omega t - 2\vec{k}.\vec{r} - \phi_1 - \phi_2) >= 0$ because $\omega \neq 0$, we obtain:

$$I = \frac{1}{2}A_1^2 \ + \ \frac{1}{2}A_2^2 \ + \ A_1A_2 cos(\Delta\phi) \qquad . \tag{2.6}$$

Which can be rewritten as:

$$I = I_1 \ + \ I_2 \ + \ 2\sqrt{I_1 I_2} cos(\Delta\phi) \qquad . \tag{2.7}$$

$\Delta\phi$ can itself be decomposed as $\Delta\phi = \frac{2\pi\delta}{\lambda} + \Delta\varphi$, and we finally obtain:

$$I = I_1 \ + \ I_2 \ + \ 2\sqrt{I_1 I_2} cos\left(\frac{2\pi\delta}{\lambda} + \Delta\varphi\right) \qquad , \tag{2.8}$$

with I_1 and I_2 the intensities of the two sources, δ the optical path difference, and $\Delta\varphi$ the phase difference between the two sources. In blue, we have the interferometric term. To maximize this term and thus obtain the strongest interferences, we should have : $\frac{2\pi\delta}{\lambda} + \Delta\varphi = 0$. Thus, the smaller the wavelength, the smallest the authorized path difference. In fact, the path difference δ can go from zero to the wavelength, to obtain the maximum interferences. When $\Delta\varphi$ is at $0[2\pi]$, for given δ and λ, the interferometric term is at its maximum, and thus we are in a bright fringe. When it is at $\pi[2\pi]$, the interferometric term is at its minimum, and thus we are on a dark fringe.

In astronomy, interferometry is used to increase the resolution beyond the size of the primary mirrors. Indeed, the angular resolution of a single telescope θ_s is defined as the fwhm of the core of the PSF, and wirtten as follows for small angles:

$$sin(\theta_s) \ \approx \ \theta_s \ \approx \ 1.029 \ \frac{\lambda}{D} \approx \frac{\lambda}{D} \qquad , \tag{2.9}$$

with λ the observing wavelength, D the diameter of the primary mirror and θ the angular resolution. According to Equation 2.9, the larger the diameter of the primary mirror, the

better the angular resolution. When using interferometry instead of a single telescope, the equation for the interferometric angular resolution θ_i, defined as the fwhm of the central fringe, becomes:

$$\theta_i \approx \frac{\lambda}{2B} \quad , \tag{2.10}$$

with B being the baseline of the interferometric array. The resolution is thus no longer ruled by the size of the primary mirror but by the maximum separation between the telescopes from which the light is recombined. Interferometry thus allows for much better angular resolution, as it overcomes the limitation of the primary mirror size. However, the sensitivity of such an interferometric array is limited by the primary mirrors of the telescopes in the array.

Let us now consider the dependence of the angular resolution with respect to the wavelength. Indeed, for a given D or B, the smallest the wavelength, the better the angular resolution. The smallest wavelength will thus be able to resolve the smallest objects. However, the smallest the wavelength, the smallest the limit on the authorize path difference. In order to use interferometry in the visible or in the ultraviolet, the path difference must not exceed a few hundred nanometers, in the X-ray domain, a few hundredth to ten nanometers. Today, if radio, infra-red and visible interferometers are used for astronomy, the level of precision required for UV and X-ray interferometers has yet to be achieved.

The history of interferometry in astronomy started when Fizeau wanted to measure the stars' diameter with this method. So, how do we measure sizes with interferometry? The approach is to use the fringe visibility, defined as :

$$V = \frac{I_{max} - I_{min}}{I_{max} + I_{min}} \quad , \tag{2.11}$$

with I_{max} the intensity of the central bright fringe and I_{min} the intensity of the two first dark fringes. In Figures 2.2 and 2.3 we propose a schematic of the relation between visibility and measurement of star diameter.

Figure 2.2 shows the case of an interferometer with a small baseline. The resolution element is of the size of the star diameter or even larger. In this case, the star is unresolved and the fringes are aligned. The visibility in this case is maximum and equal to 1. Now, if we increase the baseline and consequently reduce the size of the resolution element, we can start to resolve the star. As we start to resolve the star, the interferometric patterns from the two elements on the stellar surface will no longer overlap perfectly as seen in the top panel of Figure 2.3. As the baseline grows larger and the resolution element smaller, the number of elements seen by the interferometer on the star will increase. All of those points will have their own interferometric pattern, which will be misaligned with the others, which is shown in the bottom panel of Figure 2.3. The addition of all those patterns will result in completely blurred fringes and the

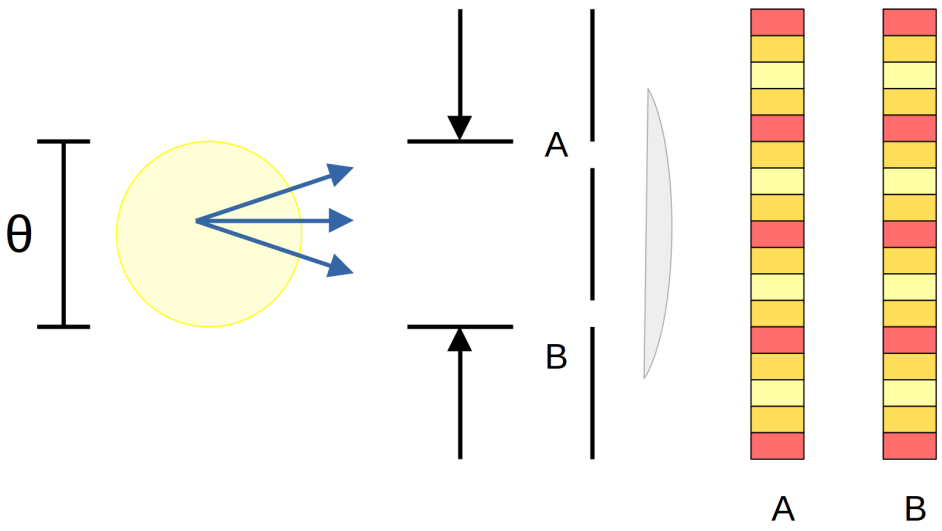

Figure 2.2: Schematic of the interferometric pattern of an unresolved star. In this case, a single resolution element covers the whole star. The resulting interferometric pattern is thus identical for the whole star, as illustrated with the two pattern A and B on the right.

fringe visibility will then drop to zero.

When observing with interferometry, one can vary the baseline of the observations and search for the baseline at which the visibility of the fringes starts to decrease. With knowledge of this baseline, one can simply retrieve the diameter of the stars using Equation 2.9. Indeed, when the baseline is in this configuration, the angular resolution θ is equal to the diameter of the star S_s and we have the following.

$$S_s = \theta \qquad and \qquad \sin(\theta) = \frac{J_1(x)\lambda}{D\ \pi} \quad . \tag{2.12}$$

with $J_1(x)$ the first Bessel function, and λ the wavelength of observation. Of course, this is an ideal case and one should account for the errors intrinsic to the observations.

If the measurement of star diameters was one of the first envisioned applications of interferometry, it is far from the only one. With its resolving power, the interferometer will be able to separate the star from its surroundings, opening a window to study them. This is the case for multiple stars systems for which can be distinguished one star from another or debris disks which can be separated from their hosts star. With the information of the fringe intensities and visibilities, it is possible to constrain the brightness of the different components. If those components are resolved themselves, one can even get spatial information on individual components.

The case of exozodiacal disks and coronographs

We have seen at the very beginning of this chapter that exozodiacal dust could not, in most cases, be detected in the total photometry of the system. Indeed, those objects

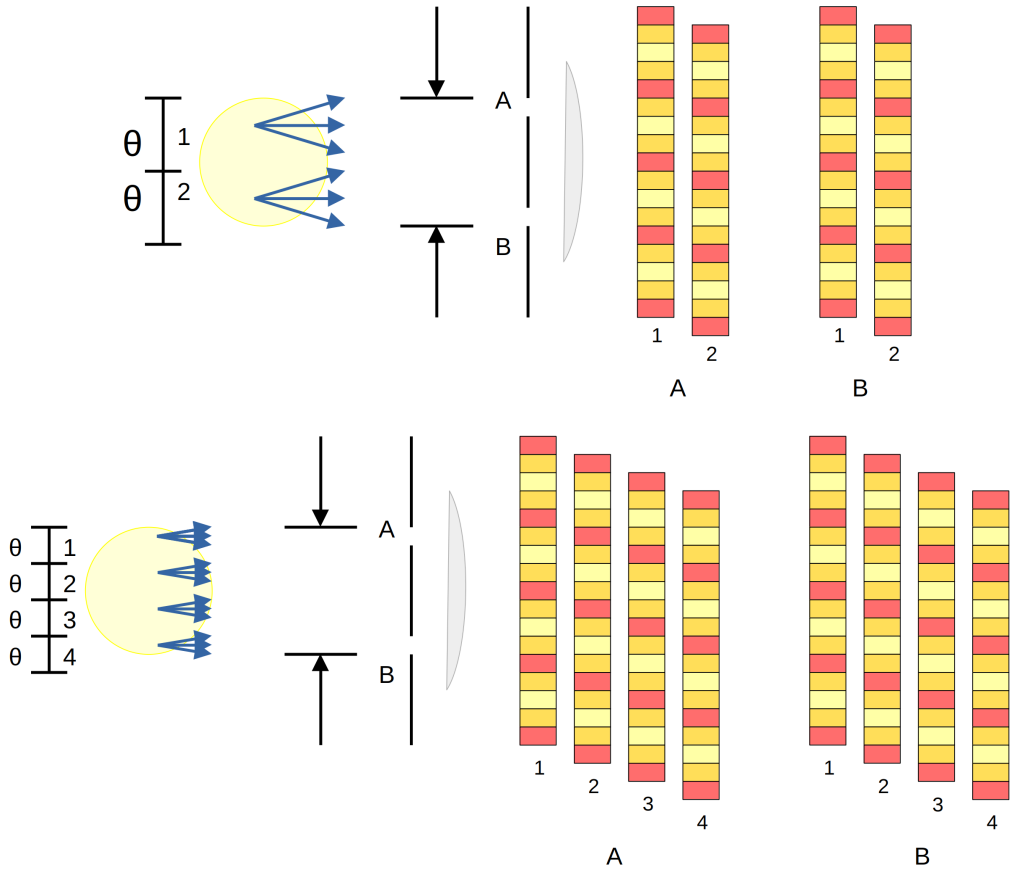

Figure 2.3: Schematic of the interferometric pattern of a partially resolved (top panel) and a completely resolved star(bottom panel). On the top panel, the star is about the size of two resolutions elements. These two resolution elements will each produce slightly misaligned interferometric patterns, as illustrated on the right, reducing the intensity of the fringes. On the bottom panel, the resolution is even smaller, and a larger number of resolution elements are needed to cover the whole star. Each resolution element will produce an interferometric pattern, slightly misaligned with the others. The addition of these, as illustrated on the right, will result in a visibility of 0.

are too faint and the measurements are not precise enough to enable those detections. To disentangle their photometry from the star photometry and allow for detection of faint disks, we need a smaller resolution element. If the need for resolving power is met by interferometry, the challenge coming from the contrast between the star and the disk is still problematic. Indeed, considering the contrast between the two, the light from the disk will be completely buried by the noise. To detect such faint objects, we thus need to remove the starlight.

To remove the starlight, high-contrast imaging and interferometry mainly rely on coronographs. The coronographs mask the region of the star, significantly reducing its contribution to the observations. With this method, objects much fainter than the star can be observed.

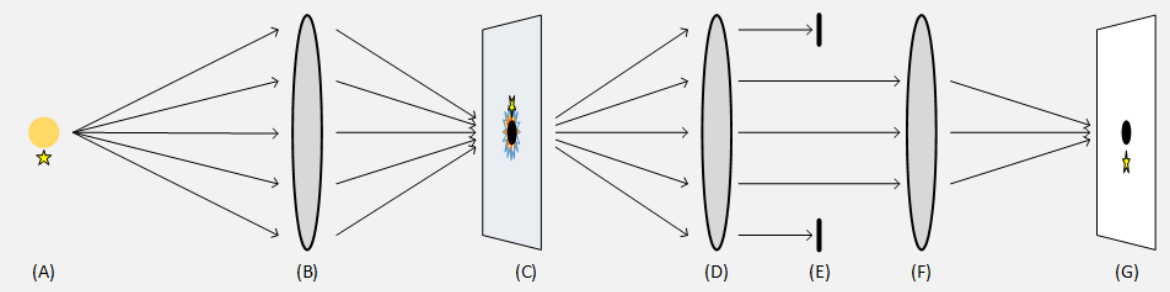

Figure 2.4: Schematic of a Lyot coronograph, with the star (A), the entrance pupil (B), the central mask in the focal plane (C), a lens for collimation (D), the Lyot stop (E), and the detector (G).

The concept of the coronograph, introduced in 1931 by Bernard Lyot Lyot (1931), seems simple: masking the star to block the starlight and observing fainter objects that would have been hidden in its glare. However, its application is a bit more complex. In Figure 2.4 we present a schematic of a Lyot coronograph.

We consider a star, with a fainter object orbiting close around it. The star is on the optical axis of the system, while the object is slightly off-axis. When light enters the system, it is focused on an intermediate focal plane (C) on which a central mask is placed. This mask blocks a large part of the starlight. However, the remaining starlight will be diffracted by the mask, creating residuals which cannot be blocked by a central mask anymore. After the light is collimated (D), an additional stop is placed on the light path: the so-called Lyot stop (E). It removes an important part of the diffracted starlight. The remaining light is then focused on the detector (G).

Nowadays, increasingly complex coronographs are designed to reduce the starlight residuals but also the inner working angle of those instruments. Indeed, coronographs have one major limitation, the size of the region they mask. The inner working angles of the coronographs are generally expressed as:

$$\frac{N\lambda}{D} \quad , \tag{2.13}$$

with D the diameter of the primary mirror, lambda the observing wavelength and N equal or slightly inferior to one for the most performing coronographs (JWST documentation, Itoh & Matsuo, 2022). If we consider such a coronagraph, at an observing wavelength of 11um where the contrast between habitable-zone dust and its host star is the most favorable, and observations with eight-meter-class telescopes such as the Very Large Telescope (VLT, European Southern Observatory, 1998) Unit Telescopes (UTs) or a single LBT aperture, the inner working angle is still of the order of 200–300 mas. This is already insufficient to resolve the habitable zone of a sun twin at 5 parsec.

Considering this limitation, using a coronograph to study the habitable zone of a system is not an option in most cases. This is in particular true for exozodiacal disks. We thus need another method to remove the starlight: nulling interferometry.

2.1.2 Nulling interferometry

A very short story of Nulling interferometry

In the year 1978, only three years after the breakthrough brought by Labeyrie, Bracewell had the idea that studying the star close-in surroundings was possible because of interferometry. For this, one only had to shift by π one of the sources (Bracewell, 1978). And soon, with this idea, nulling interferometry was born.

In the same years, the search for extrasolar planets became more and more of a hot topic, and nulling interferometry developed quickly. Only ten years later, Angel proposed to search for those extrasolar planets using nulling interferometry (Angel & Woolf, 1997). Angel also suggested increasing the number of apertures when using nulling interferometry, to be able to detect those very faint sources that interferometry alone could not find. About ten more years later the first implementation of nulling interferometry started, on the Multiple Mirror Telescope (Hinz *et al.,* 1998). Only two years later, the Steward Observatory designed BLINC, and demonstrated how much they could suppress the star through nulling interferometry (Hinz *et al.,* 2000).

Despite its quick evolution, ten more years were needed for the first nulling interferometry mission to appear. It started with the Keck interferometric nuller with whom they search for bright exozodiacal disks (Millan-Gabet *et al.,* 2011), then the Palomar Fiber Nuller a year later (Hanot *et al.,* 2011), and finally in 2015, the Large Binocular Telescope Interferometer. In 2018, 150 years after Fizeau started the interferometric journey and 40 years after the invention of nulling interferometry, the HOSTS survey was completed (Ertel *et al.,* 2018, 2020a).

Today, nulling interferometry is still evolving, demonstrating the strength of the method on new instruments such as DRAGONFLY/GLINT with Subaru/SCEXAO (Spalding *et al.,* 2024). But the story will not end there. A new project is now under development for one of the most famous interferometers: the NOTT project on the VLTI (Defrère *et al.,* 2024), and we hope that soon, as Bracewell and Angel had wished for, nulling interferometry will be used on a space-based mission to search for extrasolar planets, with the LIFE mission.

Concept of Nulling interferometry

Let us take a closer look at Equation 2.14:

$$I = I_1 \ + \ I_2 \ + \ 2\sqrt{I_1 I_2} cos(\Delta\phi) \qquad , \tag{2.14}$$

which gives the intensity of a fringe as a function of the intensity of the individual sources and of $\Delta\phi$. To obtain a fringe of maximum intensity, $cos(\Delta\phi)$ must be equal to 1. On the other hand, to obtain a destructive fringe of minimum intensity, $cos(\Delta\phi)$ must be equal to -1.

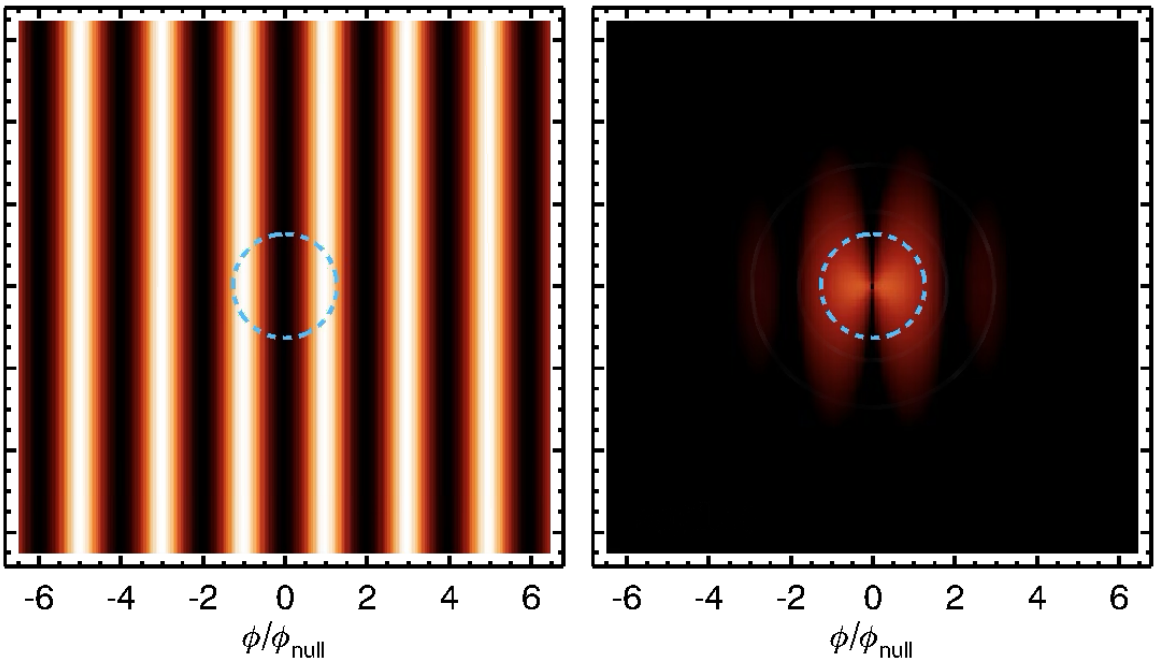

Figure 2.5: The transmission pattern of the LBTI in its nulling mode (left panel) and the transmitted signal of a disk through this transmission pattern (right panel).The dashed circle represents the Earth Equivalent Insolation Distance (EEID) of a G0 star at 10pc.

$\Delta\phi$ can be rewritten as $\Delta\phi = \frac{2\pi\delta}{\lambda} + \Delta\varphi$. To obtain a constructive interference of maximum intensity, $\Delta\phi$ has to be equal to 0, for a destructive interference, to π. To maximize the visibility of an interferometric pattern, we want $\frac{2\pi\delta}{\lambda}$ to be as close to 2π as possible. The constructive fringe is then obtained when $\Delta\varphi$ is equal to 0 $[2\pi]$. The destructive fringe, on the other hand, is obtained when $\Delta\varphi$ is equal to $\pi[2\pi]$. Thus, there is a phase shift of π between constructive and destructive interferences.

Let us now come back to a standard interferometric pattern, a constructive fringe with maximum intensity is at its center, and surrounded by two dark fringes of minimum intensity. The other fringes further away from the center decrease in intensity. Thus, if we want to use maximum intensity fringes, one should focus on the central fringe rather than the lateral ones. In addition, except for the central fringe, all fringes suffer from chromaticity. Thus, working with the central fringe is necessary to prevent any chromatic effect. This is why using the optical path difference δ to obtain $\Delta\phi = \pi$ is not a good solution. A better solution is rather to apply the π phase shift to one of the sources, which will inverse the entire interferometric pattern. With this method, we thus obtain a nulling-interferometric pattern with a destructive fringe of minimum intensity at the center, surrounded by two constructive fringes of maximum intensity. In Figure 2.5 we show the nulling-interferometric pattern of the LBTI, along with the signal transmitted to a disk through this transmission pattern.

In the left panel of Figure 2.5, the central fringe is destructive, and the light coming

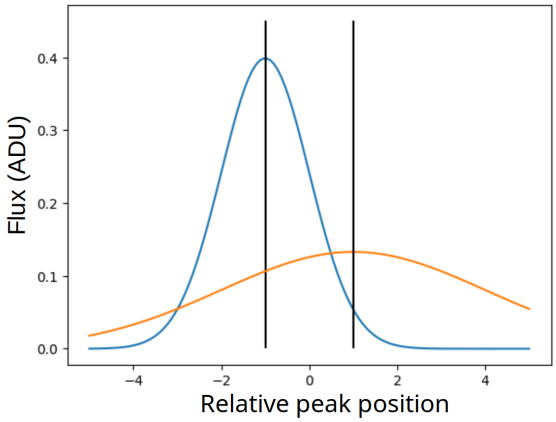

Figure 2.6: Two gaussian representing respectively the star (blue) and the disk (orange) with their respective maximum intensity highlighted by the vertical black lines.

from this position is suppressed as shown in the right panel. The light from the star which will fall on the central destructive fringe is thus suppressed by this method, whereas the light from the disk which extend beyond the central destructive fringe will be kept.

We can now consider a more complex case, where we observe not only a point-source star but a star and its disk. Let us assume that each source produces a perfect Gaussian. The two gaussians will overlap, as shown in Figure 2.6

It is clear in Figure 2.6 that the maximum intensity of the two sources does not overlap. This is of course an exaggerated schematic and in a real-life situation separating the two maximums is extremely challenging, and requires the resolving power of interferometry. Nevertheless, the idea of nulling interferometry is to place the destructive fringe with minimum intensity on the star's gaussian maximum intensity, which does not coincide with the disk's maximum intensity. Thus, a significant portion of the starlight is suppressed due to the destructive interference of the central dark fringe. On the other hand, the maximum intensity of the disk falls on a constructive interference and remains. This method thus allows for significant starlight suppression without the use of a standard coronograph and its limited inner working angle. Indeed, the fringe width Δx can be written as:

$$\Delta x = \frac{\lambda d}{B} \quad , \tag{2.15}$$

with λ the wavelength of observation, d the distance from the source, and B the baseline of the interferometer. If we compare it with the expression for the inner working angle θ of a standard coronograph we have:

$$\theta \propto \frac{\lambda}{2B} \quad (nulling\ interferometry) \qquad \text{and} \qquad \theta \propto \frac{\lambda}{D} \quad (coronograph) \quad . \tag{2.16}$$

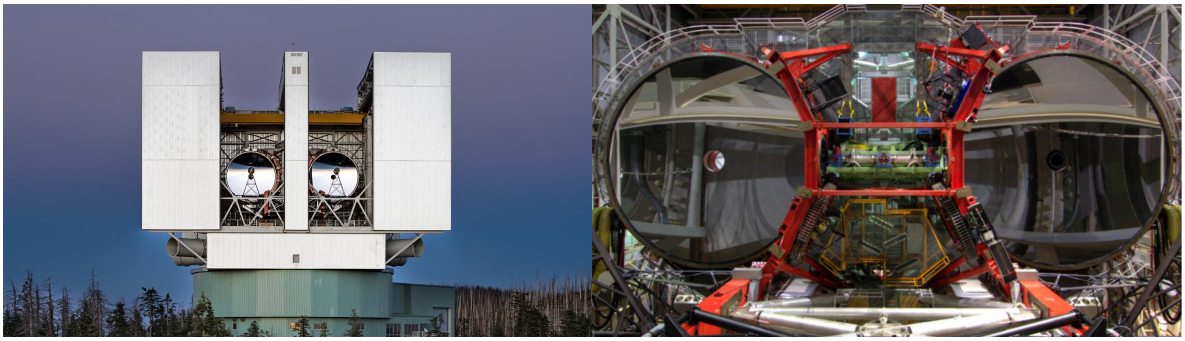

Figure 2.7: Photographs of the Large Binocular Telescope (LBT) on the left and of the Large Binocular Telescope Interferometer (LBTI) on the right. The LBTI is the central green structure in the right image.

With this inverse proportionality it is clear, since we have the baseline B much larger than the primary mirror size D, that nulling interferometry can provide a much smaller inner working angle.

With a more precise estimation, as presented in Equation 2.13, we can compute the inner working angle of the LBTI when operating with a coronograph. For this, we have to consider the size of the primary mirror D, of 8.4 meters. With a standard coronograph on the LBTI we would obtain an inner working angle of 273 mas (Equation 2.13, N = 1) and down to 192 mas (N = 0.7) with a state of the art coronograph at 11μm.

In the context of nulling interferometry, on the other hand, we have $\frac{\lambda}{B}$ the separation between the two constructive fringes closest to the center. The FWHM is in this case only $\frac{\lambda}{2B}$. The closest point at which a detection could be made would therefore be $\frac{\lambda}{4B}$, which is considered the inner working angle. To compute the inner working angle of the LBTI with nulling interferometry, we therefore have to consider a center-to-center separation of 14.4m. At 11μm, the inner working angle is thus 40 mas, almost five times smaller than with the state-of-the-art coronographs. Compared to a state of the art coronograph, this allows us to multiply the distance at which it is possible to resolve the habitable zone of a Sun twin by five and thus allow for a much larger number of targets. Using interferometers with larger baselines, such as the VLTI and its baselines of 130 meters (UTs) and 200 meters (Auxiliary Telescopes, ATs), it is clear that the inner working angle can become extremely small. The NOTT instrument will benefit from those very large baselines and will be able to look for exoplanets much closer-in than any instruments in direct imaging.

The case of the LBTI

The Large Binocular Telescope (LBT) is composed of two 8.4-meter primary mirrors on a single mount, a baseline of 22.7 meters, and a center-to-center separation of 14.4m.

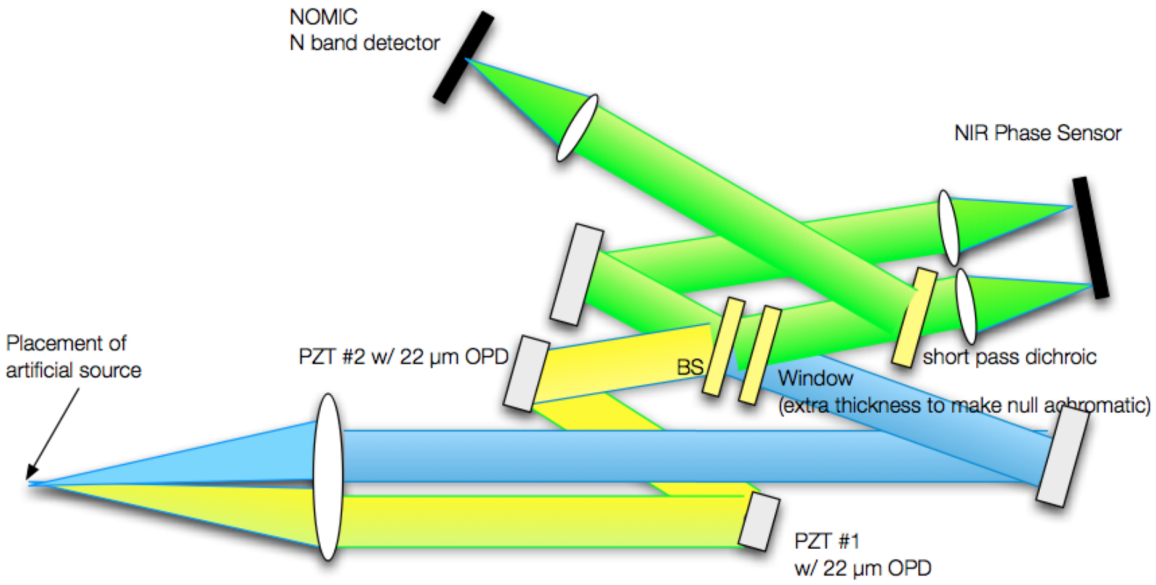

Figure 2.8: Schematic of the optics in the cryogenic Nulling Infrared Camera (NIC) of the LBTI. Figure from Defrère *et al.* (2014)

The secondary mirrors are equipped with adaptive optics and can correct for atmospheric effects. After a third reflection on the tertiary mirrors, the lights enter the cryostat of the LBTI. Compared to other interferometers, with much longer baselines, the number of warm reflections of the LBTI is much smaller. Each warm reflection results in some thermal background, which will itself result in additional photon noise. Reducing the number of warm reflection thus reduces the amount of thermal background link to it, and consequently the related photon noise. The LBTI thus strongly benefits from its configuration with only three warm reflections compared to other long-baseline interferometers.

However, the LBTI is really a particular type of interferometer as it can provide actual images of the observations, without using image reconstruction. In fact, with traditional interferometers, only the visibility is measured. With the parallactic angle range and the variation of the baseline length, an image can then be reconstructed through post-processing. In contrast to those interferometers, the baseline of the LBTI cannot change; it is, however, directly able to produce images and not only visibility. Compared to a standard interferometer, the LBTI is thus able to obtain the spatial information much more effectively because it is contained entirely in the images of the observations. Indeed, most interferometers inject the light from the PSF into integrated optics such as optical fibers, and by doing this loose the spatial information. The LBTI, on the other hand, is an interferometer with a field of view that uses a beam splitter, as shown in Figure 2.8.

The light from the two telescopes, corresponding to the yellow and blue beam in Figure 2.8, is superposed in the pupil plane, at the level of the beam splitter (BS), to

perform nulling-interferometry. The Window, with this extra thickness, ensures that the null is achromatic. The K-band light is then directed toward the phase-sensing camera, while the N-band light is directed toward NOMIC, the N-band detector, used for nulling-interferometry. The light is finally reimaged thanks to the lens before NOMIC.

This particularity of the LBTI allows its data to be treated in an imaging or an interferometric way. Indeed, the data on which this thesis focus are nulling interferometric data, however, they can be processed as any high-contrast imaging dataset, on which contrast curves can be obtained, even though their main purpose is to provide null measurements. The LBTI is thus a very versatile instrument, able to accommodate a wide range of observations. Indeed, many observing programs with the LBTI do not even use interferometry.

2.2 Sources of errors and thermal background

In this section, we consider the noise and background sources and contribution in the context of the LBTI. We first consider the noise link to the detector and the fundamental photon noise, which results in uniform random noise, which increases the uncertainty of the measure. Then we consider the non-uniform static and non-static contributions which create background structures. Finally, we briefly discuss two nulling-related sources of errors that can impact noise.

2.2.1 Uniform random noise sources

When it comes to the sources of uniform random sources, we can distinguish three types of noise. The first is the read-out noise of the detector. This type of noise is completely dependent on the technical specification of the detector and is thus unique to each detector. This noise consists in the counts of electrons obtained when only reading the detector. More precisely, the count of electrons is obtained when no light is shed on the detector and minimal integration is used.

A second source of noise, closely related to the read-out noise, is the dark current. In this case, we consider the electron counts obtained when reading the detector, without any light on the detector but with a given integration time. Indeed, the detector itself has a given temperature and its quantum variation randomly creates electrons. This source of noise is linked to both the technical specification of the detector and to the integration which is considered.

The third, and most well-known, source of random noise is, of course, the photon noise, which is described by a random Poisson distribution. The photon noise is a fundamental limit to the precision of the measures and cannot be reduced by any means. It solely depends on the photon counts that reach the detector. We can distinguish between two main components of the photon noise: the background and the source. The

total photon noise $n_{p,tot}$ would then be expressed as:

$$n_{p,tot} = \sqrt{(n_{p,background})^2 + (n_{p,source})^2} = \sqrt{N_{p,background} + N_{p,source}} \quad , \quad (2.17)$$

with $n_{p,background}$ and $n_{p,source}$ respectively, the photon noise from the background and the photon noise from the source, and $N_{p,background}$,$N_{p,source}$ respectively, the number of photons from the background and the number of photons from the source. In this case, assuming the background is uniform, the component of the photon noise coming from the background will be uniformly distributed over the image, whereas the photon noise coming from the source will be contained in the PSF.

In the case of the LBTI and in particular the configuration used for the HOSTS survey, the photon noise is the dominant source of noise, followed by the read-out noise of the detector, which is as high as a third of the photon noise level, and the dark current. In the case of the HOSTS survey, which this thesis focuses on, the dark current is negligible compared to the other noise sources. However, for different applications, such as spectroscopy, where the light is dispersed with respect to the wavelength and thus requires longer integration times, the dark current can become much more problematic. In addition, in the N' band, in which the data used in this thesis were acquired, the background is much brighter than the source itself. It is in particular true in the case of nulling-interferometry for which only a few percent of the starlight remains.

Now, let us take a closer look at what is included in the background component. Indeed, the thermal background is a complex entity which encompasses various sources, themselves producing a wide variety of effects. It is important to understand that the photons coming from this background can be corrected for, but that the photon noise resulting from those photons cannot. The number of photons produced by those various components can be expressed as a function of a black-body emission at the temperature of the component and at the wavelength of the observation. The number of photons of a perfectly opaque component of temperature T_{opaque} at an observing wavelength λ could then be expressed as :

$$N_{p,opaque} \propto B(T_{opaque}, \lambda)\eta \quad , \quad (2.18)$$

with B the Planck function for black body emission and η the opacity of the component. The number of photons of a perfectly transparent or reflective component on the other hand will be 0. With this, we can decompose the contribution to the background photons in the LBTI as follows:

$$N_{p,tot} = N_{p,atm} + N_{p,M1} + N_{p,M2} + N_{p,M3} + N_{p,win} + \overset{i}{\Sigma} N_{p,M_i} \quad , \quad (2.19)$$

with $N_{p,atm}$ the photon from the atmosphere, $N_{p,M1}$,$N_{p,M2}$ and $N_{p,M3}$ respectively the photons from the primary, secondary, and tertiary mirrors, $N_{p,win}$ the photon from the window by which the light enters in the LBTI, and N_{p,M_i} the photon from the i^{th} mirror

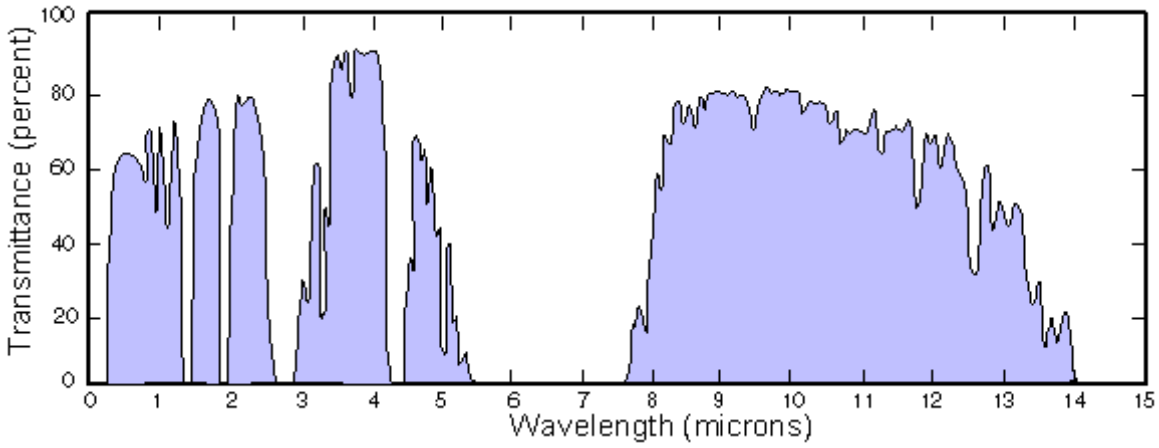

Figure 2.9: Atmospheric windows from 0 to 15 microns, displaying the transmittance of the atmosphere in percent. Image credits: Wikipedia, public domain.

in the cryostat of the LBTI. The number of photons for the atmosphere and the window is expressed in the form of :

$$N \propto (1-\tau)B(T,\lambda) \quad , \tag{2.20}$$

with τ the transmittance, while the number of photons for the various mirrors is expressed in the form of:

$$N \propto (1-R)B(T,\lambda) \quad , \tag{2.21}$$

with R the reflectivity of the mirror. In the LBTI, the reflectivities of the mirrors are about 90% and the transmittance of the window is of the order of 99%. The nulling-interferometric observations, used in this thesis, were obtained in the N band at 11 μ m, for which the atmosphere has a transmittance of about 80%, as can be seen in Figure 2.9.

The total expression of the number of background photons can thus be re-expressed as:

$$\begin{aligned} N_{p,tot} \approx\ & 0.2.B(T_{atm},\lambda) + \quad 0.1.B(T_{M1},\lambda) + 0.1.B(T_{M2},\lambda) + 0.1.B(T_{M3},\lambda) \\ & +0.01.B(T_{win},\lambda) + \quad \sum_{i} 0.1.B(T_{M_i},\lambda) \quad . \end{aligned} \tag{2.22}$$

In order to compare the contribution of the various terms in Equation 2.2.1, one needs to consider the various temperatures. The orange terms correspond to the elements that are at ambient temperature inside the dome of the telescope, T_{amb}. The blue term, on the other hand, corresponds to the reflective components at the temperature inside the cryostat, T_{cryo}. T_{amb} is the higher than T_{atm}, as T_{atm} considers the temperature of the entire column of the atmosphere. Compared with those two temperatures, T_{cryo} is much lower, and thus the terms with which it is associated are generally negligible. It is thus

clear, considering the respective temperatures of the components, that the combined effect of the three warm reflections are the dominant component of the background photons. It is thus important to consider in more detail the impact on background of these three terms.

Indeed, in addition to the reflectivity of the mirror, imperfections and temperature gradients can modify the number of photons created by the element. Those imperfections and gradients have the potential to create structures in the background and thus non-uniform effects. In the case of the LBTI, the primary and secondary mirrors are located in the pupil plane. Thus, any such effects would be average over the whole detector and only result in an increased uniform random background level, as well as a higher photon noise. The tertiary mirror, as well as the window and the mirrors in the cryostat, are not located in the pupil plane, so that any imperfection or gradient might result in background structures.

2.2.2 Structured effects on the background

In the previous subsection, we only considered the uniform random component of the noise. However, assuming that the background is uniform is not realistic. Indeed, apart from the photons associated with the primary and secondary mirrors, all the other components can lead to background structures, in addition to the uniform component. We can, however, distinguish two cases: the static and non-static background structures. In the first case, the total number of photons of an element can thus be reexpressed as:

$$N_{p,elmt_{tot}}(r) = N_{p,elmt_{uniform}} + N_{p,elmt_{struct}}(r) \quad , \tag{2.23}$$

with r, the position on the detector. While, in the second case we would need to express it as:

$$N_{p,elmt_{tot}}(r,t) = N_{p,elmt_{uniform}} + N_{p,elmt_{struct}}(r) + N_{p,elmt_{struct}}(r,t) \quad , \tag{2.24}$$

with t the time (or frame) considered.

Static structures

We mentioned in the previous subsection that background structures could appear for the different elements outside of the pupil plane, due to temperature gradients or element imperfections. Equation 2.2.1 would in this case be rewritten:

$$N_{p,tot} \approx N_{p,uniform} + 0.2.B(T_{atm},\lambda) + 0.1.B(T_{M3},\lambda) + 0.01.B(T_{win},\lambda) + \sum^{i} 0.1.B(T_{M_i},\lambda). \tag{2.25}$$

As already stated, the temperatures T_{M_i} of the reflective elements in the cryostat are really small compared to the temperatures of the other elements, but are also controlled,

thus preventing the change of temperature gradients. If structures appear from those optics, then they should occur because of mirror imperfections and static temperature gradient. Additionally, since the cryostat is a closed, pressure-controlled enclosure, mirror imperfections are also unlikely to change during the observations.

The case of the background caused by the window is slightly different as its temperature is not controlled. However, since the size of this element is fairly small, it is unlikely that a temperature gradient appears on it. The same argument can be made for the optical imperfections. Indeed, if it is not theoretically impossible for these conditions to change during the observations, it is very unlikely, and even more unlikely, that they will result in a significant impact on the background. We thus consider, in the case of the LBTI, that the potential nonuniformity of this element will only result in static background structures.

In addition to the sources presented in Equation 2.2.2, the detector itself can be a source of static structures. In fact, hot and dead pixels or rows of pixels will not change during the observations. In addition, temperature gradients due to detector imperfections will also not change during the observation, as the detectors are located in the cryostat. However, these effects can create important background structures.

If the tertiary mirror is likely to produce static structures, its conditions are not controlled enough for this element to only be described by a static behavior.

Similarly to the uniform components, those static background structures can relatively easily be corrected with an appropriate background subtraction; the resulting photon noise of those background structures, however, will only add up to the uniform component of the photon noise and remain a fundamental limit.

Non-static structures

When it comes to background subtraction optimization, the most challenging component is the non-static structures. Indeed, the ability of the correction to capture those structures will entirely depend on the timescale of the variation of those structures and the frequency at which the background is sampled. In addition, those structures cannot be corrected by simple background subtraction methods, such as subtracting a single correction image from each image that one wants to correct. Indeed, even if those structures are present in the correction image, its variation over time will not be taken into account, leading to imperfect removal of the structure.

If we consider once again Equation 2.2.2, which we rewrite to highlight the components for which non-static structures are likely to arise, we obtain:

$$N_{p,tot} \approx \; N_{p,uniform} + N_{p,static} + 0.2.B(T_{atm}, \lambda) + 0.1.B(T_{M3}, \lambda) \qquad , \tag{2.26}$$

In the context of optimization of background subtraction, as highlighted in Equation 2.2.2, the two most problematic components of the background will come from the atmosphere and the tertiary mirror. It is difficult to clearly assess which of the two components will be dominant. Indeed, if the temperature of the tertiary mirror is higher, the global transmittance of the atmosphere is lower than the reflectivity of the tertiary mirror. Furthermore, the strengths of the gradient are likely to differ strongly, rendering a general statement on the relative strength of one term over the other useless.

The background originating from the atmosphere is a really complex quantity, as it can be impacted by numerous factors. Just as optical elements, it can, of course, be impacted by temperature gradient, but also pressure gradient, water vapor concentration and gradient, cloud coverage, wind, etc. All of these sources have the potential to create non-static background structures, which variations can also span a wide range of timescale, amplitude, and shape. In the case of the LBTI and in particular of the nulling observations, this problem is somewhat simplified by the small field of view. In fact, only a very small portion of the sky ($\sim$ 2 arcsec) is observed. The variation of temperature, pressure, and water vapor concentration will thus be limited in such a small area. In addition, the nulling observations requesting excellent observing conditions, they would not occur with a high cloud coverage or wind. Altogether, the strength of the background structures coming from the atmosphere will thus be rather limited, facilitating the background correction. However, background structures originating from the atmosphere have such a wide variety of sources that the timescale of their variation can still pose a serious challenge for a precise background correction.

Another important source of nonstatic background structure is the tertiary mirror. Indeed, in contrast to the primary and secondary that are in the pupil plane, and the mirror in the cryostat, which temperature is controlled, the tertiary mirror can experience a temperature gradient which would propagate in the form of background structure up to the detector. In addition, since the tertiary mirror is not in an enclosure, dust or humidity can impact it and lead to the appearance of background structure. Similarly to the atmosphere, these variations can occur on a wide range of timescales. However, as previously mentioned, nulling observation being performed only when the observing conditions are excellent, strong wind, or sudden temperature drop, which could lead to variations with very small timescales are unlikely.

Besides the sources of background directly linked to the optical elements of the LBTI, we can add another source of structured, varying background: the varying optical path. Indeed, the LBTI has two delay lines which correct for the optical path difference and the phase shift between the beams coming from the two telescopes. As those delay lines are correcting for those effects, their mirror will move and thus lead to slightly different optical paths. This means that the light at a given detector position will come from a slightly different position on the optics ahead of the delay line. This light can thus go through different optic imperfection or a region with a slightly different temperature.

The optical path will change, for example, when nodding. Indeed, the HOSTS survey used nodding to correct for slowly varying background and systematic effects from the detector, but by doing so introduced smaller effects from the varying optical path. A smaller effect, which leads to optical path variation and thus introduces background variations, is the systematic pathlength and pointing drift. The pathlength corrector will correct for these drifts and thus slightly modify the optical path.

When the delay lines are operating on closed-loop feedback, those differences are expected to be small, as the difference in the optical path would itself be rather small. If the feedback loop opens, on the other hand, the changes will be much more significant and so will be the variations of the background structures.

2.2.3 Nulling Errors

In addition to the background sources, two sources, specific to nulling-interferometry can be identified. As mentioned previously in the case of nulling-interferometry, only a few percent of the starlight remains. The photon noise resulting from the starlight is thus rather small compared to the photon noise resulting from the background sources. It can, however, still contribute to the total photon noise, in particular when the star is not well nulled.

The images of the stars by the two telescopes of the LBTI are, in the case of nulling-interferometric observations, overlapped on the detector. The first rough overlap is done manually before the phase camera search for the precise position of both stars, which allows for an optimal overlap. Any error on this overlap will lead to additional star leakage, hence more starlight which will not be nulled, and more photons from the star on the detector. This increase in the number of photons will similarly increase the photon noise link to it. This problematic is, of course, not only important when setting up the observations but throughout the whole observation, during which the phase camera will have to maintain this overlap as precise as possible. Due to instrument imperfection and the changing observing conditions, it is very likely that the quality of this overlap will vary during the observations. The resulting photon noise will also vary with respect to the quality of the overlap.

The first source of error comes from the phase itself. In fact, in nulling-interferometry, the beams from each telescope are combined with a phase shift of π to obtain destructive interference on the line of sight. Throughout the observations, the phase camera will keep this phase shift between the beams, to null the star. In real observing conditions, the phase will constantly require adjustments, and the phase camera operates on a feedback loop to keep the phase shift between the two beams. Small variations are expected that will create fairly small errors and hence a fairly small contribution to the star leakage.

If those two sources of errors do not directly impact the background, they will nonetheless impact the total photon noise and thus reduce the overall sensitivity of the

observations. However, those are fairly small contributions compared to the photon noise coming from the background itself.

2.3 High Contrast Imaging and PSF subtraction

In high-contrast imaging (HCI), the objective is to uncover faint circumstellar sources. In this context, depending on the observing wavelength, background subtraction can be extremely important but will never be sufficient. At mid-infrared wavelength, where the contrast between the star and the planet is the most favorable, the background dominates. However, the next dominant source in the image is the star. Observing techniques such as coronography and nulling-interferometry can already remove an important part of the starlight, but the residuals can still dominate and prevent faint planet detection. This problem is, of course, even more challenging when observations are made without any of these techniques. Thus, in order to remove as much of the residual starlight, and uncover faint sources, one has to rely on post-processing and effective PSF subtraction. To remove the PSF, HCI relies mainly on three techniques: Angular Differential Imaging (ADI, Marois *et al.,* 2006), Reference-star Differential Imaging (RDI, Lafrenière *et al.,* 2007) and Spectral Differential Imaging (SDI, Smith, 1987). Another technique mainly used for disk imaging makes use of the polarization of the observations to subtract the PSF, the Polarized Differential Imaging (PDI, Kim *et al.,* 1987). In this thesis, we only make use of the ADI and RDI techniques, as the LBTI nulling data do not contain several observed wavebands or polarization measurements, rendering the application of SDI and PDI impossible for these data.

2.3.1 Angular Differential Imaging

The ADI technique is based on an observing strategy that allows the observed system to rotate in the image through the observation. In other words, the system is observed in a range of parallactic angle. During the observation, the star remains at the center, whereas everything surrounding will appear to rotate in the image. We present the principle of ADI in Figure 2.10.

In step A represented in Figure 2.10, the star is well centered on the rotation axis, and the planet around it is rotating. In this example, the planet is rather bright and can still be distinguished even without the PSF subtraction. However, a fainter planet could at this stage be confused with speckles from the star. Thus, one needs to retrieve the PSF in the image in order to subtract it. The simplest method would thus be to compute the mean image of all the raw images to estimate the PSF. Indeed, as the planet rotates and is thus never at the same position in the star, it will only weakly contribute to the mean image, whereas the star, in the center, will contribute strongly. The resulting mean image will thus be sensitive to the star and not to the planet. When subtracting this mean image from all individual images (step C), the planet will thus mostly not be

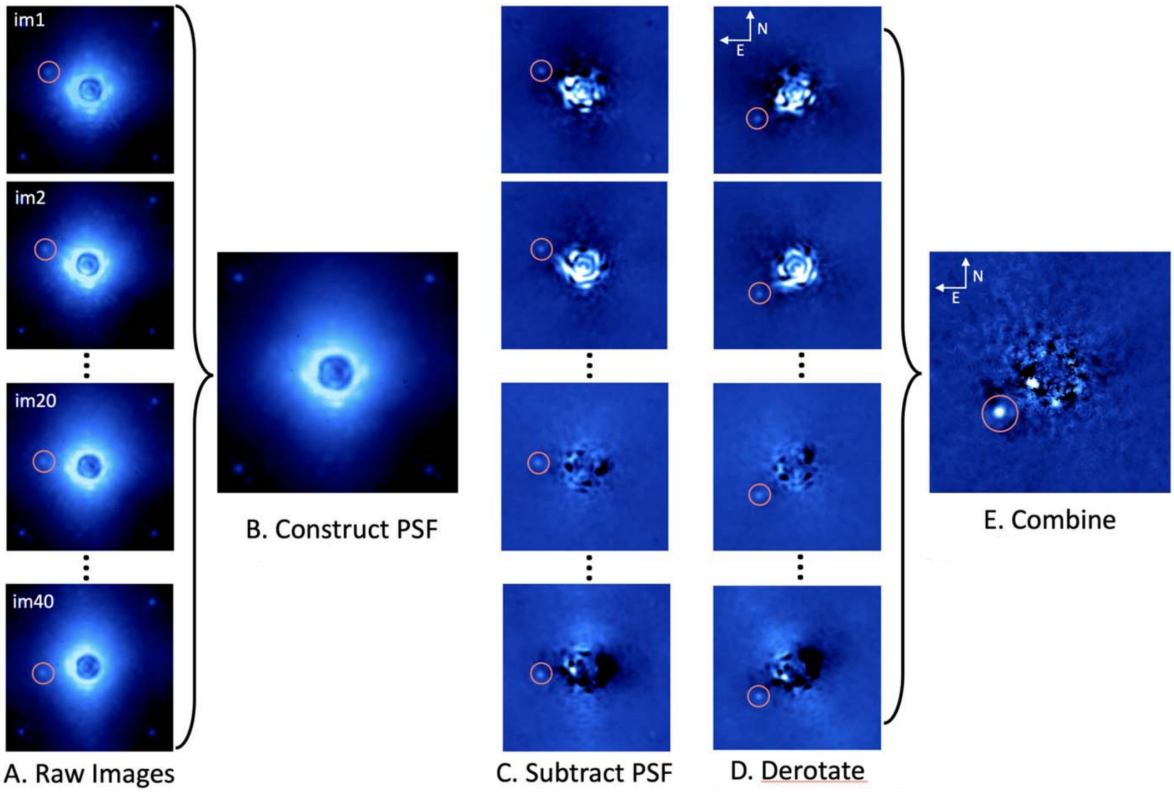

Figure 2.10: Schematic representation of the ADI technique. The images A represent the images before the start of the PSF subtraction process. In the context of this thesis, they correspond to the background-subtracted images. The step B retrieve everything which is not rotating in the image to construct the PSF, and can be performed with various methods. In step C, the reconstructed PSF (B) is subtracted from every individual image. The images are then de-rotated in step D, depending on the parallactic angle at which they have been observed. Finally, the images are stacked in step E, to construct a final image. Original image from Follette (2023).

subtracted, while the star will almost completely be removed. Of course, the use of the mean image limits both the quality of the PSF reconstruction and still presents a strong risk of self-subtracting the planet. Thus, a much more complex procedure is usually used for PSF reconstruction, in particular PCA (see Section 2.4.3). The reconstruction of the PSF is the most important step of the procedure and will determine the quality of the PSF subtraction, hence the necessity of more precise methods. After this step, the reconstructed PSF is subtracted from each individual image, which are then de-rotated and stacked.

An important parameter, when using ADI for PSF subtraction, is by how much the circumstellar source will rotate during the observation. The more the star will rotate, the less the PSF reconstruction will risk including the circumstellar source signal. Indeed, if the observations are made with a very limited parallactic angle range, the circumstellar source will barely move from one image to another, and thus risk being self-subtracted. With observations probing a large parallactic angle range, one can exclude frames which are too close in terms of parallactic angles, and in which the companion is likely to

overlap, to prevent the self-subtraction.

The strength of this technique is that it directly uses the images to be corrected to build the correction. The reconstructed PSF will thus be extremely similar to the real PSF, and left very few residuals. However, this method has two main limitations : it requires an important range of parallactic angles to function at its best, and it self-subtracts any circularly symmetric structures around the star. Indeed, when looking for a circumstellar disk, there will be disk emission at all azimuth, so when the disk rotate some emission will always be at these locations. Any spatially constant feature in the disk would thus be taken into account by the PSF reconstruction, and subtracted out. Only irregular features such as clumps would remain. In this case, the ADI technique is thus not well adapted, and RDI is preferred.

2.3.2 Reference-star Differential Imaging

The RDI technique, instead of relying on the rotation of the system in the image, relies on the observations of calibrator stars. The difficulty with this method is to select calibrator stars that will match the PSF of the science target, and in particular match the color of the science target in the observations bandwith, without harboring circumstellar emission which might mimic those of the science target. Indeed, with this method, the reconstructed PSF is built solely on the images from the calibrators stars. The principle of RDI is represented in Figure 2.11.

When using RDI, no rotation is needed; however, the rotation could still occurs during the observations and would not hinder the method. In fact, in Figure 2.11, shows in step A that the disk is observed at different angles. As in the case of ADI, the most critical step of the procedure is the PSF reconstruction. For RDI however, as we do not use the image to be corrected to build the correction, there is usually more residuals than in the ADI case. As shown in step B of Figure 2.11, the PSF of the calibrators are both different from each other and different from the PSF of the science target. The method chosen to reconstruct the PSF is thus critical and should be able to discard individual effect of the calibrators while combining the effect that can be found in many of them, but also adapt the reconstructed PSF to the data to be corrected. PCA is commonly used for PSF reconstruction in the case of RDI PSF subtraction (see Section 2.4.3). The reconstructed PSF is then subtracted from any individual images (step D), derotated (step E), and stacked (step F).

With this technique, since the reconstructed PSF is usually less similar to the real PSF than in the case of ADI, residuals tend to be stronger. Besides the higher residuals, another drawback of this method is the necessity to observe calibrator stars, thus taking time from the observations of the science target. However, in contrast to ADI, this technique prevents self-subtraction of symmetrical circumstellar emission. Thus, this technique is preferred for observing disks and extended structures. This method is also useful when no or little parallactic angle range can be covered during the observations,

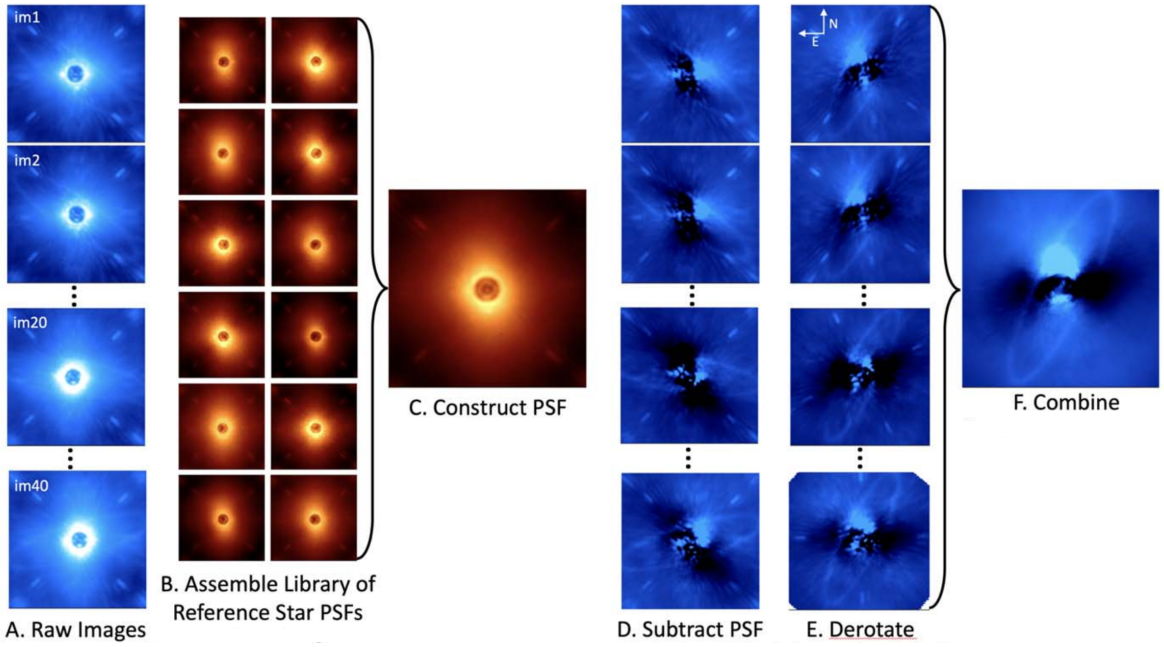

Figure 2.11: Schematic representation of the RDI technique. The raw images (A) represent the images before the start of the PSF subtraction process. In the context of this thesis, they correspond to the background-subtracted images. The images in B are taken from calibrator stars, from which we expect no circumstellar emission and a similarity to the PSF of the science target. Step C construct a PSF based on the calibrators' PSF. In step D, the reconstructed PSF (C) is subtracted from every individual images. The images are then de-rotated (E) and stacked (D).Original image from Follette (2023).

as this method is not sensitive to the rotation of the circumstellar emissions.

2.4 Principal Component Analysis

The Principal Component Analysis (PCA) is a statistical method that was developed independently in 1901 by Karl Pearson (Pearson, 1901) and in 1933 by Harold Hotelling (Hotelling, n.d.). This method is extremely versatile and can be applied in very different fields such as signal processing, mechanical engineering, meteorological science, structural dynamics, etc., and has many names depending on the field. This powerful method allows us to describe the data by the different axes (the principal components) that encompass the largest variation of those data. The more principal components one chooses to use, the more axes of maximum variations are determined, and the finest the data description. In Figure 2.12, we show a basic representation of the principal components.

We can see in this figure that the first principal component is the largest and represents the extension of the data points in the direction in which they are most scattered. The second principal component is much smaller and represents the width of this set of data points along the first axis, or the first principal component. With those two axes, we can describe the general behavior of the set of data points. However, they

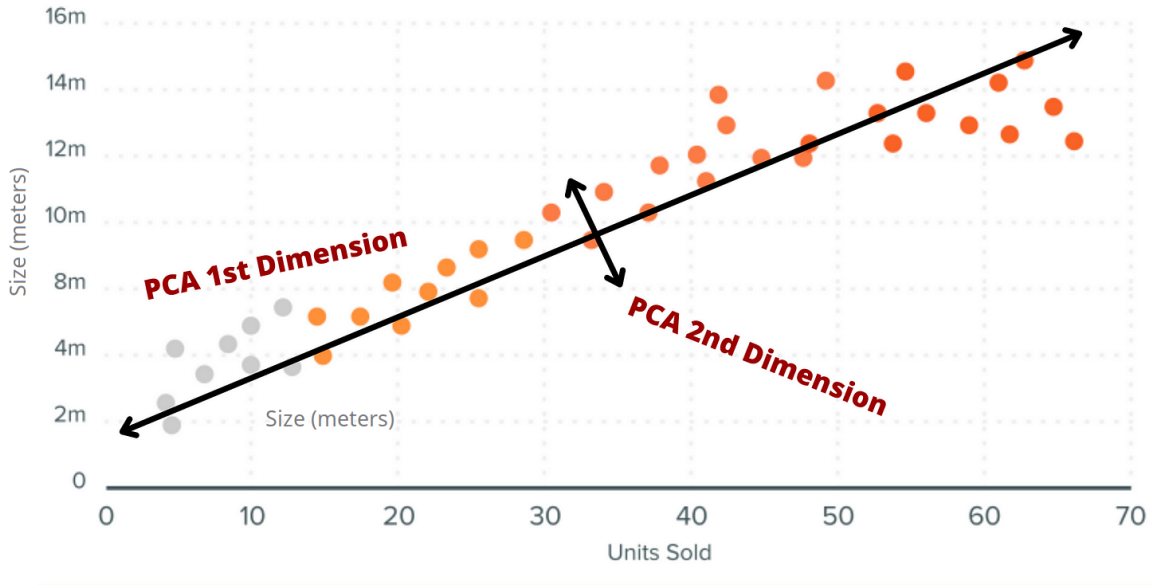

Figure 2.12: Schematic representation of the two first principal components of a set of data points.

fail to describe the small curvature toward the right extremity of the set of data points. In order to describe this curvature, one would need to use more principal components. However, those data points contain only two pieces of information (size and number of sales) which limits the number of principal components at two, preventing a finer description of the data.

2.4.1 Mathematics

Let us take the example of a dataset composed of K images, themselves composed of N pixels. We want to study the variation of the pixels in the image for each image. To do so, we put our data, the values of pixels V, for each pixel n and each image k in a matrix M. This matrix is written as follows:

$$M = \begin{pmatrix} V_{1,1} & \cdots & V_{1,N} \\ \vdots & \ddots & \vdots \\ V_{K,1} & \cdots & V_{K,N} \end{pmatrix}$$

This first case represents the situation discussed in Chapter 3. The red frame represents all the pixels contained in one given image, it is referred to as one realization, whereas the blue frame represents the value of one given pixel for all the images. If, rather than studying the variation of the pixel value within an image for all images, we wanted to study the variation of the pixels over time, as discussed in section 3.6, then the matrix should be written:

$$M' = \begin{pmatrix} V_{1,1} & \cdots & V_{K,1} \\ \vdots & \ddots & \vdots \\ V_{1,N} & \cdots & V_{K,N} \end{pmatrix}$$

In the following, we will use the example of matrix M. To prepare the data for PCA, each matrix M containing the data is associated to a diagonal matrix W containing the weight of each realization. In a standard case, each realization has the same weight $\frac{1}{K}$. In Chapter 3 this is the case which is used. However, one can choose to give more weight to some realizations. For example, if we know that some images are more representative than some others, it could be advantageous to give those images more weight to obtain better-suited principal components. As a first preliminary step, the matrix M is thus multiplied by the matrix W, this step is called weighting the data.

$$M_W = W.M = \frac{1}{K}.M \quad , \tag{2.27}$$

The second preliminary step to prepare the data for the PCA is to center the data on the center of gravity (most of the time, the average or the median) of the data and to reduce the dataset. This step allows avoiding one outlier realization to completely monopolize the principal components. Indeed, if an outlier introduces a variance which is larger than the variance of the rest of the dataset, the principal component will rather represent the variance introduced by this outlier than the variance of the rest of the data in which we are interested. The matrix M is thus transformed as follows:

$$\mathrm{M}_R = \begin{bmatrix} \frac{V_{1,1}-\overline{V}_1}{\sigma(V_1)} & \cdots & \frac{V_{1,N}-\overline{V}_N}{\sigma(V_N)} \\ \vdots & \ddots & \vdots \\ \frac{V_{K,1}-\overline{V}_1}{\sigma(V_1)} & \cdots & \frac{V_{K,N}-\overline{V}_N}{\sigma(V_N)} \end{bmatrix}$$

with $\overline{V}_n$ the center of gravity of the point through the realization and $\sigma(V_n)$ their variance. After those preliminary steps, in our case, where all the realizations have the same weight and the data have been centered and reduced, PCA computes the correlation matrix, which is simply done by multiplying it by its transposed.

$$M_C = M_R^T.\frac{1}{K}.M_R \quad , \tag{2.28}$$

with M_C a matrix $N \times N$. PCA will then determine unit vectors that maximize the variance of the data around this vector. In Figure 2.12 the first unit vector would be along the axis of the PCA first dimension. The second unit vector would similarly follow the axis of the second dimension of the PCA represented in the figure. We therefore define a unit vector u, such as the projection of the data on u providing the maximum variance, and $P_u(M_R)$ the projection of the data onto this unit vector. We therefore want

$P_u^T(M_R).\frac{1}{K}.P_u(M_R)$ the variance, V_a, of this projection to be maximal. If we develop the expression of V_a, we obtain:

$$V_a = P_u^T(M_R).\frac{1}{K}.P_u(M_R) = u^T.M_R^T.\frac{1}{K}.M_R.u \quad , \tag{2.29}$$

and from Equation 2.28 we can rewrite it as:

$$V_a = u^T.M_C.u \quad , \tag{2.30}$$

The matrix M_C is, by its construction, a square matrix $N \times N$ that can be diagonalized by determining the N eigenvalues λ_n:

$$det(\lambda I - M_C s) = 0 \tag{2.31}$$

and the eigenvectors v_n with:

$$(\lambda_n I - M_C)v_n = 0 \tag{2.32}$$

Thus this diagonalization allows one to define eigenvalues associated to eigenvectors, each of which will successively describe the maximum variance of the data. If we define B the change of basis, and D the diagonal matrix composed of N eigenvalues λ_n, we can thus rewrite V_a as:

$$V_a = u^T.B^T.D.B.u = v^T.D.v \quad , \tag{2.33}$$

with v,

$$v = \begin{bmatrix} v_1 & v_2 & \cdots & v_N \end{bmatrix} \quad , \tag{2.34}$$

the matrix containing the unit vectors v_n in the new basis. We therefore search for the unit vector u that maximizes V_a. By definition of the eigenvalues, the maximum variance will be achieved by:

$$v_1^T.D.v_1 = \lambda_1 \quad . \tag{2.35}$$

with λ_1 the highest eigenvalue. The unit vector v_1 that solves Equation 2.35 is thus the first principal axis of the data. When the data are projected on this first principal axis, we obtain the first principal component. The second principal component will be described by the same equation, but replacing λ_1 by λ_2 and so on. The principal components PC_n are then described as:

$$PC_n = M_R.v_n \quad . \tag{2.36}$$

When performing PCA, we determine the number of principal components n_{PC} in which we are interested. Thus, PCA determines the first n_{PC} eigenvectors, corresponding to the first n_{PC} eigenvalues of the diagonal matrix D.

If this process allows finding the principal components, it is not optimal for numerical applications. Another method, the singular value decomposition (SVD), allows

optimizing its numerical application. It should be noted that in this thesis, we are using the Vortex Image Processing PCA algorithm (Gomez Gonzalez *et al.,* 2017) in which we can choose to compute the principal component through the determination of the eigenvectors, as described in this section, but we chose instead to use the numerically optimized SVD method.

2.4.2 Singular Value Decomposition

The SVD is a method that generalizes the spectral theorem to the non-square matrix and allows their factorization. The first to apply SVD to rectangular and complex matrices were Eckart and Young in 1936 (Eckart & Young, 1936). However, the first effective method for computing the SVD does not appear before 1965 with the Golub-Kahan algorithm developed by Gene Howard Golub and William Kahan (Golub & Kahan, 1965). Today, most numerical applications are using a variant of this theorem, developed in 1970 by Golub and Christian Reinsch (Golub & Reinsch, 1970).

Let us show that the SVD method is equivalent to the determination of eigenvectors. We have seen in Section 2.4 that the variance V_a is described by Equation 2.33 and the principal components by Equation 2.36. When performing the singular value decomposition, the reduced data M_R can be written as:

$$M_R = U.S.V^T \quad , \tag{2.37}$$

with U a unitary matrix whose columns contain the left-singular vectors of M_R, S the diagonal matrix of singular values s_n and V the matrix which columns are the right singular vector. If we now combined this results with Equation 2.28, we obtain:

$$\frac{1}{K}.M_R^T.M_R = \frac{1}{K}.V.S.U^T.U.S.V^T = V.\frac{S^2}{K}.V^T \quad . \tag{2.38}$$

This result is very similar to Equation 2.33 with V being equivalent to v, and $\frac{S^2}{K}$ to D. The relation between the eigenvalue λ_n and the singular values s_n is thus written:

$$\lambda_n = \frac{s_n^2}{K} \quad , \tag{2.39}$$

and the definition of the principal components became:

$$PC_n = M_R.v_n = U_n.s_n.V_n^T.v_n = U_n.s_n.v_n^T.v_n = U_n.s_n \quad . \tag{2.40}$$

Using the singular value decomposition is thus equivalent to determining the eigenvector to perform the PCA. We describe in more detail how the singular value decomposition works in the appendix 6.1.

2.4.3 Applications in Astronomy

PCA is a very widely used method in Astronomy. Its versatility allows it to be applied not only for data correction and optimization but also for their interpretation. A few examples are the classification of stellar (Singh *et al.,* 1998) and galactic spectra (Ortiz & Galaz, 2009), the characterization of stellar abundances (He & Zhao, 2019), the correlation of certain spectral parameters (Czarnik-Matusewicz & Pilorz, 2006), the search for variable star (Moretti *et al.,* 2018), the correction of stellar activity (Cretignier *et al.,* 2022), etc. Indeed, as PCA is able to identify common characteristics in a set of data, it is very well suited to detect correlations between two sets of data, or several parameters. This particularity makes PCA a very useful tool for data interpretation. In this thesis, we are making use of another of its strength: data reconstruction. In fact, once the principal components have been identified, one can use them to reconstruct a realistic synthetic data set. Those cleaned datasets will be much easier to interpret as a lot of small, random, or outlier features will be absent. This reconstruction can also be used, outside of interpretation, as a correction. In fact, when one is interested in what is not a major feature of the dataset, the reconstruction, which contains those major features, can be subtracted from the original data. In this case, PCA is used as a correction tool. We can thus identify three main ways to use PCA: to identify correlations, to extract important features, and to remove dominant features.

Identifying correlations with PCA

As we have seen in previous sections, the principle of PCA is to identify axes that encompass the maximum variance in the data. This procedure allows retrieving the mean features of a data set. To identify correlations, PCA can thus be used in a variety of ways depending on the correlations that one wants to uncover.

Let us digress for a brief moment to introduce the notion of the PCA library. When performing PCA on a dataset, one defines a library that contains all the data that one wants PCA to take into account to define the principal components. If the dataset consists of a cloud of points, each instance of the library will be one of those points, in the case of a sequence of images, a possible library is to take each image as an instance. It is also possible to select the instances to include in the library in order to suppress outliers that might impact the principal components, or to study some particular aspect of the dataset.

When one wants to identify similarities between two datasets, a first simple way to proceed is to merge the library of the two datasets. In this way, PCA will take both datasets into account when building the principal components. The resulting principal components will thus represent the maximum variance of the two combined datasets. However, this method presents strong limitations. Indeed, if the two datasets do not have the same weight, for example, one being larger than the other, or having more variance, the dataset with the more weight will have a stronger impact on the principal

components which will in turn bias any search for similarities. Another issue comes from the possible variance introduced by the differences between the two original datasets. If that variance is significant, then the principal components could represent this variance rather than the variance of a possible correlation. Although this method can still be used with some datasets that do not suffer from those limitations, it cannot be applied to the vast majority of cases.

Another simple method, which does not suffer from those limitations, is to run PCA on both datasets separately and later compare the principal components extracted from each. However, the interpretation of such correlations would need translation of the similarity between two or more principal components into physical correlations, which, depending on the complexity of the dataset, becomes extremely difficult.

Rather than blindly searching for correlation in the datasets, it is better to search for correlation between their parameters. The method will thus be similar to what is done to identify correlations in a given data set containing several parameters for which we want to identify the correlation. In this context, the focus of PCA is shifted from the main features of the data set to the main similarity of a given set of parameters. Let us take the example of spectra that contain a certain number of absorption lines. If PCA is run directly on the data points measuring the flux at a given wavelength, the principal components will represent the maximum variance of the spectra, such as a possible offset, a strong slope, etc. but will not help identify correlations.

To find correlations, the data need to be re-expressed as a function of the parameters. The easiest solution is to select a library that corresponds to a certain parameter. For example, in the case of a stellar spectrum, one can choose to reduce the library to a given stellar type and run PCA to identify the most representative features of the spectra of this stellar type. If one does that for every stellar type, those representative features can be linked to the stellar spectra, and correlation can be identified. However, in most cases, selecting the library significantly reduces the precision and the number of correlations that can be identified. In this example, one can find correlations with the spectral type but cannot find correlation with age, or a more precise correlation with temperature.

Thus, instead of proceeding to a library selection, one should rather rearrange the library as a function of a given parameter. For example, for a temporal serie of images, one can order the spectra as a function of temperature, age, distance, etc. instead of time so as to obtain a more continuous sample of the parameter we want to establish correlations with. The principal component analysis can then be apllied to the axis of interest : temperature, age, distance, etc. In our example, the standard library would be expressed as :

$$\mathrm{L}_\lambda = \begin{bmatrix} V_{1\lambda_1} & V_{2\lambda_1} & \cdots & V_{M\lambda_1} \\ V_{1\lambda_2} & V_{2\lambda_2} & \cdots & V_{M\lambda_2} \\ \vdots & \ddots & \vdots & \\ V_{1\lambda_N} & V_{2\lambda_N} & \cdots & V_{M\lambda_N} \end{bmatrix}$$

Where V_1 and V_M are, respectively, the first and last spectra of our dataset, $lambda_1$ the smallest wavelength, and λ_N the largest wavelength. The library can be rewritten as :

$$\mathrm{L}_T = \begin{bmatrix} V_{T_1\lambda_1} & V_{T_2\lambda_1} & \cdots & V_{T_M\lambda_1} \\ V_{T_1\lambda_2} & V_{T_2\lambda_2} & \cdots & V_{T_M\lambda_2} \\ \vdots & \ddots & \vdots & \\ V_{T_1\lambda_N} & V_{T_2\lambda_N} & \cdots & V_{T_M\lambda_N} \end{bmatrix}$$

Where V_{T_1} and V_{T_M} are, respectively, the spectra of the cooler and hotter star. With this new library, PCA will be able to identify the main spectral features that vary as a function of temperature. Of course, depending on the complexity of the data, a more complex rearrangement of the library might be needed; however, the principle remains similar. Once this rearrangement is done, if PCA finds significant principal components, then a correlation can be established, on the other hand, if the principal components appear random or poorly representative of the dataset, a correlation is to be discarded.

Extracting important features with PCA

Another type of PCA use is the extraction of the most representative features. Let us take the example of a time series of spectra of the same star with a very short amount of time in between each acquisition. Each spectrum will be affected by a certain amount of noise coming from the atmosphere, the optics, the electronics, etc. which will modify the "true" flux values. Let us assume that the noise is random and does not contain any systematics. The measured values will thus be randomly modified compared to the true values, and we thus obtain a "dirty" data set.

In this example, PCA will identify the spectral features that appear in a large number of the spectra. The more prominent and recurrent this feature is, the easier it will be for PCA to identify it. With an increasing number of principal components, PCA will retrieve smaller or less recurrent features up to the point where the noise is becoming dominant, and the remaining principal components will no longer be representative. By selecting the right number of principal components, one can thus retrieve the spectral features, without retrieving the noise associated with it. Those principal components can then be combined to build a synthetic spectrum from which the noise will be absent. To a certain extent, even structures smaller than the noise randomness can be uncovered as they will create a systematic effect in the data which PCA can retrieve given a certain number of principal components.

In a more realistic case, of course, the noise is likely not to be fully random and to be significantly larger than the smaller structures, preventing a perfect extraction. The resulting synthetic spectra will thus contain noise residuals, from the systematics which would be mistaken by PCA as a spectral feature, but also potential randomness depending on the level of details one wants to achieve.

As in the previous case, the library onto which PCA is performed can also be modified or optimized as a function of what one wants to retrieve. For example, if some spectra appear to be of lesser quality, with a higher noise level, they can be removed from the library or included with a smaller weight so as to have a lesser impact on the determination of the principal components. The library can also be rearranged to be studied from a different perspective. The "standard" perspective is indeed to study the variation of the flux in function of the wavelength. The noise in this case can be problematic, as it will modify the differences between two given wavelengths. Another possible perspective is to study the variation of the flux of the wavelength over time. In this case, the noise will modify the differences between two given times. However, using this other perspective could help uncover nonrandom flux variations created from a physical event such as an object passing in front of our target, a surge in brightness, etc. The combination of those two approaches can also benefit the synthetic spectrum reconstruction, as noise will not impact the different approaches in a similar way.

Removing dominant features with PCA

A third possible utilization of PCA is to remove the dominant features of a dataset, which hide the features of interest. This utilization is somewhat similar to the previous one but focuses on the noise rather than the signal. This is also the utilization made of PCA in this thesis. Two obvious examples of this utilization are to remove the thermal background so as to unveil the star (Hunziker *et al.,* 2018; Rousseau *et al.,* 2024), and to remove the star so as to unveil circumstellar emissions(Amara *et al.,* 2015; Amara & Quanz, 2012; Soummer *et al.,* 2012). Both applications allow to improve the detection limits.

Let us take the case of an N'-band nulling observation dataset, such as the ones studied in this thesis. The thermal background in this data set is much higher than the signal of the star, let alone any circumstellar emission. The dominant features of the data set will thus come from the thermal background itself. Using PCA, we can thus determine the principal components of the thermal background and reconstruct a synthetic data set that contains the main noise features. This is what is done for the signal in the previous case. However, the interest here is to remove this synthetic noise data set from the original data set, in order to obtain a cleaned data set without noise.

However, in a realistic case, some of this thermal background is rather constant or slowly changing, some is varying at higher frequencies, and some are finally totally random. PCA will identify the structures coming from the constant or slowly changing

component of the noise, as long as the structures are not too faint in comparison with other sources. For the random component, PCA cannot help as it will not identify significant structures. For the varying component, everything will depend on the sampling frequency, i.e, either the frequency at which references are taken (calibrators, background measurements, etc.), or depending on the implementation, the exposure time itself. It is clear indeed that if the variation of the background is happening on a smaller timescale than the exposure time, PCA will be totally unable to detect it. Similarly, if the library used to build the principal components is different from the images onto which the correction is applied, and if the background has significantly changed in between those two acquisitions, PCA will be blind to those changes.

Let us now describe in more detail how PCA works when used in these two cases. When using PCA for background removal (Hunziker *et al.,* 2018; Rousseau *et al.,* 2024), one needs a library of background frames, which do not contain the signal, is needed. The principal components are built on this library and thus cannot reproduce the signal as the library does not contain it. Once the principal components are built, the data containing the signal are projected onto the principal components to build a synthetic dataset of the noise. Depending on the case, one might need to mask the region of interest when performing this projection. The synthetic data set is then subtracted from the original data set, and the noise is removed, allowing the signal to appear. In this case, the self-subtraction of the signal is prevented as the principal components are built on a library that does not contain the signal. However, over-subtraction can happen and precautions should be taken according to the science case. This procedure is used in Chapter 3.

The second example is to use PCA to remove starlight in order to uncover a fainter circumstellar signal(Amara *et al.,* 2015; Amara & Quanz, 2012; Soummer *et al.,* 2012). One way to proceed is the Reference-star Differential Imaging (RDI), for which the method is identical to the case of background subtraction. Another method is to use Angular Differential Imaging (ADI), for which the library onto which the principal components are built and onto which the correction is applied is the same. The advantage of ADI is that the signal of the star is more similar than in the case of RDI. The principal components will thus be more representative and the star better subtracted. However, contrary to the previous case, if we build the principal components on the data containing the signal, we have a risk of self-subtraction. This risk is avoided to some extent because of the rotation of the dataset. Indeed, the star at the center will not move, but the circumstellar emission will rotate, and thus will not appear as a highly recurrent feature. In addition, the circumstellar emission being much fainter than the star, it will also be much less dominant than the star. However, by using a too large number of principal components, this signal can still be retrieved and subtracted. Another drawback of this method is that a symmetrical emission around the star will be subtracted too; it is thus preferred for point-source-like emission, but usually avoided for

disk-like structures. Both ADI and RDI applications of PCA for starlight suppression have been extensively used in previous works in direct imaging. We also use those two techniques in the high-contrast imaging application in Chapter 3.

Chapter 3

Improving the background subtraction with PCA

Contents

Infrared data, and in particular thermal infrared data, are known to be strongly impacted by thermal background. Indeed, it can easily outshine the signal observers are interested in. This is in particular true, in the N band (centered on $\lambda_c = 11.11\,\mu$m). In high contrast direct imaging, in the L and M bands, many efforts have been directed to tackle this background challenge (LOCI, M band -Galicher *et al.,* 2011, PCA, L and M band- Hunziker *et al.,* 2018). With this work, we propose to extend those efforts to both the N band, and nulling interferometric data. In this context, we developed a pipeline for the background subtraction with PCA, of nulling interferometric data from the HOSTS survey. Our pipeline is making use of the VIP library (Gomez Gonzalez *et al.,* 2017), which we adapted for background subtraction (an implementation for background subtraction was developed in parallel in VIP independently), in particular for the mask implementation, the de-rotation of the images, and the pre-subtraction step. The various steps of our pipeline, as well as the implementations of PCA are described in Section 3.2, and the source code can be found on github[1]. In addition, previous works have focused on contrast curve improvements for high contrast imaging, whereas we extend our analysis to aperture photometry and the accuracy of the photometry retrieval. The results of this analysis, with improvement factors ranging from 1.2 to 1.7 for HCI and from 2 to 3 in aperture photometry, were published in Rousseau *et al.,* 2024.

At the end of this chapter, we turn our focus on the temporal axis of the data. Indeed, the temporal dimension is also impacted by the background, and to correct

[1] https://github.com/HeleneRousseau/HOSTS-PCA-background-subtraction.git

for it can both improve the precision of the time-series measurement and help remove structures by taking their temporal information into account. Previous works in HCI have also been focusing on this temporal dimension such as Bonse *et al.,* 2018 which focuses on frequencies as a function of time to subtract speckles and Samland *et al.,* 2021 which starting from the LOCI concept switched the axis to study the temporal dimension for PSF and speckles subtraction. In this chapter we present a second PCA-based method to correct the background on the temporal axis. The approach of this work is similar to Long *et al.,* 2023 although both methods have been developed in parallel and independently. This method, which can also be used independently, is here presented in combination with spatial PCA background subtraction to demonstrate its potential benefits on aperture photometry.

3.1 Introduction

3.1.1 Observations

The observations were made in the broad N' filter ($\lambda_c = 11.11\,\mu$m, $\Delta\lambda = 2.6\,\mu$m), with the Nulling-Optimized Mid-Infrared Camera (NOMIC) of the LBTI. The HOSTS survey made use of the nulling-interferometric mode of the LBTI to suppress the starlight. For this nulling mode, the light collected by the mirrors is sent to two cameras. The K and H bands are sent to the fringe tracking camera, PHASECam, and the N band to NOMIC. The phase control to null the star is thus performed by PHASECam, with a closed loop, which allows one to maintain the null on the central star. Unlike most interferometers, the LBTI behaves like an imaging instrument with pupil stabilization, and the sky thus rotates across the detector during the observations. The images obtained during this survey can thus be used as a proxy for general AO-assisted N-band imaging data for both high-contrast imaging (HCI) and aperture photometry (AP). Furthermore, the field rotation of these observations allows the use of techniques such as angular differential imaging (ADI) for HCI.

The observations of the science targets were separated by calibrator observations, using several calibrators for each scientific target. Each observation of a star consists of three parts: (1) nulling observations interfering the starlight by overlapping the images from the two apertures in the pupil plane and offsetting between two detector positions (nodding) for background observations typically every 5–10 minutes, (2) photometric observations placing the star images from the two apertures next to each other on the detector, and (3) background observations for the latter where the star images from the two apertures are moved off the detector. The HOSTS observing strategy is detailed in Defrère *et al.* (2016).

The HOSTS survey was conducted from September 2016 to May 2018, for a total of 38 stars surveyed. The data used in this work were taken on UT 2015 February 8 and UT 2015 November 11, during the commissioning time.

- Two datasets of β Leo, taken on UT 2015 February 8, with, respectively, 8000 and 8800 frames of 60ms exposure time. The nodding frequency of those datasets is 1000 frames, but for one group of 1800 images. The parallactic angle ranges of the two datasets are respectively from 41.11° to 45.02° and from 53.67° to 57.41°. Those two data sets were observed on the same night and are thus treated as a single data set in this work. Along with the observations of β Leo, the calibrators HD104979, HD108381, and HD109749 were also observed. Those data sets are used for the HCI application, for which we produce contrast curves. The parallactic angle range allows for ADI PSF subtraction and calibrators for RDI background subtraction.
- A background-only dataset, taken on UT 2015 November 11, with 24000 frames. This data set does not have any sky offset. In order to reproduce conditions similar to the target's observations, we artificially created groups of images to mimic the nodding. For most of the work described in this chapter, we used groups of 1000 images, following the model of the β Leo datasets. However, we also simulated shorter and longer nodding frequencies, from 10 to 3000 images. This data set is used for the aperture photometry application. As this dataset does not contain any star, we would ideally retrieve a photometry of 0 on this dataset, which allows us to estimate the deviation of the real measurements and the bias which they contain.

The data sets taken during the commissioning time of the HOSTS survey for β Leo are slightly different from those taken during the main survey. In particular, the nodding frequency was longer for the data taken between 2016 and 2018. If we were unable to reproduce those conditions in the β Leo data set, we were able to confirm that increasing the nodding frequency to 2000 images was not significantly changing our results. This will be discussed in more detail in Section 3.5.1.

Since we are nodding in two nod positions, our groups of images alternate between those with the star in the top left quadrant and in the bottom left quadrant of the images. For the background-only dataset, we artificially chose the configuration to be top-bottom-top-bottom or bottom-top-bottom-top. In the following we refer to the top left and bottom left quadrants, respectively, to the top and bottom images. Similarly, we consider the empty quadrant as background frames, and the quadrant with the star as on-source frames.

3.1.2 Current background subtraction and biases

The background subtraction, used for the HOSTS results, consists of a simple mean background subtraction, i.e., the correction is the mean image of the background library frames. The background library itself is defined as the 2000 frames closest in terms of time, which are not at the same nod position (Defrère *et al.*, 2016, see Figure 1.7). It thus consists of the images contained in the groups immediately before and after

the group of images we want to correct. Once computed, the correction is uniformly applied to all images of the group. After this background subtraction, to estimate the remaining background behind the star, the mean value of the background is computed in an annulus around the region of interest (ROI) and subtracted from the photometry of the ROI.

During the analysis of the HOSTS survey, it was demonstrated that the dominant factor for the sensitivity limitation of the measurements was their bias. In other words, the accuracy of the measurements rather than their precision. With the current background subtraction approach, two types of bias can be identified: spatial and temporal biases.

- The temporal bias comes from the library of background images. In fact, the frames in this library were taken before and after the images to be corrected. The background thus changes between these images. For the HOSTS survey, and its mean background subtraction, it was considered that those effects were negligible compared to other sources of background errors. However, with a more effective background subtraction this assumption might not be true anymore.
- The spatial bias comes from the background annulus, which is used to estimate the remaining background in the aperture, behind the star. With this solution, it is considered that the background does not change significantly between the ROI and the background annulus. Similarly, this assumption can also introduce a bias in the data.

The combination of those two types of bias results in the scatter of the measurements being larger than the error bars of those measurements. Thus, removing this bias will significantly improve the uncertainty of the measurements and might allow confirming or ruling out detections, with a higher sigma. Thus, we developed a background subtraction method, based on principal component analysis and similar to Hunziker *et al.* (2018), to reduce both contributions to the bias. There are, however, a few differences between our implementation and the implementation developed by Hunziker *et al.,* 2018, notably our code is based on the PCA routines of VIP and was designed to be integrated within the library, whereas Hunziker *et al.,* 2018 was based on the PynPoint library. Their code was also developed for high contrast imaging data, with a much larger field of view (much smaller proportion of the data is masker, larger background library, no enlargement needed, etc.), four nodding positions instead of two and a much brighter star (not nulled, re-centering is possible before hand, star signal well above the background level, etc.). The implementation of Hunziker *et al.,* 2018 is also directed to observations dedicated to point-source detections, with large parallactic angle ranges. By contrast, our data are much more sensitive to self-subtraction due to the lack of rotation, and the extensions of the disks we aim to observe. Thus, additional precautions in the mask implementation were also taken.

3.2 Background subtraction methodology

3.2.1 Background subtraction pipeline steps

To compare the mean and the PCA background subtractions, with as little bias as possible, I developed a pipeline to prepare the images in the exact same way for both methods. The steps to prepare the images consist of:

- **sorting the images** per pointing and then per group of images. This first step is configured for the summary files of the LBTI nulling data and would need a significant amount of work to make it flexible for various instruments.
- **cutting the quadrant**: The stars is only positioned on the top left or bottom left quadrants. The right part of the detector is thus removed and the top and bottom left quadrants separated into independent subimages. The user can choose which part of the images to keep, how much to cut the edges of the subimages, and the number of nod positions.
- **sorting the subimages** into a two-level list. The first level differentiates between the top and bottom images, and the second level differentiates between the group of images. The top and bottom images are treated separately in the following.
- **correcting bad pixels**, for which we use the routine from the Vortex Image Processing (VIP, Gomez Gonzalez *et al.,* 2017) library, which allows one to correct for both isolated and clumps of bad pixels. The bad pixel correction is optional and can be skipped. The bad pixel map can also be created directly by the pipeline or provided by the user.
- **correcting for offsets** by subtracting from every image their own mean value.

The pipeline then differs for the background subtraction itself. The user can choose the method or a list of methods, among mean, median or PCA, for the background subtraction. If a list is provided, a dataset will be produced for each method. The pipeline can subtract the background of both the on-source and off-source frames.

For the mean/median background subtraction, we directly perform background subtraction, that is, we subtract the mean/median image of the background library from the images we want to correct.

For the PCA background subtraction,

- we start by a pre-subtraction which compute a single image from the background library and subtract it from every frames we want to correct (see section 3.2.2). The user can choose to do a standard mean background subtraction or a pre-PCA subtraction. For the second option, the user must indicate the number of principal components to use.
- then perform a full-frame PCA background subtraction (see section 3.2.2), with a number of principal components also chosen by the user. The user can provide a list of the number of principal components, and the pipeline will produce all the corresponding datasets.

After background subtraction, the pipeline has two modes: imaging and nulling. The imaging mode, which is designed for HCI and the production of contrast curves, but is also used for aperture photometry. The nulling mode, which is specifically designed to reconstruct the images to re-inject in the HOSTS data reduction pipeline for flux and null computation.

Image mode specific steps First we re-center the star in each frame. With nulling data, the star can only be seen by stacking images, which is possible in a group because of the very high stability of the star position in our data. We thus determined the star center on the sum image of the group, that we indicate as a first guess in our re-centering routine. For each frame, the routine will search the star center in a box of 5 pixels around the first guess value. If no center is found in this box, the routine keeps the first guess value to recenter the star. This step is optional and can be skipped.

The list of images is then recombined into a single chronological data set, ready to be used with HCI or aperture photometry without further processing. To save computational time one can optionally average the images by stacks. Images can also be enlarged, using a random distribution centered on the mean of the image and its standard deviation to fit routines standards (such as VIP PSF subtraction routine).

Nulling mode specific steps The nulling mode differs in particular because we want to reconstruct the images with their original size, so they can be compatible with the nulling pipeline. For this, we first need to retrieve both the on-source background subtracted images and the off-source background subtracted images. The option to keep the off-source background subtracted images is automatically set to true when using the nulling mode. We then produce for each pair of those images an artificial image with the original size, which we fill with a random distribution centered on the mean of the off-source frame and its standard deviation. All those images are thus slightly different since based on the real data. We then replace both quadrants at their original location. Each reconstructed image is then saved separately with the same name as the raw image provided as input to the pipeline. The quadrants are replaced following the quadrant chosen by the user when selecting the quadrant to keep.

The pipeline developed for background subtraction is expected to be used for a re-reduction of the whole HOSTS survey, and the future reduction of HOSTS-like data for the LBTI. However, the method in itself, excluding the sorting of the images at the beginning of the pipeline, can be used for a much wider range of data.

3.2.2 Background subtraction principle and library

The background corrections are built on the off-source images at the same position than the on-source images to be corrected. There are two applications that must be

distinguished: the pre-PCA subtraction, a single correction image is computed and subtracted from all the images to correct; and the PCA background subtraction, for which an optimized correction image is computed for each image to correct.

Choice of libraries In order to build an optimal correction, one needs to find the optimal library to build it on. With our data configuration, we have three options: using one of the groups of off-source images adjacent to the group we want to correct (1Nod), using the two adjacent groups whenever possible (2Nods), or using all the off-source groups of the list (AllNod). The first solution's main advantage is to use fewer frames, and thus to be less expensive in terms of computational time. The second option uses frames both from before and after the images of interest, and is thus more complete, but needs more computational time. The last configuration allows for a much wider variety of images in the library which can help reconstruct extreme backgrounds; however, it would also include frame less relevant which might degrade the correction; and it will need much longer computational time. For the first two options, a background library is created for each on-source group; for the last option, one library is used for all the on-source groups.

For the mean background subtraction, we used the 2Nods library, as it was both the solution currently implemented in the HOSTS reduction and the library providing the best results. For PCA one needs to balance both the positive effect of having a larger library to build the principal components from and the negative effect of having frames unrelated to the image we want to correct. For HCI, the 2Nods library has proven to be both more effective and efficient. For aperture photometry, the 2Nods and AllNods libraries appear to provide similar results, but to save computational time, we kept the 2Nods option.

PCA implementation The PCA Python routine we use in the pipeline for background subtraction and pre-subtraction is based on the full-frame PCA routine from the VIP library (Gomez Gonzalez *et al.*, 2017). We modified this routine to adapt it to background subtraction. For background subtraction, the frames are not de-rotated on contrary to the PSF subtraction.

The data cube and the eventual reference cube are reshaped into matrices, respectively M and M_{ref}. The principal component vector V is then built using SVD (see Section 2.4.2). Our version creates two different principal component vectors: one with a mask at the star position (V_M) and one without (V). The code then computes:

$$R = (V_M.M^T).V \quad (PCA\,subtraction) \quad or \quad R = (V_M.M_{ref}^T).V \quad (pre{-}subtraction) \quad , \tag{3.1}$$

R is the reconstruction of the data cube by PCA with a given number of principal components. In our case, R does not take into account the star at all. R is then subtracted from M to obtain the background-subtracted dataset.

In this pipeline, we are using this routine in two different ways:

- **pre-subtraction:** In this case, we only use the background frames, the star is not present, and thus does not need a mask. Consequently, V_M and V are the same, unmasked principal component vectors. We then average the residuals R and subtract them from every frames, as a first rough correction. This step is really important for the PCA background subtraction since its second step needs a mask and will thus lose a part of the information to build the principal components. Without this step, the background correction behind the mask is of a much lower quality.
- **PCA background subtraction:** V and V_M are computed on the background library, while the matrix is computed on the images to correct. Here, we need to introduce a mask because the matrix contains the star information. Without any mask, the reconstruction of the data by PCA would thus take the star into account, and it would be self-subtracted in R. The R obtained through this routine is the fully background subtracted group of on-source images.

An important aspect to consider about the mask used for PCA background subtraction is its impact on the principal components. In fact, the presence of the mask breaks the orthogonality between the principal components. In doing so, it introduces possible errors in the principal components themselves, reducing the overall quality of the PCA background subtraction. The larger the mask, the higher the errors in the principal components can be. The size of the mask thus should be as small as possible to limit this effect. For exoplanet detection (HCI case), the mask is limited to the PSF size to avoid any star self-subtraction. In the HOSTS case, because we want to detect exozodiacal light (aperture photometry case), we need to cover the entire expected emission, which can go up to several times the size of the PSF.

3.3 Application to High Contrast Imaging

3.3.1 Pipeline configuration and specifics for HCI

For the HCI application, we use the two datasets of β Leo. These datasets are treated separately for background subtraction, to avoid the large time separation between the background library frames and the on-source images. The two datasets are only combined after they have been averaged, for similar reasons. This combined data set is composed of 168 frames (16800 averaged by groups of 100 images) with an exposure time of 60 μ s.

In addition to the previously described pipeline, in the context of HCI, we developed a small routine to filter the poor-quality images. The user can use the level of filtering with respect to the maximum photometry. As we are using nulling data, in our case, the best images would be the ones with the lowest photometry in an aperture centered on the star. If the user provides a list of filtering levels, then the pipeline will produce a

dataset per filtering.

In the HCI configuration of the pipeline, we can have datasets for the different methods, the different pre-subtraction methods, the different filtering levels, and for PCA background subtraction, the different principal components number. To make a comparison as less biased as possible, we exploited all those possibilities and thus created 5 datasets for mean background subtraction and 1350 datasets for PCA background subtraction (3 options for pre-subtraction, 5 options of filtering -100, 80, 60, 40 and 20 % of the star photometry-, principal components ranging from 1 to 30).

As we wanted to produce contrast curves, we had to produce final images, for which we explored 3 options: angular differential imaging (ADI), reference-star differential imaging (RDI) and without any PSF subtraction (WSPSF). For the first two options, we used full-frame PCA for the PSF subtraction. For the last one, we only de-rotated the images and computed the median image of the resulting dataset. For ADI and RDI, we explored principal component numbers ranging from 1 to 30. We thus obtained a total of 305 contrast curves for mean background subtraction and 82350 contrast curves for background subtraction. In order to compare them efficiently, we developed a small routine to compute the sum of every point of the contrast curves and compare them.

Once the best contrast curves were determined, we obtained two contrast curves for mean background subtraction and two for PCA background subtraction. One is the unfiltered curve, the other the best filtered curve. We then separately compared the results obtained for ADI, RDI and WSPSF.

3.3.2 Contrast curves analysis

In this analysis, we are using contrast curves as a metric for improvements due to background subtraction. However, due to the way contrast curves are produced, generally on PSF subtracted images, one needs to be careful to distinguish between the effects of the background subtraction and those of the PSF subtraction. Studying the improvement of the contrast curves with PCA background subtraction is also important, as it can be compared with the effect of the residual starlight. Indeed, in the ADI case we will have the least star residuals; however, we might also take out symmetrical extended emission such as disks. For RDI, we will have more starlight residuals than in the ADI case, but we will avoid this self-subtracting effect of extended symmetrical structures. For WSPSF finally, we would be able to measure the effect of the background subtraction only, but with contrast curves strongly dominated by the starlight, which might hide any effect from the background subtraction.

In Figure 3.1 we present the contrast curves obtained with ADI (top panel) and RDI (middle panel) PSF subtraction and WSPSF bottom panel. All contrast curves presented for ADI and RDI were obtained with 20 principal components for the subtraction of PSF. For RDI we had two different reference datasets: HD108381 and HD104979, which are both composed of 8000 frames with 60 ms exposure time. We first tried both calibrators,

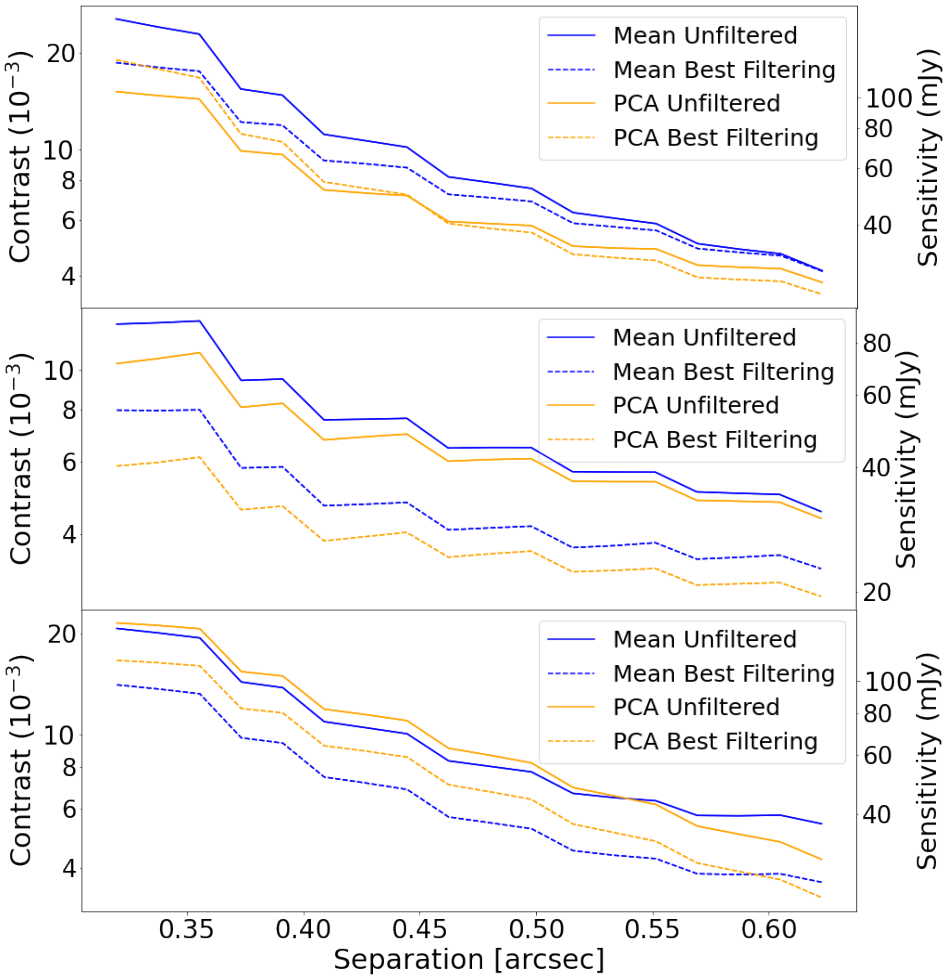

Figure 3.1: Contrast curves obtained with ADI (top panel), RDI (middle panel) and WSPSF (bottom panel) with (dashed lines) and without optimal filtering (straight lines) for mean background subtraction (blue) and PCA background subtraction (orange). A pre-PCA-subtraction has been applied on the PCA background subtracted cube before we applied the 9-pixel mask on the star.

but determined that HD104979 was consistently providing poorer results, and therefore did the main analysis for RDI with HD108381. For WSPSF, the contrast curves were directly computed from the final image through companion injection.

For ADI, with the Mean background subtraction, the best filtering level has been determined to be 60 %, for the PCA background subtraction, 80%. For RDI with both mean and PCA background subtraction, the best contrast curves were obtained with a filtering level of 20 %. For the pre-subtraction on the PCA-background-subtracted dataset, we used 10 principal components for both ADI curves and, respectively, 8 and 10 principal components for the filtered and unfiltered case. The contrast curves WSPSF for PCA background subtraction were both obtained with only one principal component for background subtraction. The optimal filtering level WSPSF for both mean and PCA background subtraction is 20%

The top and middle panels of Figure 3.1 shows that we obtain a significant improvement over most of the contrast curves for both the unfiltered and filtered cases. Surprisingly, the improvements obtained with PCA background subtraction are more significant closer to the star. This already indicates that the effects of background subtraction are not clearly isolated from other effects such as PSF subtraction. This also emphasize the fact that the residual starlight still significantly impacts the contrast curves. Even if PCA background subtraction does bring an improvement for this dataset, it is, however, limited by these starlight residuals for both ADI and RDI. On a purely background-limited region, with little to no impact of the starlight residuals, we thus expect a much larger improvement with the PCA background subtraction. On the other hand, the bottom panel of Figure 3.1 shows that WPSF PCA background subtraction tends to degrade the reachable contrast for most of the distance range that we investigate. Indeed, PCA background subtraction seems to become effective only further away than 0.6 arcsec. At these distances, starlight residuals become less dominant, and the improvement of the background removal starts to produce visible impacts.

In terms of quantitative comparison, with ADI we obtain for the unfiltered case, improvement factors ranging from 1.1 at 0.6 arcsec to 1.7 at 0.3 arcsec. For the ADI filtered case, on the other hand, we obtain improvement factors ranging from 1 at 0.3 arcsec to 1.2 at 0.6 arcsec. For the RDI case, on the other hand the improvement is rather constant for all separation and about 1.2 for the non-filtered cases and 1.3 for the filtered case. It is also interesting to see that the RDI PSF subtraction techniques combined with the PCA background subtraction allows for a much better sensitivity close to the star than the ADI case. This result is partly due to the self-subtraction that occurs with ADI when using a too small parallactic angle range, which directly reduces throughput.

With those three cases, we demonstrated that PCA background subtraction has the potential to significantly improve the reachable contrast. However, in our data, the sensitivity limitation mainly comes from the starlight residuals. In addition, as β Leo is a relatively bright star, one must take into account the effect of vibration, which would not be negligible, and directly impact the contrast curve quality. Indeed, Defrère *et al.* (2016) has shown that if the impact of vibration was relatively weak for faint stars, it becomes more and more dominant for brighter stars. For bright stars, vibrations could have effects comparable to those due to imperfect background subtraction in terms of sensitivity limitation.

3.4 Application to Aperture Photometry

For the aperture photometry analysis, we are using a background-only dataset, composed of 24000 frames. This data set has been acquired without nodding. In order to represent our data, we artificially sorted the images to create a nodding sequence

similar to the β Leo dataset. We chose this dataset as, containing background only, its photometry with a perfect background subtraction would be zero.

In this case, after background subtraction, we measure the photometry inside an aperture, whose size depends on the case and is centered on our region of interest. In our present case, the apertures are centered on the center of the frame. In a real case, the apertures would be centered on the star.

For this analysis, we distinguish three main cases: the general case, where we want to probe the whole extension of the emission (star, disk, galaxy, etc.), the HOSTS case, where we want to probe aperture smaller than the size of the emission of the exozodiacal dust, and a specific target case, β Leo, where we want to use several aperture sizes for a given extended emission.

3.4.1 General case

The first case we explore for aperture photometry is a case where one wants to probe the entire emission of its source, which can be a point source (stars, planets) or an extended source (galaxies, etc.). For this case, we thus use a configuration where our aperture is of the same size as the emission, the mask for PCA background subtraction covers the whole emission, and the background annulus for mean background subtraction has an inner radius which is one pixel larger than the radius of the aperture. This configuration can be considered optimal in terms of background subtraction. Indeed, the mask is of the size of the aperture, which limits the loss of information and thus the errors introduced on the coefficients measured by PCA. For the mean background subtraction, the background annulus is as close as possible to the aperture, and thus as similar as possible.

Ideally, if the background subtraction was perfect, the histograms of the individual measurements would form a Gaussian centered on zero, and only impacted by Poisson noise. We did those measurements for aperture sizes of 8, 13 and 32 pixels in radius, with the corresponding mask and background annulus sizes. The results are presented in Figure 3.2.

The top panel of Figure 3.2, shows that for an 8-pixel aperture, the mean-background-subtracted dataset (in blue) provides a rather smooth curve. By comparison, the PCA-background-subtracted dataset (in orange) seems to provide even better results. Indeed, but for one group of 1000 images (frames 12000-13000) with a strong offset toward negative values, PCA-background subtracted dataset provides a smoother curve. For the 13-pixel aperture (middle panel), the mean-background-subtracted curves shows 6 groups with an offset. With PCA background subtraction, on the other hand, we observe three groups with stronger photometric variations, in addition to the previous outlier already identified with the 8-pixel aperture. Nonetheless it provides an overall smoother curve than mean background subtraction. The most dominant features in the bottom panel Figure 3.2, corresponding to the 32-pixel aperture, are certainly the

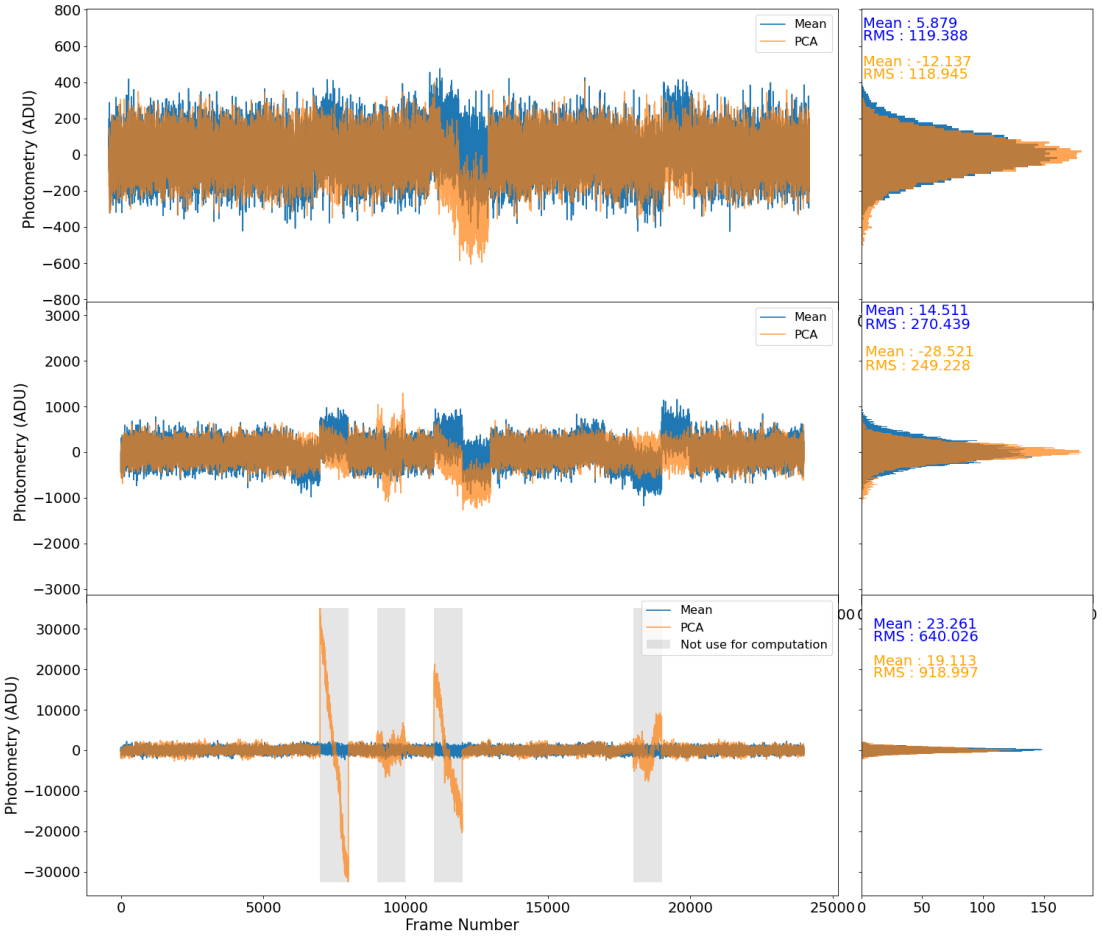

Figure 3.2: Left panel: Photometry in a central aperture of 8 (top pannel), 13 (middle pannel) and 32 (bottom panel) pixels for each frames of the mean-background-subtracted dataset (blue) and PCA-background-subtracted dataset (orange). Right panel: Histograms of the mean values in the corresponding aperture.

spikes in the photometry of the PCA-background-subtracted datasets. These variations are so large that without removing them, it is not possible to really compare the two methods. Once those spikes removed, we can see than both method seems to provide similar results.

Beside the qualitative appreciation of the curves, it is also interesting to consider the mean retrieval and RMS values, and in particular to verify wether the mean retrieval values is consistent with zero, given the RMS. Indeed this can indicate the remaining bias in the data after the background subtraction. For this we can compute the 1 σ following the equation: $\sigma = RMS/\sqrt{N_\mathrm{f}}$, with N_f being the number of frames in the dataset. We summarize those values in Table 3.1

We can see that in general, the groups with offset present in the mean-background-subtracted curve tend to average themselves out, thus providing a better mean retrieval

		RMS	1σ	Mean retrieval	# of σ
8-pixel	Mean	119	$\pm$ 0.77	5.88	7.5
	PCA	118	$\pm$ 0.77	-12.13/0.52	15.5/1
13-pixel	Mean	270	$\pm$ 1.75	14.51	13
	PCA	240	$\pm$ 1.61	-28.52/0.48	12/1
32-pixel	Mean	640	$\pm$ 4.13	23.26	5.6
	PCA	918	$\pm$ 5.93	19.11	3.2

Table 3.1: Caption

than the PCA-background-subtracted curves for which the outlier group is not averaged out. Without this , it is clear that PCA background subtraction provides much better results. However, it is more complicated to remove similar outliers for the mean background subtraction, since they are more numerous and less extreme than the single group for PCA background subtraction. This situation again tends to show that PCA background subtraction removes the bias from the data more effectively than mean background subtraction.

For the 32-pixel aperture, on the other hand, the four groups with spikes have mean values close to zero, and the mean retrieval is thus not degraded as much. However, the RMS is significantly degraded, with PCA background subtraction being almost 50% worse than mean background subtraction. The decrease of the sigma values is mainly due to the increase of the RMS. Thus, the uncertainty on the measurements starts to become more significant with respect to the impact of the bias, with such a large aperture. However, this is not an indication that the bias is better removed in the largest aperture.

However, in both cases, the large sigma values make it clear that Poisson noise alone cannot explain the mean retrieval value difference from zero, and that both methods still contain a significant bias after background subtraction.

The comparison of mean and PCA background subtraction through this method is however strongly biased. As already mentioned, a first issue comes from the outlier groups of the mean-background subtracted curve which average themselves out, which leads to underestimating the bias remaining in the data. In addition, each of these long sequences, and their mean retrieval value, is only one random realization of the photometry and is thus affected by the quasi-statistical background bias and by large random errors. As the quasi-random effect of the background bias may result in a positive or negative offset with the statistical mode of its probability distribution centered on the bias value, a single measurement close to zero may be serendipitous and is not proof of a lack of background bias. As a consequence, the mean retrieval values of these long sequences are not suitable to compare the performance of the methods, as a method that performs worse can get 'lucky' and produce a more accurate value than a method generally performing better due to random errors. It is thus not surprising that PCA

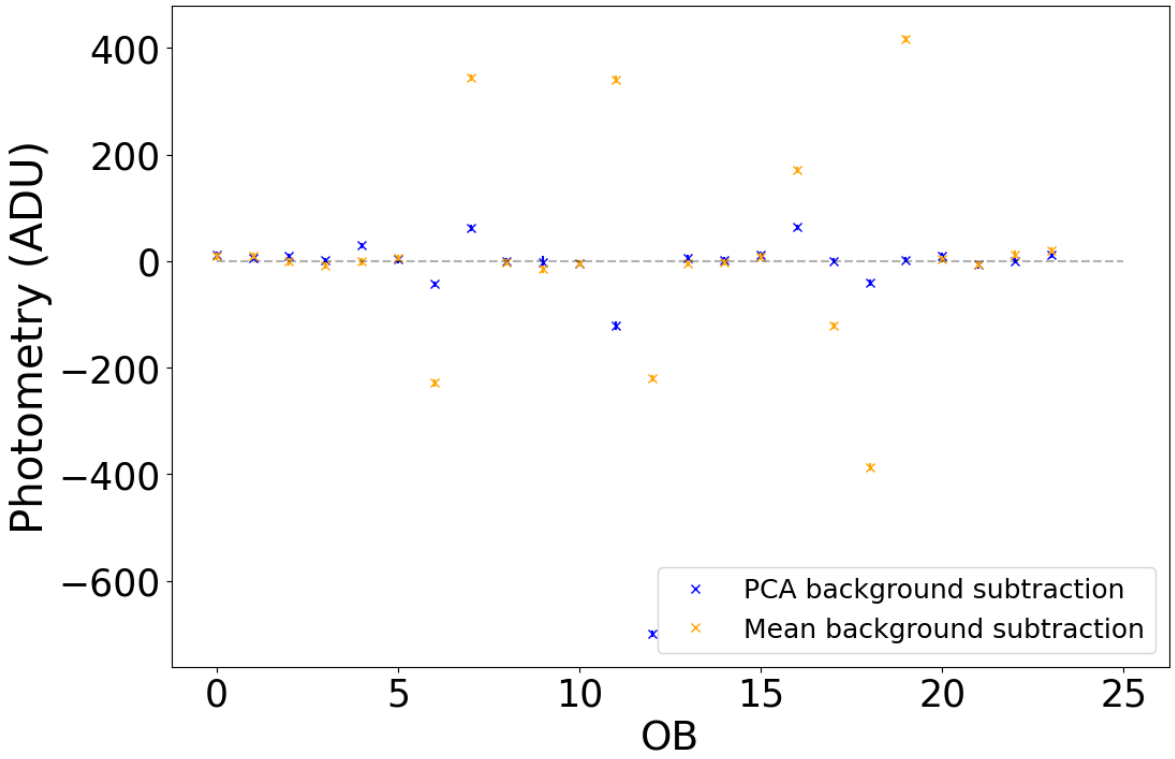

Figure 3.3: Mean retrieval values per group of 1000 images along with their errors bars. The mean retrieval is the mean photometric value of the photometry in a central aperture of 13 pixels in radius. The errors bars are computed for 1σ.

produces a mean retrieval value that is further from zero than the result from the mean background subtraction in two of the three cases, and it is not a reliable indication that PCA performs worse than the mean background subtraction.

To more reliably evaluate the performance of the two methods, we performed a statistical analysis on a per-group basis. We thus computed, for each group of a thousand images (OB), the mean retrieval value and its RMS. This comparison allowed us to both estimate the bias remaining in the data, if the points are significantly offset from zero, and the uncertainty of those values. We present these results in Figures 3.3 for the 13-pixel aperture which has been determined to be the optimal one for the HOSTS survey in terms of SNR.

In Figure 3.3, we can easily distinguish the outlier group for PCA background subtraction, which has a much lower value than all the other groups. However, more importantly, we can compare the scatter of the measurements with respect to their error bars. Indeed, the error bars are way too small to explain the scatter of the measurements. This is due to the bias still present in the data after background subtraction. This observation is true for both methods and all the apertures. However, if we now compare the two methods with one another, and exclude the outlier group of PCA background

subtraction, the measurements provided by this method are much less scattered than those for mean background subtraction. Thus, it is clear, with Figure 3.3, that PCA background subtraction significantly reduces the bias in the data for the 13-pixel aperture.

The results for the 8-pixel aperture are extremely similar to those obtained for the 13-pixel aperture. The main difference is indeed the scale of the scatter. With the 8-pixel aperture, PCA also performs slightly better. This tendency is explained by the size of the mask. Indeed, as the principal components are built, in a part, on a masked dataset, they differ from the "true" coefficient obtained without this mask. The larger this mask, the larger the potential errors in those coefficients. However, if we want to study extended sources, such as circumstellar emissions, we need larger apertures, and thus larger masks.

With the largest aperture, mask, and background annulus,the results are strongly degraded. In particular, for PCA background subtraction, we observe four outliers points with very large error bars. It is very clear that, if we take those outliers into account, PCA background subtraction performs poorly compared to the mean background subtraction. However, if we discard those groups as outliers and focus on the remaining OBs, the scatter of the mean background subtracted points is higher than for PCA background subtraction. Nonetheless, with an aperture and a mask as large as 32 pixels in radius, the improvement brought by PCA background subtraction is significantly reduced.

It is nonetheless clear from Figure 3.3 that PCA background subtraction brings a significant improvement in terms of bias removal, compared to mean background subtraction. Thus, in order to estimate quantitatively the improvement brought by this new method, we computed the ratio of the mean retrieval values of both methods in order to obtain improvement factors. We proceed in a similar manner for the RMS. For this analysis, we used aperture and mask sizes of 8,9,11,13,17,21,25,29,32 pixels in radius. The inner radius of the background annulus is systematically one pixel larger than the aperture and mask sizes. We present these results in Figure 3.4 and Figure 3.5, respectively.

Figure 3.4 shows that although some particular groups are degraded when using PCA background subtraction, most of them are improved. In particular, this is visible with the geometric mean of the improvement factors, which is positive for all apertures, masks, and background annulus sizes, but the largest one. Indeed, even if the improvement factor varies significantly with respect to the size of the aperture, and of the mask, we observe for most of them factors ranging from 1.7 to 2.5.

Taking into account the consideration about the mask size and its effect on the computed PCA coefficient, it is expected that this new background subtraction will perform better at small apertures. If no clear trend can be established with Figure 3.4, we can still observe that the improvement factors are all significant for small apertures, where we expect the most effect. For larger apertures, it seems difficult to predict the real amount of improvement in a particular dataset and configuration. However, it is

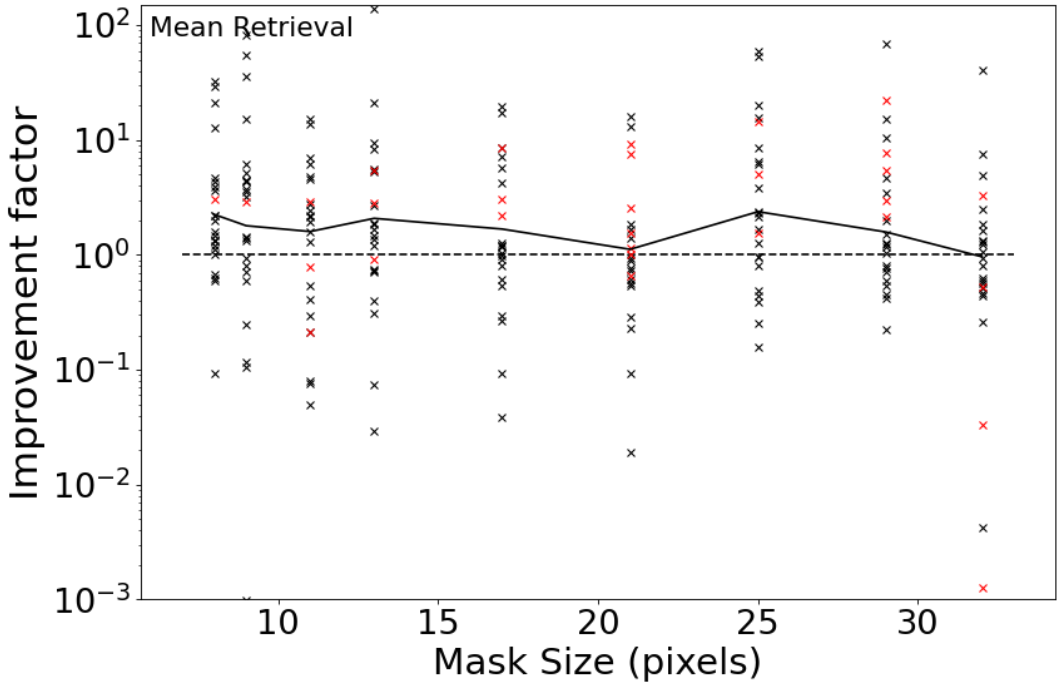

Figure 3.4: Ratios between the value of the mean retrieval per group, obtained with the mean background subtraction and the PCA background subtraction (black crosses) and the outliers in terms of RMS (red crosses). The black line represents the geometric mean of the values without the outliers.

important to note that PCA background subtraction, in worse case, does not improve the mean retrieval. It never degrades the results compared to those obtained with mean background subtraction.

In Figure 3.5, we show the impact of PCA background subtraction on the RMS. Outliers aside, for small apertures, we observe a small improvement. However, we observe a clear trend of degradation toward larger apertures and mask sizes. In both cases, improvement and degradation, the factors are relatively small. Thus, PCA background subtraction has only a limited impact on the RMS itself. In addition, if PCA background subtraction still seems to degrade the RMS with large aperture, it is important to remember that the uncertainty on those data is dominated by the bias. An increased RMS might thus in our case provide a more realistic estimate of the total uncertainty. However, it is still drastically underestimated considering the bias left in the data. Thus, we consider the results in Figure 3.5 to not demonstrate any significant improvement or degradation.

All considerations together, we concluded that in a general case, with a mask of the size of the aperture, and a background annulus right outside of this region, PCA

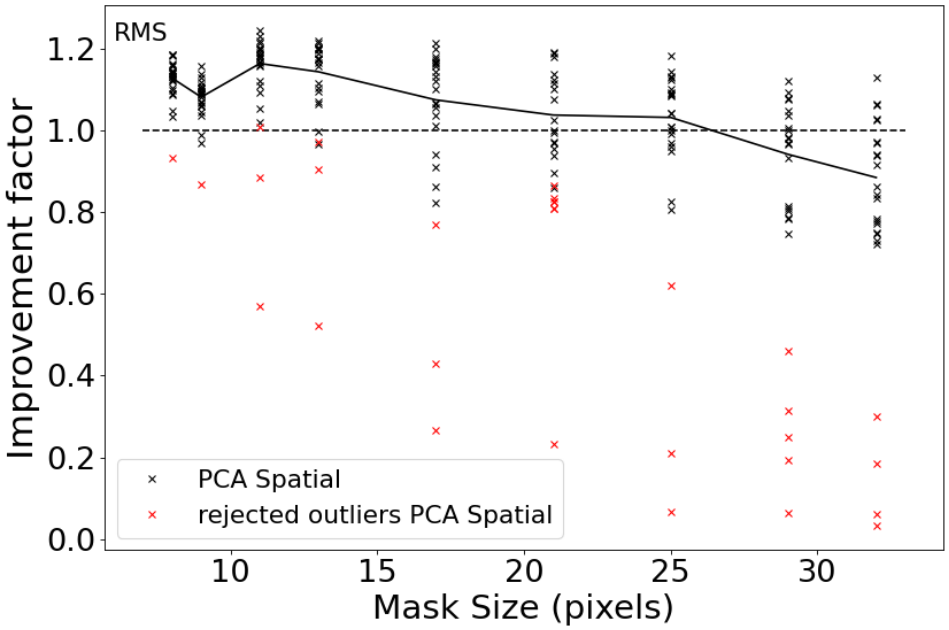

Figure 3.5: Ratios between the value of the RMS per group, obtained with the mean background subtraction and the PCA background subtraction (black crosses) and the outliers discarded for a too high RMS (red crosses). The black line represents the geometric mean of the values without the outliers.

background subtraction significantly improves the background removal. Indeed, Figure 3.3 show a reduction of the scattering and thus an overall reduction of the bias in the data. Figure 3.4 quantified this improvement, with improvement factors ranging from 1.7 to 2.5. It is thus clear that, with such a case, the use of PCA background subtraction is strongly beneficial for the reducing the bias.

3.4.2 HOSTS case

The motivation behind this work is to improve the sensitivity of the HOSTS survey data, in particular by removing a part of the important bias remaining after the background subtraction. This case is meant to assess the improvement achieved through PCA background subtraction on configurations as close as possible to what was used for the HOSTS survey measurements. During the HOSTS survey, three aperture sizes were used: the 8-pixel aperture for a point source, the 13-pixel aperture which provides the best SNR, and a conservative aperture which takes into account the whole emission of the source. This last aperture size varies for the various targets and ranges between 17 pixels to above 40 pixels in radius. Since the emission of the target will go up to this

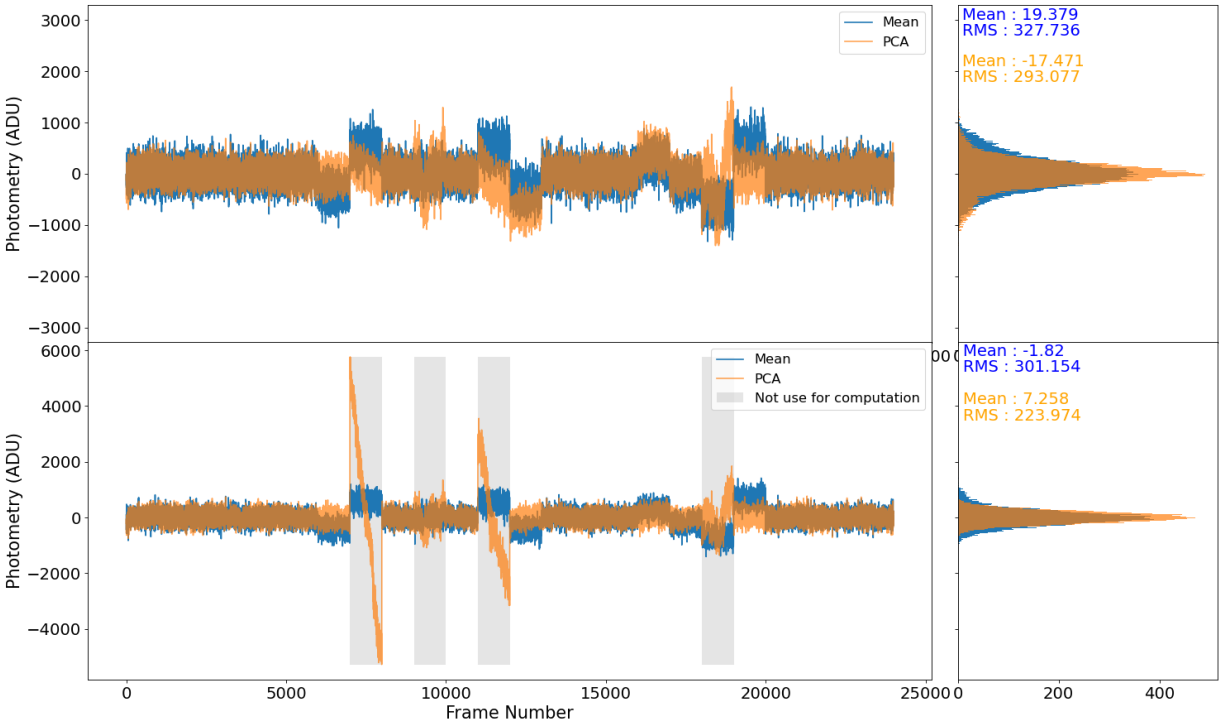

Figure 3.6: Left panel: Photometry in a central aperture of 13 pixels for each frames of the mean-background-subtracted dataset (blue) and PCA-background-subtracted dataset (orange). The mask radius is set to 17 (top panel) and 32 (bottom panel) pixels and the background annulus inner radius to 18 (top panel) and 33 (bottom panel) pixels. Right panel: Histograms of the mean values in the corresponding aperture.

separation, one needs to mask this entire region to prevent the background correction to subtract it. In this particular case, we thus have apertures which are smaller than the mask size and than the background annulus inner radius. In particular, we used mask sizes ranging from 17 to 32 pixels in radius, and background annulus inner radius ranging from 18 to 33 pixels in radius, for aperture of 8 and 13 pixels in radius. For the conservative aperture, this case will be identical to the general case.

Following the same methodology as for the general case, we first analyze the photometry per frame in two specific cases: a mask of 17 pixels in radius, which corresponds to the smallest conservative aperture of our sample, and a mask of 32 pixels in radius, which corresponds to the conservative aperture of β Leo. We did not use larger masks, as we were already noticing a degradation of the results for a mask of 32 pixels in radius. In Figures 3.6, we present the results for those two cases, respectively, and a 13-pixel aperture, i.e., the aperture optimized for SNR.

In the top panel of Figure 3.6, it is interesting to see that if PCA background subtraction still significantly improves our measurements compared to mean background subtraction, the larger mask size compared to the case presented in the middle panel of Figure 3.2 significantly degrades the photometry per frame for particular groups of

images. With this comparison, we indeed start to notice the effect of the mask size. This effect is even more visible in the bottom panel of Figure 3.6 where the mask size is 32 pixels in radius.

In the bottom panel of Figure 3.6, we observe the same spikes as in the bottom panel of Figure 3.2 although not on the same scale. In fact, those spikes are about a factor of 5 smaller than those in Figure 3.2. This behavior shows that both the mask size and the aperture size play an important role in these spikes. In fact, with a smaller mask, those spikes are not present for a 13-pixel-radius aperture, as can be seen in the middle panel of Figure 3.2. This means that those spikes can be subtracted effectively when the principal components are built on a background library including the pixels in the annulus with an inner radius of 13 pixels and an outer radius of 32 pixels. However, there is still a significant contribution from the aperture size, which explains the difference in scale between the two cases. This can be explained if a structure in the background, with a strong and rapid brightness variation, has not been removed by the background subtraction and is only partially contained by the 13-pixel aperture, and extends beyond the 32-pixel aperture.

The mean retrieval values and scattering are very similar to the general case, with their error bars considerably too small to account for the variation from zero. In order to quantitatively estimate the improvement, we now consider the improvement factors obtained for the HOSTS configuration. We used mask sizes ranging from 17 to 32 pixels in radius, and apertures of 8 and 13 pixels in radius. The results are presented in Figure 3.8 for the aperture of 13 pixels for the mean retrieval. The results for the aperture of 8 pixels in radius are very similar, but slightly better.

Figure 3.8 shows that, as in the general case, PCA background subtraction provides an improvement for the majority of the 1000 image groups. However, in contrast to the general case, here the improvement is still significant for the mask of 32 pixels in radius. The geometrical mean of those improvement factors oscillates around 2 for all mask sizes. This result is particularly interesting for the HOSTS survey since the optimal aperture have been determined to be 13 pixels in radius, and for this aperture we consistently obtained a factor 2 improvement on the bias removal.

Regarding the RMS, PCA background subtraction brings a slight improvement compared to the mean background subtraction. Indeed, outside the few outliers already identified with the frame-per-frame photometry, a large majority of the RMS of the groups of 1000 images are improved with the PCA background subtraction. However, as in the general case, the improvement in the RMS is relatively small. We consider here that the RMS is not improved by the use of PCA background subtraction, but rather that this proves that PCA background subtraction does not significantly degrade the RMS.

It is interesting to see that this HOSTS case mostly retrieves the same results as the general case. However, the differences are generally to the advantage of the

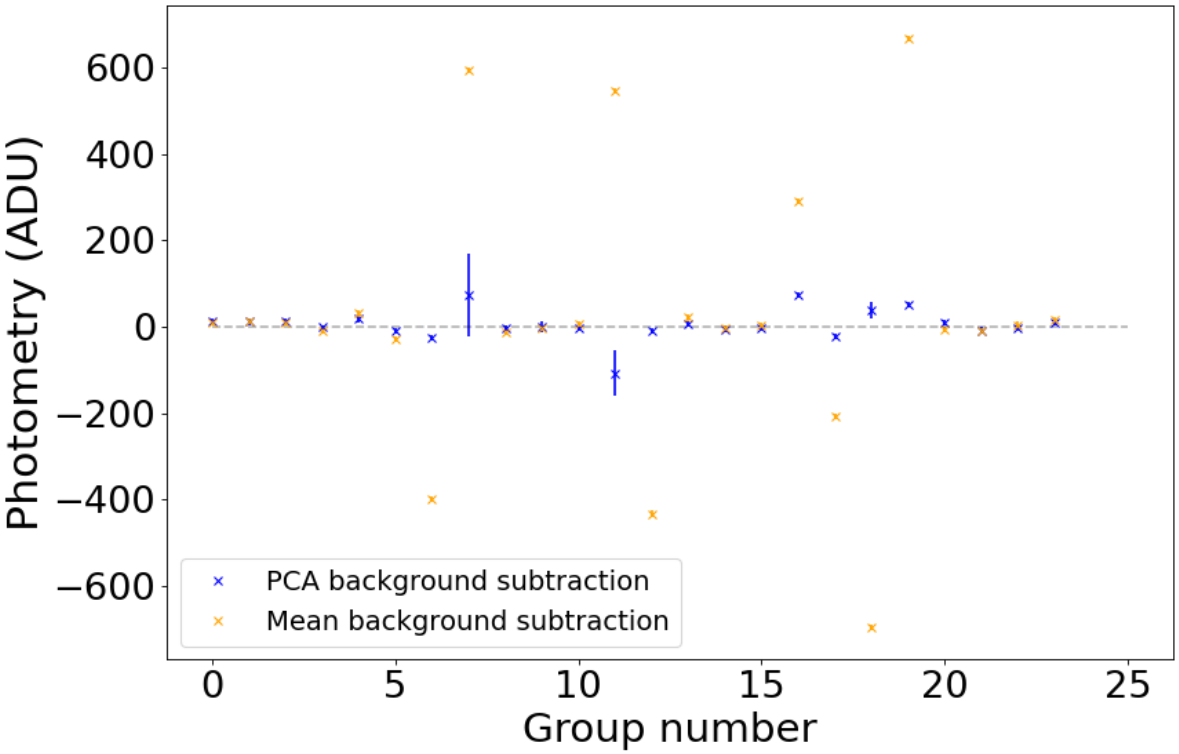

Figure 3.7: Mean retrieval values per group of 1000 images and corresponding errors bars. The mean retrieval is the mean photometric value of the photometry in a central aperture of 13 pixels in radius. The mask used for the background subtraction is of 32 pixels in radius. The background annulus use to compute the photometry for the mean-background-subtracted dataset is 33 pixels in radius. The errors bars are computed for 1σ.

PCA background subtraction, as we tend to retrieve slightly better results on the mean retrieval and on the RMS. Indeed, in this particular configuration, the mean background subtraction is at disadvantage, since the background annulus is further away from the aperture than for the general case, thus leading to stronger improvement factors.

3.4.3 β Leo case

In this section, we study in more detail the effect of aperture size variation with respect to fixed mask and background annulus sizes. We took the example of β Leo, for which we used aperture radii ranging from 8 to 32 pixels, a mask size of 32 pixels in radius, and a background annulus inner radius of 33 pixels. We then measure the improvement factors on the mean retrieval and on the RMS for each group of 1000 images. The mean retrieval results are shown in Figure 3.9.

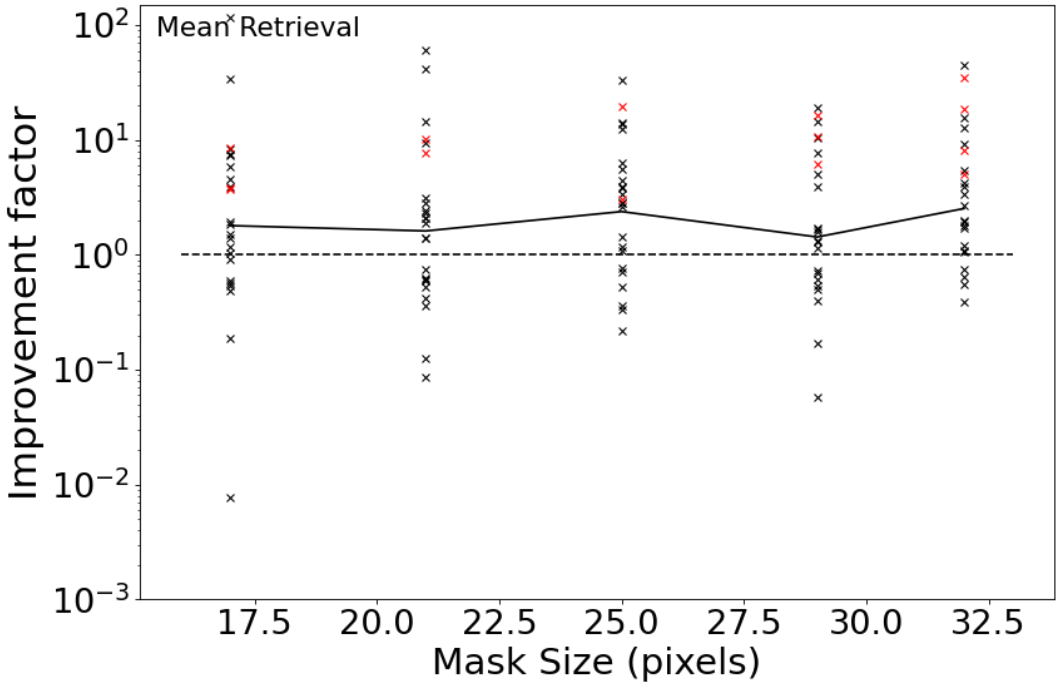

Figure 3.8: Ratios between the value of the mean retrieval per group, obtained with the mean background subtraction and the PCA background subtraction (black crosses) and the outliers in terms of RMS (red crosses). The black line represents the geometric mean of the values without the outliers. The aperture radius is fixed at 13 pixels. The mask radii are ranging from 17 to 32 pixels and the background annulus inner radii from 18 to 33 pixels.

Figure 3.9 shows that in this case, again, we retrieve improvement factors up to 3. However, the interest of this figure results mainly in the clear tendency we observe from the smallest apertures to the largest apertures. Indeed, we observe a clear degradation with the size of the aperture. Several reasons can explain this degradation. The first, already mentioned in the HOSTS case section, is that the mean background subtraction performs better compared to PCA when the background annulus is right outside of the aperture. The second is the increase of the RMS with the size of the aperture. Since in the previous cases, PCA background subtraction had very little impact on the RMS, its main advantage was to better remove the bias in the data. Thus, if the RMS becomes the dominant source of error, then PCA background subtraction will perform very similarly than the mean background subtraction.

As in the other cases, the RMS is only slightly impacted by the choice of background subtraction method. Both the improvement, toward small apertures, and the degradation, toward large apertures, are relatively small.

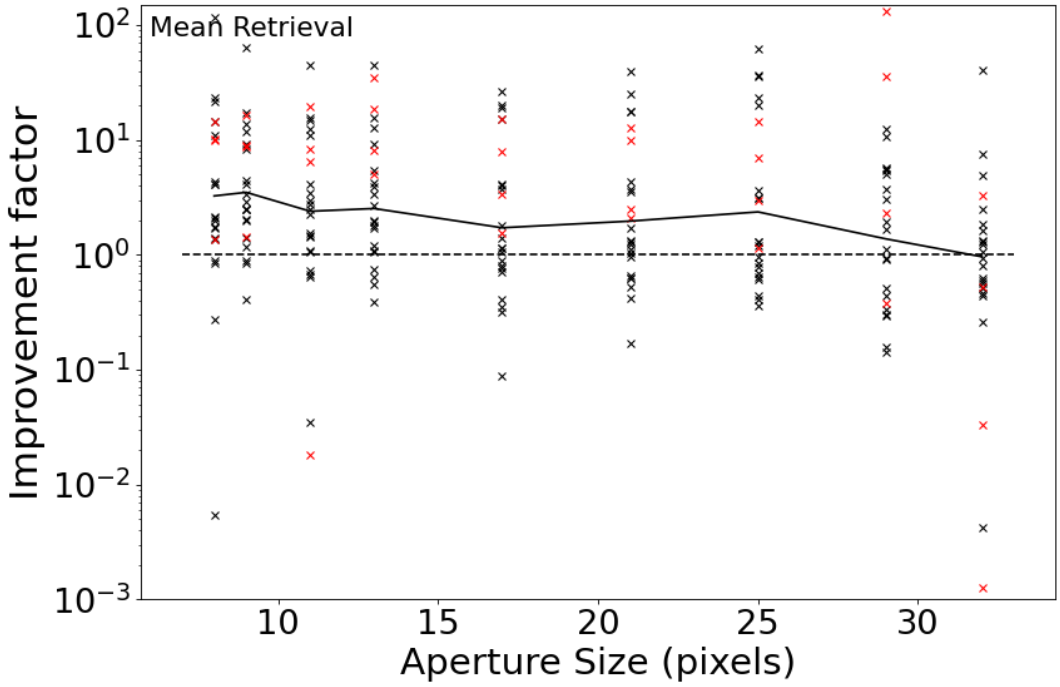

Figure 3.9: Ratios between the value of the mean retrieval per group, obtained with the mean background subtraction and the PCA background subtraction (black crosses) and the outliers in terms of RMS (red crosses). The black line represents the geometric mean of the values without the outliers. The aperture is varying from 8 pixels to 32 pixels in radius. The mask radius is fixed to 32 pixels and the background annulus inner radius to 33 pixels.

3.5 Discussion

3.5.1 General considerations

In this chapter, we demonstrated the effectiveness of PCA background subtraction to reduce the background residuals and improve the sensitivity, or reliability, of our measurements in high-contrast imaging and aperture photometry. Those two applications already show that PCA background subtraction can be adapted and used in various situations. However, all of those analyses use the nulling-interferometric data obtained during the HOSTS survey. Those data have a particular set of parameters such as the nodding cycle, the nodding frequencies, the SCI-CAL pattern, etc. but also parameters directly tied to the instrument. In particular, the impact of the bias, the RMS or the instrumental variation will be unique to each instrument. We thus present here a brief analysis considering the impact of such parameters on the results presented in this chapter.

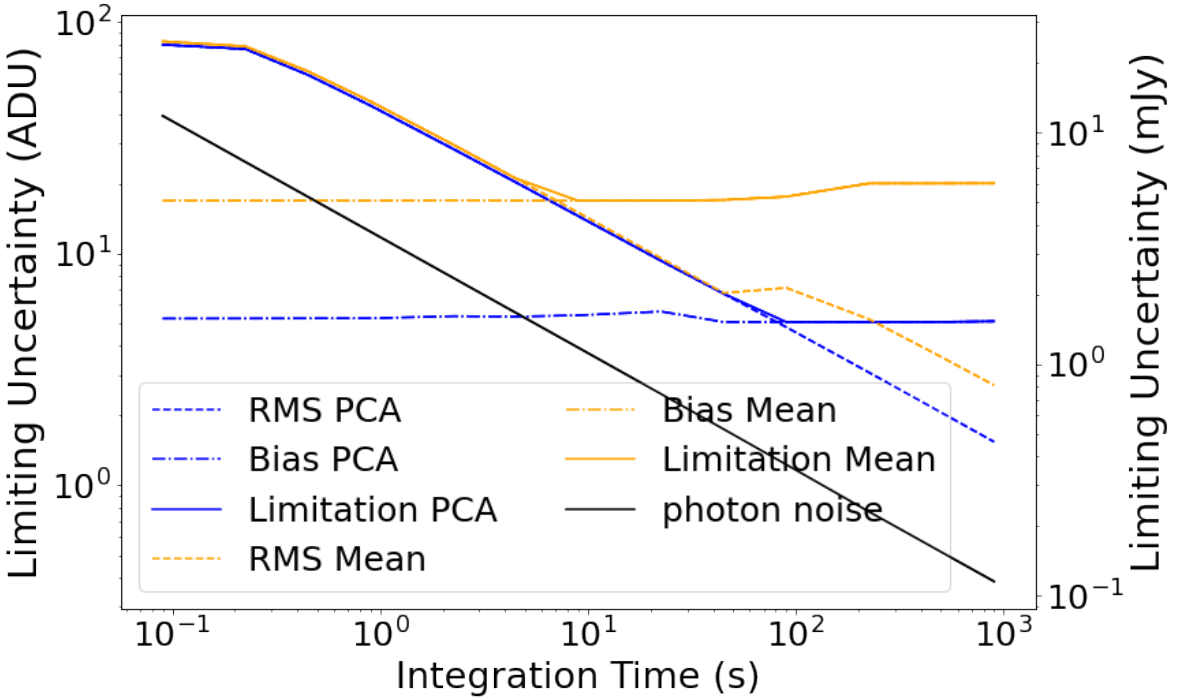

Figure 3.10: Main sensitivity limitation in background-subtracted data, with an aperture radius of 13 pixels for mean background subtraction (orange) and PCA background subtraction (blue) for the N' band LBTI data in its nulling mode. The photon noise is indicated in black.

The main parameter which can impact the improvement demonstrated in this chapter is the predominance of the bias with respect to the other sources of noise in the data. In Figure 3.10, we show the sensitivity limitation for the mean and PCA background subtraction, taking into account the bias, the RMS and the photon noise.

A first important result from Figure 3.10 is that, for both methods, significant improvement is still required to approach the photon noise limit. Indeed, even if Figure 3.10 clearly shows the improvement achieved by PCA, we are still far from reaching the photon noise limit. Another important information is the dominant source of errors depending on the integration time. For both methods, the RMS dominates up to a certain integration time and that after this point the bias becomes dominant. It is very clear in Figure 3.10 that before reaching the integration time needed for the mean background subtraction to be limited by the bias rather than the RMS, PCA background subtraction does not bring any advantages. Starting from this point and up to the integration time needed for the PCA background subtraction to be limited by the bias rather than the RMS, the advantages of using the PCA background subtraction rather than the mean background subtraction keep increasing. After that point, we reach a plateau where using the PCA background subtraction brings a constant improvement independently of the integration time.

In order to obtain a better sensitivity, considering solely the photon noise, one needs to use longer integration times. However, the bias remaining in the data limits the sensitivity that can be reached beyond a certain integration time. To improve the sensitivity, one thus needs to further reduce the bias. However, this sensitivity limit could be reached with a shorter integration time if the RMS was lower. Reducing the RMS will therefore allow for shorter integration times for a given sensitivity.

The predominance of the bias with respect to the RMS for each instrument will determine how much PCA can help improve the sensitivity for a given integration time. However, using a hypothetical integration time that reproduces a situation where the sensitivity is limited by the bias rather than the RMS, the improvement should be similar to those obtained in this chapter. However, it is important to note that we compare here only the impact of the background on the sensitivity and do not consider the limitations due to the star residuals and/or leakage.

Another important parameter to take into account while assessing the improvement of PCA background subtraction, in terms of sensitivity, is the nodding frequency. In fact, this frequency translates into the frequency at which the background can be sampled. The smaller the sampling time, the more similar the background from which we build the correction. In Figure 3.11, we present the sensitivity limitations, considering only the RMS and the bias, depending on the background sampling time.

As expected, Figure 3.11 shows that the shorter the sampling time, the better the sensitivity. Similarly, at a shorter sampling time, and thus a shorter integration time, the RMS is the dominant limiting factor for both methods before the situation reverses after reaching a certain sampling time. Thus, these results corroborate those presented in Figure 3.10. The important information to retrieve from Figure 3.11 is that the results obtained by the mean and PCA background subtraction are rather similar, up to the point where the bias starts to dominate for the mean background subtraction. After that, PCA background subtraction allows for a significantly better sensitivity. In other words, PCA background subtraction can allow for a longer sampling time than mean background subtraction. However, as mentioned above, a shorter sampling time allows for better sensitivity for both methods. We have seen in Figure 3.10 that to reach the sensitivity limit in a shorter integration time, one needs to reduce the RMS. Thus, this improvement on the RMS will provide a double benefit, as it will also allow for shorter sampling time, and thus an overall better sensitivity.

The sampling time at which the bias starts to dominate the effect of the RMS, and thus at which PCA background subtraction starts to become more advantageous than the mean background is dependent on every instrument and data. The impact of a correction method that reduces the RMS will also depend on the prevalence of the bias with respect to the RMS. The background-only dataset used in the aperture photometry section and for which improvement factors between 2 and 3 have been obtained is using a nodding frequency of 45s. It is clear in Figure 3.11 that for this configuration, we do

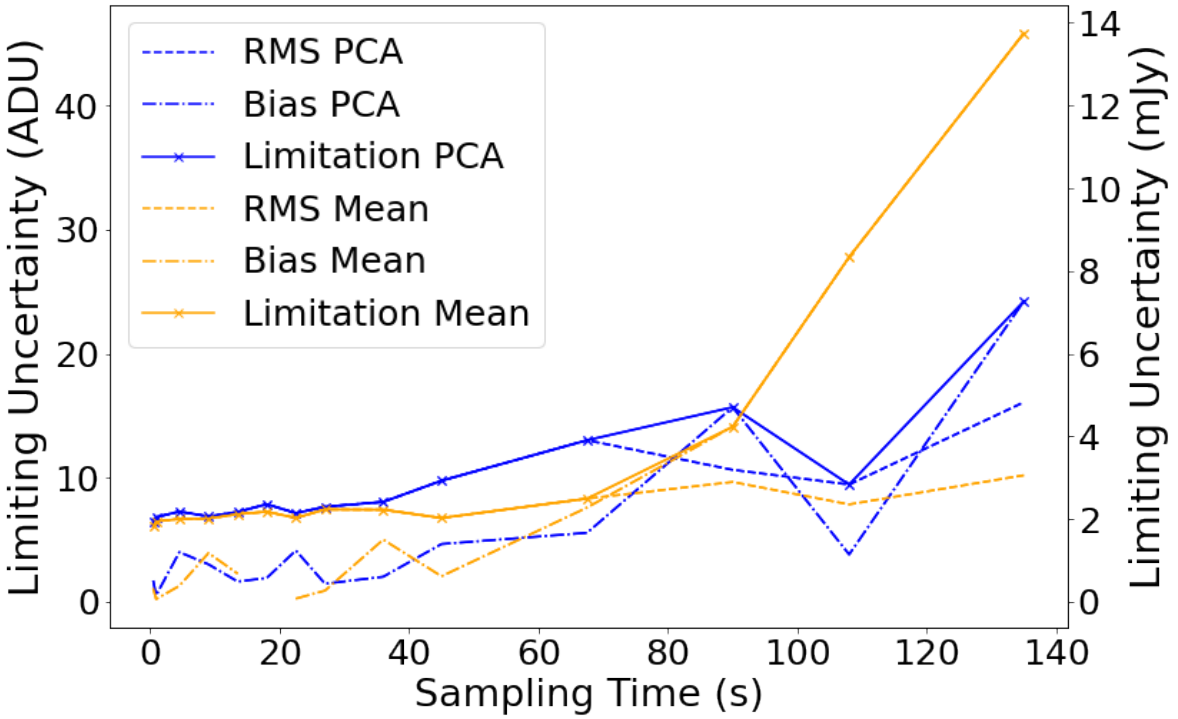

Figure 3.11: Sensitivity limits for mean (orange) and PCA (blue) background-subtracted data as a function of the nodding frequency, or the background sampling time.

not have an important difference between the sensitivity limitation between the mean or the PCA background subtraction. Configuration with longer sampling time could thus lead to larger improvement factors when using PCA background subtraction rather than mean background subtraction.

The background-only dataset was acquired without any nod and the groups were created artificially. This simulates an instantaneous nodding, which is an ideal case. We simulated longer nodding times by removing the corresponding number of frames between our groups. As expected, the larger the time gap, the worse the background subtraction. However, we did not observe any significant differences between the mean and the PCA background subtraction. This parameter should thus have little to no impact on the improvement that can be obtained with the PCA background subtraction.

Finally, the wavelength at which the data are acquired strongly impact the potential improvement due to PCA background subtraction. Indeed, the impact of PCA background subtraction on the overall sensitivity completely depends on the importance of the background in the data in the first place. In the N' band, in which our data were taken, the thermal background is significantly higher than at shorter wavebands. Previous works with PCA, in the L and M bands (Hunziker *et al.,* 2018), demonstrated a much smaller impact of the PCA background subtraction, despite a more accurate reconstruction of the background behind the star. It should be noted, however, that

Galicher *et al.,* 2011 obtained similar improvement factors to this work (≈ 3) in the M band with the LOCI algorithm. Similar work should be performed for longer wavebands to assess the potential of PCA background subtraction in those.

In addition to those considerations, the PCA background subtraction presented in this chapter can be used for a much wider range of data types, as it only needs a nodding sequence in order to be applied. Additionally, this method could be modified to use dedicated background sequences rather than nodding sequences, and extend its scope to even more data types.

3.5.2 Limitations

As seen in Figure 3.10, even with the improvement obtained with PCA background subtraction, there is still significant bias remaining in the data. This demonstrates that even though PCA background subtraction successfully reduces the bias and improves the sensitivity of the data by a factor 2 to 3, it still has limitations.

In fact, if we consider the PSD for the background-subtracted data, we can determine which frequencies are impacted by the PCA background subtraction. We display the PSD for mean and PCA background subtractions in Figure 3.12.

The top panel of Figure 3.12 shows that PCA background subtraction significantly improves the correction of the low spatial frequency structures, e.g. the large structures. However, at higher spatial frequencies, mean and PCA background subtraction provide very similar results. This shows a limitation of PCA background subtraction which fails to reconstruct smaller structures, and hence limits the precision of the correction. Additionally, on the bottom panel of Figure 3.12, we display the temporal PSD of the background subtracted data. It is clear this time that PCA background subtraction does not bring any improvement on the correction of the temporal axis, and even tends to degrade the correction compared to mean. This inability to correct the temporal dimension is also in itself a limitation of the PCA background subtraction.

Another limitation is that, to be optimal, it would require shorter integration time, and for that a reduced RMS. However, PCA background subtraction does not bring any improvement in terms of RMS; on the contrary, we have seen in Section 3.4 that it can create large photometric spikes that strongly degrade the RMS. They are also problematic because they render the measurements of those groups of images unusable. Those spikes are likely due to remaining background structures, whose brightness varies rapidly and are not identified and removed by the PCA background subtraction. In order to address this problem, we investigated a PCA-based temporal correction that could flatten those spikes by removing the photometric variations due to background fluctuations. The origin of those spikes, as well as the temporal PCA method, are presented in section 3.6.

In the same way, the inability of PCA background subtraction to reduce the RMS compared to the mean background subtraction is a limitation in itself, as it prevents

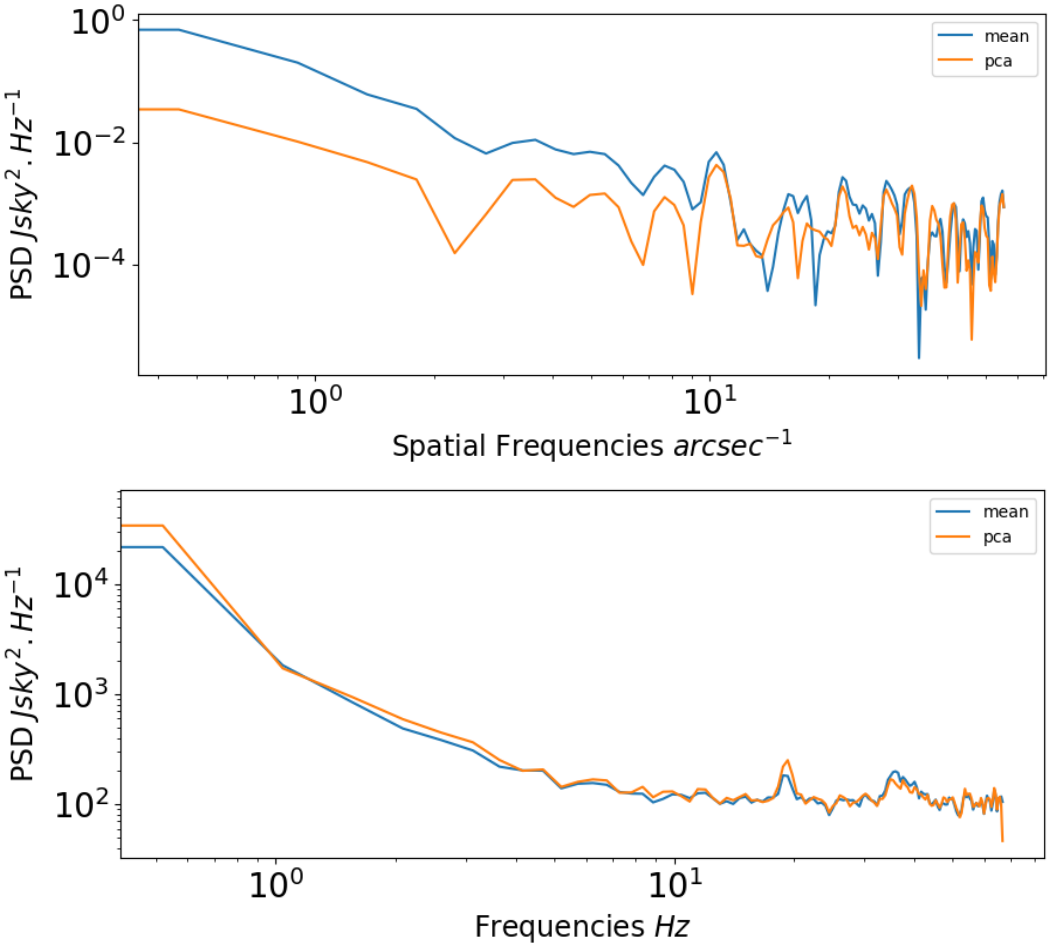

Figure 3.12: Power Spectral Distribution on the spatial (top panel) and the temporal (bottom panel) dimensions with a mean (blue curve) and a PCA (orange curve) background subtraction. The spatial PSD has been obtained on a random background subtracted image of the background-only dataset. The temporal PSD has been obtained on the photometry measured in an aperture of 8 pixels in radius, for 24000 frames of 15μm of exposure time.

the use of shorter sampling time that would provide much more accurate corrections for the background.

Finally, the need of a mask to prevent over-subtraction is another strong limitation. The mask breaks the orthogonality of the masked principal components. Their differences with the unmasked principal components introduce an error which degrades the PCA correction. The larger the mask, the larger the potential errors and the worse the correction. This limitation thus prevents using this method for datasets where a large portion of the images must be masked. As mentioned in Section 3.4, we also performed an aperture photometry analysis on unmasked data. This analysis has shown that PCA without a mask is far more effective, so that with a method mitigating the effect of the mask, the improvement obtained by PCA background subtraction would also be far superior to those demonstrated in this chapter.

3.6 Correcting the background on the third axis

We have seen in the previous sections a PCA-based background subtraction method dedicated to the suppression of the spatial background structures. However, those structures are not the only impact of the background on the accuracy and the precision of the data. Indeed, the background also varies over time and according to the wavelength, limiting the accuracy of the time series or spectral measurements. In addition, despite achieving an important improvement, the spatial PCA background subtraction has strong limitations. In particular, the large photometric variations over time that remain after background subtraction for certain groups of images. In this section, we explore a possible temporal PCA solution to address background variations over time, which could be used in combination with spatial PCA background subtraction to provide further improvement on both the accuracy and the precision of our measurements. Besides the case of HOSTS measurements, this temporal PCA correction could also be used independently, on its own, in particular when the spatial information is not kept in the data. In addition, this method is not limited to the temporal dimension and can also be used, for example, on spectral series, either on its own or in combination with a spatial background subtraction.

3.6.1 Origins of the photometric spikes

We have shown that with spatial PCA starting from a certain size of aperture or mask, spikes start to appear in the photometry. Those spikes grow with the size of both the aperture or of the mask. Those spikes are, in particular, visible in the bottom panel of Figure 3.2. However, they can also be seen, on a smaller scale, in the middle panel of Figure 3.6. It is interesting here to compare the different sequences of photometry to determine what impact the mask and aperture have, respectively, with the appearance of those spikes. In the middle panel of Figure 3.2 and in the top panel of Figure 3.6 those spikes are not visible, indicating that the size of the mask plays an important role in their appearance. In fact, with a smaller mask, spatial PCA can better detect this feature and remove it. However, for a given mask size, the spikes appear and then grow with the aperture size. This indicates that the background structures, behind the mask, and uncorrected starts to enter the aperture. It is also important to note that the spikes in the photometry are not only a PCA background subtraction feature. Indeed, in the mean background subtraction case, such spikes also appear in the photometry but are removed by the use of the background annulus.

With these considerations in mind, we investigated the nature of these problematic background structures. We considered four possibilities: (1) a small structure fully contained in the aperture, (2) a small structure brought by PCA background subtraction into the aperture, (3) an extended structure both inside and outside of the aperture, and which brightness varies rapidly, and (4) an overall rapid brightness variation of the

whole images.

We first exclude the possibility (2). Indeed, if the small structure was brought into the aperture by PCA background subtraction, such spikes would not be visible in the photometry of the mean background subtraction, even without the background annulus. We then exclude the possibility (1), because the background annulus would not be able to correct it if the structure was fully contained in the aperture. Finally, since an overall brightness variation would have been seen independently of the aperture size if not corrected by the background annulus, we also exclude the possibility (4).

We thus determined that the structure responsible for those spikes should cover a part of the aperture, starting from a certain size, be mostly contained in the area covered by the mask, and slightly extended in the region of the background annulus. We thus want to find a way to reduce this background structure variation, and ideally remove it.

3.6.2 The return of the background annulus

As stated previously, in the case of mean background subtraction, the spikes are effectively removed thanks to the background annulus. An easy solution would thus be to implement this background annulus in the case of PCA background subtraction as well. We performed this test with a background annulus with an inner radius of 33 pixels. The mask in this case is set to 32 pixels in radius. We then compare the cases of PCA background subtraction with and without the background annulus. Those results are presented in Figure 3.13, for comparison, we also show the results with and without annulus for the mean background subtraction.

The top panel of Figure 3.13 shows that the use of a background annulus for PCA background subtraction effectively removes the spikes. With the annulus, the curve is, by comparison, perfectly smooth. By using the background annulus, the RMS of the whole sequence is in fact improved by a factor 7. For the mean retrieval, we almost obtain a factor 2 of improvement. The use of the background annulus thus seems to be perfect to remove the spikes and push further down the sensitivity of the data. However, one should remember that as for the spatial background subtraction case discussed in the previous chapter, the sequence is only one random realization, and the groups of images can average themselves out. Thus, it is important to consider the group per group mean retrieval and RMS to assess the success of this method.

We thus performed a group-per-group analysis between PCA background subtraction without annulus and the PCA background subtraction with the annulus. We computed the improvement factors we would obtain by using the case with the annulus, over the case without. We computed those improvement factors for the RMS and for the mean retrieval. Those results are shown in Figures 3.14 and 3.15, respectively.

Figure 3.14 shows two interesting features. First, indeed, using the background annulus is extremely effective to remove the spikes. Second, the majority of the points

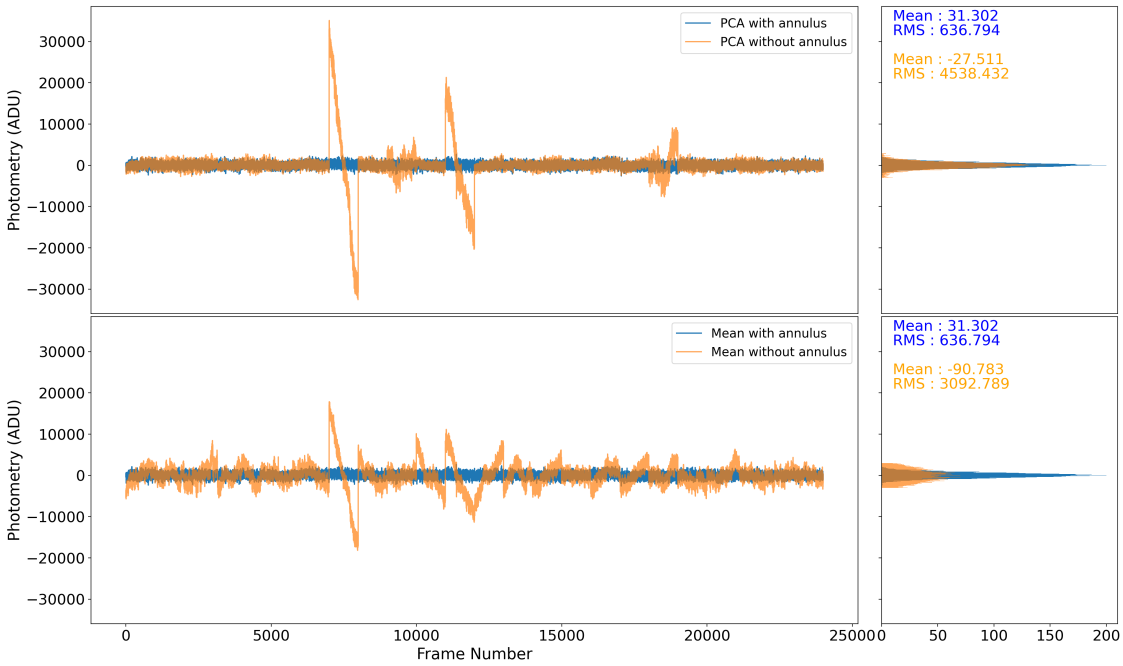

Figure 3.13: Left panels: Photometry in a central aperture of 32 pixels for each frames of the dataset with (blue) and without (orange) the background annulus, for PCA background subtraction (top panel) and Mean background subtraction (bottom panel). Right panels: Histograms of the mean values in the aperture.

for the 8 and 13 pixels apertures are around 1 with a slight tendency to degradation, which explain the low geometric mean obtained for the RMS. Indeed, for those apertures, the improvement shown by the geometrical mean is only due to the outliers with the spikes; the RMS of the other groups are degraded by the use of the background annulus. In contrast, for the largest aperture, most of the groups benefit from the background annulus. However, apart from the groups with the spikes, the improvement remains relatively small. We can thus see, thanks to Figure 3.14 that if the background annulus allows the removal of spikes, it is far from being an optimal method.

In Figure 3.15, we show the improvement factors for the mean retrieval. We observe on this curve a most problematic feature. Indeed, for the aperture of 8 and 13 pixels in radius, the mean retrieval is degraded by a factor of 2 to 3. This degradation corresponds to the improvement brought by the PCA background subtraction. With the 32-pixel aperture, on the other hand, we observe an improvement. This is due to the improved RMS, which with these large apertures is strongly dominant. This figure strongly demonstrates that unlike suggested by Figure 3.13, the use of the background annulus does not improve the sensitivity but rather degrades it. It is thus clear with this analysis that we should find another solution to remove those spikes. We thus developed one of those potential solutions: a temporal PCA correction.

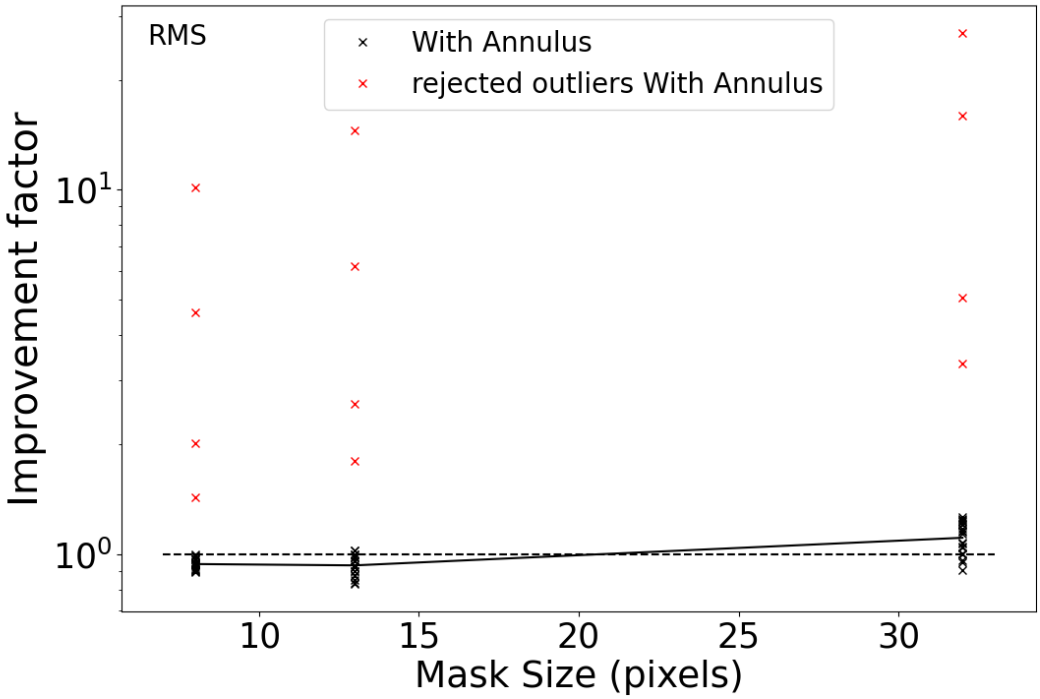

Figure 3.14: Ratios between the value of the RMS per group, obtained with the case without and with the background annulus(black crosses) and the outliers (red crosses). The black line represents the geometric mean of the values without the outliers. Values above one show an improvement due to the presence of the background annulus. The outliers are defined as the measurements which results in a RMS superior to 1.15 the median value of the RMS of all measurements.

3.6.3 Switching the axes

We have determined that the structures causing the spikes are extended and cover the aperture (if the aperture is large enough), the mask region, and the background annulus. Furthermore, these background structures are only present in some groups and are not seen in the majority of the groups. This background structure should thus create an important variation of the pixel values with time. If this variation can be detected by PCA, then it can be removed.

To develop the temporal PCA concept, we started from the spatial one. For this last one, we study the variation of the pixel within an image, and this for all images. This axis switch has been previously used in Samland *et al.,* 2021 for the LOCI algorithm for PSF and speckles subtraction, Long *et al.,* 2023 also developed in parallel to this work a similar approach with PCA also for PSF and speckles subtraction. The matrix of the data is then expressed as:

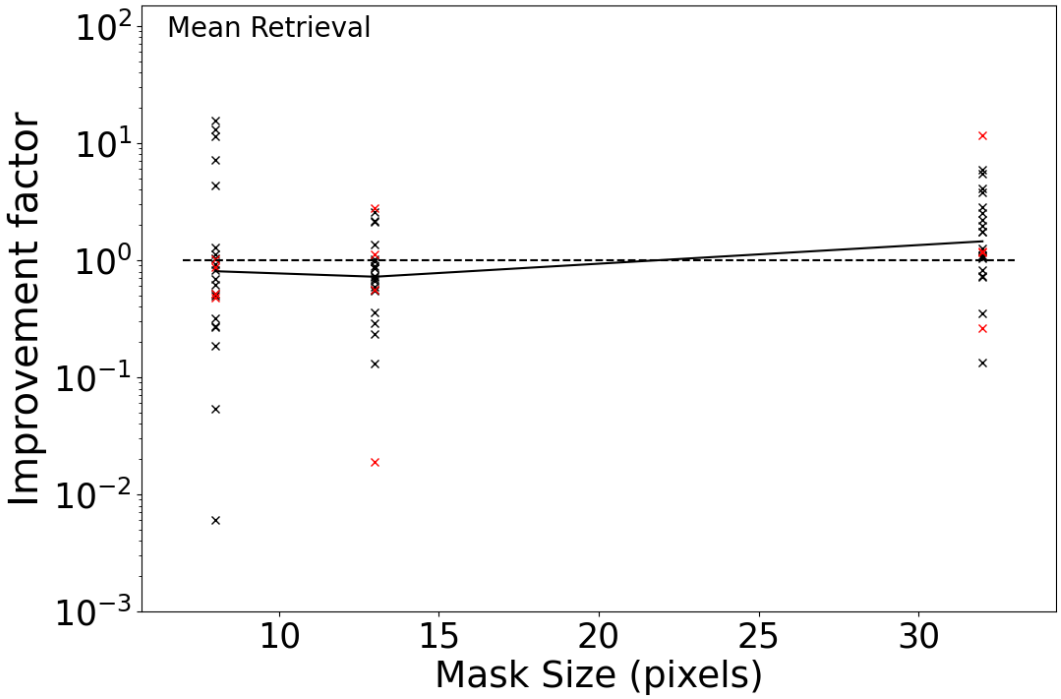

Figure 3.15: Ratios between the value of the mean retrieval per group, obtained with the case without and with the background (black crosses) and the outliers (red crosses). The black line represents the geometric mean of the values without the outliers.Values above one show an improvement due to the presence of the background annulus.

$$M = \begin{pmatrix} V_{1,1} & \cdots & V_{1,N} \\ \vdots & \ddots & \vdots \\ V_{K,1} & \cdots & V_{K,N} \end{pmatrix}$$

where the red frame represents all the pixels contained in one given image, and the blue frame represents the value of one given pixel for all the images. The role of PCA is then to determine the recurring features that best describe the images. Then it builds the principal components accordingly to reconstruct those recurring features. Those principal components are then combined and scaled to fit the image to correct as closely as possible. This correction is then subtracted from the image.

In the case of temporal PCA, we follow a very similar approach, but instead of studying the variation of the pixel values inside an image, for each image, we study the variation of one pixel values through all the images, for each pixel. The matrix of the data then becomes:

$$M' = \begin{pmatrix} V_{1,1} & \cdots & V_{K,1} \\ \vdots & \ddots & \vdots \\ V_{1,N} & \cdots & V_{K,N} \end{pmatrix}$$

Temporal PCA will then proceed, just as its spatial counterpart, and reconstruct the recurring features that best describe the variation of pixels at other time. In order to be detected, this feature should appear in a significant number of instances, here, the pixels variation through time.

The idea of temporal PCA is thus to analyze with PCA the temporal dimension rather than the spatial dimensions. Ultimately, one would want to analyze all three dimensions at once, for a complete spatio-temporal background subtraction. However, the design of such correction is significantly more complex, and beyond the framework of this thesis. In addition, a spatio-temporal background subtraction would require much larger computational time than separated spatial and temporal background subtractions. To analyze the temporal dimension, we developed a method in which we simply switch the axis on which PCA is performed. The corrections obtained are thus adapted for the pixels variation through time, and not for the images directly. Such correction thus allows us to flatten the overall brightness variation of the pixels through time. With this method, we can thus reduce the brightness variation of the remaining background structures responsible for the spikes, which is our main goal, but also reduce the overall RMS of the different groups. We describe in more detail the concept and implementation of temporal PCA in the appendix 6.2.

3.6.4 Application to Aperture Photometry

In this section, we used artificially injected sources and added the background-only dataset. Using this combination allows both for a realistic background and to check for any potential over-subtraction.

To obtain a correction as precise and as devoid of noise as possible, it is preferable to limit our library to the impacted group itself. In the following we call this option the 1Group post-TPCA. However, since the 1Group post-TPCA is limited to the group itself, it has no information about the offsets in between the various groups. We thus consider a second configuration for which we build the library on three consecutive groups : off-source, on-source, off-source. We refer to this configuration in the following as the 3Group post-TPCA. However, this last configuration would be less sensitive to variation of the photometry in the on-source group alone.

As mentioned in the previous section, in order to prevent over-subtraction of the source, the data needs to be modified before the projection to remove any signal above the background level. In the case of the 1Group post-TPCA, the signal above the background is computed in concentric annuli of 1 pixel width for the whole aperture of

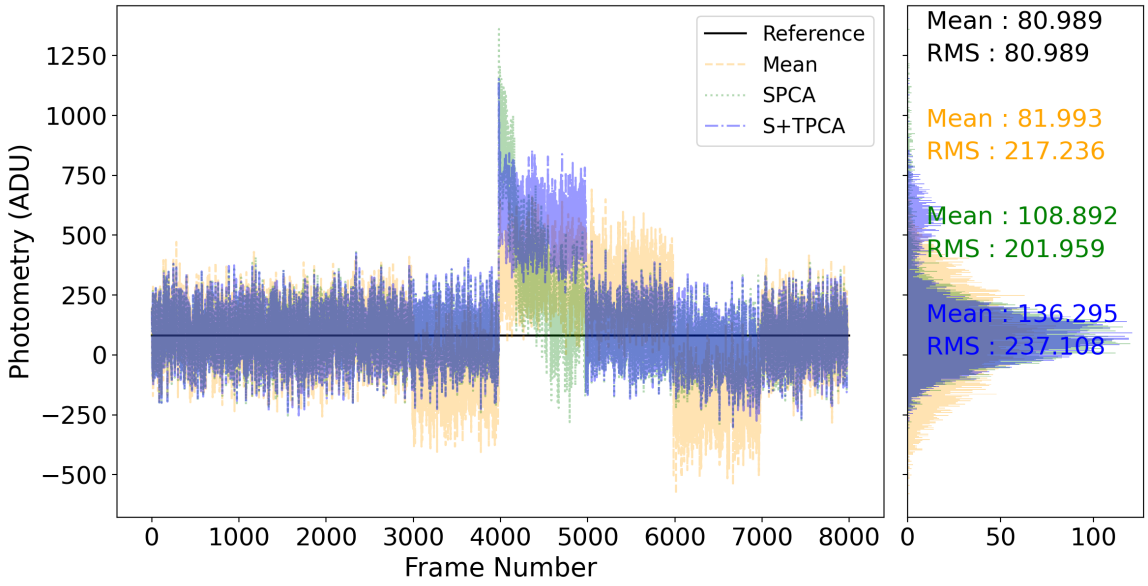

Figure 3.16: Photometry per frame for the mean (orange), spatial PCA (green) and spatial+temporal PCA (blue), with respect to the reference, injected photometry (black).

interest. The background values for each annulus can then be computed in two slightly different ways : for each frame (frame-by-frame approach) or the mean value of all frames of interest (mean approach). Those values are then subtracted frame by frame for each annulus. In the following, we present both methods and discuss their advantages and drawbacks, starting by the frame-by-frame approach.

Figure 3.16, presents the results obtained by measuring the photometry in a central aperture of 8 pixels in radius, when using the mean background subtraction, spatial PCA background subtraction alone, and the background subtraction combining spatial PCA and the 1Group post-TPCA.

Figure 3.16 shows that the mean background subtraction provides an overall estimate of the photometry slightly above the reference photometry but is overall very close. However, this method creates 4 offset groups for which the photometry is either too low or too high. The overall good value of the photometry thus cannot be trusted, as it results from the lucky average of the 4 offset groups. The spatial PCA background subtraction provides by comparison a much smoother curve, with the exception of the group impacted by the spike. The resulting photometry is higher; since no other groups came to counterbalance the higher photometry of this group, this offset is more representative of the error introduced by PCA background subtraction. Indeed, mean background subtraction creates more offsets in groups for which PCA background subtraction provides a really good correction, but since they average each other out, the error of the method is underestimated. The 1Group post-TPCA correction provides very similar results than spatial PCA for all groups, to the exclusion of the group impacted by the spike. Indeed, instead of a spike, we now have a flat offset group. This result

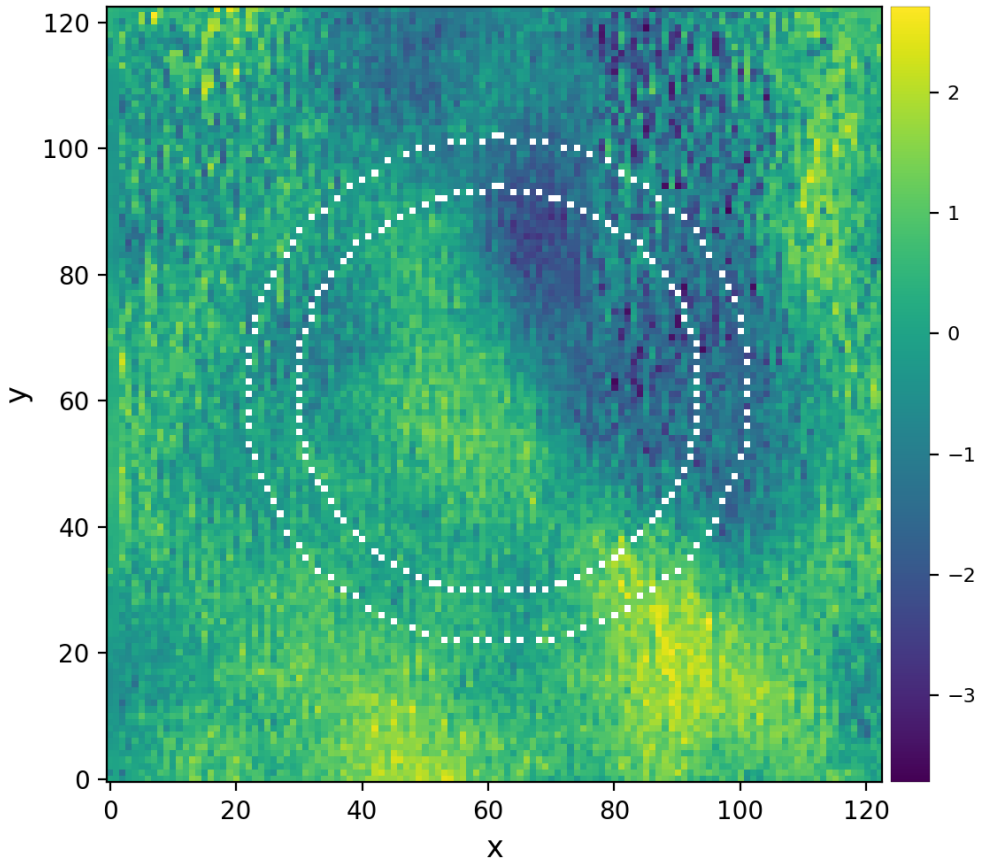

Figure 3.17: Mean image of the 1000 frames responsible for the spike, after background subtraction with spatial PCA. The innermost dotted circle represents the radius of the aperture and the inner radius of the background annulus. The outermost dotted circle represents the outer radius of the background annulus.

demonstrates that the temporal correction can indeed detect principal components related to this variation in the background annuli around the aperture and subtracted it effectively. However, since we are using the 1Group post-TPCA, temporal PCA cannot detect the offset.

It is important to note that the spike with spatial PCA and the offset with the additional temporal PCA results from a very poorly subtracted group of images. This group is poorly subtracted by both mean and PCA background subtraction. We show in Figure 3.17 the mean image of this problematic group after the spatial PCA background subtraction. The corresponding image for the mean background subtraction being extremely similar, we only display the result with spatial PCA here.

It is clear from Figure 3.17 that strong background structures remain after the

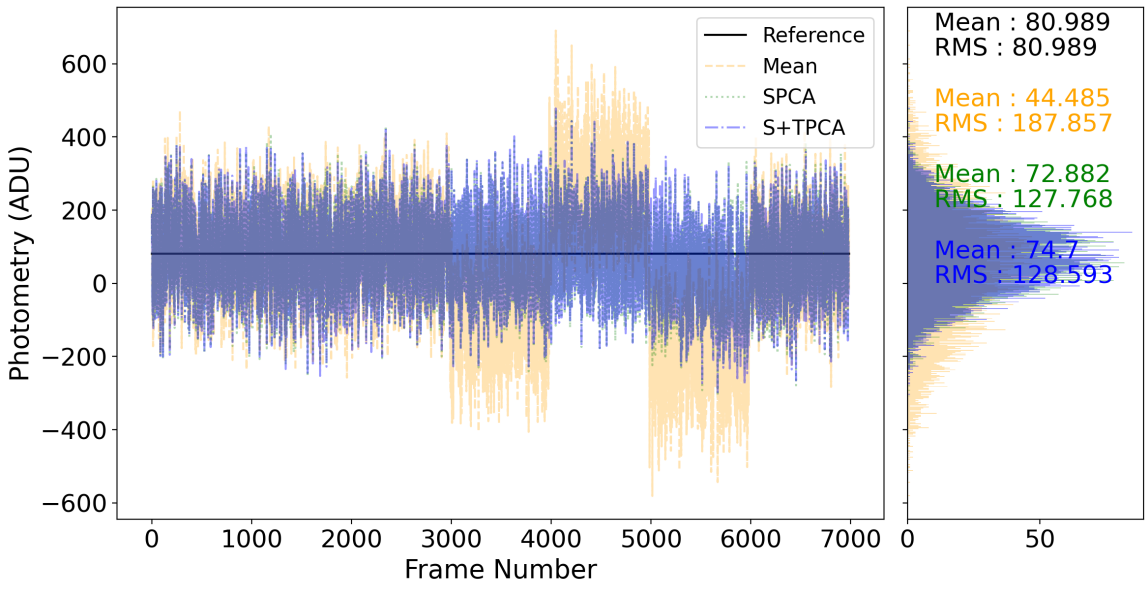

Figure 3.18: Photometry per frame for the mean (orange), spatial PCA (green) and spatial+temporal PCA (blue), with respect to the reference, injected photometry (black).

initial background subtraction, both inside and around the aperture. The approach which consists of subtracting the signal above the background here fails to properly describe the star and is responsible for the remaining offset. In order to manage this kind of exception, a mask would need to be introduced.

But let us put this problem aside to return to the groups that show variations in Figure 3.16. The most obvious is in fact the group impacted by the spike. The variation of this group is effectively suppressed despite the subtraction of the signal above the background frame per frame. This suggests that the mean value above the background in the annuli in the aperture is not significantly impacted by this background structure . Thus, the background structure responsible for the spike should cover only a relatively small part of each annulus. Another group, however, shows variations between frame 6000 and 7000. In Figure 3.18, we show the same results as in Figure 3.16, but without the group impacted by the spike, to focus on smaller variations.

In Figure 3.18 the new group of interest appears between frames 5000 and 6000, for which we observe a decrease in the photometry. Thus, temporal PCA fails to correct for this decrease in the photometry. Indeed, Figure 3.18 shows no differences for this group between spatial PCA background subtraction alone (green curve) and with the additional temporal PCA correction (blue curve). This can be explained by two different arguments:

- There are no similar variations in the background annulus from which principal components can be built to correct this structure.
- The mean value above the background in each annulus in the aperture is significantly impacted by this structure, and the variation is subtracted in the modified data,

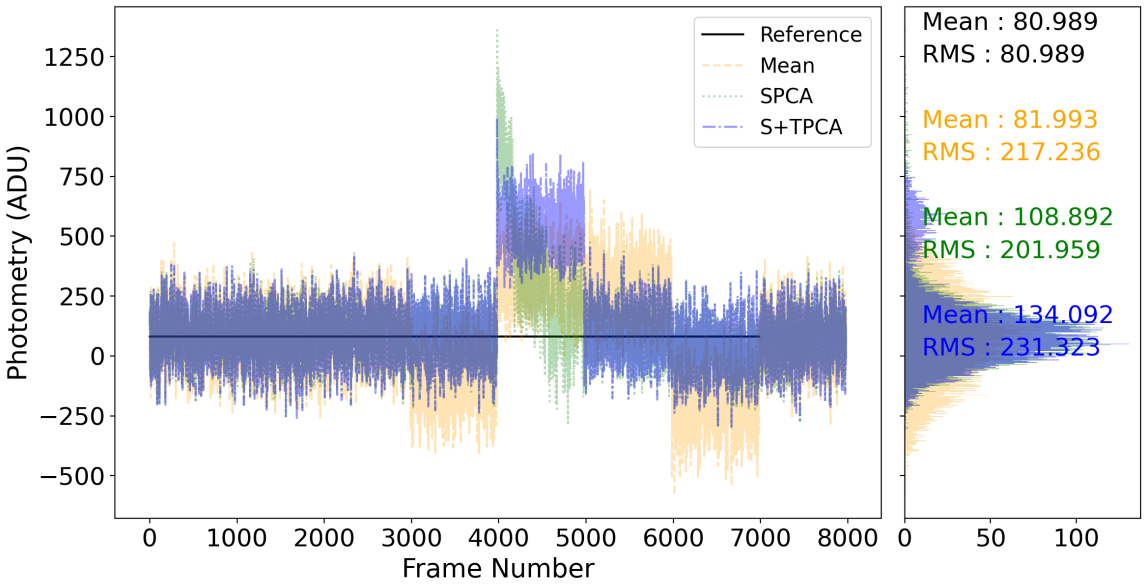

Figure 3.19: Photometry per frame for the mean (orange), spatial PCA (green) and spatial+temporal PCA (blue), with respect to the reference, injected photometry (black).

rendering the temporal PCA blind to this structure.

If the second proposition is correct, a simple way to allow temporal PCA to detect the structure is by not removing the value of the annuli per frame, but rather subtracting the mean value of each annulus through the 1000 images. This is what is shown in Figure 3.19, with the mean approach.

In Figure 3.19, the variation of the group impacted by the spike and the group with the small photometric decrease are corrected. This confirms the hypothesis according to which the structure significantly affected the value of the annuli. Thus, this structure should cover most of each annulus. However, it is worth noting that the small decrease in photometry of the second group has been replaced by a small offset. Indeed, just as in the case where the values of the annuli are subtracted frame by frame, 1Group post-TPCA is blind to this offset. In addition, and by comparison with the frame-per-frame approach, this approach assumes that the mean value of the group is the "correct" value. Depending on the dataset, this approach can thus introduce an important bias. It is thus clear in this case too that a mask is needed to better correct these types of structures.

In addition to the offsets, and to quantitatively estimate the benefits of using the temporal PCA correction after the spatial PCA background subtraction, we calculated the improvements factors, in a similar way as in Section 3.4, for the mean retrieval and RMS of each group, for both spatial PCA alone, and the combination of spatial and temporal PCA. We present in Figures 3.20 and 3.21 the improvement factors for the mean retrieval and the RMS respectively with the first approach to prevent over-subtraction.

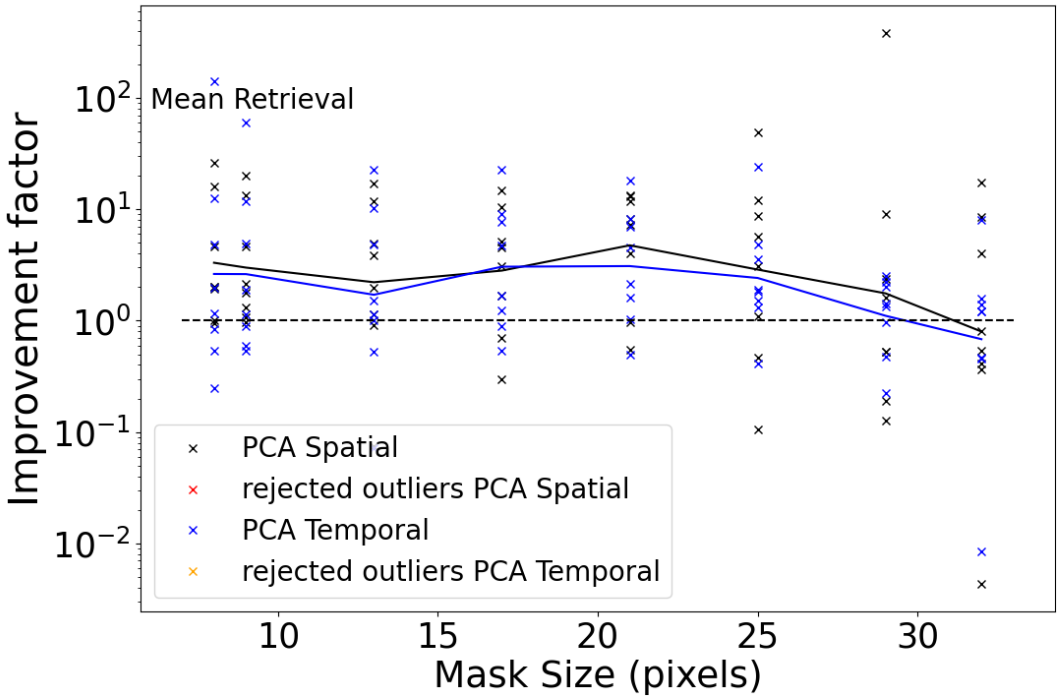

Figure 3.20: Ratio of the values of the mean retrieval per group between mean background subtraction and: 1. spatial PCA alone (black) and 2. spatial + 1Group post-TPCA Mean (blue). Values above one represents an improvement with respect to mean background subtraction.

The motivation of a temporal PCA correction, was to remove the photometric variation due to the background, without re-injecting bias. Figure 3.20 shows that this goal has been achieved, as the improvement factors obtained with spatial PCA background subtraction alone and with the 1Group post-TPCA are extremely similar for both approaches. As mentioned previously, however, the second approach could, depending on the dataset, degrade the mean retrieval by introducing back some bias.

Figure 3.21 on the other hand shows an important improvement of the RMS when using the temporal PCA correction in addition to the spatial PCA background subtraction. This difference is mainly due to the group impacted by the spike, which is effectively flatten, by the temporal correction. However, the other groups also benefit from the temporal correction, which slightly reduces their RMS too. This effect is more pronounced with the largest apertures, where the uncertainty caused by the photon noise (RMS) starts to dominate the uncertainty caused by the bias. However, by using the frame-per-frame approach to prevent over-subtraction, we also limit the ability of the temporal correction to further reduce the RMS of the individual groups. The second approach, on the other hand, does not suffer from this limitation. In Figure 3.22, we compare the impact on the RMS of the two different approaches.

As expected, Figure 3.22 shows that the second approach provides better results for

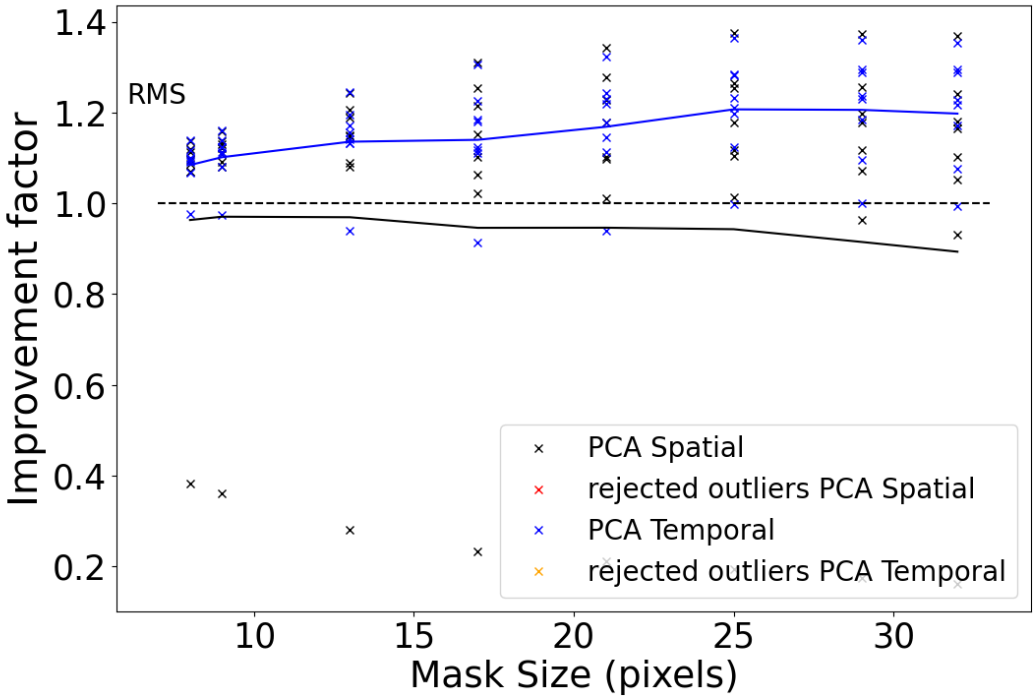

Figure 3.21: Ratio of the values of the RMS per group between mean background subtraction and: 1. spatial PCA alone (black) and 2. spatial + 1Group post-TPCA Mean (blue). Values above one represents an improvement with respect to mean background subtraction.

the RMS. Indeed, the second approach is able to detect much more variation in the aperture than the first approach can, since a portion of those are subtracted with the first approach. If the second approach is "too risky" to be used in practical cases with its potential to add back bias to the data, Figure 3.22 shows that the first approach is in itself an important limitation to the possibility offered by the temporal PCA correction.

In order to remove the offsets that occurred in groups of on-source images, it is necessary to use adjacent off-source groups to build the library, and the principal components, that is, the 3Groups post-TPCA configuration. For this configuration, the library is thus composed of the value of the background pixels through the 3000 images (1000 off-source, 1000 on-source, 1000 off-source) which comprise the 3 successive groups.

Principal component analysis describes the data by determining the principal components that encompass the most variation. The first principal component of a dataset is usually its floor level. For some data sets, this floor level can be represented by the mean or median value of the data. In our case here, the floor level cannot be described by a simple value, as the three groups are likely to have different floor levels, due to the remaining background. The first principal component, which best describes the three groups together, will therefore consist of a step-like curve that represents the floor level of each group. This is true in the background library, in which we will measure

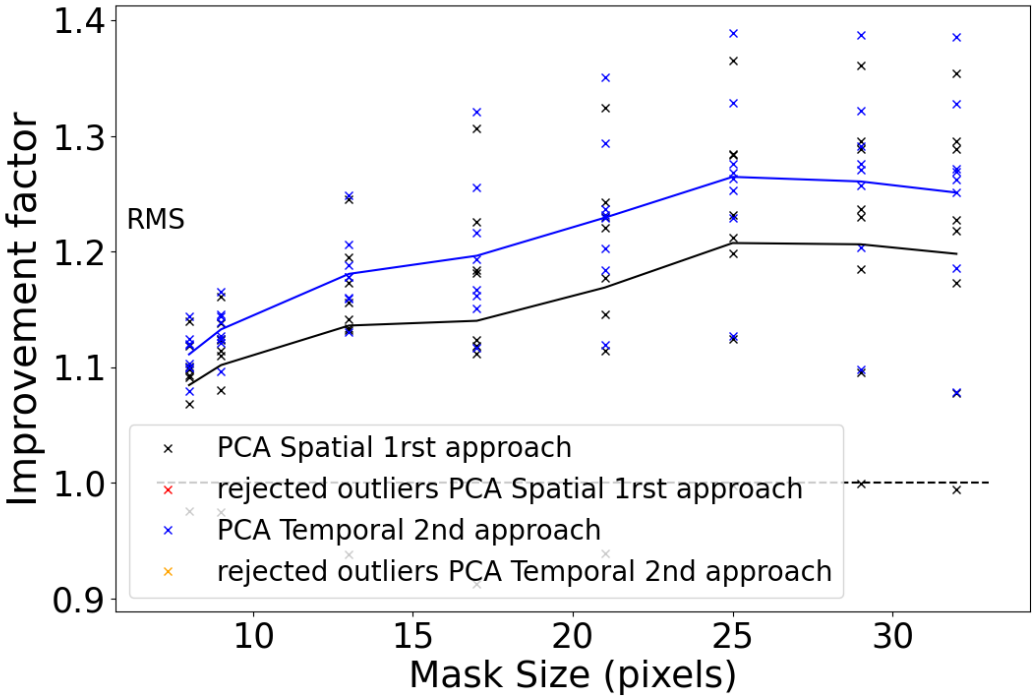

Figure 3.22: Ratio of the values of the RMS per group between mean background subtraction and: 1. spatial PCA + 1Group post-TPCA 1rst approach (black) and 2. spatial + 1Group post-TPCA 2nd approach (blue). Values above one represents an improvement with respect to mean background subtraction.

the background floor level for each group, and in the aperture, where the floor level of the on-source images will be a combination of the background floor level, and the star emission floor level. In Figure 3.23 we show the first principal component of the 2 first groups of our dataset.

As shown in Figure 3.23, the first principal component mainly represents the step in the background floor in between the first, on-source group of 1000 images, and the second, off-source group. If not corrected, these differences in background floor level can be responsible for an offset in the final photometry, and thus should be corrected. However, it is also important to take into account the variation in the floor level of the photometry due to the presence or absence of the star in the dataset. Indeed, this situation will also introduce a step in the photometry inside the aperture, which will be very similar in shape to the step in the photometry inside the background annulus. When the first principal component of the background is projected onto the aperture, its intensity will be "adapted" to the step of the photometry inside the aperture, thus completely subtracting the source. This can be seen in Figure 3.24 where the principal components obtained in the background annulus are used without any preparation of the data set and the star is fully self-subtracted.

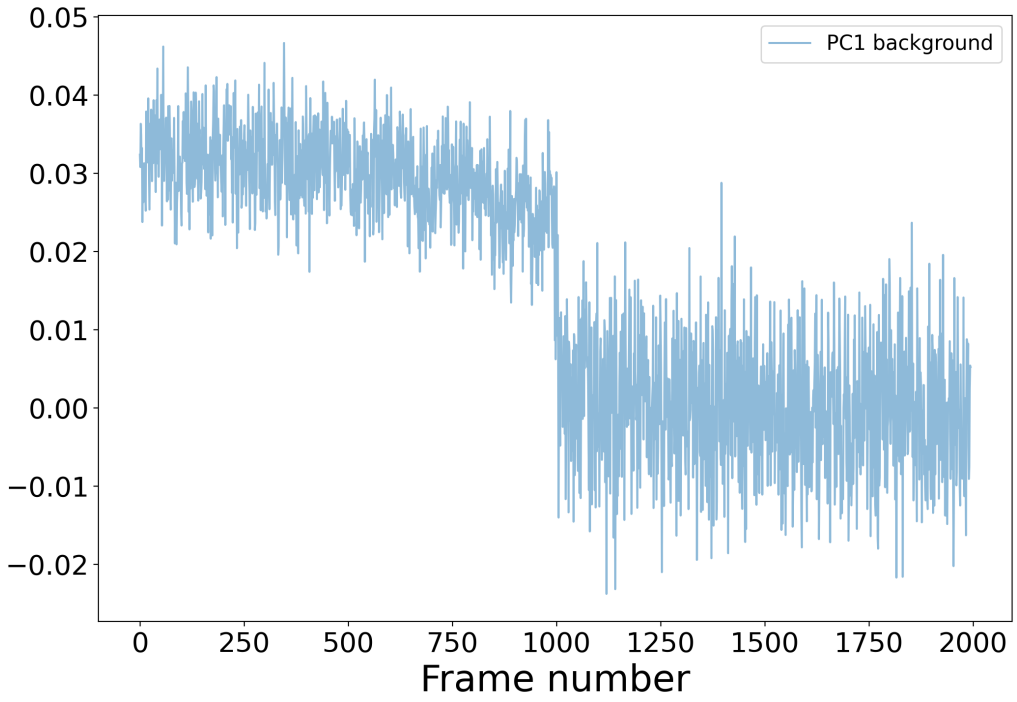

Figure 3.23: First principal component obtained with the background library on the first and second groups of the dataset, respectively on and off-source groups (1000 frames each).

Just as in the 1Group post-TPCA case, the signal above the background should thus be subtracted (or masked) beforehand in order to prevent over-subtraction. For this, we use the same frame-per-frame approach as used for the 1Group post-TPCA case. Following this methodology, we obtained results similar to those presented in Figure 3.16. The main difference from this other case was the degradation of the mean retrieval. Indeed, if the 3Groups configuration allows seeing the offset, it also introduces errors, due to the remaining background present in each group and their differences. This is in fact the first motivation to use the 1Group configuration. When using the 3Groups post-TPCA along with the frame-per-frame approach, the offset also becomes visible again; worse, when using the first principal component, describing the floor levels, it became even stronger than it used to be with the 1Group post-TPCA configuration. To understand this behavior, we show the first principal components inside the aperture, before and after removal of the signal above the background, and the first component in the background aperture, in Figure 3.25.

The first important information that can be drawn from Figure 3.25 is how different the first principal component is in the aperture and in the background. In the aperture, we observe a clear step upward in the photometry, which can be due to the star presence, but also to the bright structures visible in the aperture region in Figure 3.17. In contrast, the first principal component in the background annulus shows a strong step downward,

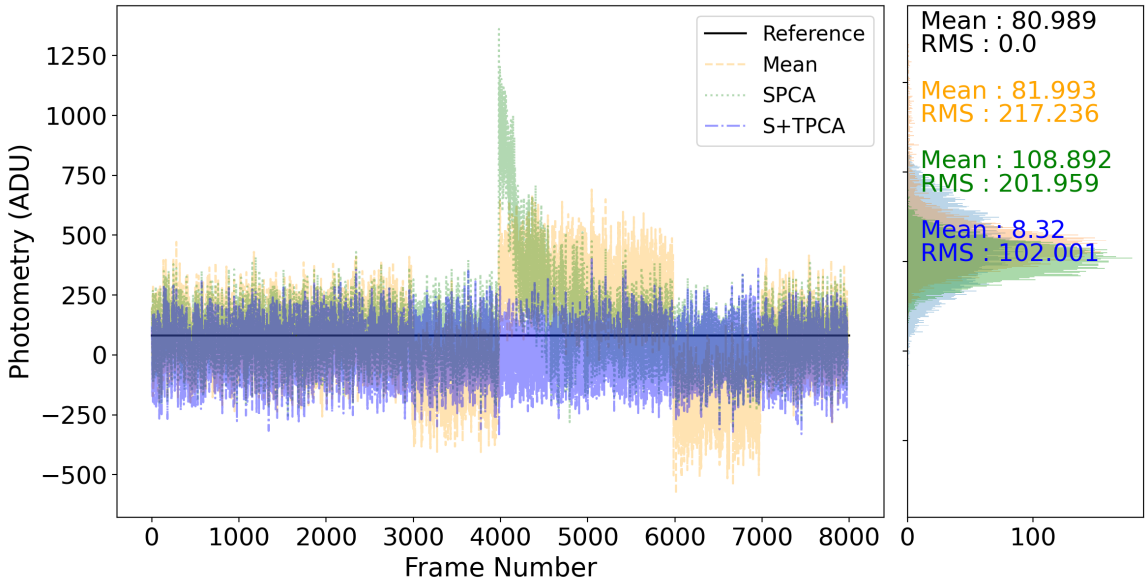

Figure 3.24: Photometry per frame for the mean (orange), spatial PCA (green) and spatial+temporal PCA (blue), with respect to the reference, injected photometry (black), for the 3Groups post-TPCA when not using any precaution to avoid source over-subtraction.

which is most likely due to the presence of the negative structure in the upper right part of the image in Figure 3.17. This situation explains not only the offset in the photometry for this particular group but also why this offset increases when using the first principal component of the background in the correction. Indeed, this first principal component being downward, it will correct the aperture as if its step was downward too, thus increasing its floor level. Another important information comes from the first principal component in the aperture after the signal removal. In fact, if the signal removal approach worked perfectly, the first principal component in the aperture after the signal removal should be identical to the first principal component in the background. This behavior occurs not only on those particular three groups but on most of them. This also explains why removing the first principal component of the background from the correction usually provides a higher quality of mean retrieval. However, removing the first principal component means that temporal PCA is once again blind to the offset between the groups. Rather than using this simple solution, it is preferable to mask the region of interest.

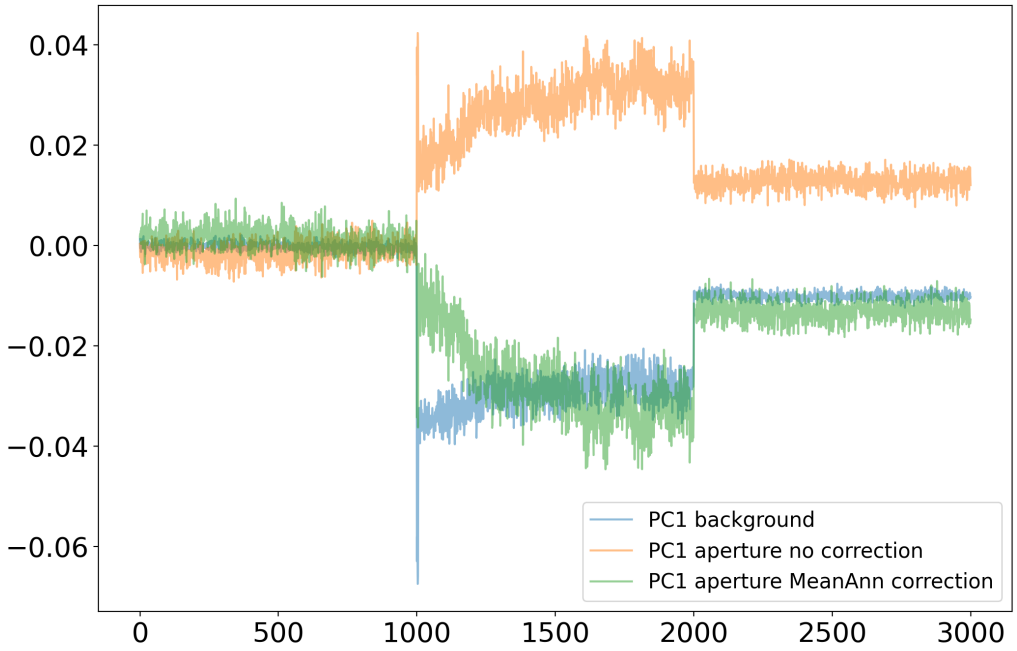

Figure 3.25: First principal component obtained with the background library (blue), on the aperture before the signal removal (orange) and after the signal removal (green). For the group immediately before the group impacted by the spike (frames 0 to 999, off-source), the group impacted by the spike (frame 1000 to 1999, on-source), and the group immediately after the group impacted by the spike (frame 2000 to 2999, off-source).

3.6.5 Limitations

However, considering the current method explored for signal removal, the temporal PCA correction failed to correct the resulting offset of the flatten spike.

In our analysis, we have shown that the approach to remove the signal above the background, which is needed to prevent PCA to build principal component on the signal itself, is a major limitation to the temporal PCA correction. The two main approaches considered, using annuli, both failed to correct the offset from the group impacted by the spike. Because this group is very poorly background subtracted, strong background structures remain in the background and in the aperture, rendering the computation of the signal above the background difficult. This led to an over-subtracted aperture responsible for the offset in both cases. Moreover, the approach consisting of a frame-per-frame subtraction limits the sensitivity of the temporal PCA correction, since it removes some background variation with this subtraction. This approach thus limits the expected improvement of the RMS. However, using the mean approach to subtract a constant value from a whole group allows to achieve a better sensitivity to those

background variations but in turn poses a risk of introducing bias by assuming that the mean value of a group is the "correct" value of the photometry. We have explored various methods to improve the signal removal, but none have been satisfactory, with the majority of them under-subtracting the signal and leading to an over-subtraction of the source in the final photometry. Thus, for this method to provide satisfactory results, a mask would need to be introduced.

In addition, we have shown that the annuli approach for signal removal was producing unrealistic PSF in the mean final images of the groups. In particular, the annuli are visible after the temporal PCA correction. This issue comes from the fact that the residual noise is lower than the differences in the different annuli introduced by signal removal. However, this is both a demonstration of how well temporal PCA can perform, as it effectively reduces the noise in the mean final image of a group by a little less than a factor 10 (see Figure 3.17), and the need for a mask.

3.6.6 General applications

Besides aperture photometry, the temporal correction can be adapted and applied to various methods, data types, and dataset configuration. In contrast to the spatial PCA background subtraction, which requires nodding, the temporal PCA correction in its 1Group configuration can be applied to virtually any series of data. Indeed, the only images needed in this configuration are those to correct. We thus briefly discuss other applications of this method.

Nulling measurements

We will show in Chapter 4, that in order to integrate the PCA background subtraction in the nulling pipeline, a few changes had to be operated, in particular in how the off-sources images were subtracted. Indeed, the nulling pipeline uses the self-calibration approach, which requires representative background sequences. Thus, the correction between the on-source quadrant and the off-source quadrant must be as similar as possible. This also applies to the additional temporal correction.

For spatial PCA background subtraction, the issue was that the library onto which the principal components were built would have been on-source images if we had used the exact same procedure for on-source and off-source groups. In the case of the temporal correction, the library is not built on images but on individual pixel through time. This particularity makes the libraries of temporal PCA independent of whether the groups which composed them are on-source or off-source. Indeed, the star is never present at those locations. When using the 3Groups configuration, the library could thus be selected as they would have been if the group was on-source. When using the 1Group configuration, the library can also be selected as if the group was an on-source group.

However, in addition to the choice of library, the problem of masking the signal remains. Indeed, for on-source groups, the signal above the background level would need to be masked. This mask can both blind temporal PCA to a certain amount of background variations and introduce an error on the values in this aperture. For the off-source groups, the mask is of course useless, as no source is present in the images. As a result, off-source groups will benefit from a much better correction than on-source groups. This difference can later pose a problem in the nulling pipeline, as the background quadrant will be less similar to the on-source quadrant. It is thus possible that the off-source images should be processed in the exact same way as the on-source images and use a mask to allow the correction of the on-source and off-source parts of the image to be as similar as possible.

The main gain expected by using the temporal PCA correction for nulling data is to allow to use the data from the groups impacted by the large photometric variations and to prevent their extreme error bars. In fact, those extreme error bars on individual null measurements can significantly impact the total uncertainty on a pointing. Reducing those error bars can therefore lead to a more precise estimate of the uncertainty on the total null measurements. The reduction of the RMS on other groups could also lead to slightly smaller error bars on individual measurements; however, as the current error bars of the total measurements are dominated by the scattering of the individual measurements, this is likely to have little to no impact. Thus, temporal PCA has the potential to strongly benefit datasets that are impacted by large photometric variations or are limited by the RMS rather than by bias. However, more work is needed to finalize temporal PCA so that it can be used for nulling measurements. In particular, the use of a mask rather than a signal removal method should be investigated carefully for each configuration of temporal PCA (before/after spatial PCA background subtraction, 1/3 group(s)).

High contrast imaging

A second possible application is high-contrast imaging. Indeed, as illustrated in Figure 3.17 beside the unrealistic PSF, the remaining noise in the image is much lower than after the spatial PCA background subtraction. If the signal from a companion is not subtracted, it could thus be detected with a much higher SNR. Of course, in its current form, the temporal PCA correction cannot be used to search for an unknown companion. Indeed, without any precaution to protect the companion signal, it would be subtracted, just as the star would have been. It is thus excluded to systematically use this temporal PCA correction in order to detection companion without prior knowledge.

However, temporal PCA can be used to improve the SNR of faint or tentative detection. In this case, an approach similar to that used to mask the signal in the aperture should be used at the expected location of the companion. On the other hand, the signal of the star, which is not of interest in this case, does not need to be kept, and

do not need to go through any masking. However, a risk of contamination can arise if the companion is relatively close to the star. To avoid this situation, an application of temporal PCA after the PSF subtraction is also possible. Another precaution should be taken while selecting the background region onto which the principal components will be built. Indeed, to prevent both erroneous correction and over-subtraction, this background region should be carefully selected so as to avoid the star

It is also worth mentioning that all of this discussion can be applied not only for companion but also for circumstellar disks. Indeed, the only required change would be to perform the signal removal on a region which encompasses the whole disk, and not only a circular aperture. Similarly, the selected background region should be adapted so as to exclude the star and the disk.

Spectral series

The name temporal PCA is quite misleading. Indeed, we chose to name it temporal PCA because the third dimension of our datasets is the temporal dimension. With the axes switch, PCA thus analyses the temporal dimension. However, this method can be applied to any third dimension. It could in particular be applied to datasets composed of snapshots taken at different wavelengths. The "temporal" PCA will thus analyze the variations of the pixel value through the different wavelengths rather than through time.

Let us take the example of wide field images of a nebula taken at different wavelengths. The images contain several stars, and the cloud. For each star, we will select an aperture and a background annulus centered on this aperture. The signal removal would thus be performed to remove any signal from the star that is higher than the mean signal of the cloud in the background annulus. The library can then be selected either by region or on a more global scale to build the principal components. The principal component will then represent the variation of the cloud photometry through the wavelength of the snapshots. Those principal components can then be projected onto the apertures to suppress the contribution of the cloud in the aperture. The remaining variations on the wavelength dimension should then come from the star itself.

Similarly, series of spectra, such as those that the Asgard/NOTT instrument (Defrère *et al.,* 2024) will obtain, could also benefit from this method. In this case, the spectral dimension could be treated as the spatial dimension, and the temporal PCA will consider the variation over time of each pixel within the spectra. Alternatively, this method could also be used on the spectral dimension so as to correct or retrieve features which are reproduced in every or most wavelength.

3.7 Conclusion and Perspectives

In this chapter, we have demonstrated the ability of spatial PCA background subtraction to significantly improve the sensitivity of the data. In HCI (see Section 3.3),

for which starlight residuals dominate, we obtained improvement factors ranging from 1.2 to 1.7 in the contrast curves. On the other hand, for Aperture Photometry (Section 3.4), we obtained improvement factors ranging from 2 to 3 for mean retrieval, and 1.2 for the RMS of small apertures. The Aperture Photometry analysis has shown that spatial PCA background subtraction provides results which are more accurate, but not necessarily more precise.

In the context of the HOSTS survey, the accuracy of the results is the main concern. Indeed, the bias remaining in the data after the background subtraction leads to a scatter of the individual measurements, which dominates the uncertainty. The process of obtaining null measurements is rather similar to the Aperture Photometry case. Indeed, the photometry is measured in an aperture centered on the star and in another aperture centered on the previous star position. Each aperture has its own background annulus to estimate the remaining background in the aperture. We know that the background annulus is a strong source of bias, already in the Aperture Photometry case. Using spatialPCA background subtraction for null measurements, thus avoiding the use of two background annuluses, would thus be strongly beneficial. In Chapter 4, we discuss the modifications needed in our method and on the nulling pipeline to enable spatial PCA background subtraction for nulling measurements, as well as its potential impact on zodi measurements and modeling.

Despite the improvement achieved by spatial PCA background subtraction, in particular for aperture photometry, we identified limitations, as discussed in Section 3.5. In particular, the large photometric spikes prevent the use of a portion of the data. In Section 3.6, we present a method aiming at removing the spikes and mitigating the effects of poor background subtraction on particular groups. We demonstrated the capability of an additional temporal PCA correction, taking place after spatial PCA background subtraction, to remove important photometric variation through time, when those variations are linked to a background structure. Indeed, we have seen that the different strategies of temporal PCA considered in this chapter, 1Group post-TPCA and 3Group post-TPCA, can both effectively flatten the spike. Depending on the choice of signal removal approach, we have also seen that much fainter variations could be corrected, and the RMS was improved throughout the whole dataset. However, the current implementation of temporal PCA, with the signal removal approach, is far from optimal and offsets remains in the final photometry. To prevent this limitation, an implementation of temporal PCA with a mask should be considered.

In addition, spatial PCA background subtraction, as presented in this chapter, can only be used for data sets using a nodding sequence to sample background. Future works should aim at adapting this method for a wider range of datasets, such as those using chopping for background sampling, dedicated background observations, or even to wield field photometric data. Furthermore, PCA background subtraction does not specifically require imaging data to work with, and adapting this method to spectroscopic data, for

example, could also be strongly beneficial.

Chapter 4

Applying Principal Component Analysis background subtraction to HOSTS nulling data

Contents

The HOSTS survey provided the first estimate of the median exozodiacal dust level around nearby stars (see Section 1.3). Those findings have shown that exozodiacal dust will not systematically prevent the detection of Earth-like exoplanets by future direct imaging missions such as HWO or LIFE (Ertel *et al.,* 2018, 2020a). However, in addition to the remaining uncertainties on those measurements, addressed in Chapter 3, little is known about the dust itself, such as its composition, spatial distribution, circulation, etc. With a PCA treatment of the HOSTS data, we expect the scattering of the individual null measurement to be reduced, leading overall to a reduction of the global null measurement error bars. In this chapter, we first present a proof of concept by reducing artificially the error bars of data from Vega (which thus became non-physical), to estimate the impact of this error bars reduction on the modeling procedure. We then present our current results on nulling measurements obtained with the PCA background subtraction through the HOSTS pipeline, and finally model in detail the 110 Her system for which the HOSTS survey has made a detection.

4.1 Data reduction and Modeling tools

4.1.1 Data reduction

The HOSTS data are reduced with the official LBTI pipeline (Defrère *et al.,* 2016), which can be decomposed into three main steps :

- Preparation of the files and background subtraction
- Computation of the fluxes
- Null computation with Null Self Calibration (NSC)

The first step of the pipeline consists in creating a file per observation block, the L0 files, containing all relevant headers, including telemetry, the star position in the image, etc. and to subtract the thermal background. The pipeline uses the mean background subtraction technique by default. To use the PCA background subtraction method, the background subtracted images are replaced in the L0 files so that all headers remain identical and the process is transparent to the next steps of the pipeline.

The flux computation is then performed on a total of four regions: the aperture of interest, a corresponding aperture in the background region, and two background annuli around both apertures. The flux in the background annulus is then subtracted from their respective apertures. This step allows removing the remaining background behind the star. This method introduces significant bias, and that is why in the case of the PCA background subtraction, as detailed in Section 4.3, the two background annuli are removed. These steps are performed on both the scientific and the calibrator stars. The flux computation thus provides two outputs, which are the corrected fluxes of the aperture of interest and of the background aperture. Then those two outputs are used by the NSC and are referred to as L1 files.

With those inputs, the NSC builds a synthetic distribution of null-depth measurements, which it then fits to the distribution of the observed null-depth measurements. This procedure is going through a Markov Chain Monte Carlo (MCMC) procedure which determines the best possible fit to the data. This step is performed on both the scientific and the calibrators stars, for each of their observational blocks. Those measurements are then combined to provide a calibrated null-depth measurement per pointing.

Those steps can be performed for various aperture sizes, thus providing null-depth measurements at different distances from the star. The null-depth measurements per pointing for those different apertures, for both the scientific and the calibrator stars, are then used for the modeling. Those apertures are concentric circular apertures, usually set to 8,24 and 40 pixels in radius, the 16 pixels width increment corresponds to the PSF obtained with the LBTI/NOMIC detector. Those results are saved in the L2 files.

Note that a variant of this procedure is to use ring apertures instead of filled circular apertures (Faramaz et al., prep). In this approach, after the flux computation step, the flux measured in the aperture of 24 pixels in radius is subtracted from the flux of the aperture of 40 pixels in radius, and similarly down to the smallest aperture that remains a circular filled aperture of 8 pixels in radius. The NSC is then performed similarly to the standard case. In addition, intermediary apertures were introduced, with an increment of 8 pixels rather than 16, using the PSF's HWHM and increasing the number of measurements as a function of radius. One of the main advantages of this method

is that it separates the emissions coming from the different regions and thus can help uncover radial structures in the emission.

4.1.2 Disk model

The model for the exozodiacal disks is based on that established by Kennedy *et al.* (2015), which describes a disk as a surface brightness profile S_{disk} seen face-on as follows:

$$S_{disk} = 2.35 * 10^{-11} \Sigma_m B_\nu(\lambda, T_{BB}) \quad , \tag{4.1}$$

with the blue term being the conversion factor allowing the surface brightness to be expressed in Jy.arcsec^{-2}, Σ_m the disk's face-on surface density of cross-section area, B_ν the grain emission at the wavelength λ of the observation and for a dust temperature T_{BB}. For the HOSTS survey, the observation were made at $\lambda = 11\mu m$. The temperature of the dust grain is expressed as a black body temperature in Kelvin, such as:

$$T_{BB}(r) = f \times 278.3 \; L_{star}^{0.25} \; r^{-0.5} \quad , \tag{4.2}$$

with f the temperature modification factor, generally set to 1, L_{star} the star luminosity and r the distance to the star. The Σ_m term is analogous to the optical depth and can be expressed following a power law such as :

$$\Sigma_m(r) = z \; \Sigma_{m,0} \; (\frac{r}{r_0})^{-\alpha} \quad , \tag{4.3}$$

or in terms of optical depth:

$$\tau(r) = z \, \tau_0 (r/r_0)^{-\alpha} \quad , \tag{4.4}$$

with $\Sigma_{m,0}$ and τ_0 normalizations to be set at a given r_0 so as to obtain the resulting value in units of zodis z and α the slope of the surface density. These values are expressed in between r_{in} and r_{out}. Due to the primary goal of the HOSTS survey, to estimate how much dust lies in the habitable zone of the system and might hinder Earth-like planet detection, the r_0 term is set to represent the Earth-equivalent distance, that is, the distance at which the equilibrium temperature around the star is the same as the temperature around the Sun at the Earth distance. Thus, r_0 is expressed in AU as :

$$r_0 = \frac{1}{1AU} \sqrt{\frac{L_{star}}{L_{sun}}} \quad . \tag{4.5}$$

In order to define the targeted system with this model, one will thus have to fit the following six parameters : the slope of the dust distribution (α), the optical depth of the disk ($\frac{\tau}{10^{-5}}$, the inner and outer radii of the disk (R_{in} and R_{out}), its inclination (i) and its position angle(PA). Each time a synthetic disk will be built with these parameters and compared to the observations through a MCMC procedure described in the next section.

4.1.3 Fitting procedure

The tool used to model the detections of the HOSTS survey uses a Markov Chain Monte-Carlo (MCMC) to fit the parametric approach model described in Section 4.1.2. Thus, the model creates laws of the form $c_0 r^\gamma$, with c_0 a constant, r the radius, and γ the power at which the parameter depends on the radius, to fit the data. It also determines parameters like the inner and outer radius, which represent the bounds which best match the data. At the very beginning of the modeling, the model uses the "first guess" values attributed to each parameter it needs to fit. It will then create an emission model from those parameters which will be processed as the observations had. It thus obtain synthetic null measurements that is compared to the data and determine how well they fit, by computing the χ^2 value, which is defined as follows:

$$\chi^2 = \Sigma \frac{(O_i - E_i)^2}{E_i} \quad , \tag{4.6}$$

with O_i the observed values, here the null measurements from the different apertures, and E_i the expected values, here the values obtained from the synthetic data created with the model. Once this first step is completed, the modeling tool will use a Bayesian approach to generate a second model, based on the first model data and probability distribution. In fact, it will attribute probabilities for each possible cause of the increase or decrease of the χ^2, creating a distribution of how probable each cause is to be responsible for this change. If the χ^2 is decreasing, this approach allows determining which causes are the most probable to be responsible for producing this positive outcome. The values for the next model will thus be changed in accordance with this most likely cause of the χ^2 diminution. On the contrary, if the χ^2 is degraded, this approach can also determine which cause is the most likely for this degradation. In this case, the values for the next model can be changed in opposition to the previous change. The new synthetic data are again compared to the observed values, giving a new value of χ^2, and a new probability distribution. A third model is then generated, only based on the second model without any knowledge kept from the first model. Each time a new model will be generated, only based on the previous one data and probability distribution, thus creating a chain of models. The probability distribution of a model will thus impact the "direction" in which the values of the next model will be changed. If the new model overshot the optimal value, the Bayesian approach will identify this overshot as a cause of the degradation of the χ^2 and thus the "direction" of the modification of the values will be impacted. With this procedure, the MC is able to determine values for each parameter that minimize χ^2, and thus maximize the similarity of the model to the observed data. This procedure will be repeated until the model converges or reaches the maximum number of steps that it can take. In our case, for most of the modeling effort, the number of steps of the MC is 9000 steps.

A drawback of this approach is that the model can be "tricked" to a local minimum.

In order to mitigate this risk, the MCMC approach introduces the use of walkers. Each walker will start with the same initial conditions but take different paths, thus producing different models with different probability distributions. The number of walkers should be adapted in function of the number of parameters to fit, and the likeliness of local minima occurring. We then consider the distribution of the results found by the models at the end of all the chains, for each parameter. In our case, modeling an exozodiacal disk requires several parameters, and each parameter is likely to create several local minima. To model the detection of the HOSTS survey, 30 walkers are usually used, as this number provides a good compromise between computational time and adequate probing of the parameter space. All those walkers will follow their own path and eventually converge. This will create a probabilistic distribution for each of the fitted parameters. In some cases, groups of walkers will converge for different solutions, creating several probable distributions which are not necessarily compatible with one another and represent degeneracies in the model.

The results from the MCMC procedure are usually presented on corner plots. The corner plots display, for each parameter, their median distribution (50th percentile, central dashed line on the distributions), which corresponds to the best-fit values, the 16th percentile (right dashed line on the distributions, best-fit value subtracted by the uncertainty toward lower values) and the 84th percentile (left dashed line on the distributions, best-fit value subtracted by the uncertainty toward higher values).

4.1.4 Predefined models

The simplest option to run the modeling tool is to fit all the parameters without assumption. In the following, we refer to this approach as the free model. The advantage of this modeling option is mostly to be unbiased. In fact, the model can determine the inner and outer radii of the disk without constraint, and thus encompass the whole dust distribution. It can also determine the slope of the dust distribution freely, as well as the inclination and the position angle. However, the lack of assumptions on certain parameters let the model with a large number of free parameters. This situation makes this modeling computationally expensive. In addition to the time needed to fit all of those parameters, such a model will also need a larger number of walkers to fully explore the much larger parameters space. Those walkers could themselves require a larger number of steps before converging and present higher risks of not converging at all.

To avoid all these drawbacks, several build-in models have been implemented to ease the modeling: the pancake-like model, the thin-ring model, and the zodi model. We describe these three options in the following paragraphs and present a comparision of their capacities, advantages and drawbacks in Table 4.1. For the analysis of 110 Her, we used all three options, along with the free model and compared the to gain an in-depth understanding of the system.

In the following analysis, the MCMC for the free model used 100 walkers, 6000 burning steps (i.e. MCMC steps which are not kept as the convergence has not been reached yet) and 3000 additional step for convergence.

Pancake-like model

The pancake-like model, makes the assumption of a very extended disk. The idea of this model is to:

- move the inner radius inside the inner working angle of the LBTI so that the precise location of the inner edge does not impact significantly the null-depth. It corresponds to the sublimation radius of silicates.
- move the outer radius to a distance where the dust temperature will prevent it from emitting significantly in the N' band. It is set to an arbitrary large distance.

For the Sun, the inner radius would be set to 0.034 AU, while the outer radius would extend to 10 AU. In the model, these values are adapted to each star with respect to its luminosity, and then converted to milli-arcseconds. Those inner and outer radius are thus defined as follows:

$$R_{in} = \frac{0.034 \times \sqrt{L_\star} \times 1000}{D_\star} \quad \text{and} \quad R_{out} = \frac{10 \times \sqrt{L_\star} \times 1000}{D_\star} \quad , \tag{4.7}$$

with $L_\star$ and $D_\star$ the luminosity and distance of the star, respectively. Once these values are determined, they remain fixed throughout the MCMC. With this modeling option, the radial extent of the disk thus cannot be fitted. On the other hand, this model allows fitting the optical depth behavior (reference value τ_0 and the slope of the power law it follows), as well as the orientation (inclination i and position angle PA). In the following analysis, the MCMC for the pancake-like model used 30 walkers, 6000 burning steps, and 3000 additional steps for convergence.

Thin ring model

When using the thin-ring option, the model assumes that the inner and outer radii are linked by a ratio and can be expressed as follows:

$$\frac{\Delta R}{R} = \frac{R_{out} - R_{in}}{R} = 0.1 \quad \text{and thus,} \quad R_{out} = 1.1 \times R_{in} \quad . \tag{4.8}$$

This 0.1 ratio between the inner and outer radii is based on debris disk analysis, for which this ratio is considered a thin ring. Indeed, this ΔR is chosen because it is generally small compared to the angular resolution of the observations and to any temperature effects on the dust emission. Since the outer radius is defined as a function of the inner radius, this model only fits the inner radius. The slope cannot be fitted with this option and keeps the initial value given in the options file. It can be beneficial to gain some insight into the slope value of the system by using the pancake-like option described in the previous subsection. All other parameters, the optical depth, the

orientation, and the position angle, can be fitted with this model. In the following analysis, the MCMC for the thin ring model used 30 walkers, 6000 burning steps and 3000 additional steps for convergence.

Zodi model and level

The main purpose of the HOSTS survey was to determine the amount of exozodiacal dust present in each system, to assess the feasibility of Earth-like planet detections and draw a more general conclusion on the median zodi level around nearby stars. In particular, to prepare future direct imaging missions targeting habitable worlds, the primary focus is to determine the amount of exozodiacal dust in the habitable zone. In order to compute this value, this model option makes several assumptions. It first assumes an inner and outer radii similar to those used for the pancake-like model, with dust very close-in and very far-out. When running the MCMC with this option, the inner and outer radii are fixed and not fitted. The second assumption is to set the slope at -0.34, which corresponds to the slope of the zodiacal disk in our solar system (Kelsall *et al.,* 1993). The slope is also not fitted by this model. The amount of dust is then computed for the radius corresponding to the habitable zone of the star, which is itself derived from the star's luminosity, temperature, and distance. This model was used on all stars observed during the HOSTS survey to compute the currently published results.

In the following analysis, the MCMC for the zodi model used 30 walkers, 6000 burning steps and 3000 additional steps for convergence.

Despite its ability to estimate the amount of dust in the habitable zone of the system, this model option presents some limitations. The most important is the fixed slope value. Indeed, this value is set to match the slope observed in the solar system zodiacal disk. However, the "real" value of the slope can differ, introducing errors on the zodi level resulting from this model. Determining the slope value for each system is, of course, a preferable approach, but requires individual modeling, which is still a work in progress. The second assumption, on the inner and outer radius, could also lead to such errors, even thought at a smaller scale. With these considerations, the zodi level option should be used as a first estimate of the amount of dust in the habitable zone of the system, which should be refined with a more detailed individual analysis of the system.

4.2 Proof of concept with Vega

We have shown in the previous chapter that the spatial PCA background subtraction removes a significant part of the bias in the data, and thus has the potential to reduce just as significantly the uncertainty of the measurements. In particular, PCA background subtraction prevents offset in the photometry of certain groups, which can lead to a scattering of the measurements on individual groups, and thus increase the error bars. During the analysis of the HOSTS survey and in particular of its limita-

Models	$\frac{\tau}{10^{-5}}$	τ slope	R_{in}	R_{out}	i°	PA°	Pros	Cons
Free	✓	✓	✓	✓	✓	✓	No assumption, unbiased	Time-consuming, lots of walkers, slow convergence.
Pancake	✓	✓	X	X	✓	✓	Extended disk and realistic τ slope; Useful for fitting i and PA	No information on the location and extent of the disk.
Thin ring	✓	X	✓	X	✓	✓	Determines where most of the dust is located.	Cannot probe the dust whole extension nor its radial distribution behavior
Zodi	✓	X	X	X	✓	✓	Scales dust amount wrt solar system HZ dust	Unrealistic if τ slope far from the solar system value

Table 4.1: Comparison of the four different models available with respect to the parameters they fit: optical depth $\frac{\tau}{10^{-5}}$, the slope of the dust distribution τ slope, the inner and outer radii R_{in} and R_{out}, the inclination i° and the position angle PA°. For each model, the advantages and limitation are briefly summarized.

tions, it has been shown that this scatter usually dominates the final error bars. The reduction of this scatter should thus directly translate into a similar reduction of the final error bar on the calibrated null. The improved error bar will in turn allow for a more precise determination of the amount of exozodiacal dust in the system, but also a better modeling of its radial distribution. In particular, this will help removing degeneracies between different possible models. In this section, we compare the results obtained for the different models (thin ring, pancake-like disk, free model) with the current error bars obtained with the mean background subtraction and modified error bars for which we divided the real error bars by 2 or 3. It is important to note that the reduction of those error bars is not physical. Indeed, a real reduction of the error bars would also modify the values themselves. Thus, the models presented in this section are not physical and only intend to show the beneficial effects on the modeling that the reduction of the error bars could have, in particular to lift degeneracies. We will refer to those three cases as, respectively, the normal, reduce2 and reduce3 cases in the following. We applied this procedure to the Vega data, obtained during the nights UT 2017 April 6 and UT 2018 March 28 as those datasets are well constrained and understood.

Let us start with the thin-ring model, described in Section 4.1.4 (§3). In this case, we assume that the orientation of the system is 0, and not fitted since the orientation from the disk of Vega is well constrained by previous observations, and known to be

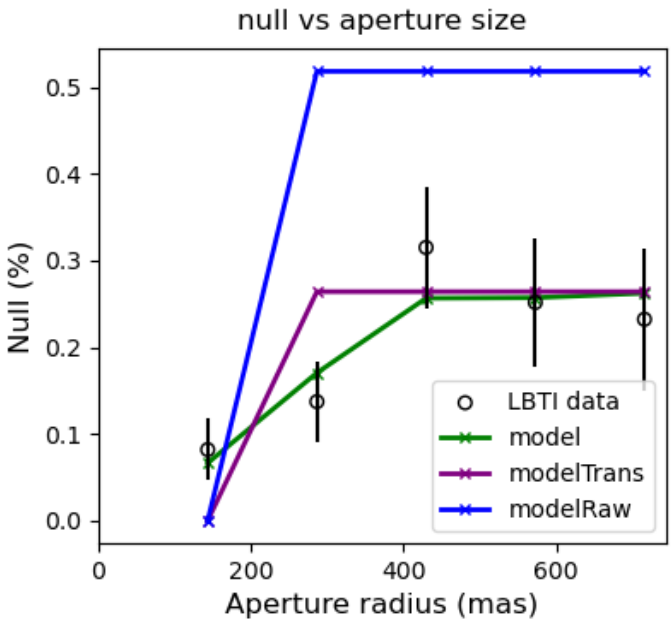

Figure 4.1: Calibrated null measurements in percent for Vega, obtained for the aperture of 8,16,24,32 and 40 pixels in radius (respectively 144, 288, 432, 576 and 720 mas) and mean-background-subtracted data. The raw model for a thin ring (blue curve), the transformed model (magenta curve) are plotted alongside the best fit model (green curve) obtained for those data.

face-on. All other parameters usually fitted with the thin-ring model are normally fitted. In Figure 4.1 we show the null measurements with fiducial error bars for the 5 apertures of 8, 16, 24, 32, and 40 pixels in radius (respectively 144, 288, 432, 576 and 720 mas), along with the best-fit thin-ring case model. We are in particular interested in how well the green curve fits into the five measurements and their respective error bars.

Figure 4.1 shows that the model (green curve) is consistent with all five points. However, it is clear that if the error bars are significantly reduced, this model will struggle to fit all the points.

In Figure 4.2, we show the corner plot obtained for the thin ring model (corresponding to the green curve in Figure 4.1) for the normal case of error bars. In particular, we display the results of the fit for the $\tau/10^{-5}$ and the inner and outer radii, since the ratio between inner and outer radii, the slope, the orientation and the position angle are respectively set to 0.1, 0, 0 and 0.

For all three fitted parameters, we obtain relatively strong constraints with small error bars and Gaussian-like distributions. The χ^2 obtained for this model is also satisfactory with a mean χ^2 of 2.66 and a reduced χ^2 of 0.88. Despite the model passing very close to the limits of the error bars for two of the five points, this model thus appears to be a good fit to the data. If this model is indeed a good representation of our system, when using the reduce2 or reduce3 error bars, the model should adapt the value of $\tau/10^{-5}$ and of the inner and outer radii, but most importantly reach a similar

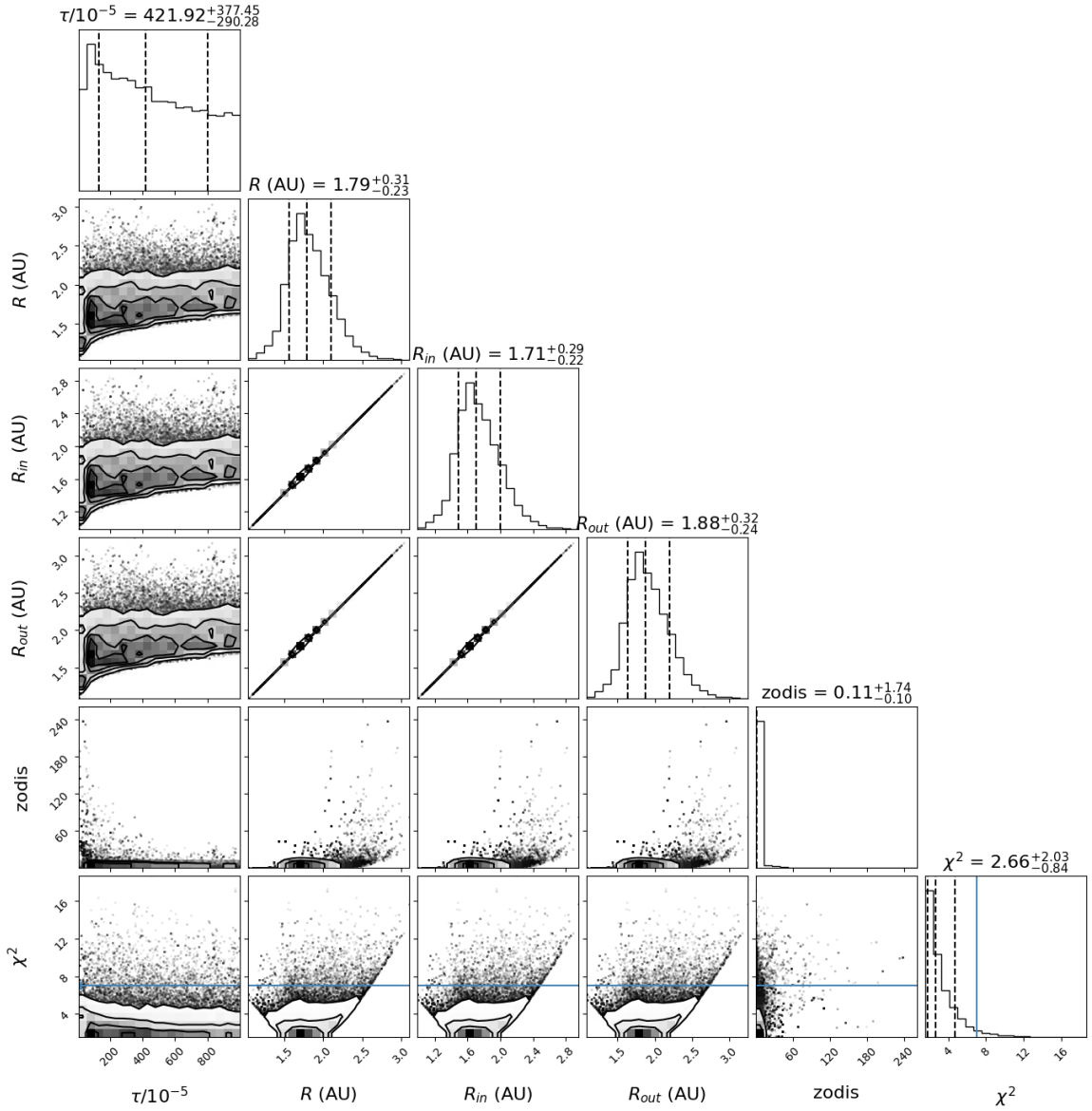

Figure 4.2: Posterior distribution obtained by MCMC for the thin ring model in the normal case for the Vega data, where only the $\tau/10^{-5}$ and the inner and outer radii are fitted. The inner and outer radii are linked by a ratio of 0.1 which is set at the start of the modeling. For each parameter, the corner plot shows the median distribution (50th percentile), the uncertainty toward lower values (subtracted from the median distribution this value gives the 16th percentile), and the uncertainty toward higher values (subtracted from the median distribution this value gives the 84th percentile). The blue lines represents the first guess values entered at the start of the MCMC procedure.

or better χ^2.

We thus re-run the fitting procedure with the thin-ring model, this time using the reduce2 error bars. The values obtained in the corner plot were rather similar and well within the error bars for the $\tau/10^{-5}$ and the inner and outer radii, albeit the error bars

	Normal		reduce2		reduce3	
	value	error bars	value	error bars	value	error bars
$\tau/10^{-5}$	421.92	+377.45/-290.28	4.36	+1.00/-0.65	4.52	+127,03/-0.62
R (AU)	1.79	+0.31/-0.23	1.72	+0.17/-0.17	1.77	+5.66/-0.13
R_{in} (AU)	1.71	+0.29/-0.22	1.64	+0.17/-0.16	1.69	+5.39/-0.13
R_{out} (AU)	1.88	+0.32/-0.24	1.80	+0.18/-0.17	1.85	+5.93/-0.14
χ^2	2.66	+2.03/-0.84	7.56	+2.28/-1.12	15.82	+307.03/-1.54
reduced χ^2	0.88	+0.67/-0.28	2.52	+0.76/-0.37	5.27	+102.34/-0.51

Table 4.2: Summary of the best-fit values obtained for all the parameters fitted in the context of the thin ring model, along with their errors bars. The case with the real errors bars on the null excess is compared to the case of errors bars artifically reduced by a factor 2 and 3.

returned were smaller. In particular, for the inner and outer radius best-fit values, the error bars were also reduced by about a factor 2. The most notable difference is the χ^2, which more than doubles compared to the case with fiducial error bars.

If we instead use the reduce3 error bars, the situation starts to change quite significantly. The best-fit values themselves are similar; however, the upper limit for their error bars becomes 50 to 100 times larger. In Figure 4.3, we show the corner plot obtained for the thin ring model fit to the data with reduce3 error bars. The increase in upper limits can be explained by the two distinct populations which appear with the reduce3 error bars. Indeed, we find an inner radius R_{in} at 1.69, which is the most predominant hence why the model retains this value, but also a second mean radius around 7. The same behavior is observed for the outer radii. A similar behavior can also be observed for $\tau/10^{-5}$. Indeed, the predominant value found is the one retained by the model, 4.52, but a second much smaller maximum can be found around 150. This second population poses a problem for the thin-ring model, as it is limited to one component and cannot, obviously, fit the two populations. However, it is important to remember for this case, that the data are unphysical. Indeed, in a real case, we would not observe a diminution of the flux with the increasing size of the aperture, and no physical model could describe this particular behavior.

We summarize all the results in Table 4.2, which shows that with the reduction of the error bars in all the values fitted by the model, the cases reduce2 and reduce3 result in a higher χ^2. It is possible to estimate how much or less likely a model is with respect to another by using the following expression:

$$\mathcal{L} = e^{\frac{\Delta\chi^2}{2}} \quad \text{with} \quad \Delta\chi^2 = \chi_2^2 - \chi_1^2 \qquad , \tag{4.9}$$

with $\mathcal{L}$ the factor by which the second model is more likely than the first and χ_1^2 and χ_2^2 the respective χ^2 of the first and second model which are compared. In our case, we consider the first model to be the normal case and the second either reduce2 or reduce3. We then obtain, respectively, $\mathcal{L}_{2-1} = 6.16$ and $\mathcal{L}_{3-1} = 17.54$. The model of thin rings

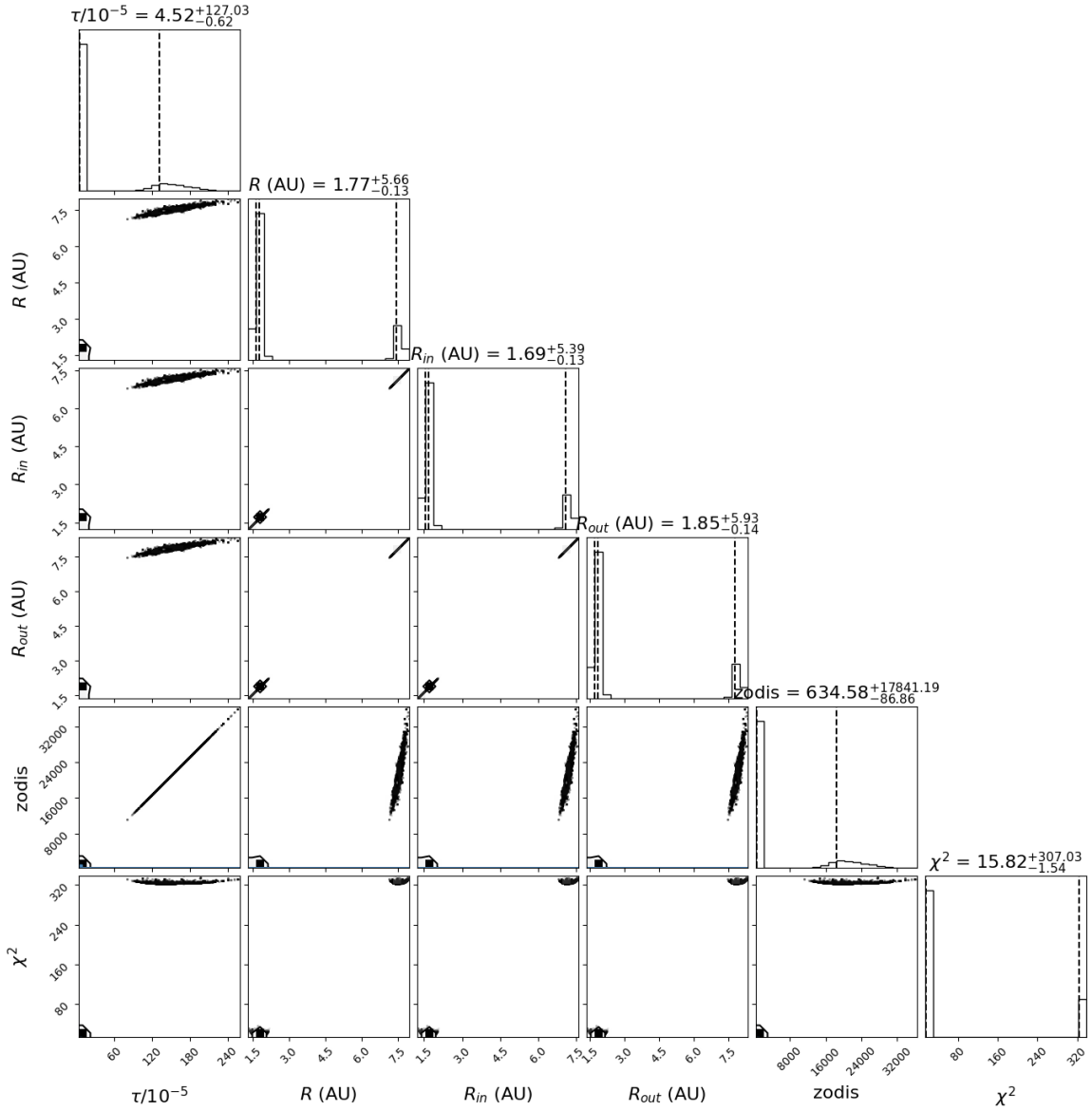

Figure 4.3: Posterior distribution obtained by MCMC for the thin ring model in the reduce3 case for the Vega data, where only the $\tau/10^{-5}$ and the inner and outer radii are fitted. The inner and outer radii are linked by a ration of 0.1 which is set at the start of the modeling. For each parameter, the corner plot shows the median distribution (50th percentile), the uncertainty toward lower values (subtracted from the median distribution this value gives the 16th percentile), and the uncertainty toward higher values (subtracted from the median distribution this value gives the 84th percentile). The blue lines represents the first guess values entered at the start of the MCMC procedure.

thus becomes 6 times less likely when the error bars are divided by 2, and 17 times less likely when divided by 3. If we assume that the reduction of the error bars is real and disregard the unphysicality of the data, in the context of our proof of concept, the more precise the measurements, the less the thin ring models appear to represent well our

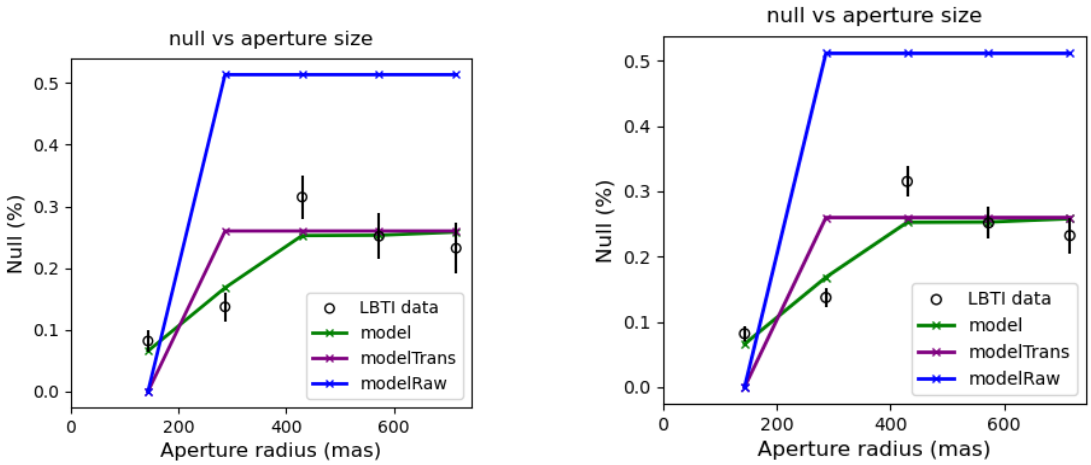

Figure 4.4: Calibrated null measurements in percent for Vega, obtained for the aperture of 8,16,24,32 and 40 pixels (respectively 144, 288, 432, 576 and 720 mas) in radius and mean-background-subtracted data. The raw model for a thin ring (blue curve), the transformed model (magenta curve) are plotted alongside the best fit model (green curve) obtained for those data. For the errors bars in the reduce2 case (left) and reduce3 (right).

system. If we now compare how the model fits into the measurements for each aperture, such as what is shown in Figure 4.1, we observe a similar problem. In Figure 4.4, we present the same plots for the reduce2 and reduce3 cases.

The left panel of Figure 4.4 shows, in the reduce2 case, that the model does not go through the measurements in the apertures of 16 and 24 pixels in radius (respectively 288 and 432 mas) anymore. This behavior is even more visible on the right panel for the reduce3 case. The thin ring model thus failed to fit those points with reduced error bars. If we assume that those measurements are indeed correct with the reduction of the error bars, twice or three times smaller error bars could lift the degeneracies in whether the thin-ring model is a good representation of this system. Moreover, in the case of reduce3, we can see that in addition, it would be possible to distinguish between different populations, and to identify whether the model needs to be composed of several components, or to include gaps.

We proceed to the same comparison with the pancake-like disk model, described in section 4.1.4 § 2. Similarly to the thin-ring case, the orientation and the position angle are set to 0, as previous observations have established that the disk of Vega is face-on. All the other parameters usually fitted by the pancake-like disk model are let free. In Figure 4.5, we show how well a pancake-like disk model fits the normal case data.

It is already clear in Figure 4.5 that the pancake-like disk model is not as good a fit as the thin-ring model. Indeed, the pancake-like disk model does not fit the measurement within 1 σ in the aperture of 24 pixels (432 mas) in radius, whereas the thin-ring model does. In addition, the model passes at the limit of the 1 σ measurement in the aperture

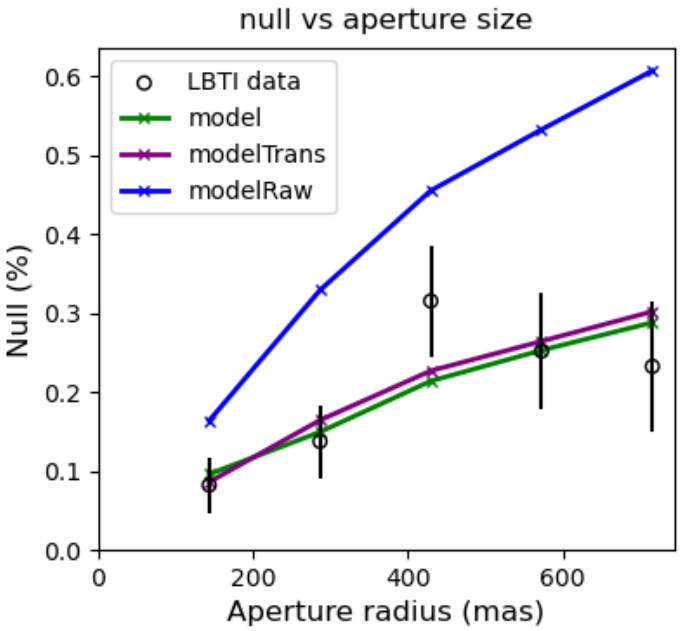

Figure 4.5: Calibrated null measurements in percent for Vega, obtained for the aperture of 8,16,24,32 and 40 pixels (respectively 144, 288, 432, 576 and 720 mas) in radius and mean-background-subtracted data. The raw model for a pancake-like disk(blue curve), the transformed model (magenta curve) are plotted alongside the best fit model (green curve) obtained for those data.

of 40 pixels (720 mas) in radius when the thin-ring model fit is more centered within the 1σ error bars. The reduction of the error bars for the pancake-like model will thus most likely prevent the model from passing through the measurement of the largest aperture. In Figure 4.6, we present the corner plot obtained with the pancake-like disk model in the normal case. In this case, only the τ slope and $\tau/10^{-5}$ are fitted.

It is interesting to note that $\tau/10^{-5}$ differs significantly from the value previously obtained with the thin ring model. The τ slope value, on the other hand, is consistent with the fixed 0 value of the previous model. As expected, the χ^2 value for this model is also higher than with the thin-ring model. If we use Equation 4.2, we can determine that the pancake-like model is 1.6 times less likely to correctly represent our system than the thin ring model. It is nevertheless interesting to determine how this difference will evolve with smaller error bars.

We thus re-run the fitting procedure with the pancake-like disk model on the reduce2 error bars and obtained very similar values for both parameters. As in the thin-ring model case, the error bars on those parameters were also reduced when using the reduce2 error bars. Once again, the main difference between these two models resides in their respective χ^2, which increase from 4.18 in the normal case to 12.42 in the reduce2 case. We summarize the results of both models in Table 4.3.

Using Equation 4.2, the pancake-like disk model became 11.2 less likely with the reduce2 case. Furthermore, if we compare the thin-ring model and the pancake-like

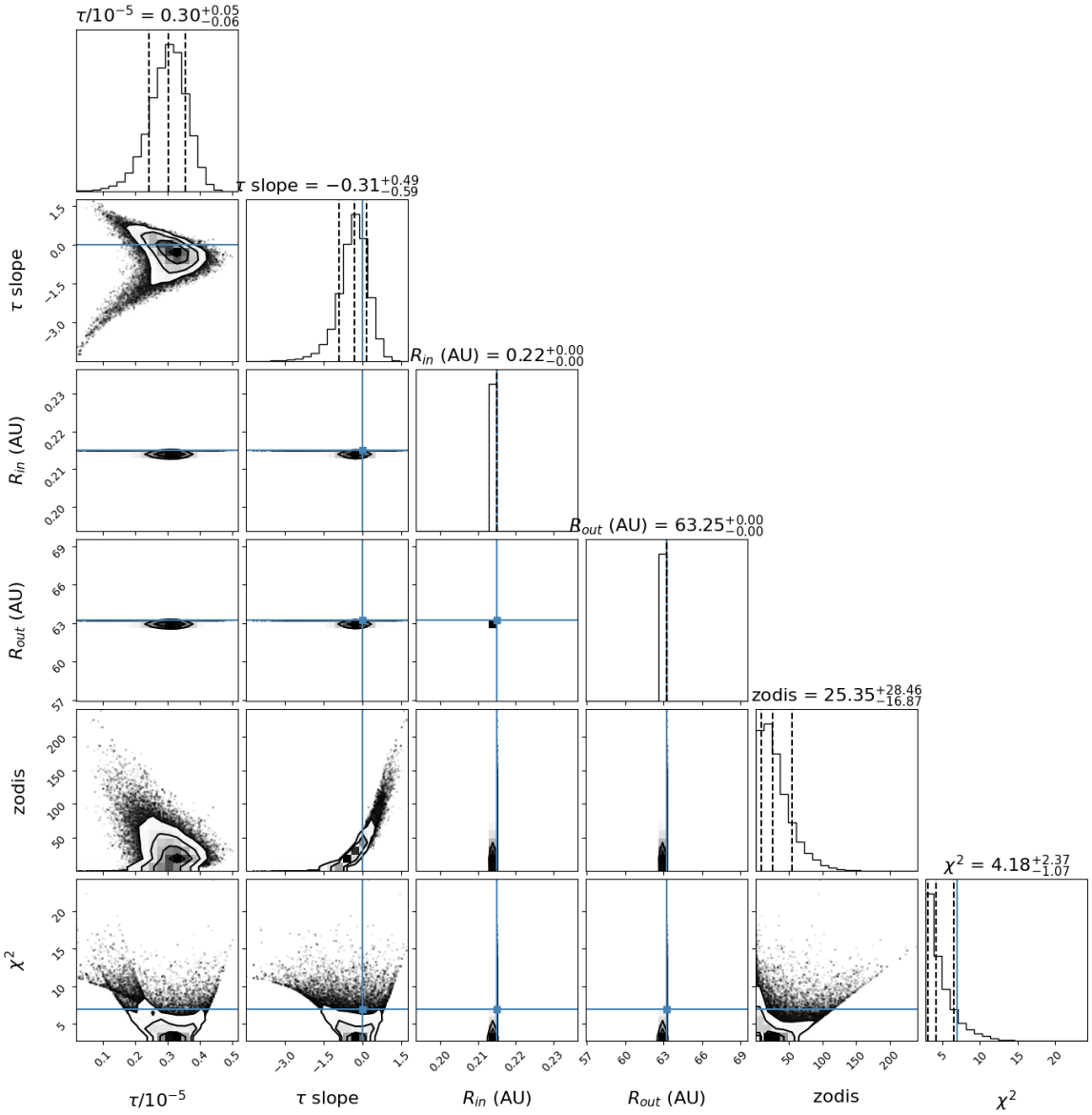

Figure 4.6: Posterior distribution obtained by MCMC for the pancake-like disk model in the normal case for the Vega data, where only the optical depth and τ slope are fitted. The inner radius is set at the sublimation radius of silicates, and the outer radius to an empirically large value. For each parameter, the corner plot shows the median distribution (50th percentile), the uncertainty toward lower values (subtracted from the median distribution this value gives the 16th percentile), and the uncertainty toward higher values (subtracted from the median distribution this value gives the 84th percentile). The blue lines represents the first guess values entered at the start of the MCMC procedure.

disk model in the reduce2 case, the last model is 6.6 less likely to properly describe the system. Considering the relatively similar χ^2 in the normal case, and the small difference in likelihood, this situation could have been considered degenerate. However, when comparing the models in the reduce2 case, this degeneracy is lifted as it became

	Normal		reduce2	
	value	error bars	value	error bars
$\tau/10^{-5}$	0.30	+0.05/-0.06	0.31	+0.03/-0.03
τ slope	-0.31	+0.49/-0.59	-0.22	+0.24/-0.25
χ^2	4.18	+2.37/-1.07	12.42	+2.33/-1.03
reduced χ^2	2.09	+1.18/-0.53	6.21	+1.16/-0.51

Table 4.3: Summary of the best-fit values obtained for all the parameters fitted in the context of the pancake-like disk model, along with their errors bars. The case with the real errors bars on the null excess is compared to the case of errors bars artifically reduced by a factor 2.

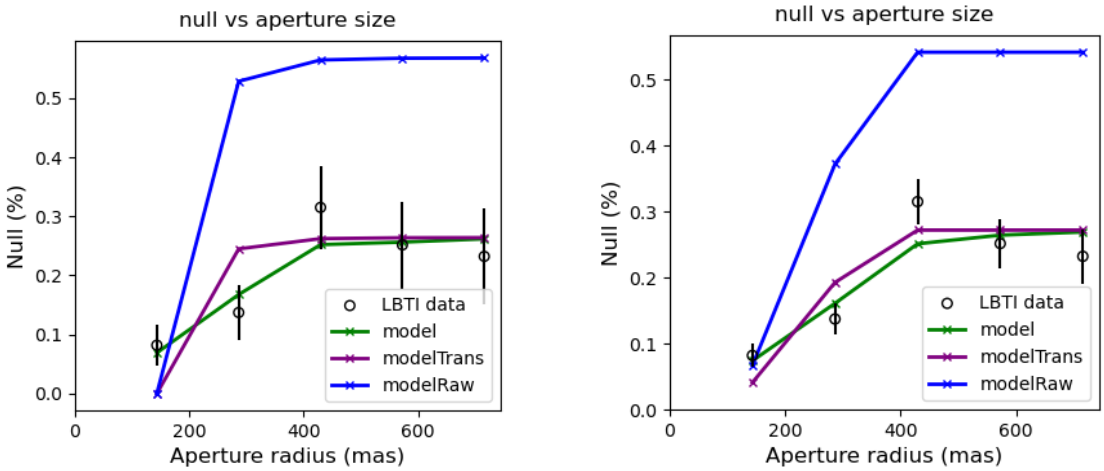

Figure 4.7: Calibrated null measurements in percent for Vega, obtained for the aperture of 8,16,24,32 and 40 pixels (respectively 144, 288, 432, 576 and 720 mas) in radius and mean-background-subtracted data. The raw model for the free model (blue curve), the transformed model (magenta curve) are plotted alongside the best fit model (green curve) obtained for those data. For the errors bars in the normal case (left) and reduce2 (right).

clear that the thin-ring model describes the system much more appropriately than the pancake-like disk model. Just as in the thin-ring case, the data of the reduced2 case are unphysical, and the flux decrease after aperture 24 cannot be properly described by any physical model. Nonetheless, the conclusion on the degeneracies remains valid.

Finally, we made the same comparison, with the free model, described in Section 4.1.4 § 5. The orientation and the position angle are once again set to 0 since the disk of Vega is known to be face-on. All other parameters are fitted. In Figure 4.7, which is equivalent to Figure 4.1 in the case of the free model, for the normal error bars.

The left panel of Figure 4.7 shows, for the normal case, that the situation is pretty similar to the situation in Figure 4.1. Indeed, in both cases, the models pass close to the limits of the error bars of the measurements in the apertures of 16 and 24 pixels (432 mas) in radius. With the reduce2 error bars, in the right panel, the model fails to fit

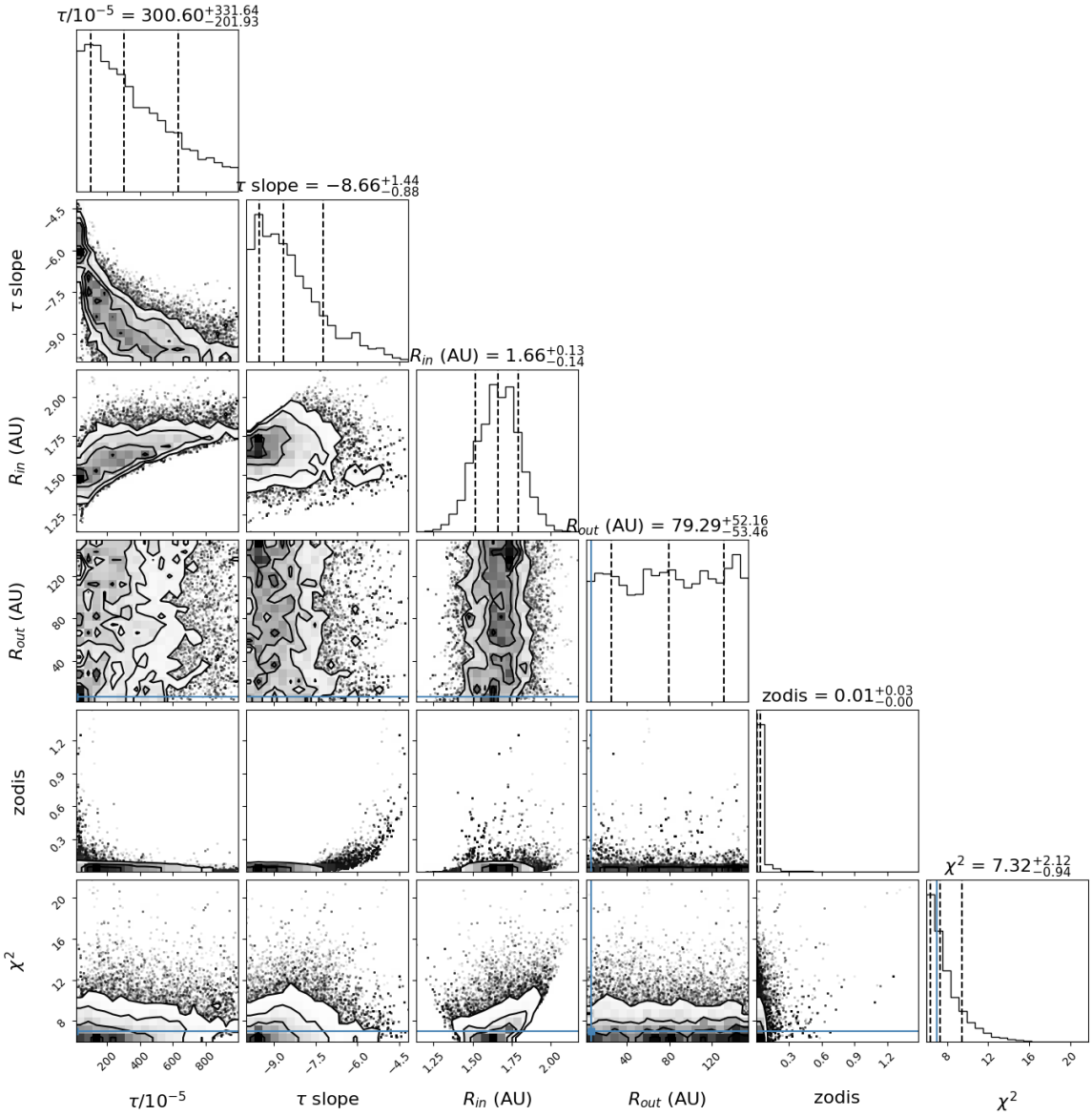

Figure 4.8: Posterior distribution obtained by MCMC for the free model in the normal case for the Vega data. The optical depth, the inner and outer radii and the τ slope are fitted. For each parameter, the corner plot shows the median distribution (50th percentile), the uncertainty toward lower values (subtracted from the median distribution this value gives the 16th percentile), and the uncertainty toward higher values (subtracted from the median distribution this value gives the 84th percentile). The blue lines represents the first guess values entered at the start of the MCMC procedure.

the measurement in the aperture of 24 pixels (432 mas)in radius but on contrary to the thin-ring model, still succeeds in fitting the measurement in the aperture of 16 pixels (288 mas) in radius. It thus appears that the free model describes the system slightly better than the thin ring model. In Figure 4.8 we present the corner plot obtained with the free model in the normal case.

The first and main difference visible in Figure 4.8 compared to Figure 4.2 is that the error bars are generally much larger. This comes from the fact that the free model has more parameters to fit than the thin-ring model. Indeed, in this case R_{in} and R_{out} are fitted separately, and the τ slope is also fitted. The values are also significantly different between the two models, except for the inner radius, for which both models found very close values well within their error bars. On the other hand, $\tau/10^{-5}$ is much higher with the free model, even taking into account the error bars. The τ slope became extremely negative with the free model, and its error bars do not account for the difference with the 0 value of the thin ring model, or the 0.3 value of the pancake-like model. The mean χ^2 of this model is 7.32 and the reduced χ^2 is 1.83.

However, the τ slope value is highly negative, and would suggest a very steep decrease in the dust amount with the distance. If the disk was really thin, such a slope could make sense, indicating a sharp outer edge. However, the disk is rather extended, and the distribution of the outer edge is rather inconsistent with a sharp edge, which would have led to a strong constraint on the outer edge value. Thus, in order to maintain a non-negative dust amount over the whole disk extension with such a steep decrease, the amount of dust close to the inner edge would be extreme. This amount of dust is in itself likely to be unphysical, but is also inconsistent with the data. We thus consider this model to be unphysical.

In this section we have shown that the possibilities of the current modeling tool would fail to properly describe the reduce2 and even more the reduce3 situations if those were real. In the context of this proof of concept,in which we assume the data reduce2 and reduce3 to be real data, we show that the diminution of the error bars by a factor of 2 to 3 could not only help lift degeneracies between the various models, but also make us reach the limits of the current modeling tool. Indeed, the current modeling tool assumes that the disk is optically thin, that it contains no gaps, and that it is composed of a single component. With the current error bars obtained with the mean background subtraction, those assumptions still allow for providing a satisfactory description of the systems. On the other hand, with the improved error bars, it became clear that it would become possible to differentiate between more complex scenarios including gaps, multi-component and non-optically-thin disks.

However, it is important to remember that in the reduce2 and reduce3 cases, the error bars have been artificially reduced from the final calibrated null measurements. In a real case, the uncertainty will be reduced on individual photometric measurements, thus translating into a different serie of measurements onto which the NSC will fit synthetic null measurements. This difference can thus change not only the width of the error bars on the calibrated null measurement but also their values. In fact, in this section we assume that the values of the calibrated null measurements did not change when reducing the error bars. Their intrinsic values are not important for this proof of concept, since only the abitility of the MCMC to fit the model to the data with

reduced error bars is considered. In the following section, we apply PCA background subtraction to the 110 Her data, and consider the real calibrated null measurements with PCA background subtraction.

4.3 Application to Nulling measurements

In order to determine the presence of an exozodi around a star, the HOSTS used nulling interferometry. If the star is at the null, in a perfect case, all remaining excess comes from circumstellar emissions. Of course, in a real case, errors add up and make this determination much more challenging. To detect exozodis, the HOSTS survey used the NSC (Defrère *et al.,* 2016), which measures the null excesses, and takes into account the various sources of errors. Nevertheless, the errors and, in particular, the background bias, are still a major concern for those measurements. In this section, we present how we adapted our method to the particular configuration needed for re-injection into the nulling pipeline, how this method was combined with the pipeline and how we modified the pipeline for an optimal integration of the PCA background subtraction method. Additionally, we determined whether PCA background subtraction is also beneficial for nulling measurements and by what factors.

4.3.1 Background subtraction of the off-sources images

One of the main differences with High Contrast Imaging and Aperture Photometry is that the background quadrant needs to be subtracted too since they will be used by the pipeline for calibration purposes. For the NSC approach to work, a representative background sequence is required. The pipeline computes the flux in an aperture, identical to the one measuring the flux of the nulled star, but in the background quadrant. This background aperture is placed at the position where the star would be if present in this quadrant. In order to obtain the highest possible data quality, the difference between the variations of the background in this aperture and in the nulling aperture must be as similar as possible. Thus, in order to obtain as little difference between both backgrounds, the background must be subtracted in the same way. Unfortunately, this is not exactly possible. To highlight this limitation, Figure 4.9 presents a schematic of the sorting of the groups, with respect to the star position.

In Figure 4.9, we can distinguish three cases: (1) the sequence starts with the star in the quadrant, and has only one group onto which to build the background library, which comes later in the observation, (2) the sequence ends with the star in the quadrant, and has only one group onto which build the background library, which comes earlier in the observation, (3) the group with the star is surrounded by two off-source groups onto which the background library can be built. Now, what is really important is that the background group should be subtracted in a way as similar as possible with the on-source group which it will calibrate. The first step is to perform a similar pre-subtraction. For

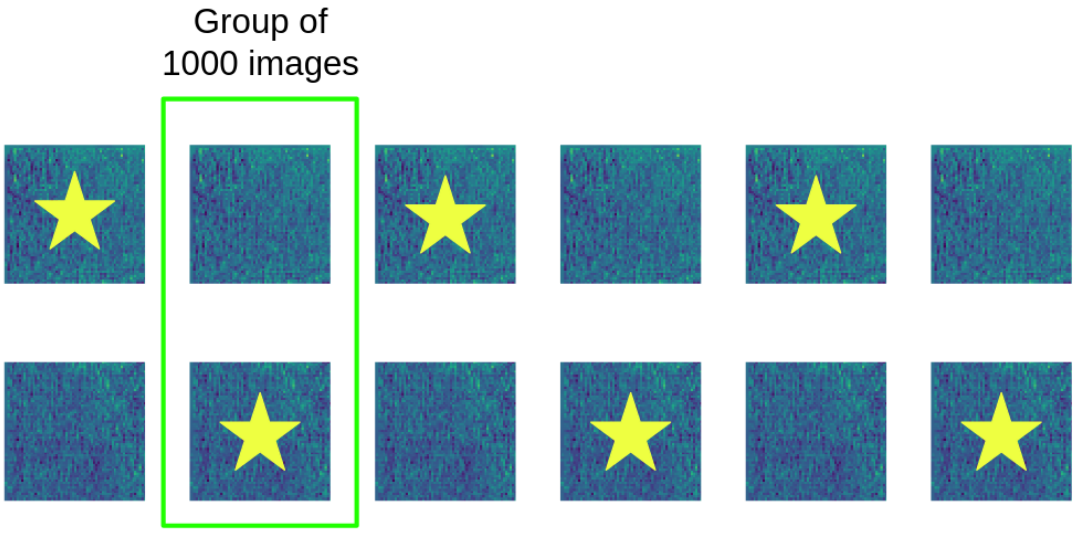

Figure 4.9: Schematic of the image quadrant sorting. The top and bottom rows corresponds to the top and bottom quadrants of the original images. Each image in this schematic represents a group of 1000 frames. The star position alternates between the top and bottom quadrants. The on-source quadrant contains the nulled star.

cases (1) and (2), the background group is used to build the correction for pre-subtraction and is subtracted from both the on-source and the off-source groups. For case (3) the two background groups are used to build the pre-subtraction correction. If the sequence starts with the star, only the next background group will be subtracted with the same correction. In contrast, if the sequence stars with a background, only the previous background group will be subtracted with the same correction.

The second step is to perform PCA background subtraction in a way as similar as possible. Figure 4.9 shows that to correct a group of on-source images, the adjacent groups are off-source groups. We can thus build the principal components for the correction on these groups. On contrary, we cannot use the two adjacent groups to correct a background group, since the star is present in those groups. If we were to build the principal components on the those groups, they would be dominated by the star, and a significant number of them would take only the star into account. Let us take the example of the group of images framed in green in Figure 4.9. The top parts of the images are off-sources, and cannot be corrected with the adjacent groups, since those contain the star. The bottom parts of the images are off-source and can be corrected with the two adjacent groups, since those are off-source. Since we want the top part to be background subtracted in a way as similar as possible to the bottom part, we thus chose to use the same library. To correct the top part, we thus use the two adjacent groups of the bottom part. This solution is not perfect, since there still is a difference in

the way we subtract the background for off-source or on-source cases, but it minimizes the differences as much as possible.

4.3.2 Integration into the nulling pipeline

In order to implement PCA background subtraction for the nulling measurements, we had to modify the HOSTS pipeline. To perform PCA background subtraction, we directly used the raw images. Once background subtraction is completed, we replaced the corrected quadrants directly in the level 1 files provided by the pipeline without changing the headers. They also contain information about the star position. The quadrant thus needs to be replaced exactly at the correct position.

The first modification we had to do on the method was the background subtraction of off-source images as described in the previous subsection. This allowed us to strongly reduce the difference between the background variation of the on-source quadrants and the background variation of the off-source quadrants. Despite this first modification, PCA background subtraction did not provide results as good as expected when running the nulling pipeline.

The second modification, was to remove the background annulus from the calibration process. Indeed, the PCA background subtraction method does not make use of these background annuli, since it is able to reconstruct the background behind the star. In fact, those background annuli introduce numerous errors and uncertainties, and removing them can be very beneficial. In order to remove them, the variation between the on-source quadrants and the corresponding off-source quadrant should be small enough. This is the case when using the PCA background subtraction as shown in Chapter 3. After this second step, we obtained results similar to those obtained with the mean background subtraction for the aperture of 8 pixels in radius. On the other hand, for larger apertures, the results were significantly degraded.

Upon investigation of the reason for such degradation, we found that some background photometry contained important steps or spikes. Those strong variations can already be responsible for the degradation of several measurements. We also noticed some significant differences between the background annulus of the on-source quadrant and that of the off-source quadrant, which can also explain the degradation of those results. In the case of a mean background subtraction, these variations in the photometry are not visible because of a lower precision. We found that most of these structures and differences were due to open-loop frames, which were kept for the background flux computation. We therefore had to introduce a third modification to remove those open-loop frames from the background measurements. In addition, since those frames were introducing unrelated photometric variation, they also had to be removed from the background subtraction, for both mean and PCA background subtraction. This modification allowed for improvement for both mean and PCA background subtraction, and is now implemented in the default pipeline as well. After this modification, PCA

		Calibrated Null (%)		
Night	Aperture (pix)	HOSTS	Mean	PCA
170408	8	0.068 ± 0.097	0.113 ± 0.114	-0.018 ± 0.089
170408	13	0.087 ± 0.204	0.179 ± 0.124	-0.038 ± 0.127
170408	24	0.561 ± 0.156	0.648 ± 0.221	0.095 ± 0.299

Table 4.4: Comparison of null and its errors for aperture sizes of 8, 13 and 24 pixels in radius. We compare the values obtained for individual observing night and the combined values. The HOSTS column refers to the results presented in Ertel *et al.* (2020a), the Mean column to a new reduction perform in 2024, the PCA column to the reduction perform in 2024 with PCA background subtracted data. The background annulus used for the HOSTS reduction was between 24 and 27 pixels, while the one used for the Mean reduction was between 33 and 35 pixels

started to perform much better, providing better results than mean for the smallest aperture and similar to mean for the intermediate ones. Despite those modifications, the larger apertures are still degraded with the PCA background subtraction, and more efforts on the integration to the pipeline would be needed.

4.3.3 Results on null measurements

In order to make a thorough comparison both between the mean and the PCA background subtraction, and with the previous results presented in Ertel *et al.* (2018) and Ertel *et al.* (2020a), we first run the reduction pipeline, with the same configuration and parameters for both methods. In particular, we used the same aperture sizes, with filled apertures, and the same background annulus. In Table 4.4, we present the comparison between the reduction of Ertel *et al.* (2020a), the new reduction with the mean background subtraction, and the new reduction with PCA background subtraction.

Table 4.4 shows that the three reductions produce consistent results for the apertures of 8 and 13 pixels in radius. For the 24-pixel aperture, the HOSTS and Mean reduction are consistent, but not the PCA reduction. For such a large aperture, the bias in the data becomes more significant. That random individual measurements of different methods obtained slightly inconsistent results is not too surprising. Nevertheless, as discussed in the following, the current performances of PCA background subtraction in the nulling pipeline, for the large apertures is far from optimal, and the values from the HOSTS and Mean background subtraction are hence more trustworthy for this aperture.

With PCA background subtraction, our purpose is to reduce the uncertainty of the null measurements. This global uncertainty is dominated by the scatter of the null measurements of individual OBs, which is directly linked to the bias remaining in the data after the background subtraction, rather than the uncertainty of those individual measurements, which is linked to the RMS of the photometry in those OBs. This has been shown in Defrère *et al.,* 2016. The main purpose of PCA background subtraction is thus to reduce this scatter. We have presented in Chapter 3 that PCA

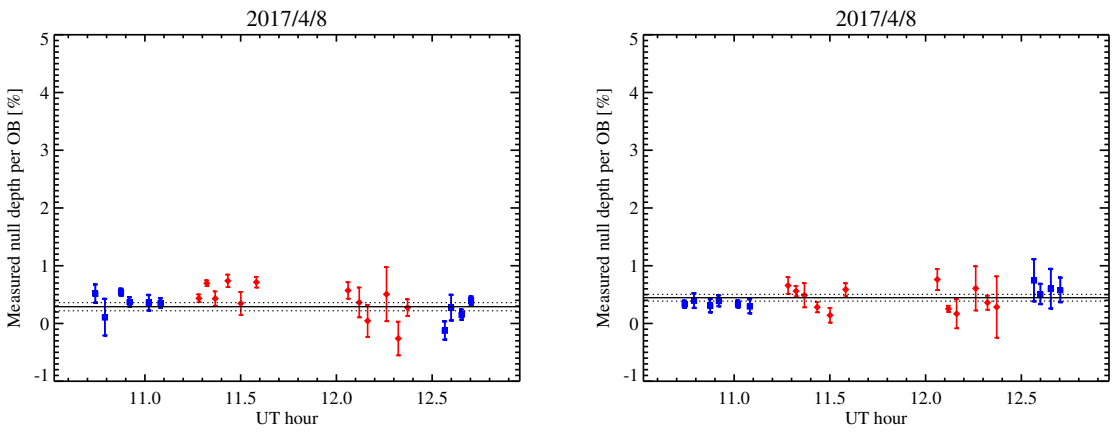

Figure 4.10: Measured null depth for an aperture of 8 pixels in radius, for each OB for the calibrators (blue) and the science target (red) for the Mean-background-subtracted data (left panel) and the PCA-background-subtracted data (right panel). The black line represent the floor level of the measured null based on the two calibrators measurements. The dashed black lines represents the 1σ uncertainty of the floor level.

background subtraction was able to remove a significant part of this bias but had a very limited impact on the RMS. We show the null measurements for both mean and PCA background subtraction, for the individual OBs of the 2017 observation of 110 Her, in Figure 4.10 for an aperture of 8 pixels in radius.

The left panel of Figure 4.10, shows that for the first calibrator (first six blue measurements), most of the points are consistent with each other. In contrast, of the first pointing of the science target (first 6 red measurements), one-half of the points are offset compared with the other half, and their error bars do not overlap. The second pointing of the science target (last 6 red measurements) has a higher uncertainty on individual measurement, thus reducing the inconsistency. Nonetheless, two OBs (the first and the fifth) are still inducing some inconsistency. The second calibrator (last 4 blue measurements) is also mostly inconsistent, and we can observe a tendency to higher measured null depth from the first to the last of those four measurements. The inconsistencies between the measurements, as well as the variation for the second calibrator, is what dominates the uncertainty of the null measurement per pointing.

By comparison, the right panel of Figure 4.10, shows that the measurements for the first calibrator are all consistent and much less scattered. Similarly, the second calibrator does not present the increasing tendency anymore, and all the measurements are consistent with each other. The individual error bars tend to be larger for the second calibrator with PCA background subtraction, but the results are more reliable since all their error bars largely overlap. Despite large error bars, the situation also seems to improve for the second pointing of the science target, since when using PCA background subtraction only one measurement appears as an outliers, for which the errors bars does not overlap all five other measurements. For the first pointing, the science target seems to be only slightly improved when using PCA background subtraction. Indeed, the

offset in between the two halves of the points disappear but we now observe a decreasing tendency, and the error bars of the measurement do not all overlap.

In general, PCA background subtraction still performs better than mean background subtraction for the aperture of 8 pixels in radius, in particular, by reducing the scattering and improving the consistency of the individual measurement of the two calibrators. With these improvements, the overall uncertainty of the null measurement is reduced by approximately 22%. It is important to note that the comparison is made between two random realizations of the reduction for both mean and PCA background subtraction, and that the exact improvement factor could be either slightly higher or lower. In order to further improve the error bars of the global measurement, PCA background subtraction should be able to further reduce the scatter of the science target measurements. Additionally, the floor levels of the first and second calibrators are slightly different, thus limiting the accuracy.

In Table 4.5, we present measurements shown in Figure 4.10, with the value of the null, the uncertainty due to the error on the background floor, the uncertainty due to the error on the NSC fit, and the total uncertainty, for a more quantitative comparison of the two background subtraction methods.

A first important result, highlighted by Table 4.5 is that the scatter of the null measurement of the individual OBs for a same target is reduced when using PCA rather than mean background subtraction. In fact, the standard deviation of the null measurement for the two calibrators (CAL1 and CAL2) are respectively reduced by 4 and 2.3. This reduction is weaker for the second pointing of the science target (SCI2) with a factor of only 1.3. The first pointing of the science target (SCI1), on the other hand suffer from the decreasing tendency, already highlighted by Figure 4.10, and the standard deviation is slightly degraded by a factor 1.15. This confirm the capacity of PCA background subtraction to effectively remove some background bias, and to reduce the scatter of individual measurements.

It is also interesting to see, that with PCA background subtraction, the uncertainty due to the error on the background floor (2) is also generally slightly lower in the case of the PCA background subtraction. In addition, in the few cases where this is not the case, the mean and PCA background subtraction provide the same results. Thus, it is clear that PCA background subtraction does not degrade the background floor estimation, and on contrary, tends to improve it. This result demonstrate that the removal of the background annulus does not degrade the background floor estimation, but, with PCA background subtraction, rather improves it, which is coherent with the results obtained in Chapter 3 in aperture photometry.

However, Table 4.5 also shows that the total uncertainty (3) is strongly dominated by the uncertainty due to the error on the NSC fit (2). On contrary, to (1), (2) does not seems to be significantly impacted by the PCA background subtraction as the uncertainties (2) are generally nor lower nor higher in between the two background

		Mean				PCA			
		Null (%)	Uncertainties (%)			Null (%)	Uncertainties (%)		
			(1)	(2)	(3)		(1)	(2)	(3)
CAL 1	OB1	0.52	0.02	0.16	0.16	0.34	0.02	0.06	0.06
	OB2	0.11	0.02	0.32	0.32	0.40	0.01	0.13	0.13
	OB3	0.55	0.02	0.06	0.06	0.31	0.02	0.11	0.11
	OB4	0.38	0.02	0.08	0.08	0.40	0.02	0.09	0.09
	OB5	0.36	0.02	0.13	0.13	0.34	0.01	0.06	0.06
	OB6	0.36	0.02	0.08	0.08	0.30	0.02	0.12	0.12
SCI 1	OB7	0.44	0.04	0.05	0.07	0.66	0.03	0.14	0.14
	OB8	0.70	0.04	0.03	0.05	0.56	0.03	0.08	0.08
	OB9	0.43	0.04	0.12	0.12	0.49	0.03	0.21	0.21
	OB10	0.74	0.05	0.10	0.11	0.28	0.04	0.08	0.09
	OB11	0.35	0.04	0.20	0.20	0.14	0.03	0.12	0.13
	OB12	0.72	0.05	0.08	0.09	0.59	0.03	0.10	0.11
SCI 2	OB13	0.57	0.05	0.13	0.14	0.76	0.03	0.18	0.18
	OB41	0.36	0.04	0.25	0.26	0.25	0.03	0.04	0.05
	OB15	0.04	0.04	0.28	0.28	0.17	0.03	0.25	0.25
	OB16	0.51	0.04	0.47	0.47	0.61	0.03	0.38	0.38
	OB17	0.26	0.04	0.29	0.29	0.36	0.03	0.12	0.12
	OB18	0.27	0.05	0.13	0.14	0.28	0.04	0.53	0.53
CAL 2	OB19	-0.12	0.02	0.16	0.16	0.75	0.02	0.36	0.37
	OB20	0.28	0.03	0.22	0.22	0.52	0.02	0.17	0.17
	OB21	0.16	0.02	0.08	0.09	0.61	0.02	0.34	0.34
	OB22	0.40	0.02	0.07	0.08	0.59	0.02	0.21	0.21

Table 4.5: Null value in percent along with the uncertainty due to the error on the background floor (1), the uncertainty due to the error on the NSC fit (2) and the total uncertainty (3), for both mean and PCA background subtraction, in an aperture of 8 pixels in radius for the data of 110 Her.

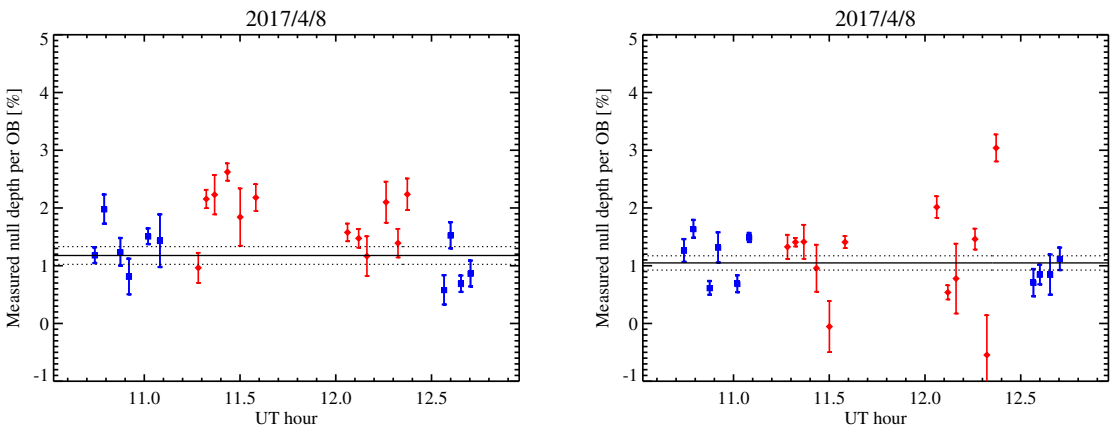

Figure 4.11: Measured null depth for an aperture of 24 pixels in radius, for each OB for the calibrators (blue) and the science target (red) for the Mean-background-subtracted data (left panel) and the PCA-background-subtracted data (right panel). The black line represent the floor level of the measured null based on the two calibrators measurements. The dashed black lines represents the 1σ uncertainty of the floor level.

subtraction methods.

The measurements obtained with an aperture of 8 pixels in radius are better when using PCA background subtraction, in particular when considering the calibrators. Nevertheless, as the aperture increases, PCA background subtraction tends to perform more poorly. As a comparison, we thus present the same measurements as in Figure 4.10, but for an aperture of 24 pixels in radius, in Figure 4.11.

In Figure 4.11, we observe a strong degradation for the aperture of 24 pixels in radius, for both methods. This is expected as the precision of the measurements decreases with the size of the aperture (the RMS increases), and the bias accumulates, thus reducing the accuracy of the measurements. Nonetheless, degradation is more important for PCA background subtraction.

As in the case of an aperture of 8 pixels in radius, the situation is worse for the science target measurements. The second calibrator remains, indeed, pretty consistent despite the increase in aperture size. However, the increasing tendency reappeared and, although not dominantly, this contributes to the degradation of the uncertainty. The first calibrator presents two points much lower than the others and completely inconsistent with them, which strongly increase the uncertainty of this calibrator. The first pointing of the science target seems rather consistent, except for one really low measurement. The second pointing of the science target is by far the worse, and presents a really high scatter which strongly dominates the global uncertainty of the null measurements for 110 Her. In particular, we observe very low and very high null measurements that are most likely unrealistic.

In a more quantitative approach, we show in Table 4.6 the same results as in Table 4.5, but for an aperture with a radius of 24 pixels.

In contrast, with the aperture of 8 pixels in radius, the aperture of 24 pixels in radius

		Mean				PCA			
		Null (%)	Uncertainties (%)			Null (%)	Uncertainties (%)		
			(1)	(2)	(3)		(1)	(2)	(3)
CAL 1	OB1	1.19	0.04	0.13	0.14	1.27	0.03	0.19	0.20
	OB2	1.99	0.04	0.25	0.25	1.64	0.03	0.15	0.15
	OB3	1.25	0.05	0.23	0.24	0.62	0.03	0.11	0.12
	OB4	0.82	0.04	0.30	0.31	1.32	0.04	0.26	0.26
	OB5	1.52	0.04	0.13	0.14	0.69	0.03	0.14	0.15
	OB6	1.44	0.04	0.45	0.46	1.49	0.04	0.07	0.08
SCI 1	OB7	0.96	0.09	0.24	0.26	1.33	0.07	0.20	0.21
	OB8	2.16	0.09	0.13	0.16	1.41	0.06	0.03	0.08
	OB9	2.23	0.09	0.33	0.34	1.41	0.07	0.29	0.30
	OB10	2.62	0.10	0.11	0.15	0.96	0.07	0.40	0.41
	OB11	1.84	0.09	0.49	0.50	-0.05	0.06	0.44	0.44
	OB12	2.18	0.10	0.21	0.23	1.41	0.06	0.08	0.10
SCI 2	OB13	1.58	0.10	0.12	0.15	2.02	0.07	0.17	0.19
	OB41	1.47	0.09	0.13	0.16	0.54	0.06	0.10	0.12
	OB15	1.17	0.09	0.33	0.34	0.78	0.07	0.60	0.60
	OB16	2.10	0.09	0.34	0.36	1.46	0.07	0.16	0.18
	OB17	1.39	0.09	0.23	0.25	-0.55	0.06	0.68	0.69
	OB18	2.24	0.11	0.25	0.27	3.04	0.09	0.22	0.23
CAL 2	OB19	0.59	0.05	0.25	0.25	0.71	0.4	0.23	0.24
	OB20	1.53	0.06	0.22	0.23	0.85	0.04	0.16	0.17
	OB21	0.69	0.05	0.13	0.14	0.85	0.04	0.35	0.35
	OB22	0.87	0.05	0.22	0.22	1.12	0.03	0.19	0.19

Table 4.6: Null value in percent along with the uncertainty due to the error on the background floor (1), the uncertainty due to the error on the NSC fit (2) and the total uncertainty (3), for both mean and PCA background subtraction, in an aperture of 24 pixels in radius for the data of 110 Her.

results are more mitigated. The first calibrator and scientific pointing show very similar standard deviations between mean and PCA background subtractions. On contrary, the standard deviation of SCI2 is strongly degraded by a factor of 2.96, while the standard deviation of CAL2 is strongly reduced by a factor of 2.46. In fact, these more mitigated results can be explained in part, in particular for CAL1 and SCI1, by the increase in the aperture size, which contains a higher RMS. However, it is clear, in the case of SCI2, that this alone cannot explain the two outliers (OB17 and OB18) which strongly increase the overall scatter.

In terms of uncertainties, on the other hand, it is interesting to see that PCA background subtraction generally improves both the uncertainties due to the errors on the background floor and those due to the errors on the NSC fit. Since the latter dominates the total uncertainty, this improvement also translates to the total error bars of each OB measurement.

This degradation of PCA background subtraction performance with increasing aperture size is rather inconsistent with the results obtained in Chapter 3. In fact, in Chapter 3, the degradations do not start before apertures of about 32 pixels in radius, even for a mask set at 32 pixels in radius, as is the case for 110 Her. In addition, if the results were consistent, we should observe a much stronger improvement for the aperture of 8 and 13 pixels in radius. This contradiction indicates an imperfect integration of the PCA background subtraction in the nulling pipeline used to reduce the data from the HOSTS survey.

While investigating this discrepancy, we found that the number of images in the background files for the mean background subtraction were, for the science target and the second calibrator, containing only half of those for the PCA background subtraction. For the first calibrator, for both methods, half of the images were missing in the background files. If the missing half of the images should in theory not change significantly the results, the reason behind those missing images could have an unexpected impact, which might degrade the results obtained with PCA background subtraction. If this were to be confirmed, this would most likely impact all the apertures, including the smaller ones. However, further investigating this situation and perfecting the implementation of the PCA background subtraction into the nulling pipeline is beyond the timeline of this thesis.

4.4 Modeling of the 110 Her system

During the HOSTS survey, ten exozodiacal disks were detected, among which one in the 110 Her system. Ertel *et al.* (2020a) computed for this system, a detection of 5.2 sigma with a zodi level of 234. In the context of direct imaging missions to detect HZ planets, this amount of dust would prevent the detection of Earth-like planets. Identifying such systems and improving our understanding of their dust content, composition, distribution,

and circulation is paramount to inform the target selection of future such missions. Thus, in this section, we propose an analysis of the 110 Her system to better constraint its dust distribution.

It is worth noting that the results of the HOSTS survey, for the zodi level, were based on the geometry of the solar system. In particular, the slope was set to the value observed in the solar system, and the amount of dust was scaled by comparison to that observed in the solar system. But, those parameters could also impact the resulting zodi level computed by the model. Thus, we do not expect our results to be systematically coherent with those presented in Ertel *et al.* (2020a). In fact, the results presented in this thesis are more accurate and a better representation of the system as we explore the physical parameters of the dust distribution.

4.4.1 110 Her

110 Her is a 2.2 Gyr old F5.5 IV-V star (Gray *et al.,* 2001), at 19.2 ± 0.2 parsecs (Marshall *et al.,* 2013). This star is 1.24 times more massive than the Sun, and has an effective temperature of 6431 K (Marshall *et al.,* 2013). Its magnitude in the K-band is 3.06 (Ducati, 2002).

110 Her was observed in the far-infrared with Herschel at 70, 100 and 160 μm, which revealed a cold debris disk emitting at 70 and 100 μm (Marshall *et al.,* 2013). Observations with CHARA/FLUOR in the K-band also revealed a near-infrared excess (Absil *et al.,* 2013), and follow-up K-band observations with CHARA/JouFLU suggested a possible binarity (Nuñez *et al.,* 2017).

4.4.2 Pancake-like disk model

The pancake-like disk model, as described in Section 4.1.4, does not fit the inner and outer radii, but set them, respectively, to 0.04 and 11.27 AU for the 110 Her system. The results of the modeling with the pancake-like disk are presented in Figure 4.12.

In the context of the pancake-like disk model, it is interesting to focus on the constraint on the inclination and the position angle. Figure 4.12 shows that the model fails to put strong constraints on the inclination, but still limits it to rather small angles, with the disk being close to face on (5.25°-35.11° from face-on). In addition, the model cannot put constraints on the position angles, which is consistent with a disk with a small inclination.

The high value of the τ slope indicates that most of the dust in the system is found toward the outer radius of the disk, here 11.27 AU, while very little dust is present closer in. Indeed, the increase in dust amount described by the τ slope is very steep and means that little to no dust is present very close to the star, whereas extreme amounts are already found at 3 AU of distance. With such amounts of dust, the null excesses in the apertures of 8 and 16 pixels (respectively 144 and 288 mas) in radius should already be significant, whereas no excesses are found. Similarly, the null excess found

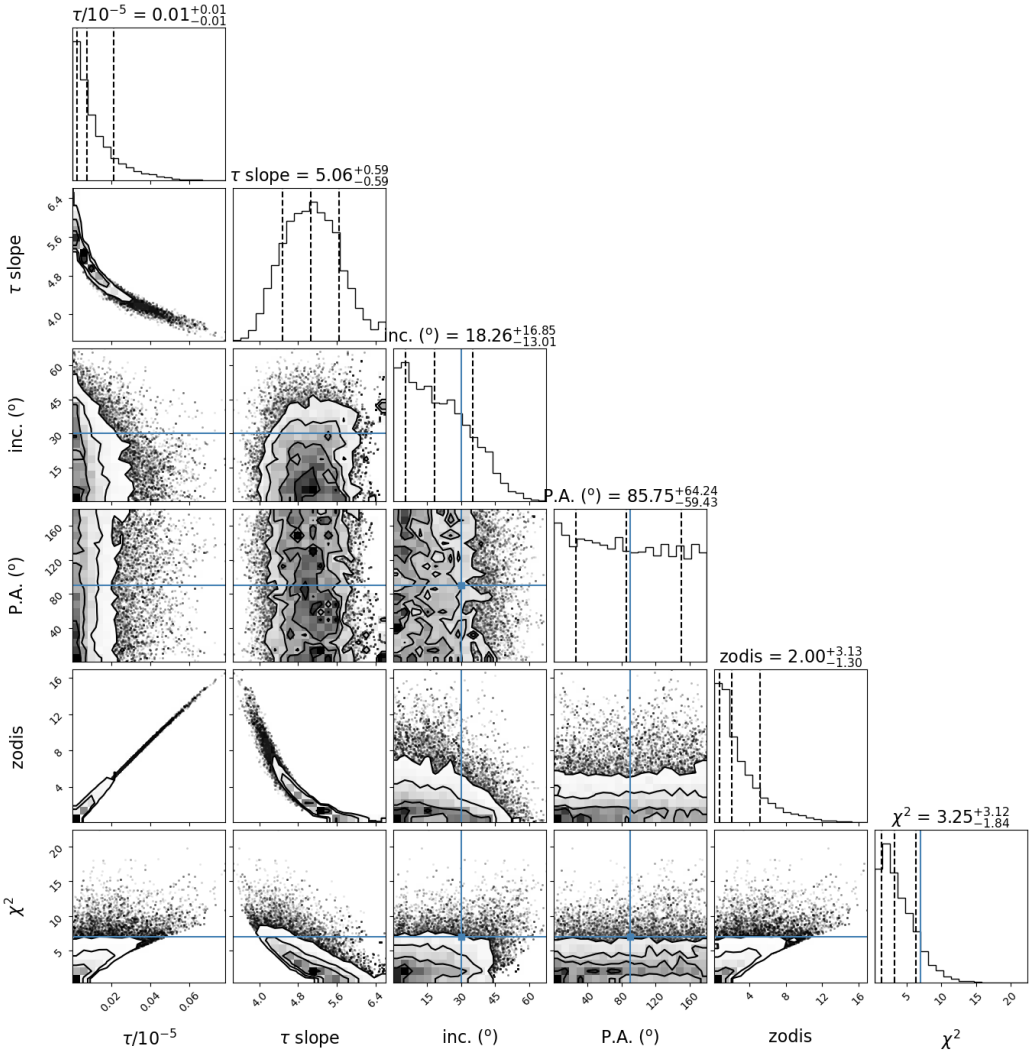

Figure 4.12: Posterior distribution obtained by the MCMC for the pancake-like disk model for the 110 Her data. The optical depth, the τ slope, the inclination and the position angle are fitted. For each parameter, the corner plot shows the median distribution (50th percentile), the uncertainty toward lower values (subtracted from the median distribution this value gives the 16th percentile), and the uncertainty toward higher values (subtracted from the median distribution this value gives the 84th percentile).

in the 24 pixels (432 mas) aperture is weak compared to what would be produced by such extreme amount of dust. Despite a mean χ^2 of 3.25, and a reduced χ^2 of 1.08 that suggests that the pancake-like disk model describes rather well the system, it is thus nonphysical and we choose to discard it in the following.

4.4.3 Zodi model

The zodi model is very similar to the pancake-like disk model with the inner and outer radii set respectively at 0.04 and 11.27 AU, but assumes a τ slope of -0.34, as in the solar system. The purpose of this model is simply to estimate the amount of dust

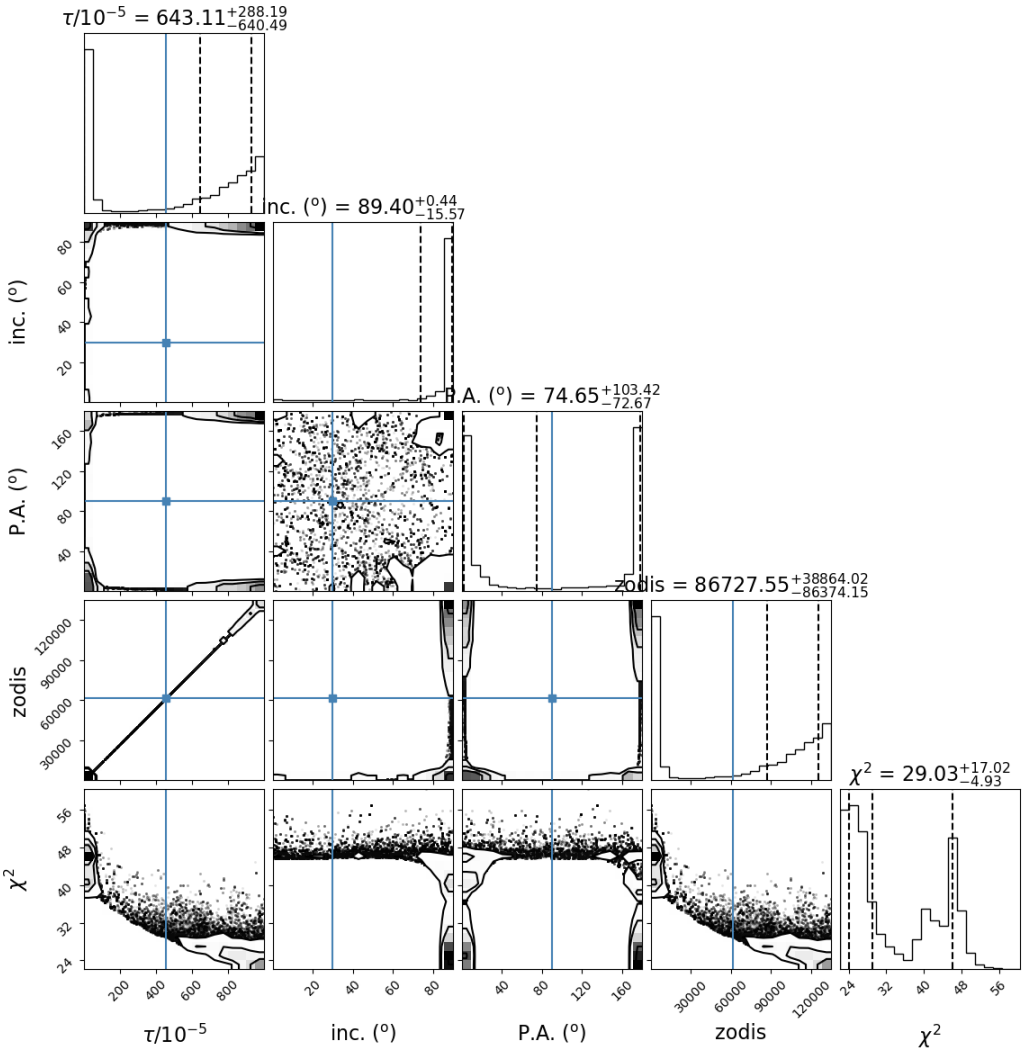

Figure 4.13: Posterior distribution obtained by the MCMC for the zodi model for the 110 Her data. The optical depth, the inclination, the position angle and the zodi level are fitted. For each parameter, the corner plot shows the median distribution (50th percentile), the uncertainty toward lower values (subtracted from the median distribution this value gives the 16th percentile), and the uncertainty toward higher values (subtracted from the median distribution this value gives the 84th percentile).

in the habitable zone of the system. This model is rather similar to the estimations made for Ertel *et al.* (2020a). We thus use this model as a sanity check. The raw results obtained for this model are shown in Figure 4.13

It is very clear in Figure 4.13, that the model identifies two distributions. The first one has a low optical depth, below 100, and the second with a much higher optical depth, above 400. The distribution of possible zodi levels is directly impacted by the optical depth and presents the same duality. The position angles also present two distributions, but those are in reality due to the symmetry between the case of position angles around 0° and 180°. This particular double distribution should therefore not be considered as two distinct distributions. The two pics in the distribution of the χ^2 are thus most likely

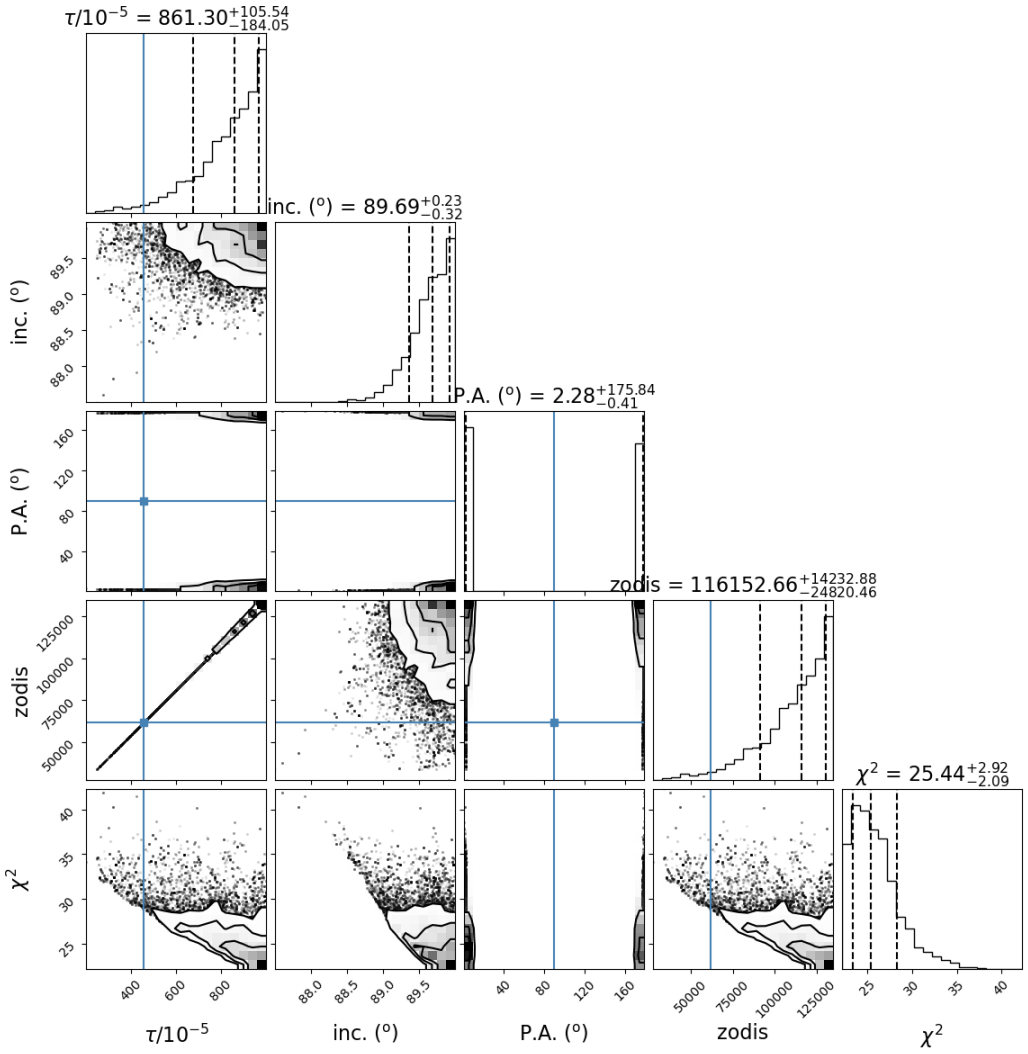

Figure 4.14: Posterior distribution obtained by the MCMC for the zodi model for the 110 Her data and filtering the low optical depth walkers. For each parameter, the corner plot shows the median distribution (50th percentile), the uncertainty toward lower values (subtracted from the median distribution this value gives the 16th percentile), and the uncertainty toward higher values (subtracted from the median distribution this value gives the 84th percentile).

due to the two distinct distributions of optical depth.

For a more comprehensive analysis of this model, we separated both distributions and considered them separately. For the case of high optical depth, we filtered all walkers below 200. In this case, most of the walkers are kept. We present the results of this sub-case in Figure 4.14.

In Figure 4.14, despite filtering between the solution of high and low optical depth, the double distribution of the position angle remains, demonstrating that the origins of these two distributions are not related to those of the optical depth. The inclination of the model remains mostly unchanged compared to the unfiltered case. The value obtained here is, however, in complete contradiction with the inclination obtained with

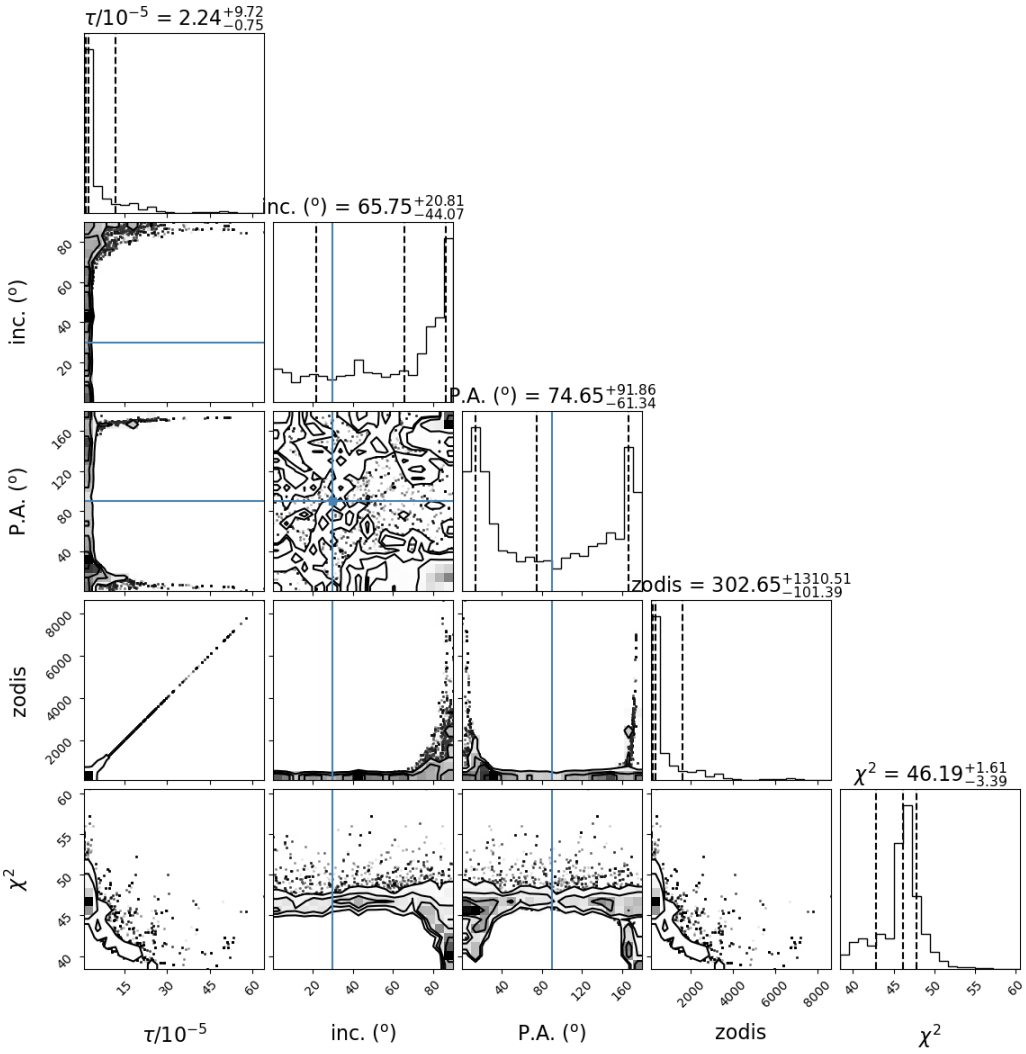

Figure 4.15: Posterior distribution obtained by the MCMC for the zodi model for the 110 Her data and filtering the high optical depth walkers. For each parameter, the corner plot shows the median distribution (50th percentile), the uncertainty toward lower values (subtracted from the median distribution this value gives the 16th percentile), and the uncertainty toward higher values (subtracted from the median distribution this value gives the 84th percentile).

the pancake-like disk model. Indeed, here the disk is almost perfectly edge-on. In addition, the PA distribution is $\pm 90°$, which means that the disk is aligned with the central destructive fringe of the nulling pattern. Consequently, no amount of dust would produce any significant excess, hence the extreme amount of zodi found with this model. The results shown by this model thus cannot describe the data, as the disk itself would be nulled in this case. In consequence, we discard this sub-case. In the following we only the low optical depth solution is considered for the zodi model.

For the case of the low optical depth, we filtered all the walkers above 100. In this case, we are left with very few walkers. We present the results of this sub-case in Figure 4.15.

In the sub-case presented in Figure 4.15, the inclination and position angles are much less constrained due to the low number of walkers remaining. On the other hand, the optical depth value is much more realistic and, consequently, so is the distribution of zodi level. In fact, with this sub-case the disk is not egde-on, and not perfectly aligned with the central fringe, thus it is not fully nulled, and some emission from the disk would indeed be detected. In particular, with this sub-case, the zodi level is of the same order of magnitude as the estimates found in Ertel *et al.* (2020a) for the 110 Her system, and both are consistent. Despite this sub-case being more physically reasonable, χ^2 is much higher than the case with the high optical depth.

For both cases, it is very clear that the pancake-like disk model, despite being nonphysical, would still provide a much better description of the system. The only difference in the assumptions made between these two models is the τ slope value. Considering the degradation of χ^2 with the zodi model, it is clear that the value of the solar system, -0.34, does not adequately describe the situation of the 110 Her system. This result is important because previous estimates of the zodi level in this system (Ertel *et al.,* 2020a) were also made with this assumption. New estimates using a more accurate slope for the 110 Her system could thus lead to significantly different zodi levels.

4.4.4 Thin ring model

The thin ring model, as described in Section 4.1.4, makes the assumption that the ratio between the inner and outer radii is 0.1. Furthermore, since this model does not fit the τ slope , we set it to 0.5. We present the results for this model in Figure 4.16.

Figure 4.16 shows that the inclination found by fitting procedure for the thin ring model for the 110 Her system is consistent with the results obtained with the pancake-like disk model, that is, smaller than $\sim 30°$ from face-on. What is particularly interesting in this model is the inner radius of the thin ring. Indeed, the thin-ring model found a best value for the inner radius at 7.64 AU, much further away from the star than the habitable zone. According to the thin-ring model, there is no dust inward of the inner edge. Considering the position of this inner edge, the optical depth and thus the zodi level hold no meaning as they are measured in the HZ (roughly 2.5 AU for the 110 Her system), where there is no dust. As the outer radius is directly computed from the inner radius, it has in itself little meaning and does not constitute a hard constraint on the outer edge of the disk.

The χ^2 for the thin-ring model is very satisfactory and the χ^2 of 0.37 is even better. This suggests that there is indeed no dust close to the star and up to about 7 AU, making an extending disk with a very close-in inner edge, like the pancake-like disk, a terrible fit to the reality. In addition, beside the optical depth and zodi level, the thin ring model does not seem nonphysical.

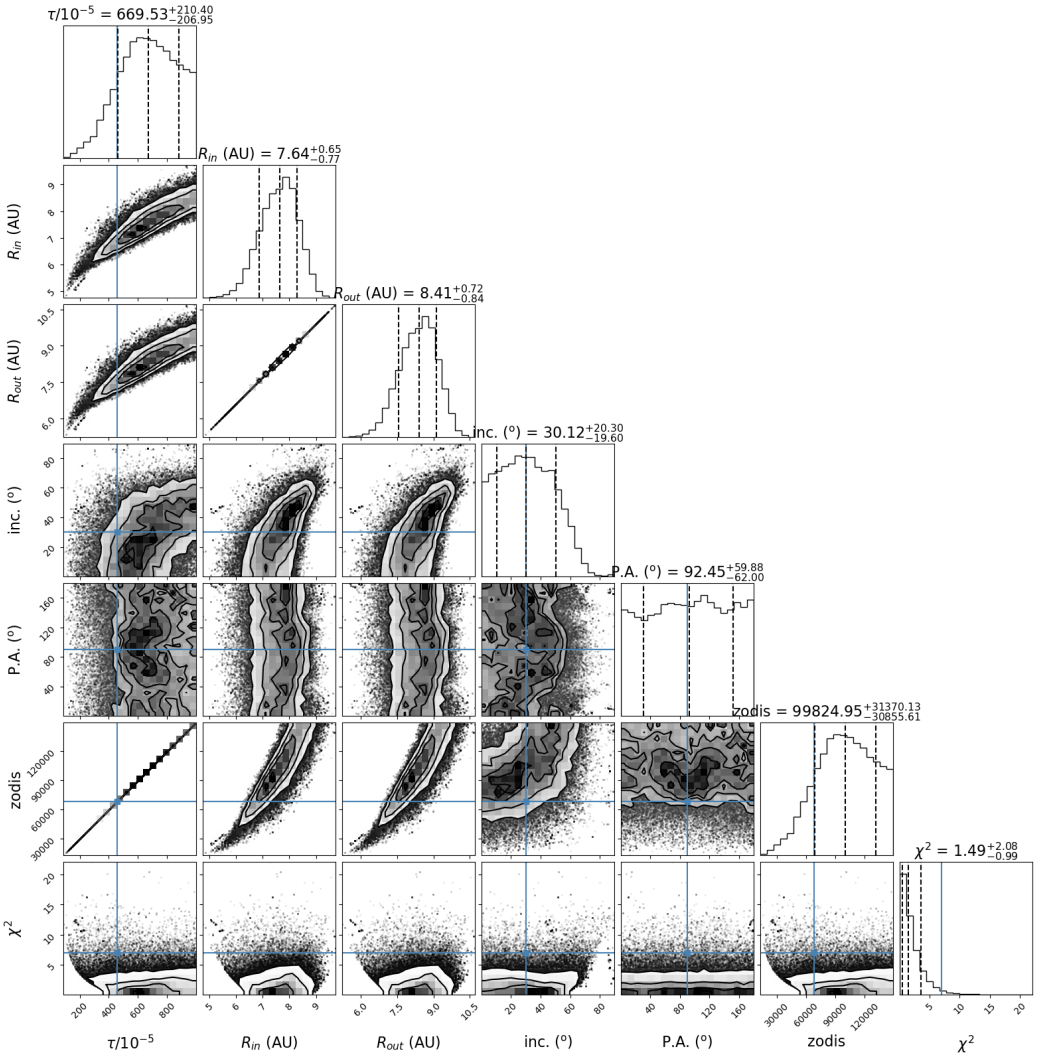

Figure 4.16: Posterior distribution obtained by the MCMC for the thin ring model for the 110 Her data. The optical depth, the inner radius, the inclination, the position angle and the zodi level are fitted. For each parameter, the corner plot shows the median distribution (50th percentile), the uncertainty toward lower values (subtracted from the median distribution this value gives the 16th percentile), and the uncertainty toward higher values (subtracted from the median distribution this value gives the 84th percentile).

4.4.5 Free model

The free model, as described in Section 4.1.4, allows fitting both inner and outer edge, the τ slope, the inclination and position angles, without any prior hypothesis. However, because of this high degree of freedom, fitting all parameters at the same time could be challenging. In order to optimize the computational time and prevent non-convergence, we thus proceed iteratively. The first iteration fitted the inclination and position angle. The second iteration set these two parameters to the best-fit values obtained by the first iteration and fitted the inner and outer radii. Finally, the third iteration set all the previously determined parameters to the best-fit value and fitted the

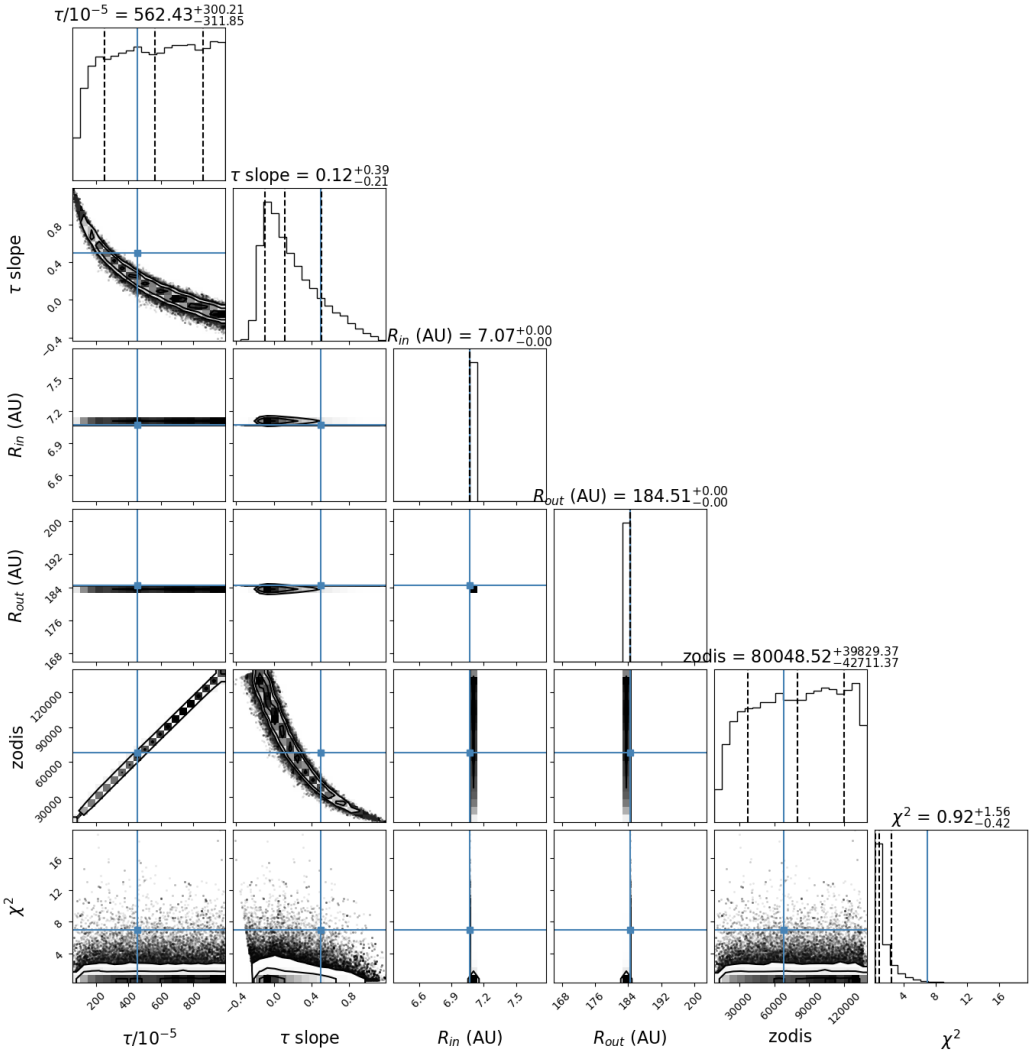

Figure 4.17: Posterior distribution obtained by the MCMC for the free model for the 110 Her data in its third iteration. The inclination and position angle were fitted in the first iteration and their best-fit values used as priors in the following iterations. The inner and outer radii were fitted in the second iteration and their best-fit values used as priors in the third iteration. In the third iteration, the optical depth, the τ slope and the zodi level are fitted. For each parameter, the corner plot shows the median distribution (50th percentile), the uncertainty toward lower values (subtracted from the median distribution this value gives the 16th percentile), and the uncertainty toward higher values (subtracted from the median distribution this value gives the 84th percentile).

τ slope. The first iteration determines a best-fit value for the inclination of 25.29° from face-on, which is consistent with the thin-ring model. As a result from this near face-on configuration, the position angle is not well constrained, similar to the two other models. We then set its value to 92.53°, as it was the best fit found for the first iteration. In Figure 4.17 we present the results of the third iteration.

As shown in Figure 4.17, the inner edge found in the free model is very similar to the inner edge found in the thin-ring model, and both are consistent. This strengthens

Models	Pancake-like	Zodi	Thin Ring	Free
optical depth	0.01 ± 0.01	$643.11^{+288.19}_{-640.49}$	$669.53^{+210.40}_{-206.95}$	$562.43^{+300.21}_{-311.85}$
τ slope	5.06 ± 0.59	-0.3	0.5	$0.12^{+0.39}_{-0.21}$
R_{in} (AU)	0.04	0.04	$7.64^{+0.65}_{-0.77}$	$7.07^{+0.86}_{-0.80}$
R_{out} (AU)	11.27	11.27	$8.41^{+0.72}_{-0.84}$	$184.51^{+135.05}_{-142.18}$
inclination (°)	$18.26^{+16.85}_{-13.01}$	$89.40^{+0.44}_{-15.57}$	$30.12^{+20.30}_{-19.60}$	$25.29^{+16.66}_{-16.58}$
position angle (°)	$85.75^{+64.24}_{-59.43}$	$74.65^{+103.42}_{-72.67}$	$92.45^{+59.88}_{-62.00}$	$92.53^{+59.55}_{-61.42}$
χ^2	$3.25^{+3.12}_{-1.84}$	$29.03^{+17.02}_{-4.93}$	$1.49^{+2.08}_{-0.99}$	$0.92^{+1.56}_{-0.46}$

Table 4.7: Summary of the best-fit values obtained by the MCMC for the four models: pancake-like disk model, zodi model, thin ring model and free model. The values in blue indicates the parameters for which the values has been set and is not fitted with the MCMC. The outer radius value is indicated in teal for the thin ring model, as its values is computed based on the inner radius value, and is not fitted independantly.

the hypothesis of a very little amount of dust inward this distance. On the other hand, the outer radius of the disk differs significantly from the thin-ring model, since it was fitted separately. But at such a large distance, the dust would be too cold to be detected in the N-band. In addition, dust at this distance would be outside of the field of view of our data. Thus, the best fit value for the outer edge is not meaningful. Nevertheless, this large value hint at a solution without a sharp edge on the outer part of the disk. The τ slope of this model is slightly lower than for the thin-ring model, but both values are consistent. In the free model case, however, as the disk is much larger, this τ slope value is much more significant and is likely to be more accurate.

As in the thin-ring model, the values for the optical depth and the zodi level are both too high to be physical. But similarly to the thin-ring case, with the free model, no dust is present inward of 7.07 AU. The values of the optical depth and of the zodi level, measured at the EEID (roughly 2.5 AU for the 110 Her system), thus do not hold any significance.

The χ^2 of this model is slightly better than the thin-ring model, in particular considering the reduced χ^2 of 0.18 but the two distributions overlap significantly, and thus the two models can be considered almost as likely to describe the reality.

4.4.6 General interpretation

We summarize the best fit values obtained for each of the four models we tried for 110 Her in Table 4.7. We also highlight the parameters which are not fitted for each models and their initial values.

We have shown, with the pancake-like model, that a very extended disk is highly unlikely to describe the reality. In fact, in addition to the higher χ^2 for this model, the best solution found is nonphysical. The slope is too high, which suggests a huge amount of dust, which would have led to a much stronger HOSTS detection. The thin-ring model, on the other hand, is designed to fit a very narrow ring, outside of which we

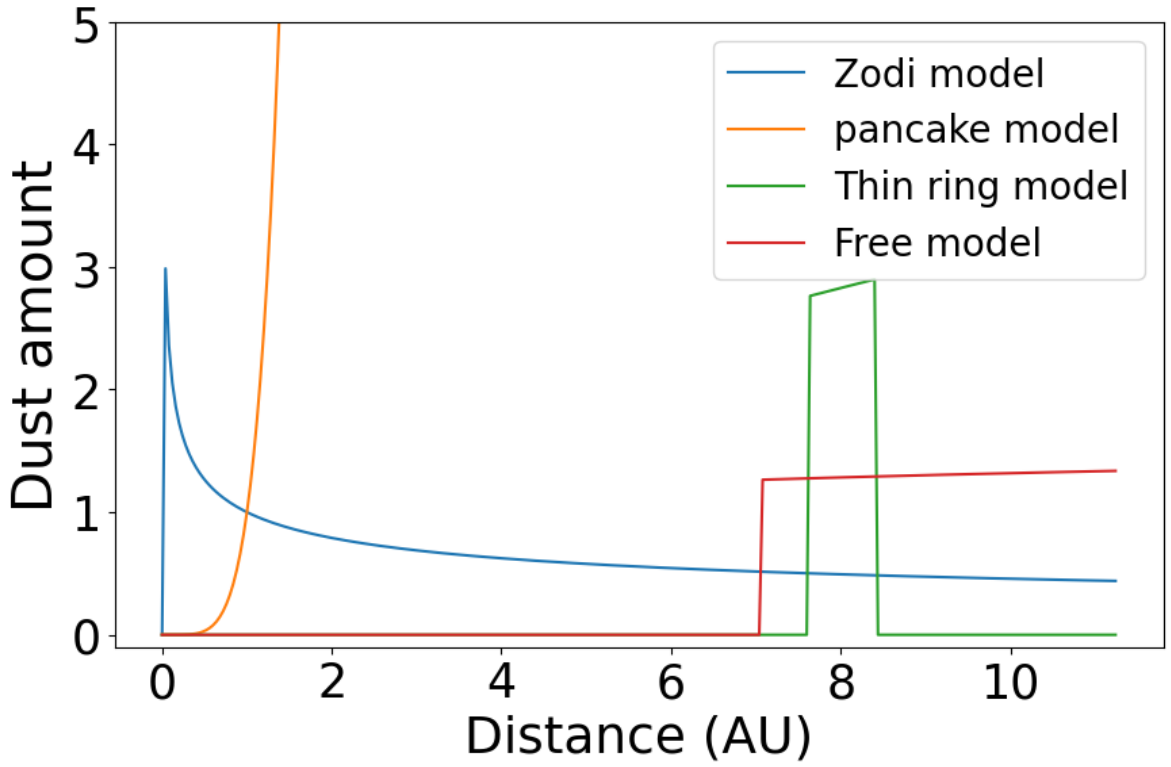

Figure 4.18: Schematic representation of the variation of the dust amount according to the low optical depth zodi model (blue), the pancake-like disk model (orange), thin ring model (green) and free model (red) with respect to the distance. The respective curves are not scaled with respect to each other due to the lack of a physical zodi level.

assume that no dust is present. If this narrow ring is not situated at the habitable zone position, the optical depth and zodi level provided by this model hold no significance, which is our case for the 110 Her system. The free model also points toward a system in which no dust is present in the habitable zone, but much further away. In contrast to the thin-ring model, it finds an outer radius which is much further away, and from which we can only conclude that this model does not find a sharp outer edge to the disk. We sum up the results in Figure 4.18.

As shown in Figure 4.18, the pancake-like model would suggest a very sharp increase as close as 1AU, which contradicts the zodi level it found and the HOSTS observations. This model thus does not properly the data, and is non-physical.

The two best-fitting models, the thin-ring and free models, on the hand rather agree that dust is only present starting at about 7, 7.5 AU. The thin ring model design makes it impossible to determine if dust is present in a lesser quantity outside of the edges it determines. The only conclusion that can be drawn is that the majority of the dust lies between those distances. The free model, on the other hand, is not limited by this ratio and can determine the full extension of the disk. Indeed, in Figure 4.18, the inner radius found by fitting procedure for the free model is slightly closer-in than the one

found for the thin ring, and that the outer radius is much further away. Despite the lack of constraints on its radii, the free model still found an inner radius at 7 AU which suggests a sharp edge around this distance. The combined interpretation of the thin ring and the free model suggests that the dust amount increases around 7 AU and that most of the dust is found between 7.64 and 8.41 AU. The free model then suggests that the disk continues up to very large distances. As the temperature of the dust decreases with the distance, such a large outer radius makes little sense. Indeed, the dust at this distance would have a temperature comprise between 32 K (black body) and 48 K (f = 1.5) which is unlikely to be detected by a N-band camera such as NOMIC. But, that the model do not find a much closer-in outer radius, both suggest that there is detectable dust beyond 8.41 AU, and that no sharp outer edge is found. The amount of dust is therefore likely to gradually decrease beyond 8.41 AU.

The difference between the dust distribution found by the HOSTS survey in the 110 Her system and this analysis, is thus really interesting. Indeed, in the context of the search for HZ exoplanets, the exozodiacal dust would not be a major issue, despite the large amount of dust, as it is not located in the HZ. In addition, the sharp edge at 7 AU means that something is depleting the dust at smaller distances. Indeed, the dust in between 7 and 8 AU could be produced by a planetesimal ring, however, without an effective clearing mechanism inward of the inner edge, PR drag would bring material closer to the star. Furthermore, the collisions which would occur as the material travels inward would not be sufficient to explain such a major gap (Rigley & Wyatt, 2020). This sharp edge and gap could, instead, be carved by a giant planet or be due to a resonance with planets elsewhere in the system. If a giant were to be responsible for this sharp edge, it could shield inner planets from high cometary rate and large impacts, as Jupiter is believed to have done in the early stages of our solar system (Wetherill, 1994).

Nevertheless, we currently have several strong limitations that prevent us from drawing strong conclusions. Indeed, the uncertainty of our data prevent us from detecting a very small amount of dust. We thus cannot rule out a small dust population inward of the 7 AU inner edge. To overcome this limitation, we aim to further implement PCA background subtraction into the nulling pipeline to be more sensitive to the fainter population. Additionally, our models can currently only use one component to fit the system. Thus, if the disk was composed of two or more components, the model would not be able to fit it. Similarly, if the disk contains gaps, the model could either be blind to them, or consider them as the real inner or outer edge of the total disk. For a more detailed understanding of the dust distribution and of the system architecture, more complex models would have to be implemented.

4.5 Conclusion and Perspectives

We have shown in this chapter (Section 4.2), that reducing the uncertainty of HOSTS null measurement could significantly impact the modeling. In particular, with the proof of concept on Vega, we have shown it is possible to break the degeneracies between the pancake-like disk model and the thin ring model with an uncertainty reduce by a factor 2. Pushing the sensitivity even further, by reducing the error bars by a factor 3 even allows determining that simple, single-components models without gaps were insufficient to describe the data. In Chapter 3, these improvement factors have been achieved for the mean retrieval for aperture photometry, with PCA background subtraction.

We thus tried to integrate PCA background subtraction into the nulling pipeline. Several adjustments have been made, both to the method and to the pipeline, as described in Section 4.3.2. In particular, we removed the use of the background annulus, which was previously identified as a major source of bias. We obtained encouraging results, especially for the 8-pixel aperture for which we observed a reduction of the uncertainty of 22%. In addition, the uncertainty of the 13-pixel aperture was pretty similar for both PCA and mean background subtraction, despite not using the background annulus for PCA background subtraction. However, we observed an increase in the uncertainty of 26% for the 24-pixel aperture. Those results are not consistent with those obtained in Chapter 3 for aperture photometry, for which significant improvement was achieved up to aperture radii of 29 pixels.

This suggests that further work is needed to integrate PCA background subtraction to the nulling pipeline and that PCA-background-subtracted datasets are not yet ready to be used for modeling. Indeed, the analysis of the very low and very high null measurements obtained for the 24-pixel aperture (see Figure 4.11), which seem unrealistic, do not present any spike-like structures as those identified in Chapter 3, which would explain those values. Nonetheless, we identified potential pipeline issues that could have an impact on those measurements. Finalizing the integration of PCA background subtraction to the nulling pipeline would thus allow for a better accuracy of the individual OB measurements, thus reducing their scatter. In turn, this reduced scatter will produce more precise null measurements for the science target, allowing for the detection of fainter population, more precise modeling, and breaking degeneracies.

Thus, the modeling was performed on mean background-subtracted datasets only, with the improved version of the pipeline which discards the open-loop frames from the background measurements. In particular, we were able to rule out the hypothesis that the exozodiacal disk of the 110 Her system was a very extended disk, with dust very close to the star. Indeed, the pancake-like disk model led to nonphysical results which

were inconsistent with the null excesses found for 110 Her. Additionally, we were also able to determine that the zodi model was an even worse fit than the pancake-like disk model, in particular due to its τ slope set to -0.34, as in the solar system. That the zodi model does not provide a good fit is interesting, as the previous estimates for zodi levels in the HOSTS survey (Ertel *et al.,* 2018, 2020a) were all made with the assumption that the τ slope of the solar system would be a good first approximation. The combination of the thin-ring and free models then allowed one to determine that the dust amount detected during the HOSTS survey for 110 Her was located beyond a sharp inner edge at 7 AU, with most of the dust contained roughly between 7.5 and 8.5 AU. The free model additionally tends to indicate that the disk does not have a sharp outer edge. We were also able to put a small constraint of the inclination of the disk as the pancake-like disk, the thin ring and the free models all found a best fit for the inclination around 18-30°.

In addition to the improvement PCA background subtraction could achieve once fully integrated, more complex models would have to be developed to obtain more precise and accurate dust distributions in HOSTS detections. In particular, we have shown with the proof of concept on Vega (Section 4.2) that more than one component could be needed and that gaps should also be considered. Further modeling efforts should aim to integrate these aspects.

Chapter 5

Conclusions and Perspectives

Contents

Today, the field of exoplanetology is focusing more and more on the search for Earth-like planets. In addition to the two well-known challenges posed by the angular separation and the contrast of such planets to its host star in direct imaging, the exozodiacal dust can also hinder Earth-like planet detection. Despite this risk, exozodis are poorly known and more precise measurements, by a factor 2 at least, and characterization are required to prepare future direct imaging missions. The most precise survey of exozodiacal dust to date, the HOSTS survey is limited, in terms of sensitivity, by its imperfect background subtraction. This thesis, by exploring both spatial and temporal background correction methods, and by modeling one of the HOSTS's exozodiacal disk detection, contributes to a more precise and comprehensive understanding of exozodiacal dust in nearby systems.

5.1 Pushing direct imaging N-band sensitivity

N-band observations are particularly interesting in the search for habitable zone dust and temperate planets, as they provide a favorable contrast compared to visible wavelength. However, ground-based observations in this waveband are hindered by the large thermal background that dominates the signal from the star itself. Observations as demanding as those of exozodiacal dust thus require a very high quality background subtraction.

PCA is a very powerful and versatile method which has demonstrated the ability to remove PSF very effectively in direct imaging (Amara *et al.,* 2015; Amara & Quanz, 2012; Soummer *et al.,* 2012). More recently, it has been used for background subtraction in the L and M bands by Hunziker *et al.* (2018). This last study has shown that PCA was able to accurately reconstruct the background behind a mask, and thus provide much cleaner final images with less background residuals. However, it was concluded that the improvements of the resulting contrast curves remained limited.

In this thesis, we developed a background subtraction pipeline for HOSTS data, and a method, based on Hunziker *et al.* (2018) for PCA background subtraction. We

extended the field of application of the previous study to N-band imaging (Chapter 3, Section 3.3), aperture photometry (Chapter 3, Section 3.4) and nulling measurements (Chapter 4, Section 4.3).

Compared with the L and M bands, the thermal background is much higher in the N band. An imperfect background subtraction thus has much more impact in the N band, since it strongly dominates the signal. In fact, compared to the results obtained for HCI in Hunziker *et al.* (2018), we show in this thesis a more significant improvement of contrast curves (up to 1.7), which is mainly due to the higher thermal background in the N band.

PCA background subtraction, applied to aperture photometry, provides even more significant improvements, with an accuracy improved by a factor of 2 to 3 depending on the aperture and masks sizes. The accuracy of the nulling measurements currently limits the sensitivity of the HOSTS, it is thus expected that those factors remains similar for the sensitivity improvement. The first tests on nulling measurements have shown that PCA background subtraction already benefits small apertures and reduces their overall uncertainty. However, more work is needed to optimize PCA background subtraction use for nulling measurements.

The HOSTS survey has established upper limits on the median zodi level around nearby stars. However, as previously mentionned, constraints would need to be at least twice as precise to fully assess the risks and feasibility of a direct imaging mission dedicated to Earth-like detection and characterization. We have shown, in Chapter 3, that PCA background subtraction has the potential to improve this sensitivity by a factor of 2 to 3, thus meeting the requirements.

In addition to accurate results, one usually wants precise results as well. PCA background subtraction has demonstrated its ability to improve the accuracy of the background correction and consequently of the photometric measurements. However, it could do very little for the precision of these measurements. In certain cases, it even degrades this precision. The temporal variation of the photometry in the aperture is responsible for limiting the precision.

The current mean background subtraction, used for the HOSTS survey, uses a background annulus to prevent this effect but, by doing so, reduces the accuracy of the measurements. Indeed, using the background annulus forces the assumption that the background at the annulus position is a good estimate of the background in the aperture. In this thesis, we therefore developed a PCA-based method to correct the photometric variations of the background over time (Chapter 3 section 3.6), rather than using a background annulus.

In contrast to the use of a background annulus, our temporal PCA correction does not add bias back into the data. We also demonstrated that the large photometric variations that remain after PCA background subtraction are effectively corrected by the temporal PCA correction. The temporal PCA is thus able to reduce the photometric

variation of the background through time, thus increasing the precision of the global measurements, without reducing its accuracy.

The combination of spatial PCA background subtraction and temporal PCA background correction thus has the potential to improve both the accuracy and the precision of the measurements. However, in cases where precision is the dominant limiting factor rather than accuracy, temporal PCA could also be used on its own.

5.2 Modeling exozodiacal dust around 110 Her

Improving the sensitivity of exozodiacal dust measurements will allow establishing better constraints on the amount of dust in nearby systems, and the risks they will pose to future direct imaging missions. However, to assess those risks and the impact of the dust in the system, it is also necessary to understand the dust distribution, by modeling individual systems.

The system 110 Her, is one of the 10 detections made during the HOSTS survey with an estimated zodi level of 234.9 (Ertel *et al.,* 2020a). This amount of dust would prevent the detection of Earth-like planets in the habitable zone. However, those estimates were obtained with a certain number of assumptions, and in particular that the τ slope, the slope describing the evolution of the dust concentration with respect to the distance to the star, of the system was identical to that of the solar system.

In this thesis, we used four different models to fit the data obtained for 110 Her during the HOSTS survey. Assuming the τ slope of the solar system, we were able to retrieve zodi levels similar to Ertel *et al.* (2020a). However, we learned that the geometry of the zodiacal cloud in the solar system was not a good description of this system (zodi model). Indeed, two other models (thin-ring and free models) have shown that the inner edge of the disk of 110 Her was located at about 7 AU, further away from the star than the EEID at 2.5 AU. According to these models, there is therefore little to no dust in the habitable zone and most of the amount detected by HOSTS is located between 7.5 and 8.5 AU.

This situation is a perfect example of why the study of individual systems is important to better constraint the risks posed by the exozodiacal dust for direct imaging missions. In fact, results from Ertel *et al.* (2020a) suggest that the 110 Her system would not be a suitable target for Earth-like detections due to the large amount of dust detected. However, our results show that the dust would not be as problematic as expected, since it is not located in the habitable zone around 2.5 AU but at 7AU, where those missions will search for planets. In addition, the low levels of dust detected inward of 7AU could even suggest the presence of a planet, which would make 110 Her a very interesting target for Earth-like detections.

In addition, the results of the modeling hint at an exozodiacal disk with a sharp inner edge. Such an edge could be due to the presence of a planet around this location,

cleaning the orbit and shielding the inner system, preventing the dust to form and maintaining inward its orbit. It could also be linked to resonances in the system, likewise clearing the orbits inward of the inner edge.

5.3 Perspectives

The preparation of future direct imaging missions involves the study of exozodiacal disks. To study this dust, more accurate and more precise measurements are needed. With this thesis, we provided two methods to improve the sensitivity of N-band flux measurements. While the application of spatial background subtraction to nulling measurements requires more work, we have shown that this method could improve the accuracy of the photometric measurements by a factor 2 to 3, which is generally expected to carry forward to nulling measurements of exozodi and improve their sensitivity. The application to this new background subtraction method to the whole HOSTS survey will allow to better quantify the improvement of the sensitivity and the robustness of the method.

Increasing the precision and accuracy of the data will allow one to obtain more sensitive null measurements, make new, fainter detections, and model the dust distribution in the systems more accurately. The re-analysis of the HOSTS survey with this improved sensitivity will thus allow stronger constraints on the amount of exozodiacal dust in nearby systems, and inform future direct imaging missions.

In terms of precisions, we have seen that the current temporal PCA implementation is lacking a mask. Thus to further improve the our results and the precision of our measurements it should be implemented in future works. In addition, the temporal PCA method, presented in this thesis, is not limited to the temporal axis and can be used on a wider variety of data and instrument. Indeed, the same approach could be used for the spectral axis, where instead of studying the variation of the photometry over time, one would consider the variation of the photometry over different wavelengths. Thus, this technique can be applied to a wide variety of data and is not limited to time series nor to direct imaging. For example, the NOTT instrument (Defrère *et al.,* 2018) on the Asgard suite, to be installed on the VLTI, uses an integrated optics beam combiner and thus loses the spatial information. It does, however, retain both temporal and spectral information, both of which could be corrected by a variation of the temporal PCA method.

In addition, a sensitivity improved by a factor 2 to 3 also means a required observation time reduced by a factor 4 to 9. In fact, the same telescope, while observing in the N-band, will require less integration time to reach a given sensitivity when using PCA background subtraction instead of the classical mean background subtraction. PCA background subtraction would thus be extremely beneficial for optimizing mid-infrared observations in general by optimizing the science return with respect to the total integration time.

This will in particular be interesting for future instruments such as ELT/METIS, and for the ELTs in general, which are likely to be largerly over-subscribed (Rousseau *et al.*, 2023).

Finally, the systematic modeling of the detections made during the HOSTS survey, and possible new ones uncovered with the improved sensitivity, is also extremely important. It would indeed provide more accurate constraints on the risks posed by exozodiacal dust for direct imaging of Earth-like planet in the habitable zone, the system architecture, and the dust circulation.

Indeed, despite the constraint, put on the dust distribution around 110 Her, more complex models would be needed to draw strong conclusions. Indeed, the models currently used for the detections of the HOSTS survey do not allow for multi-components or gaps in the disk. The disk represented by the models could thus be only one part of the dust in the system. Both more precise measurements and more complex models would thus be needed to determine whether there is really no dust in the habitable zone or if our current models are simply unable to see it. The increased precision achievable through PCA background subtraction will significantly contribute to these goals.

Chapter 6

Appendix

6.1 Singular Value Decomposition

We here describe how the SVD is performed numerically, as implemented in Golub & Kahan (1965). The first step of this procedure is to decompose the matrix M_R, which contains the data, into the following product:

$$M_R = P.J.Q^T \quad , \tag{6.1}$$

with P and Q two unitary matrices and J a bidiagonal matrix. The demonstration of this relation is given in Golub & Kahan (1965). The matrix J can be further decomposed as:

$$J = X.S.Y^T \quad , \tag{6.2}$$

where X and Y are unitary matrices and S the diagonal matrix containing the singular values of J, which are also the singular values of A and are expressed as the positive values of $\sqrt{J^T.J}$. We thus have a total expression:

$$M_R = P.J.Q^T = P.X.S.Y^T.Q^T = U.S.V^T \quad , \tag{6.3}$$

by defining U = PX and V = YQ, where we retrieve Equation 2.37. The next step is then to compute the eigenvalues of $J^T.J$. This product results in a tridiagonal hermitian matrix for which it is possible to find a diagonal matrix Δ such as the product $\Delta(J^T.J).\Delta^T$ defines a matrix K which is real, symmetric, positive semi-definite and tridiagonal. The eigenvalues of such matrix can then be determined with the Sturm sequence algorithm.

The Sturm theorem, established in 1829 by Charles Sturm (Sturm, 2009), enunciates that the number of distinct real roots of a polynomial with real coefficients, in an interval [a,b] and for which a and b are not roots of this polynomial, is the number of sign changes of the Sturm suite of this polynomial in this interval. The Sturm suite of a polynomial P is a suite of polynomials defined as:

$$\begin{aligned} P_0 &= P \\ P_1 &= P' \\ P_2 &= remainder(\tfrac{P'}{P''}) \\ P_i &= remainder(\tfrac{P_{i-1}}{P_i}) \quad . \end{aligned}$$

With P' the first derivative of P, P" its second derivative. The maximum length of this suite is the degree of the polynomial P. With this theorem it is also possible to isolate the various roots and constrain their values, by modifying the interval [a,b]. In fact, the interval can be chosen so that only one root remains in this new interval and then further refine it to minimize the uncertainty over the value of the root.

After determining the roots of the matrix K, and thus the eigenvalues contained in S, the next step is to compute X and Y. The elements of those matrices follow two relations :

$$J.y_n = s_n.x_n \qquad and \qquad J.x_n = s_n.y_n \qquad . \tag{6.4}$$

To compute y_n and x_n, the deflation method is used. This method allows setting the eigenvectors to zero as they are found, to ensure that the next eigenvectors will be orthogonal to the previous ones.

The deflation of a matrix is a method that allows us to remove the eigenvector that has been found, in order to find the next one and ensure the orthogonality between the two. The simplest deflation method is Hotelling's deflation method. Let us assume a matrix M of rank 2 for which we have two eigenvalues λ_1 and λ_2 and two eigenvectors u_1 and u_2. The matrix M can thus be written:

$$M = \lambda_1.u_1.u_1^T + \lambda_2.u_2.u_2^T \qquad . \tag{6.5}$$

We then compute the first eigenvalue λ_{1C}, and u_{1C}, the first eigenvector. If both λ_{1C} and u_{1C} are determined with a perfect precision, then $\lambda_{1C} = \lambda_1$, and $u_{1C} = u_1$ and the deflation method proceed as follows:

$$\begin{aligned} M_D &= \lambda_1.u_1.u_1^T - \lambda_{1C}.u_{1C}.u_{1C}^T + \lambda_2.u_2.u_2^T \\ M_D &= \lambda_1.u_1.u_1^T - \lambda_1.u_1.u_1^T + \lambda_2.u_2.u_2^T \\ M_D &= \lambda_2.u_2.u_2^T \end{aligned} \tag{6.6}$$

However, if an error impact λ_{1C} and/or u_{1C}, the first term is not completely removed. Worse, the residuals of this term can be too significant compared to the second term to be ignored. It is in particular likely to happen when the second eigenvector is significantly smaller than the first one. When using a larger number of eigenvectors and eigenvalues, the errors can also quickly add up.

The deflation method used in the case of the SVD as described by Golub & Kahan (1965), is significantly more complex than Hotelling's deflation method, and based on Wilkinson (1954), although the principle remains similar and the aim is to reduce the accumulation of errors. In this method, 2x2 rotations are applied in sequence to the matrix to eliminate or render negligible the previous elements, as shown in the following

matrix, with the rotation being represented in order by the red, blue, green, and yellow squares.

$$J = \begin{pmatrix} a_1 & b_1 & 0 & \cdots & \cdots & \cdots \\ 0 & a_2 & b_2 & 0 & \cdots & \cdots \\ \cdots & \ddots & \ddots & \ddots & \ddots & \cdots \\ \cdots & \cdots & \cdots & 0 & a_n & b_n \end{pmatrix}$$

Ideally, the rotation would set the previous elements to zero, but due to errors, those elements are only set to negligible values.

Once the matrix J completely deflated, its last row and columns are deleted, and the process is repeated until the matrix J became a matrix 1x1 or until it became negligible. The rotations found in the previous step are then multiplied in reverse order to build X and Y. Now, returning to Equation 6.3, we have determined P,X and Y,Q and are thus able to compute U and V. With U,S and V known, we can thus obtain the principal components defined by $u_n.s_n$.

Although this method is much more complex than the determination of the eigenvector to perform PCA, its main advantage lies in its numerical stability, which is why this method is largely preferred when developing PCA coding algorithms.

6.2 Temporal Principal Component Analysis

6.2.1 PCA libraries and implementation

In the implementation of temporal PCA we chose to study, the temporal correction is performed after the spatial correction. Its goal is to remove the large brightness variation of the remaining background structures that have been overlooked or poorly corrected by the spatial correction. This implementation has the potential to reduce the RMS but would have very little impact on the bias. In fact, this implementation assumes that the values obtained after spatial PCA background subtraction are correct, and only search to reduce the variation of the photometry around those values. The temporal PCA code works on the spatially background subtracted cube for which we have kept the off-source frames and provides a data cube in the same shape as the spatially background-subtracted data cube, without the off-source frame. The recombination is then performed in the same way as for spatial PCA alone.

Another possible implementation would first perform temporal PCA, to reduce strong photometry variation over time, and renders the images more similar to one another. This implementation should be able to both improve the RMS and the bias. However, due to the limited time-frame of this thesis, this option was not fully explored.

Building the temporal background library

One of the main differences with Spatial PCA is the library used to build the principal components. Indeed, for the spatial implementation of PCA, we build the principal component on the group of off-source images. The equivalent of those off-source images is the pixels in the background in opposition to the pixels at the star position. All those pixels, and their variation through time, are thus gathered in our background library. The spatial information on those pixels is not taken into account. For the matrix on which the principal components are projected, it is now composed of all pixels, including those at the star position.

An important challenge with temporal PCA is to exclude as much random noise as possible from the principal components. In addition to the careful selection of the number of principal components, it is also important to optimize the background library. For aperture photometry and nulling measurements, for example, we want in priority to improve the correction inside the aperture. For this, the pixels far away from the aperture are not especially useful. Indeed, their variation is likely to be significantly different from those in the aperture. Reducing the library to a ring around the aperture can thus improve the correction by limiting the number of unrelated principal components that will be computed. The width of the ring must then be adapted depending on the size of the mask and on the relevant background structures.

To obtain the background library, we simply add the values of pixels outside of the region of interest in a list, and we do that for each image. As the spatial information is not relevant for this analysis, we have thus one dimension that contains all the relevant pixels values of one image, and one dimension that contains all the images. In contrast to Spatial PCA, here we use only one, unmasked library to build the correction. We found, in our analysis, that this situation is not optimal and that a mask should provide a better temporal correction. However, we did not explore this solution in this thesis.

We distinguish two types of implementation for the temporal PCA correction : 1Group and 3Groups. The 3Groups implementation is extremely similar to the spatial PCA case. We use indeed the two adjacent off-source groups along with the on-source group to build and project the correction. The 1Group implementation, on the other hand, only makes use of the group we want to correct. Both implementations have their pros and cons and will be discussed in further detail in the various cases presented in the following.

The matrix is built in a very similar way as in the spatial PCA case. However, in order to prevent Temporal PCA to wrongly amplify principal components due to the presence or absence of the star, we need to modify the data cube before building the matrix on which the principal components will be projected. This step consists in removing the signal of the star above the background in order to prevent an over-subtraction by the temporal correction. It is important to understand here that we are not trying to remove all the signal from the star, but rather the part of the signal

that would create a step in the photometry when the star is present versus when it is not. However we found that, despite the small number of principal components used for temporal PCA, it systematically reproduce this step, and a mask would be needed to prevent the signal self-subtraction. We also used an unmodified matrix, from which we subtract the correction, at the end of the process. After this step, both the modified and unmodified matrices are prepared through the VIP function "prepare_matrix". In this function, we create a mode for temporal analysis, which switches the axis of the matrix. The output is then a matrix oriented on the temporal axis on which we can project the temporal principal components.

Computing the principal components and reconstructing the correction images

The principal components are computed on the background libraries, on the temporal axis, and thus provide a principal component vector with a length corresponding to the number of pixels in the library. We then project those principal components on the transformed of the modified, unmasked matrix. The transformed of the result of this projection is then projected onto the principal components. The result of this projection is the temporal correction. However, we first need to normalize this correction to 0 in order to avoid introducing an offset on the mean photometry. We then subtract the normalized correction from the unmodified temporal temporal matrix. The normalization is simply made by subtracting the mean of the temporal correction to the temporal correction, before subtracting it from the unmodified matrix.

The last step of the Temporal PCA routine is to reconstruct the images by switching back the axes. Indeed, we do not modify the matrices, as we need them to keep the spatial information for the image reconstruction afterward. After the subtraction of the temporal correction from the temporal matrix, we thus switch back the axis to reconstruct a data cube composed of 2D images. The data cube is thus re-injected in the standard pipeline developed for Spatial PCA and is treated in the exact same way for the following steps.

6.2.2 Verification for over-subtraction

In order to make sure that the temporal correction would not introduce any self- or over-subtraction, we first apply this method to a synthetic data cube. This data cube is simply composed of a point source, which is convolved with a disk-like emission and some Poisson noise. We tuned the brightness of the sources and the Poisson noise in order to obtain a realistic dataset, without any remaining background structure. We also introduce a random variation in the photometry of the star to reproduce the photometric variations introduced by nulling interferometry. As the background is purely random, the temporal correction should not result in significant subtraction. We also know the flux of the sources and can check for any self- or over-subtraction. We did this verification for all three methods: mean, spatial PCA, and spatial + temporal PCA.Figure 6.1 shows

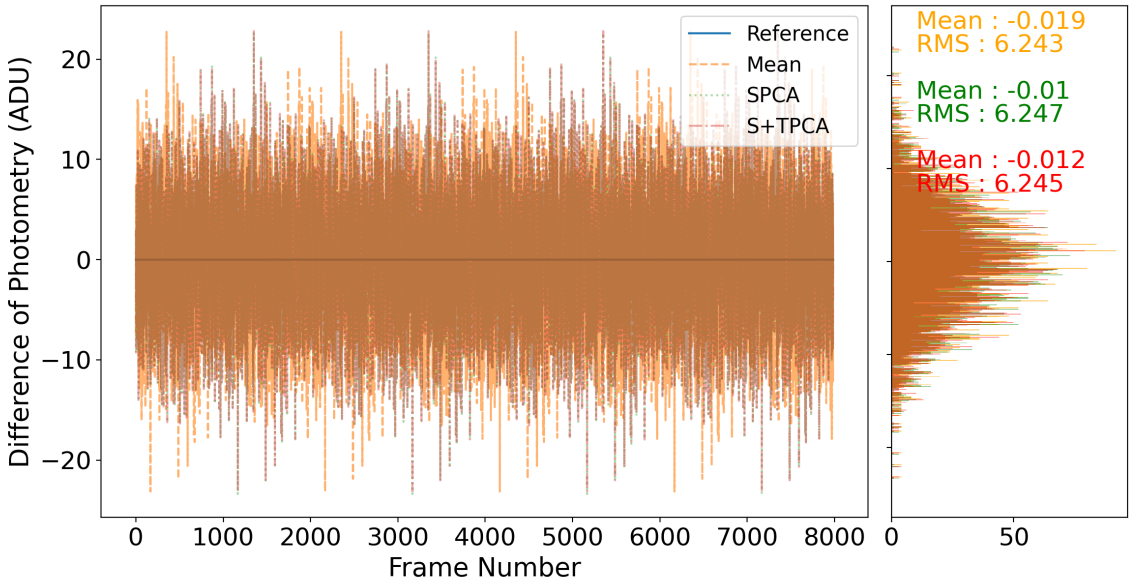

Figure 6.1: Difference of the measured photometry with respect to the injected photometry, per frame, obtained after the mean (orange), spatial PCA(green) and spatial+temporal PCA (red) background subtractions. The injected source account for 80 counts, without any Poisson noise.

the deviation from the true photometric value of the injected sources for the mean, the spatial PCA and the spatial+temporal PCA background subtraction.

Figure 6.1 shows in its right panel the mean values of the differences between the real photometry and the photometry obtained by the methods, for each frame. For each method we observe a slight under-subtraction. However, the mean background subtraction is the method with the largest mean difference, and the spatial PCA is the method with the smallest one. In a case like the one presented in Figure 6.1, no background structures are left to correct, so that the temporal correction cannot add any benefits to the spatial PCA background subtraction alone, but will only add some noise. However, we can still verify with Figure 6.1 that this additional correction does not add any significant over-subtraction.

Bibliography

1. Absil, O. *et al.* A near-infrared interferometric survey of debris-disc stars. III. First statistics based on 42 stars observed with CHARA/FLUOR. *A&A* **555,** A104. https://ui.adsabs.harvard.edu/abs/2013A&A...555A.104A (July 2013).

2. Amara, A., Quanz, S. P. & Akeret, J. PynPoint code for exoplanet imaging. *Astronomy and Computing* **10,** 107–115. https://ui.adsabs.harvard.edu/abs/2015A&C....10..107A (Apr. 2015).

3. Amara, A. & Quanz, S. P. PynPoint: an image processing package for finding exoplanets. *MNRAS* **427,** 948–955. https://ui.adsabs.harvard.edu/abs/2012MNRAS.427..948A (Dec. 2012).

4. Angel, J. R. P. & Woolf, N. J. An Imaging Nulling Interferometer to Study Extrasolar Planets. *ApJ* **475,** 373–379. https://ui.adsabs.harvard.edu/abs/1997ApJ...475..373A (Jan. 1997).

5. Bonse, M. J., Quanz, S. P. & Amara, A. Wavelet based speckle suppression for exoplanet imaging - Application of a de-noising technique in the time domain. *arXiv e-prints,* arXiv:1804.05063. arXiv: 1804.05063 [astro-ph.IM]. https://ui.adsabs.harvard.edu/abs/2018arXiv180405063B (Apr. 2018).

6. Bracewell, R. N. Detecting nonsolar planets by spinning infrared interferometer. *Nature* **274,** 780–781. ISSN: 1476-4687. https://doi.org/10.1038/274780a0 (1978).

7. Cretignier, M., Dumusque, X. & Pepe, F. Stellar activity correction using PCA decomposition of shells. *A&A* **659,** A68. https://ui.adsabs.harvard.edu/abs/2022A&A...659A..68C (Mar. 2022).

8. Czarnik-Matusewicz, B. & Pilorz, S. Study of the temperature-dependent near-infrared spectra of water by two-dimensional correlation spectroscopy and principal components analysis. *Vibrational Spectroscopy* **40,** 235–245. https://ui.adsabs.harvard.edu/abs/2006VibSp..40..235C (Jan. 2006).

9. Defrère, D., Stark, C., Cahoy, K. & Beerer, I. *Direct imaging of exoEarths embedded in clumpy debris disks* in *Space Telescopes and Instrumentation 2012: Optical, Infrared, and Millimeter Wave* (eds Clampin, M. C., Fazio, G. G., MacEwen, H. A. & Oschmann Jr., J. M.) **8442** (Sept. 2012), 84420M. https://ui.adsabs.harvard.edu/abs/2012SPIE.8442E..0MD.

10. Defrère, D. *et al. Co-phasing the Large Binocular Telescope: status and performance of LBTI/PHASECam* in *Optical and Infrared Interferometry IV* (eds Rajagopal, J. K., Creech-Eakman, M. J. & Malbet, F.) **9146** (July 2014), 914609. https://ui.adsabs.harvard.edu/abs/2014SPIE.9146E..09D.

11. Defrère, D. *et al.* Nulling Data Reduction and On-sky Performance of the Large Binocular Telescope Interferometer. *ApJ* **824,** 66. https://ui.adsabs.harvard.edu/abs/2016ApJ...824...66D (June 2016).

12. Defrère, D. *et al.* The path towards high-contrast imaging with the VLTI: the Hi-5 project. *Experimental Astronomy* **46,** 475–495. https://ui.adsabs.harvard.edu/abs/2018ExA....46..475D (Dec. 2018).

13. Defrère, D. *et al.* The HOSTS Survey: Evidence for an Extended Dust Disk and Constraints on the Presence of Giant Planets in the Habitable Zone of β Leo. *AJ* **161,** 186. arXiv: 2103.03268 [astro-ph.EP]. https://ui.adsabs.harvard.edu/abs/2021AJ....161..186D (Apr. 2021).

14. Defrère, D. *et al. L-band nulling interferometry at the VLTI with Asgard/Hi-5: status and plans* in *Optical and Infrared Interferometry and Imaging VIII* (eds Mérand, A., Sallum, S. & Sanchez-Bermudez, J.) **12183** (Aug. 2022), 121830H. arXiv: 2208.08908 [astro-ph.IM]. https://ui.adsabs.harvard.edu/abs/2022SPIE12183E..0HD.

15. Defrère, D. *et al. L-band nulling interferometry at the VLTI with Asgard/NOTT: status and plans* in *Optical and Infrared Interferometry and Imaging IX* (eds Kammerer, J., Sallum, S. & Sanchez-Bermudez, J.) **13095** (Aug. 2024), 130950F. https://ui.adsabs.harvard.edu/abs/2024SPIE13095E..0FD.

16. Ducati, J. R. *VizieR Online Data Catalog: Catalogue of Stellar Photometry in Johnson's 11-color system.* CDS/ADC Collection of Electronic Catalogues, 2237 (2002). Jan. 2002. https://ui.adsabs.harvard.edu/abs/2002yCat.2237....0D.

17. Eckart, C. & Young, G. The approximation of one matrix by another of lower rank. *Psychometrika* **1,** 211–218. ISSN: 1860-0980. https://doi.org/10.1007/BF02288367 (1936).

18. Ertel, S. *et al. The HOSTS survey for exo-zodiacal dust: preliminary results and future prospects* in *Space Telescopes and Instrumentation 2018: Optical, Infrared, and Millimeter Wave* (eds Lystrup, M., MacEwen, H. A., Fazio, G. G., Batalha, N., Siegler, N. & Tong, E. C.) **10698** (July 2018), 106981V. https://ui.adsabs.harvard.edu/abs/2018SPIE10698E..1VE.

19. Ertel, S. *et al.* The HOSTS Survey for Exozodiacal Dust: Observational Results from the Complete Survey. *AJ* **159,** 177. https://ui.adsabs.harvard.edu/abs/2020AJ...159..177E (Apr. 2020).

20. Ertel, S. *et al. Overview and prospects of the LBTI beyond the completed HOSTS survey* in *Optical and Infrared Interferometry and Imaging VII* (eds Tuthill, P. G., Mérand, A. & Sallum, S.) **11446** (Dec. 2020), 1144607. https://ui.adsabs.harvard.edu/abs/2020SPIE11446E..07E.

21. Ertel, S. *et al. Imaging nearby, habitable-zone planets with the Large Binocular Telescope Interferometer* in *Optical and Infrared Interferometry and Imaging VIII* (eds Mérand, A., Sallum, S. & Sanchez-Bermudez, J.) **12183** (Aug. 2022), 1218302. https://ui.adsabs.harvard.edu/abs/2022SPIE12183E..02E.

22. Ertel, S. *et al. The Large Binocular Telescope Interferometer as an ELT pathfinder* in *Adaptive Optics for Extremely Large Telescopes (AO4ELT7)* (June 2023), 35. https://ui.adsabs.harvard.edu/abs/2023aoel.confE..35E.

23. Ertel, S. *et al.* Review and Prospects of Hot Exozodiacal Dust Research For Future Exo-Earth Direct Imaging Missions. *PASP* **137,** 031001. arXiv: 2504.00295 [astro-ph.EP]. https://ui.adsabs.harvard.edu/abs/2025PASP..137c1001E (Mar. 2025).

24. European Southern Observatory. *The VLT White Book* https://ui.adsabs.harvard.edu/abs/1998vltw.book.....E (1998).

25. Fanson, J. *et al. Overview and status of the Giant Magellan Telescope project* in *Ground-based and Airborne Telescopes IX* (eds Marshall, H. K., Spyromilio, J. & Usuda, T.) **12182** (Aug. 2022), 121821C. https://ui.adsabs.harvard.edu/abs/2022SPIE12182E..1CF.

26. Follette, K. B. An Introduction to High Contrast Differential Imaging of Exoplanets and Disks. *PASP* **135,** 093001. https://ui.adsabs.harvard.edu/abs/2023PASP..135i3001F (Sept. 2023).

27. Galicher, R., Marois, C., Macintosh, B., Barman, T. & Konopacky, Q. M-band Imaging of the HR 8799 Planetary System Using an Innovative LOCI-based Background Subtraction Technique. *ApJ* **739,** L41. arXiv: 1107.0967 [astro-ph.EP]. https://ui.adsabs.harvard.edu/abs/2011ApJ...739L..41G (Oct. 2011).

28. Gardner, J. P. *et al. Science with the James Webb space telescope* in *Space Telescopes and Instrumentation I: Optical, Infrared, and Millimeter* (eds Mather, J. C., MacEwen, H. A. & de Graauw, M. W. M.) **6265** (June 2006), 62650N. https://ui.adsabs.harvard.edu/abs/2006SPIE.6265E..0NG.

29. Garreau, G. *et al.* The HOSTS survey: Suspected variable dust emission and constraints on companions around θ Boo. *A&A* **699,** A107. arXiv: 2505.07585 [astro-ph.EP]. https://ui.adsabs.harvard.edu/abs/2025A&A...699A.107G (July 2025).

30. Gillessen, S. *et al. GRAVITY: a four-telescope beam combiner instrument for the VLTI* in *Optical and Infrared Interferometry II* (eds Danchi, W. C., Delplancke, F. & Rajagopal, J. K.) **7734** (July 2010), 77340Y. https://ui.adsabs.harvard.edu/abs/2010SPIE.7734E..0YG.

31. Gilmozzi, R. & Spyromilio, J. The European Extremely Large Telescope (E-ELT). *The Messenger* **127,** 11. https://ui.adsabs.harvard.edu/abs/2007Msngr.127...11G (Mar. 2007).

32. Golub, G. H. & Reinsch, C. Singular value decomposition and least squares solutions. *Numerische Mathematik* **14,** 403–420. ISSN: 0945-3245. https://doi.org/10.1007/BF02163027 (1970).

33. Golub, G. & Kahan, W. Calculating the Singular Values and Pseudo-Inverse of a Matrix. *SIAM Journal on Numerical Analysis* **2,** 205–224. https://ui.adsabs.harvard.edu/abs/1965SJNA....2..205G (Jan. 1965).

34. Gomez Gonzalez, C. A. *et al.* VIP: Vortex Image Processing Package for High-contrast Direct Imaging. *AJ* **154,** 7. https://ui.adsabs.harvard.edu/abs/2017AJ....154...7G (July 2017).

35. Gray, R. O., Napier, M. G. & Winkler, L. I. The Physical Basis of Luminosity Classification in the Late A-, F-, and Early G-Type Stars. I. Precise Spectral Types for 372 Stars. *AJ* **121,** 2148–2158. https://ui.adsabs.harvard.edu/abs/2001AJ....121.2148G (Apr. 2001).

36. Hanot, C., Mennesson, B., Martin, S., Liewer, K., Loya, F., Mawet, D., Riaud, P., Absil, O. & Serabyn, E. Improving Interferometric Null Depth Measurements using Statistical Distributions: Theory and First Results with the Palomar Fiber Nuller. *ApJ* **729,** 110. https://ui.adsabs.harvard.edu/abs/2011ApJ...729..110H (Mar. 2011).

37. He, W. & Zhao, G. A PCA approach to stellar abundances I. testing of the method validity. *Research in Astronomy and Astrophysics* **19,** 140. https://ui.adsabs.harvard.edu/abs/2019RAA....19..140H (Oct. 2019).

38. Hinz, P. M., Angel, J. R. P., Hoffmann, W. F., McCarthy, D. W., McGuire, P. C., Cheselka, M., Hora, J. L. & Woolf, N. J. *First results of nulling interferometry with the Multiple-Mirror Telescope* in *Astronomical Interferometry* (ed Reasenberg, R. D.) **3350** (July 1998), 439–447. https://ui.adsabs.harvard.edu/abs/1998SPIE.3350..439H.

39. Hinz, P. M., Angel, J. R. P., Woolf, N. J., Hoffmann, W. F. & McCarthy, D. W. *BLINC: a testbed for nulling interferometry in the thermal infrared* in *Interferometry in Optical Astronomy* (eds Léna, P. & Quirrenbach, A.) **4006** (July 2000), 349–353. https://ui.adsabs.harvard.edu/abs/2000SPIE.4006..349H.

40. Hotelling, H. (1933) Analysis of a complex of statistical variables into principal components. *Journal of Educational Psychology* **24(6),** 417–441. https://doi.org/10.1037/h0071325.

41. Hunziker, S., Quanz, S. P., Amara, A. & Meyer, M. R. PCA-based approach for subtracting thermal background emission in high-contrast imaging data. *A&A* **611,** A23. https://ui.adsabs.harvard.edu/abs/2018A&A...611A..23H (Mar. 2018).

42. Isbell, J. W. *et al. The LBTI: pioneering the ELT era* in *Optical and Infrared Interferometry and Imaging IX* (eds Kammerer, J., Sallum, S. & Sanchez-Bermudez, J.) **13095** (Aug. 2024), 1309506. https://ui.adsabs.harvard.edu/abs/2024SPIE13095E..06I.

43. Itoh, S. & Matsuo, T. A Coronagraph with a Sub-λ/D Inner Working Angle and a Moderate Spectral Bandwidth. *AJ* **163,** 279. https://ui.adsabs.harvard.edu/abs/2022AJ....163..279I (June 2022).

44. Kasper, M. *et al.* NEAR: Low-mass Planets in α Cen with VISIR. *The Messenger* **169,** 16–20. https://ui.adsabs.harvard.edu/abs/2017Msngr.169...16K (Sept. 2017).

45. Kelsall, T. J., Hauser, M. G., Berriman, G. B., Boggess, N. W., Moseley, S. H., Murdock, T. L., Silverberg, R. F., Spiesman, W. J. & Weiland, J. L. *Investigation of the zodiacal light from 1 to 240 um using COBE DIRBE data* in *Infrared Spaceborne Remote Sensing* (ed Scholl, M. S.) **2019** (Oct. 1993), 190–201. https://ui.adsabs.harvard.edu/abs/1993SPIE.2019..190K.

46. Kennedy, G. M. & Wyatt, M. C. The bright end of the exo-Zodi luminosity function: disc evolution and implications for exo-Earth detectability. *MNRAS* **433,** 2334–2356. https://ui.adsabs.harvard.edu/abs/2013MNRAS.433.2334K (Aug. 2013).

47. Kennedy, G. M. *et al.* Exo-zodi Modeling for the Large Binocular Telescope Interferometer. *ApJS* **216,** 23. https://ui.adsabs.harvard.edu/abs/2015ApJS..216...23K (Feb. 2015).

48. Kim, M., Keller, D. & Bustamante, C. Differential polarization imaging. I. Theory. *Biophysical Journal* **52,** 911–927. ISSN: 0006-3495. https://www.sciencedirect.com/science/article/pii/S000634958783285X (1987).

49. Labeyrie, A. Interference fringes obtained on Vega with two optical telescopes. *ApJ* **196,** L71–L75. https://ui.adsabs.harvard.edu/abs/1975ApJ...196L..71L (Mar. 1975).

50. Lafrenière, D., Marois, C., Doyon, R., Nadeau, D. & Artigau, É. A New Algorithm for Point-Spread Function Subtraction in High-Contrast Imaging: A Demonstration with Angular Differential Imaging. *ApJ* **660,** 770–780. https://ui.adsabs.harvard.edu/abs/2007ApJ...660..770L (May 2007).

51. Lebreton, J., Beichman, C., Bryden, G., Defrère, D., Mennesson, B., Millan-Gabet, R. & Boccaletti, A. Models of the η Corvi Debris Disk from the Keck Interferometer, Spitzer, and Herschel. *ApJ* **817,** 165. https://ui.adsabs.harvard.edu/abs/2016ApJ...817..165L (Feb. 2016).

52. Long, J. D. *et al.* Improved Companion Mass Limits for Sirius A with Thermal Infrared Coronagraphy Using a Vector-apodizing Phase Plate and Time-domain Starlight-subtraction Techniques. *AJ* **165,** 216. arXiv: 2303.05559 [astro-ph.EP]. https://ui.adsabs.harvard.edu/abs/2023AJ....165..216L (May 2023).

53. Lyot, B. L'Etude de la Couronne Solaire en Dehors des Eclipses. *L'Astronomie* **45,** 248–253. https://ui.adsabs.harvard.edu/abs/1931LAstr..45..248L (Jan. 1931).

54. Marois, C., Lafrenière, D., Doyon, R., Macintosh, B. & Nadeau, D. Angular Differential Imaging: A Powerful High-Contrast Imaging Technique. *ApJ* **641,** 556–564. https://ui.adsabs.harvard.edu/abs/2006ApJ...641..556M (Apr. 2006).

55. Marshall, J. P. *et al.* Herschel observations of the debris disc around HIP 92043. *A&A* **557,** A58. https://ui.adsabs.harvard.edu/abs/2013A&A...557A..58M (Sept. 2013).

56. Mayor, M. & Queloz, D. A Jupiter-mass companion to a solar-type star. *Nature* **378,** 355–359. https://ui.adsabs.harvard.edu/abs/1995Natur.378..355M (Nov. 1995).

57. Mennesson, B. *et al.* Constraining the Exozodiacal Luminosity Function of Main-sequence Stars: Complete Results from the Keck Nuller Mid-infrared Surveys. *ApJ* **797,** 119. https://ui.adsabs.harvard.edu/abs/2014ApJ...797..119M (Dec. 2014).

58. Michelson, A. A. & Pease, F. G. Measurement of the Diameter of α Orionis with the Interferometer. *ApJ* **53,** 249–259. https://ui.adsabs.harvard.edu/abs/1921ApJ...53..249M (May 1921).

59. Michelson, A. A. I. On the application of interference methods to astronomical measurements. *The London, Edinburgh, and Dublin Philosophical Magazine and Journal of Science* **30,** 1–21. https://doi.org/10.1080/14786449008619983 (1890).

60. Millan-Gabet, R. *et al.* Exozodiacal Dust Levels for Nearby Main-sequence Stars: A Survey with the Keck Interferometer Nuller. *ApJ* **734,** 67. https://ui.adsabs.harvard.edu/abs/2011ApJ...734...67M (June 2011).

61. Morales, F. Y., Padgett, D. L., Bryden, G., Werner, M. W. & Furlan, E. WISE Detections of Dust in the Habitable Zones of Planet-bearing Stars. *ApJ* **757,** 7. https://ui.adsabs.harvard.edu/abs/2012ApJ...757....7M (Sept. 2012).

62. Moretti, M. I., Hatzidimitriou, D., Karampelas, A., Sokolovsky, K. V., Bonanos, A. Z., Gavras, P. & Yang, M. Variability search in M 31 using principal component analysis and the Hubble Source Catalogue. *MNRAS* **477,** 2664–2683. https://ui.adsabs.harvard.edu/abs/2018MNRAS.477.2664M (June 2018).

63. Nuñez, P. D. *et al.* A near-infrared interferometric survey of debris-disc stars. VI. Extending the exozodiacal light survey with CHARA/JouFLU. *A&A* **608,** A113. https://ui.adsabs.harvard.edu/abs/2017A&A...608A.113N (Dec. 2017).

64. Ortiz, M. & Galaz, G. Spectral Classification of Galaxies using the Principal Component Analysis: a Web Based Tool. *arXiv e-prints,* arXiv:0909.3670. https://ui.adsabs.harvard.edu/abs/2009arXiv0909.3670O (Sept. 2009).

65. Pearson, K. LIII. On lines and planes of closest fit to systems of points in space. *The London, Edinburgh, and Dublin Philosophical Magazine and Journal of Science* **2,** 559–572. https://doi.org/10.1080/14786440109462720 (1901).

66. Rigley, J. K. & Wyatt, M. C. Dust size and spatial distributions in debris discs: predictions for exozodiacal dust dragged in from an exo-Kuiper belt. *MNRAS* **497,** 1143–1165. https://ui.adsabs.harvard.edu/abs/2020MNRAS.497.1143R (Sept. 2020).

67. Roberge, A., Chen, C. H., Millan-Gabet, R., Weinberger, A. J., Hinz, P. M., Stapelfeldt, K. R., Absil, O., Kuchner, M. J. & Bryden, G. The Exozodiacal Dust Problem for Direct Observations of Exo-Earths. *PASP* **124,** 799. https://ui.adsabs.harvard.edu/abs/2012PASP..124..799R (Aug. 2012).

68. Rousseau, H., Ertel, S., Defrère, D., Faramaz, V. & Wagner, K. Improving mid-infrared thermal background subtraction with principal component analysis. *A&A* **687,** A147. https://ui.adsabs.harvard.edu/abs/2024A&A...687A.147R (July 2024).

69. Rousseau, H., Defrère, D., Ertel, S., Faramaz, V. & Wagner, K. *Pushing ELT's sensitivity through PCA background subtraction* in *Adaptive Optics for Extremely Large Telescopes (AO4ELT7)* (June 2023), 53. https://ui.adsabs.harvard.edu/abs/2023aoel.confE..53R.

70. Samland, M., Bouwman, J., Hogg, D. W., Brandner, W., Henning, T. & Janson, M. TRAP: a temporal systematics model for improved direct detection of exoplanets at small angular separations. *A&A* **646,** A24. arXiv: 2011.12311 [astro-ph.EP]. https://ui.adsabs.harvard.edu/abs/2021A&A...646A..24S (Feb. 2021).

71. Sanders, G. H. The Thirty Meter Telescope (TMT): An International Observatory. *Journal of Astrophysics and Astronomy* **34,** 81–86. https://ui.adsabs.harvard.edu/abs/2013JApA...34...81S (June 2013).

72. Singh, H. P., Gulati, R. K. & Gupta, R. Stellar Spectral Classification using Principal Component Analysis and Artificial Neural Networks. *MNRAS* **295,** 312–318. https://ui.adsabs.harvard.edu/abs/1998MNRAS.295..312S (Apr. 1998).

73. Smith, W. H. Spectral differential imaging detection of planets about nearby stars. *Publications of the Astronomical Society of the Pacific* **99,** 1344. https://dx.doi.org/10.1086/132124 (1987).

74. Soummer, R., Pueyo, L. & Larkin, J. Detection and Characterization of Exoplanets and Disks Using Projections on Karhunen-Loève Eigenimages. *ApJ* **755,** L28. https://ui.adsabs.harvard.edu/abs/2012ApJ...755L..28S (Aug. 2012).

75. Spalding, E. *et al. The GLINT nulling interferometer: improving nulls for high-contrast imaging* in *Optical and Infrared Interferometry and Imaging IX* (eds Kammerer, J., Sallum, S. & Sanchez-Bermudez, J.) **13095** (Aug. 2024), 1309507. https://ui.adsabs.harvard.edu/abs/2024SPIE13095E..07S.

76. Sturm, M. C. in *Collected Works of Charles François Sturm* (ed Pont, J.-C.) 323–326 (Birkhäuser Basel, Basel, 2009). ISBN: 978-3-7643-7990-2. https://doi.org/10.1007/978-3-7643-7990-2_24.

77. Wagner, K. *et al.* Imaging low-mass planets within the habitable zone of α Centauri. *Nature Communications* **12,** 922. https://ui.adsabs.harvard.edu/abs/2021NatCo..12..922W (Jan. 2021).

78. Werber, Z., Wagner, K. & Apai, D. The Direct Mid-infrared Detectability of Habitable-zone Exoplanets around Nearby Stars. *AJ* **165,** 133. https://ui.adsabs.harvard.edu/abs/2023AJ....165..133W (Mar. 2023).

79. Wetherill, G. W. Possible Consequences of Absence of "Jupiters" in Planetary Systems. *Ap&SS* **212,** 23–32. https://ui.adsabs.harvard.edu/abs/1994Ap&SS.212...23W (Feb. 1994).

80. Wilkinson, J. H. The calculation of the latent roots and vectors of matrices on the pilot model of the A.C.E. *Proceedings of the Cambridge Philosophical Society* **50,** 536–566. https://ui.adsabs.harvard.edu/abs/1954PCPS...50..536W (Oct. 1954).

81. Young, T. The Bakerian Lecture: On the Theory of Light and Colours. *Philosophical Transactions of the Royal Society of London Series I* **92,** 12–48. https://ui.adsabs.harvard.edu/abs/1802RSPT...92...12Y (Jan. 1802).

Remerciements

Acknowledgements